# SAFETY ANALYSIS OF NUCLEAR REACTOR THERMAL-HYDRAULICS

EDITED BY: Liangming Pan, Jun Wang, Yanping Huang and Ki-Yong Choi
PUBLISHED IN: Frontiers in Energy Research

frontiers Research Topics

# frontiers



ISSN 1664-8714
ISBN 978-2-88966-870-0
DOI 10.3389/978-2-88966-870-0

## About Frontiers

Frontiers is more than just an open-access publisher of scholarly articles: it is a pioneering approach to the world of academia, radically improving the way scholarly research is managed. The grand vision of Frontiers is a world where all people have an equal opportunity to seek, share and generate knowledge. Frontiers provides immediate and permanent online open access to all its publications, but this alone is not enough to realize our grand goals.

## Frontiers Journal Series

The Frontiers Journal Series is a multi-tier and interdisciplinary set of open-access, online journals, promising a paradigm shift from the current review, selection and dissemination processes in academic publishing. All Frontiers journals are driven by researchers for researchers; therefore, they constitute a service to the scholarly community. At the same time, the Frontiers Journal Series operates on a revolutionary invention, the tiered publishing system, initially addressing specific communities of scholars, and gradually climbing up to broader public understanding, thus serving the interests of the lay society, too.

## Dedication to Quality

Each Frontiers article is a landmark of the highest quality, thanks to genuinely collaborative interactions between authors and review editors, who include some of the world's best academicians. Research must be certified by peers before entering a stream of knowledge that may eventually reach the public - and shape society; therefore, Frontiers only applies the most rigorous and unbiased reviews.
Frontiers revolutionizes research publishing by freely delivering the most outstanding research, evaluated with no bias from both the academic and social point of view. By applying the most advanced information technologies, Frontiers is catapulting scholarly publishing into a new generation.

## What are Frontiers Research Topics?

Frontiers Research Topics are very popular trademarks of the Frontiers Journals Series: they are collections of at least ten articles, all centered on a particular subject. With their unique mix of varied contributions from Original Research to Review Articles, Frontiers Research Topics unify the most influential researchers, the latest key findings and historical advances in a hot research area! Find out more on how to host your own Frontiers Research Topic or contribute to one as an author by contacting the Frontiers Editorial Office: frontiersin.org/about/contact

# SAFETY ANALYSIS OF NUCLEAR REACTOR THERMAL-HYDRAULICS

Topic Editors:
**Liangming Pan,** Chongqing University, China
**Jun Wang,** University of Wisconsin-Madison, United States
**Yanping Huang,** Nuclear Power Institute of China (NPIC), China
**Ki-Yong Choi,** Korea Atomic Energy Research Institute (KAERI), South Korea

**Citation:** Pan, L., Wang, J., Huang, Y., Choi, K.-Y., eds. (2021). Safety Analysis of Nuclear Reactor Thermal-Hydraulics. Lausanne: Frontiers Media SA. doi: 10.3389/978-2-88966-870-0

# Table of Contents

frontiers in Energy Research

EDITORIAL
published: 15 April 2021
doi: 10.3389/fenrg.2021.652233

# Editorial: Safety Analysis of Nuclear Reactor Thermal-Hydraulics

*Liangming Pan*[1], *Jun Wang*[2]*, *Yanping Huang*[3] and *Ki-Yong Choi*[4]

[1] School of Energy and Power Engineering, Chongqing University, Chongqing, China, [2] Department of Engineering Physics, University of Wisconsin-Madison, Madison, WI, United States, [3] CNNC Key Laboratory on Nuclear Reactor Thermal Hydraulics Technology, Nuclear Power Institute of China, Chengdu, China, [4] Thermal Hydraulics Safety Research Division, Korea Atomic Energy Research Institute, Daejeon, South Korea

**Keywords: safety, nuclear reactor, thermal hydraulics, critical heat flux, small modular reactor**

## Editorial on the Research Topic

## Safety Analysis of Nuclear Reactor Thermal-Hydraulics

A large number of nuclear power plants are under construction in Asia (McDonald, 2008). Thereby, the demand for research on reactor design and thermal hydraulics is of high priority (Sovacool, 2010). Prof. Liangming Pan from Chongqing University holds the 9th China–Korea Workshop on Nuclear Reactor Thermal–Hydraulic in 2019. There are many high-quality conference papers submitted. To select and publish the top articles in the conferences, Prof. Pan leads the Research Topic "Safety Analysis of Nuclear Reactor Thermal Hydraulics" in the journal *Frontiers in Energy Research*. Finally, 11 articles are collected, covering the experimental and numerical research, from light water to liquid metal and supercritical coolant.

There are several articles about the safety of light water reactors. Kim J. et al. contribute the "integral effect test on top-spot break scenario with 4 inches cold leg break LOCA in ATLAS Facility." Kim H. T. et al. present their "Simulation of a Station Blackout Accident for the SMART using the CINEMA Code." Du et al. write the "review of regime maps of steam submerged direct contact condensation."

Meanwhile, there are several pieces of research about the bubble and critical heat flux. Yu et al. work on the "experimental study of bubbly-slug flow transition criteria in a vertical circular tube by using WMS." Liu et al. publish the "assessment of a theoretical model to predicting forced convective critical heat flux in rod bundles." Park and Chung contribute the "simulation of critical heat flux phenomenon using a non-heating hydrogen evolving system."

There is also research on advanced reactors. Xiang et al. show their "Study on natural circulation heat transfer characteristics of different liquid metals based on factor analysis." Lv et al. present "A Critical Flow Model For Supercritical Pressures."

Finally, this Research Topic also involves work on small modular reactors and microreactors. For example, Zhang et al. publish "Thermoelectric Conversion Performance of Combined Thermoions System for Space Nuclear Power Supply." Yuan et al. show the work about "Numerical Simulation of Flow Boiling in Small Channel of Plate OTSG." Wang et al. contributes to the "Rod Ejection and Drop Accident Analysis of Aqueous Homogeneous Solution Reactor."

After almost 1-year revision and update, this Research Topic finally selected those 11 articles and published them in the journal *Frontiers in Energy Research*.

OPEN ACCESS

***Edited and reviewed by:***
*Wenzhong Zhou,*
*Sun Yat-Sen University, China*

***Correspondence:**
*Jun Wang*
*jwang564@wisc.edu*

***Specialty section:***
*This article was submitted to Nuclear Energy, a section of the journal Frontiers in Energy Research*

***Received:*** *12 January 2021*
***Accepted:*** *25 February 2021*
***Published:*** *15 April 2021*

***Citation:***
*Pan L, Wang J, Huang Y and Choi K-Y (2021) Editorial: Safety Analysis of Nuclear Reactor Thermal-Hydraulics. Front. Energy Res. 9:652233. doi: 10.3389/fenrg.2021.652233*

It allows showing those high-quality work to the public who do not have a chance to attend this meeting. The journal *Frontiers in Energy Research* will permit publishing more articles from international conferences. All the editors are open to contact for further information.

## AUTHOR CONTRIBUTIONS

LP is the leading author. JW is the contacting author. YH and K-YC are senior people. All authors contributed to the article and approved the submitted version.

## REFERENCES

McDonald, A. (2008). Nuclear power global status. *IAEA Bull.* 49:45. Available online at: https://www.iaea.org/sites/default/files/49204734548.pdf

Sovacool, B. K. (2010). A critical evaluation of nuclear power and renewable electricity in Asia. *J. Contemp. Asia* 40, 369–400. doi: 10.1080/00472331003798350

**Conflict of Interest:** The authors declare that the research was conducted in the absence of any commercial or financial relationships that could be construed as a potential conflict of interest.

frontiers in Energy Research

BRIEF RESEARCH REPORT
published: 28 November 2019
doi: 10.3389/fenrg.2019.00138

# Rod Ejection and Drop Accident Analysis of Aqueous Homogeneous Solution Reactor

*Kunpeng Wang*[1], *Chao Xu*[1], *Congxin Li*[1]*, *Yusheng Liu*[1], *Jianping Jing*[1] and *Hongchun Wu*[2]

[1] Nuclear and Radiation Safety Center, Beijing, China, [2] School of Nuclear Science and Technology, Xi'an Jiaotong University, Xi'an, China

Aqueous Homogeneous Solution Reactor concept has been proposed for producing medical isotopes (Medical Isotope Production Reactor-MIPR). However, there are several difficulties in transient calculation of aqueous homogeneous solution reactors. First, there are no assemblies in the core which is different from the traditional reactor core. Second, the operation of aqueous solution reactor at a power of 200 kW will generate radiolytic-gas bubbles. The void volume created by these bubbles in the solution core will introduce a strong negative reactivity feedback. Third, the complex structure of the coolant pipes immersed in fuel solution requires unstructured neutron diffusion calculation methods. Therefore, analytic basis functions expansion nodal method for arbitrary triangular-z node is established to solve the complex structure geometry neutron diffusion equation. Based on this, a software named TABFEN-K has been developed to solve the three-dimensional space-time neutron kinetic equations. Then, TABFEN-K code is used for typical accident analysis of a solution reactor. A simplified geometry model, bubbles generation model, thermal conduction model, and cross section feedback model are given in this paper. A software called TABFEN-MIPR is developed and used for the simulations of the control rod ejection and drop. The same characteristics in the transient process with the results from literatures are obtained.

**Keywords: solution reactor, typical accident, dynamic analysis, control rod, neutron diffusion**

OPEN ACCESS

***Edited by:***
*Jun Wang,*
*University of Wisconsin-Madison, United States*

***Reviewed by:***
*Jun Yang,*
*Huazhong University of Science and Technology, China*
*Tengfei Zhang,*
*Shanghai Jiao Tong University, China*
*Claudio Tenreiro,*
*University of Talca, Chile*

***Correspondence:**
*Congxin Li*
*licongxin@chinansc.cn*

***Specialty section:***
*This article was submitted to Nuclear Energy, a section of the journal Frontiers in Energy Research*

***Received:*** *11 September 2019*
***Accepted:*** *14 November 2019*
***Published:*** *28 November 2019*

***Citation:***
*Wang K, Xu C, Li C, Liu Y, Jing J and Wu H (2019) Rod Ejection and Drop Accident Analysis of Aqueous Homogeneous Solution Reactor. Front. Energy Res. 7:138. doi: 10.3389/fenrg.2019.00138*

## INTRODUCTION

Other than the irradiation of uranium targets in heterogeneous reactors, aqueous homogeneous solution reactors is an alternative way to produce medical isotopes (Ball, 1997). Based on many potential advantages of aqueous homogeneous solution reactors, the Medical Isotope Production Reactor (MIPR) concept has been proposed for producing medical isotopes.

However, many difficulties exist in transient calculation of aqueous homogeneous solution reactors (Briesmeister, 2002). First, there are no assemblies in the core which is very different from the traditional reactor core. Second, the operation of aqueous solution reactor at a power of 200 kW will generate radiolytic-gas bubbles. The void volume created by these bubbles in the solution core will introduce a strong negative reactivity feedback (Dunenfeld and Stitt, 1963). Third, the complex structure of the coolant pipes immersed in fuel solution requires unstructured neutron diffusion calculation methods (Lecorche and Seale, 1973).

Therefore, analytic basis functions expansion nodal method for arbitrary triangular-z node is established to solve the complex structure geometry neutron diffusion equation. The distribution of detailed neutron flux within each node is expanded into the sum of a set of analytic basis functions by accurately formulating the multi-group matrix form neutron diffusion equation and appropriately choosing the expansion order and characteristically directions. To balance between accuracy and efficiency, adjacent nodes are coupled with each other through the zero- and first-order partial current moments defined at the interface. Coordinate conversion technique is used to transform arbitrary triangle into a regular triangle to simplify the derivation of the response matrix between the incoming and outgoing partial currents. A new sweeping scheme is designed for the triangular-z node to solve the nodal diffusion equation iteratively. Then, this analytic basis function expansion nodal method is extended for solving the space-time neutron kinetic equations. The efficient fully implicit difference method is applied to discretize the time variable of the prompt neutron diffusion equation together with the time integration method employed to handle the delayed neutron precursor equations. At each step after the time variable discretization, a fixed source neutron diffusion equation is obtained. Different from the steady-state case, an intranodal neutron flux consists of two components, they are an analytic basis function expanded homogeneous terms and a heterogeneous term which can be approximated into a second-order orthogonal polynomial. Similar to the steady-state, nodal averaged volume flux and surface partial current moments are calculated by introducing the coordinate conversion scheme. Based on this, a code named TABFEN-K has been developed to solve the three-dimensional space-time neutron kinetic equations.

At last, the TABFEN-K code is used for typical accident analysis of a solution reactor. The simplified geometry model, bubbles generation model and the thermal conduction model of solution reactor are given together with the cross section feedback model. A code called TABFEN-MIPR is developed and used for the simulations of the control rod ejection and drop accident. The same characteristics in the transient process with the results from literatures are obtained.

## Calculation Model

The simplified geometry model, bubbles generation model, and the thermal conduction model of solution reactor are given together with the cross section feedback model.

## Solution of the Diffusion Equation

In a particular homogeneous mesh, the matrix form of the standard multigroup neutron diffusion equation in triangular geometry can be written as (Noh and Cho, 1993, 1994; Nam Zin and Noh, 1995):

$$-\nabla^2\Phi(\mathbf{r})+\Sigma\left(k_{\text{eff}}\right)\Phi(\mathbf{r})=0 \tag{1}$$

where $\Phi(\boldsymbol{r})=\text{col}\{\Phi_1(\boldsymbol{r}),\Phi_2(\boldsymbol{r}),...,\Phi_G(\boldsymbol{r})\}$ is the neutron flux and $\Phi_G(\mathbf{r})$ denotes the G-th group neutron flux; the matrix $\Sigma\left(k_{\text{eff}}\right)$ is a square matrix of order G with its elements $\sum_{gg'}$ as follows:

$$\sum_{gg'}=\left(\delta_{gg'}\sum_{t}^{g}-\sum_{s}^{g'-g}-\frac{\chi^g}{k_{\text{eff}}}\nu\sum_{f}^{g'}\right)/D^g \tag{2}$$

where $\delta_{gg'}$ is the Kronecker symbol and the other notations are as in conventional manner.

The solution of the diffusion Equation (1) depends on whether the eigenvalues $\lambda_m$ and corresponding eigenvectors $u_m$ of the matrix $\Sigma\left(k_{\text{eff}}\right)$ are real or complex. For simplicity, we present our derivation here only for the case in which the eigenvalues are real. In fact, the eigenvalues are exactly real for two-group problem. Then, $\Psi(\mathbf{r})$ is introduced as:

$$\mathbf{U}=[\mathbf{u}_1,\mathbf{u}_2,...,\mathbf{u}_G] \tag{3}$$

$$\Psi(\mathbf{r})=\mathbf{U}^{-1}\Phi(\mathbf{r}) \tag{4}$$

Substitute Equation (4) to Equation (1) to reduce Equation (1) to a decoupled form

$$-\nabla^2\Psi_m(\mathbf{r})+\lambda_m\Psi_m(\mathbf{r})=0,\ \ m=1\ldots G \tag{5}$$

Equation (5) is a typical Helmholz equation with analytical solution

$$\Psi_m(\mathbf{r})=\sum_{l=1}^{\infty}\left[A_{ml}e^{\sqrt{\lambda_m}\mathbf{e}_l\mathbf{r}}+B_{ml}e^{-\sqrt{\lambda_m}\mathbf{e}_l\mathbf{r}}\right] \tag{6}$$

where $\mathbf{e}_l$ is an arbitrary unit vector. In practice, the number of terms l in Equation (6) mainly depends on the number of the available nodal boundary conditions. Generally speaking, the higher of the terms result in higher accuracy but lower calculation speed, vice versa. For triangular geometry, 3 interfaces' averaged partial current and first-order partial current moment are chosen as the coupling condition to determine the expansion coefficients. Therefore, Equation (6) can be written as:

$$\Psi_m(\mathbf{r})=\begin{cases}\sum_{l=1}^{3}A_{ml}Sinh\left(k_m\mathbf{e}_l\mathbf{r}\right)+\sum_{l=1}^{3}B_{ml}Cosh\left(k_m\mathbf{e}_l\mathbf{r}\right), & \lambda_m>0\\ \sum_{l=1}^{3}A_{ml}Sin\left(k_m\mathbf{e}_l\mathbf{r}\right)+\sum_{l=1}^{3}B_{ml}Cos\left(k_m\mathbf{e}_l\mathbf{r}\right), & \lambda_m<0\end{cases} \tag{7}$$

where $k_m=\sqrt{|\lambda_m|}$, by using Equation (5) and Equation (7), the intranodal flux distribution can be eventually obtained as:

$$\Phi_g(\mathbf{r})=\begin{cases}\sum_{m=1}^{G}u_{gm}\left(\sum_{l=1}^{3}A_{ml}Sinh\left(k_m\mathbf{e}_l\mathbf{r}\right)+\sum_{l=1}^{3}B_{ml}Cosh\left(k_m\mathbf{e}_l\mathbf{r}\right)\right), & \lambda_m>0\\ \sum_{m=1}^{G}u_{gm}\left(\sum_{l=1}^{3}A_{ml}Sin\left(k_m\mathbf{e}_l\mathbf{r}\right)+\sum_{l=1}^{3}B_{ml}Cos\left(k_m\mathbf{e}_l\mathbf{r}\right)\right), & \lambda_m<0\end{cases} \tag{8}$$

where $u_{gm}$ is the element of the matrix **U** defined in Equation (3).

Based on this, a code named TABFEN-K has been developed for solving the three-dimensional space-time neutron kinetic equations. The code is verified by 3D-LMW, 3D-LRA benchmarks. Both the relative power and power distribution are in good agreement with the benchmarks (Ban et al., 2012).

### Void Bubbles Model

In aqueous homogeneous solution reactors, void bubbles affect the core state by changing the density and volume of fuel solution. The change of fuel solution density was considered by interpolating macroscopic cross-sections in terms of void fraction, while the volume change of fuel solution was considered by modifying the height of fuel solution surface.

In the volume calculation of void bubbles, the total void volume is given by (Souto et al., 2005).

$$\bar{V}_B = \left(1 + \frac{1}{\xi}\right) \frac{G\left(H_2\right)}{N_A} R_g T_g \left(\frac{r_B}{2\sigma}\right) \tau_B \cdot \bar{n} \tag{9}$$

where

$\bar{V}_B$ : total void volume ($m^3$);

$\bar{n}$ : the reactor power (MW);

$G\left(H_2\right)$ : hydrogen yield in fuel solution ($J^{-1}$);

$\xi$ : fraction of $H_2$ molecules per $O_2$ molecule produced by water radiolysis;

$N_A$ : Avogadro's constant ($mol^{-1}$);

$R_g$ : gas constant ($J{\cdot}mol^{-1}{\cdot}K^{-1}$);

$T_g$: void bubble temperature (K);

$r_B$ : void bubble characteristic radius (um);

$\sigma$ : fuel solution surface tension ($Kg{\cdot}s^{-1}$);

$\tau_B$ : the characteristic time for void bubble release from the fuel solution (s).

The distributions of void bubbles in radial and axial direction are different. In radial direction, void distribution is decided by radial power distribution; while in axial direction by the law of axial void movement. In this paper, it assumes that void distribution in axial direction obeys integral power distribution.

Fuel solution volume expansion is caused by generation of void bubbles and thermal expansion and contraction of the fuel solution. The increment of the fuel solution volume can be determined by

$$\Delta V = V_{Void} + \Delta V_{Hot} = V_{Void} + \left(\frac{\rho_{Cold}}{\rho_{Power}} - 1\right) \cdot V_{Cold} \tag{10}$$

where

$V_{Void}$ : total void volume ($cm^3$);

$\Delta V_{Hot}$ : solution volume increment caused by thermal expansion and contraction ($cm^3$);

$\rho_{Cold}$ : density of cold solution (g/l);

$\rho_{Power}$ : density of hot solution (g/l);

$V_{Cold}$ : volume of cold solution ($cm^3$).

## Temperature Model

The solution of the fluidity of liquid fuel, combined with the solution of smaller volume, so that the temperature of the solution of liquid fuel is equal, then according to the quantity of heat production and export, the calculation formula of fuel solution can be written as:

$$\frac{dT(t)}{dt} = \frac{1}{c_f m_f} p(t) - \frac{1}{\tau_T}(T(t) - T_0) \tag{11}$$

where

$c_f$ : specific heat capacity (J/Kg/K);

$m_f$ : Solution fuel weight (kg);

$p\,(t)$ : Power (W);

$\tau_t$ : Characteristics of the time (s);

$T(t)$ : volume of cold solution (K).

## Few-Group Constants Fitting

The few-group constants are fitted with the following form

$$\Sigma_x = f_1\,(Bu)\, f_2\,(v)\, f_3\left(p\right) + f_4\,(Bu) \cdot \delta\,(Cr) \tag{12}$$

where

$f_i\,(x)$ $(i = 1,2,3,4)$: a polynomial of variable x;

$\delta\,(Cr)$ : a dirac function which equals to 1 or 0 when control rods exist or not;

$Bu$ : burnup (MW·d/tU);

$v$ : void fraction;

$p$ : relative power.

At last, the TABFEN-K code is used for typical accident analysis of a solution reactor. The simplified geometry model, bubbles generation model and the thermal conduction model of solution reactor are given together with the cross section feedback model. A code called TABFEN-MIPR is developed.

### Numerical Results

The structure and material of the aqueous homogeneous solution reactor are given in **Figures 1**, **2** gives the radial mesh of the core used in the calculation, respectively.

The code TABFEN-MIPR is used for the simulations of the control rod ejection and drop accident. The same characteristics in the transient process with the results from literatures are obtained. At the beginning, the power of MIPR is 0.033MW, the temperature of the fuel solution is 344.4164K, the volume of bubble is 376.2742 $cm^3$. The control rods are at 25.68 cm from the bottom of the core.

### Rods Ejection Accident

Rods ejection accident belongs to the limit accident, accident control rod in the pop-up core in the process of introducing positive reactivity, which can cause power has arisen sharply, the safety of the pile is affected by the great, usually is the focus of the nuclear safety analysis of the research object. For rods ejection accident, the control rods eject to the top of the core at 32.05 cm, in this case 1,143 pcm reactivity are introduced. **Figure 3** gives the solution of ejection rod in the change of the power, **Figure 4**

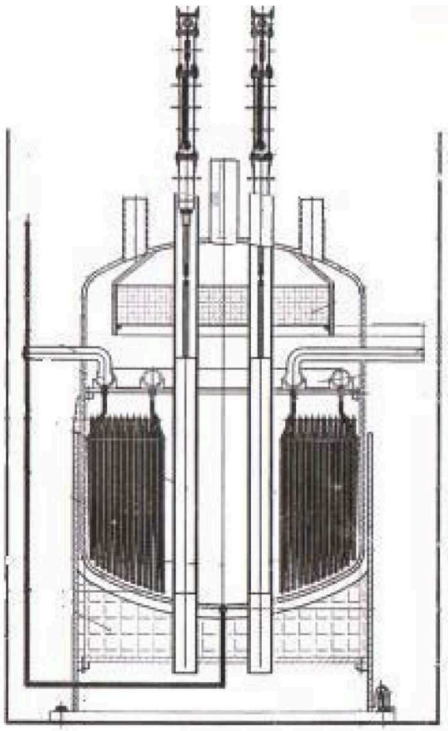

**FIGURE 1 |** Structure of MIPR.

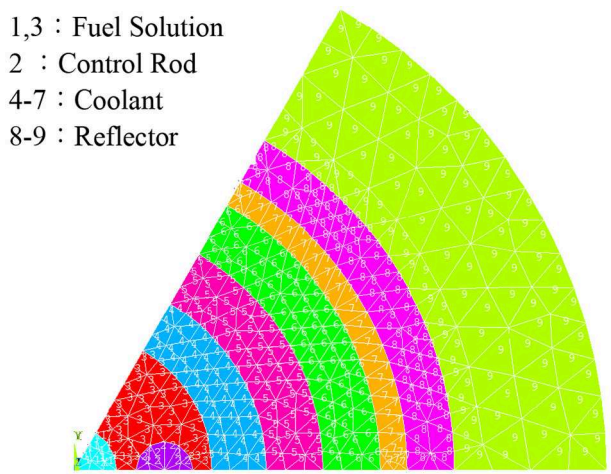


**FIGURE 2 |** The radial meshing map of MIPR.

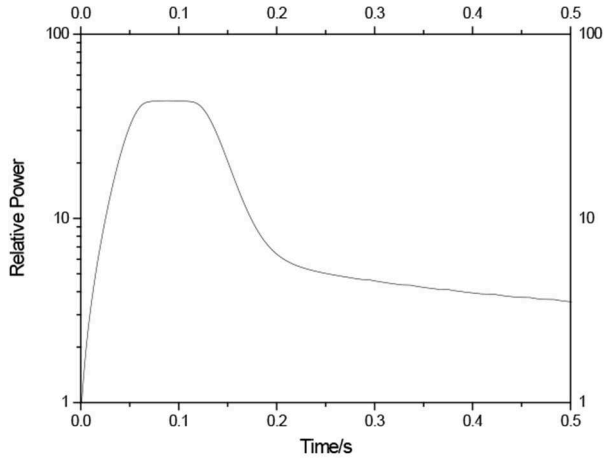


**FIGURE 3 |** Relative power variation over time.

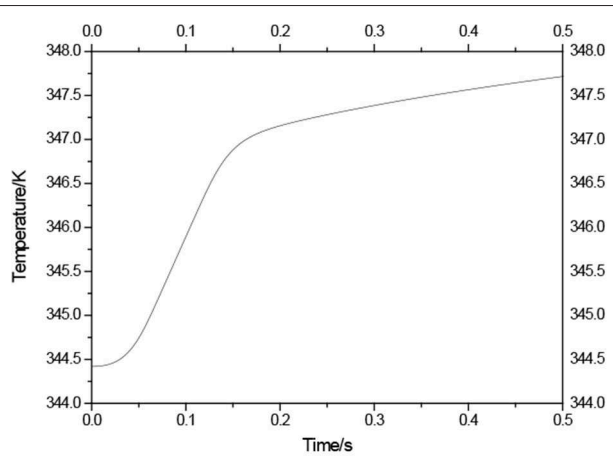


**FIGURE 4 |** Temperature variation over time.

gives the corresponding solution temperature and bubble content changes over time. We can find that, after the control rod pop-up, due to the introduction of larger positive reactivity, power rises rapidly in a short time, because of the heat transfer lag, the temperature of the fuel and air bubble content is slowly rising, then began to rapid increase in power; The increment of fuel temperature and bubble content, in turn, has affected the nuclear reaction cross section, the comprehensive result of negative feedback effect to power up to a certain value began to decline, with declining power, and the solution temperature and content of bubble growth began to slow, finally the change of power tend to flat, and finally stability on above the level of the power of the initial time, temperature, and bubble content at this time also started to become stable, and keep on the above the level of the initial time. Because of solution temperature and bubble content, are under the influence of power, has obvious lag in time, **Figure 4** also shows that the change of the solution temperature and air bubbles curve shape is consistent, and lagging behind the growth of the power, hence TABFEN-MIPR calculation results conform to play well the transient progress regularity of the accident.

## Rod Drop Accident

For rods drop accident, the control rods drop to the core at 20 cm, in this case −1,733 pcm reactivity are introduced. The negative reactivity caused power drops rapidly, but due to the

solution of temperature and air bubbles in the feedback, is likely to lead to power fluctuations, may also cause reactor shutdown, therefore must also be analyzed. The results show that, at the beginning of the rod drop, core into larger negative reactivity, core power fells sharply; With declining power, temperature, and decreases in the bubble content and temperature of the solution and the bubble content is introduced to reduce the reactivity of the reactivity makes for control rod falling into negative reactivity decreases, so power after plunging began to slow down. As the accumulation of feedback effects, stable power eventually below the initial power of the power level. And solution temperature and bubble content change lag, which makes them relatively flat. Therefore, TABFEN—MIPR calculation result is reasonable and accords with the transient progress law of rod drop accident.

## CONCLUSIONS

In this study, TABFEN-K software is used for typical accident analysis of a solution reactor. The simplified geometry model, bubbles generation model and the thermal conduction model of solution reactor are given together with the cross section feedback model. The code TABFEN-MIPR is developed and used for the simulations of the control rod ejection and drop accident. The same characteristics in the transient process with the results from literatures are obtained as well.

## DATA AVAILABILITY STATEMENT

All datasets generated for this study are included in the article/supplementary material.

## AUTHOR CONTRIBUTIONS

KW developed the code and wrote the manuscript. CX performed the calculation. CL edited the manuscript. YL and JJ analyzed the data. HW gave advice and comments. CX, CL and YL gave the technical support. HW and JJ gave advice for this project.

## FUNDING

The research was supported by National Science and Technology Major Project of China (2019ZX06005001).

## REFERENCES

Ball, R. M. (1997). *Medical Isotope Production Reactor [P]*. US: 5596611

Ban, Y., Endo, T., and Yamamoto, A. (2012). A unified approach for numerical calculation of space-dependent kinetic equation[J]. *J. Nucl. Sci. Technol.* 49, 496–515. doi: 10.1080/00223131.2012.677126

Briesmeister, J. F. (2002). *MCNP-A General Monte Carlo N-Particle Transport Code*. Version 4C*, LA-13709–M*.

Dunenfeld, M. S., and Stitt, R. K. (1963). *Summary Review of the Kinetics Experiments on Water Boilers. NAA-SR-7087*. Atomics International.

Lecorche, P., and Seale, R. L. (1973). *Review of the Experiments Performed to Determine the Radiological Consequences of a Criticality Accident*. Y-CDC-12. Oak Ridge National Laboratory.

Nam Zin, C., and Noh, J. M. (1995). Analytic function expansion nodal method for hexagonal geometry. *Nuclear Sci. Eng.* 121, 245–253. doi: 10.13182/NSE95-A28561

Noh, J. M., and Cho, N. Z. (1993). A new diffusion nodal method based on analytic basis function expansion. *Transac. Am. Nucl. Soc.* 69, 462–463.

Noh, J. M., and Cho, N. Z. (1994). A new approach of analytic basis function expansion to neutron diffusion nodal calculation. *Nucl. Sci. Eng.* 116, 165–180. doi: 10.13182/NSE94-A19811

Souto, F. J., Kimpland, R. H., and Heger, A. S. (2005). Analysis of the effects of radiolytic-gas bubbles on the operation of solution reactors for the production of medical isotopes. *Nucl. Sci. Eng.* 150, 322–335. doi: 10.13182/NSE05-A2519

**Conflict of Interest:** The authors declare that the research was conducted in the absence of any commercial or financial relationships that could be construed as a potential conflict of interest.

frontiers in Energy Research

ORIGINAL RESEARCH
published: 03 December 2019
doi: 10.3389/fenrg.2019.00139

# Simulation of Critical Heat Flux Phenomenon Using a Non-heating Hydrogen Evolving System

*Hae-Kyun Park and Bum-Jin Chung**

*Department of Nuclear Engineering, Kyung Hee University, Seoul, South Korea*

Pool boiling critical heat flux (CHF) at saturated condition was simulated using the hydrogen at the copper cathode in the aqueous solution of sulfuric-acid. The critical current density (CCD) was observed at the cell potential-current density curve, which is analogous to the CHF at the boiling curve. The CHF values calculated by the gas generation rate at the CCD condition showed large discrepancies with the existing CHF values of water boiling system. Meanwhile, the superficial mechanism triggering the CHF and the CCD showed similar characteristics except the size of bubbles. The variation of bubble departure volume with respect to the current density was similar to that of the water vapor but the bubble volume of the present system was 440 times smaller at CCD condition. The critical heat flux value using the present non-heating experiment was corrected accounting for the bubble volumes and the discrepancy with the water CHF was <10%. It is concluded that the water CHF condition can be simulated by the non-heating hydrogen evolving system.

**Keywords: critical heat flux, critical current density, hydrogen evolving system, bubble departure volume, cell potential curve, boiling curve**

OPEN ACCESS

***Edited by:***
*Liangming Pan,*
*Chongqing University, China*

***Reviewed by:***
*Keyou S. Mao,*
*Purdue University, United States*
*Ivo Kljenak,*
*Jožef Stefan Institute (IJS), Slovenia*
*Luteng Zhang,*
*Chongqing University, China*

***Correspondence:**
*Bum-Jin Chung*
*bjchung@khu.ac.kr*

***Specialty section:***
*This article was submitted to Nuclear Energy, a section of the journal Frontiers in Energy Research*

***Received:*** *30 June 2019*
***Accepted:*** *15 November 2019*
***Published:*** *03 December 2019*

***Citation:***
*Park H-K and Chung B-J (2019) Simulation of Critical Heat Flux Phenomenon Using a Non-heating Hydrogen Evolving System. Front. Energy Res. 7:139. doi: 10.3389/fenrg.2019.00139*

## INTRODUCTION

The nucleate boiling allows larger heat transfer coefficients than the single phase convection. Thus, smaller heat exchangers and cooling devices are expected using the boiling heat transfer. There exists the maximum manageable heat flux resulting in the burnout of the system, critical heat flux (CHF). The surface temperature increased rapidly after the CHF point with heat flux controlled system compared with the temperature controlled system, since the transition boiling regime is not encountered due to the boiling hysteresis (Carey, 2008). Therefore, numerous studies have been devoted to the measurement and modeling of the CHF over half a century (Kutateladze, 1950; Zuber, 1959; Gaertner, 1965; Katto and Yokoya, 1968; Van Ouwerkerk, 1972; Lienhard and Dhir, 1973; Lienhard et al., 1973; Haramura and Katto, 1983; Saylor and Simon, 1989; Sadasivan et al., 1992; Unal et al., 1992; Sturgis and Mudawar, 1999; Kandlikar, 2001; Jeong et al., 2002; Bang et al., 2005; Zhang et al., 2006; Roday and Jensen, 2009; Sakashita and Ono, 2009; Ahn and Kim, 2012; Lloveras et al., 2012; O'Hanley et al., 2013). Particularly, many of CHF researches have been performed for the water-cooled nuclear power plant systems, which are basically heat flux controlled systems, while the conventional fossil-fuelled boilers are temperature controlled system (Groeneveld et al., 2018). Hence, the CHF phenomenon is often regarded as one of the important research issue at the nuclear industry. However, the difficulties in the CHF experiments involve in the phenomenological extreme conditions such as high heat flux over 1,000 kW/m$^2$, the large thermal inertia and thermal expansion which endangers the controlling thermal condition

and integrity of the test facility. The present study motivated by these difficulties and attempted to simulate the water pool boiling CHF at saturated condition using the hydrogen gas evolving system which can be realized using aqueous solution of sulfuric acid with copper anode and cathode as shown in **Figure 1** and the hydrogen reduction process adopted in this study is shown in Equation (1).

$$\text{Cathode}: 2H^+ + 2e^- \rightarrow H_2\uparrow \quad (1)$$

$$\text{Anode}: Cu \rightarrow Cu^{2+} + 2e^- \quad (2)$$

This system enables to avoid experimental difficulties with the boiling systems by replacing the vaporization with the electrochemical reaction. The basic idea comes from the fact that the existing models for the CHF condition were based on the hydrodynamics, which means that if the existing models reflect the nature of the phenomena, any gas bubbles can simulate the CHF condition. Comparisons of bubble behaviors on the both systems were performed to establish the similarities and differences between water pool boiling CHF and the hydrogen evolving system. The aqueous solution of sulfuric-acid ($H_2SO_4$) of 1.5 M was used as working fluid, which evolves hydrogen gas on the cathode surface. Horizontal disk and thin cylindrical ribbon made of copper were employed as the cathodes to simulate heating surface.

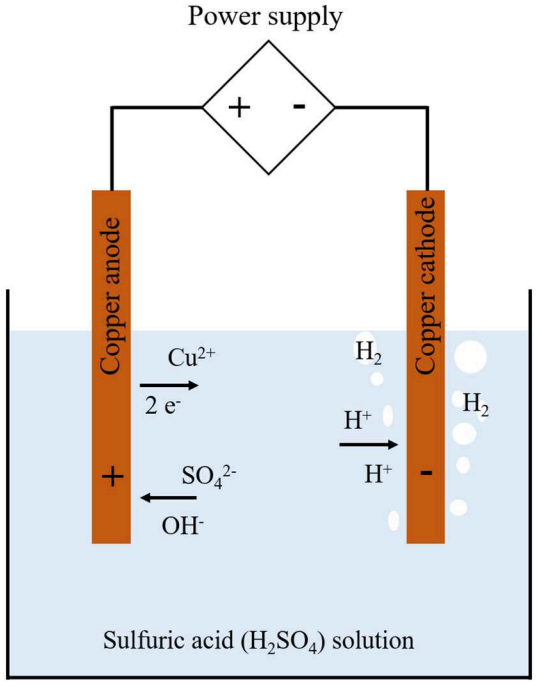


**FIGURE 1 |** Scheme of a sulfuric acid electrolysis system.

# BACKGROUNDS

## Existing CHF Models

Kutateladze (1950) developed the CHF correlation, Equation (3) based on a dimensional analysis. He insisted that the latent heat, gravity, surface tension and densities of the fluids are the important parameters on the CHF value. For water-vapor system, the value of 0.16 for coefficient $K$ was suggested.

$$q''_{CHF} = Kh_{lg}\rho_g\left[\frac{\sigma g(\rho_l - \rho_g)}{{\rho_g}^2}\right]^{1/4}, \quad (3)$$

or,

$$q''_{CHF} = Kh_{lg}{\rho_g}^{1/2}[\sigma g(\rho_l - \rho_g)]^{1/4}. \quad (4)$$

Zuber (1959) established the "Hydrodynamic instability model" developing the Kutateladze's theory. He applied instability theories to the CHF phenomena: The Rayleigh-Taylor instability for the diameters and intervals of the vapor columns which were half the size of and a unit size of critical wavelength, $\lambda_{T,c}$, respectively. He also applied the critical Kelvin-Helmholtz wavelength, $\lambda_{H,c}$, which causes the vapor columns to collapse. Then the CHF triggers as the escaping vapor has become limited. Zuber used $K$ value of 0.131 in Equation (4). Kutateladze and Zuber assumed the infinite upward facing horizontal plain surface heater, at the atmospheric pressure and saturated condition.

Katto and Yokoya (1968) investigated the influence of the fluid layer between vapor mushroom and the heated surface on the heat transfer. They reported that the heat transfer is strongly affected by the critical interference height which is similar to the height of the vapor stem investigated by Gaertner (1965). They observed that the formation and the detachment of the vapor mushroom have constant periods near the CHF. When the vapor mushroom leaves the surface, the fresh bulk fluid permeates the partially dried surface and momentary fills macrolayer. Then, the following vapor mushroom grows and thus the liquid layer is evaporated again. As the heat flux increases, this periodical phenomenon repeated, and the thickness of the macrolayer becomes thinner. And then at a certain high heat flux, the liquid in the macrolayer is fully evaporated triggering the CHF.

Haramura and Katto (1983) established the "Macrolayer dryout model." They improved Katto and Yokoya's study (1968) and developed their CHF correlation, Equation (5) with parameters reflecting macrolayer thickness and hovering time. They postulated the thickness of macrolayer as a fourth of the $\lambda_H$. According to them, the CHF occurs when the liquid in macrolayer is completely vaporized during the hovering time, which is defined as the period from the vapor mushroom generation to departure. Thus, the correlation was derived from the heat balance equation as expressed in the Equation (6).

$$q''_{CHF} = h_{lg}{\rho_g}^{1/2}[\sigma g(\rho_l - \rho_g)]^{1/4}(1+k)^{5/16}\left(\frac{\pi^4}{2^{11}\cdot 3^2}\right)^{1/16} \left(\frac{A_v}{A_h}\right)^{5/8}\left(1-\frac{A_v}{A_h}\right)^{5/16}\left[\left(\frac{\rho_l}{\rho_g}+1\right)/\left(\frac{11}{16}\frac{\rho_l}{\rho_g}+1\right)^{3/5}\right]^{5/16}. \quad (5)$$

$$\tau_d q''_{CHF} = \delta_l h_{lg}\rho_l(A_h - A_v). \quad (6)$$

$\tau_d$, $\delta_l$, $A_h$, and $A_v$ are hovering period, thickness of imacrolayer, heated area, and area of vapor stem, respectively. However,

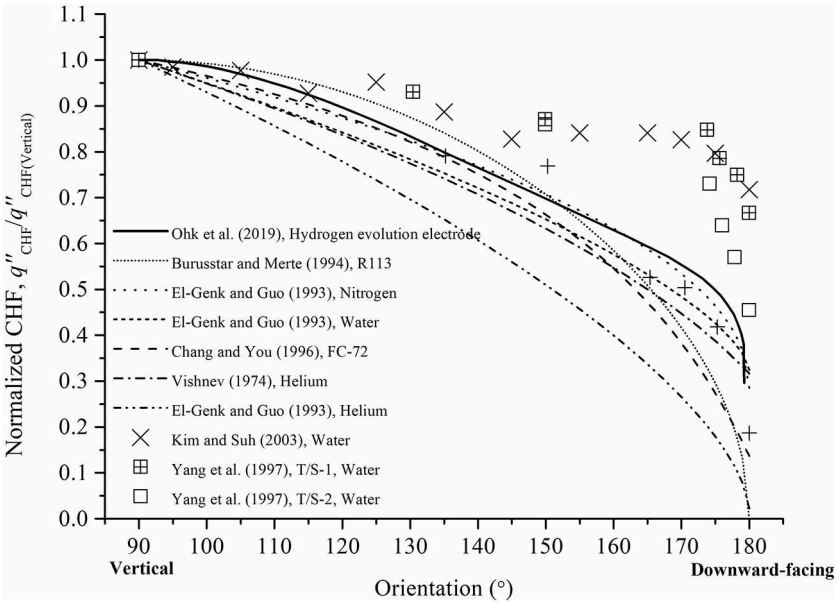


**FIGURE 2 |** Comparison of normalized CHF of existing studies with hydrogen evolution system (Ohk et al., 2019).

several researchers (Williamson and El-Genk, 1991; Sadasivan et al., 1992; Unal et al., 1992) opposed the approach of defining the thickness of the macrolayer based on the Kelvin-Helmholtz instability by Haramura and Katto (1983).

Van Ouwerkerk (1972) observed irreversible growth of dry areas at the pool boiling CHF condition using glass disk and n-heptane. The dry areas underneath the vapor mushroom were observed at 80% of CHF value regardless of the pressure. However, as pressure increased vapor shrank and thus dry areas were reduced. Hence, the CHF condition was delayed as pressure increased.

Ha and No (1998) proposed dry spot model and insisted that the critical number of bubbles surrounding an isolated bubble is five. The successive study of Ha and No (1998, 2000) hypothesized that rewetting of the microlayer under the bubble is impeded when the number of bubbles surrounding single bubble exceeds a critical number and then this disturbance of rewetting can trigger the CHF. Chung and No (2007) established nucleate boiling limitation model which predicts CHF condition based on dry area fraction studied by Ha and No (1998). As a result, they proposed the heat flux prediction equation from nucleate boiling to a CHF expressed as following relation.

$$q'' = q''_{nb}(n_{ib}/n_a) \tag{7}$$

where $q"_{nb}$, $n_{ib,}$ and $n_a$ denote nucleate boiling heat flux, number of isolated bubbles without coalescence and expected number of isolated bubbles, respectively.

## Existing Interpretation for the CCD

A gas evolving electrode system has upper operational limits so called critical current density (CCD) (Vogt et al., 2004). This limit of the gas generation rate can be roughly elucidated that the vigorous generation of bubble forms the film on the active surface and this gaseous film impedes the convection of the bulk liquid, which is quite similar to the film formation after departure from nucleate boiling (DNB). Therefore, the critical point can also be found in the gas evolving system. Some researchers (Mazza et al., 1978; Sillen et al., 1982) refereed that the boiling and gas evolving system have strong analogy analogy on the evidence of similarity between boiling curve and cell potential-current density curve, where the cell potential (potential difference between two electrodes) and current density correspond to the superheat and heat flux, respectively.

The electrochemical industry often regards the CCD phenomenon as the "anode(or cathode) effect" (Kellogg, 1950; Mazza et al., 1978; Zhuxian and Mingjie, 1987; Vogt, 2000). The anode effect was generally explained in two types: The anode effect is initiated by (1) the formation of intermediate compounds affecting surface wettability such as $CF_x$ and $COF_x$ and (2) the accumulation of gas on the surface, which reduces active surface area without formation of intermediate compounds (Zhuxian and Mingjie, 1987; Vogt, 2000). Despite of the achievements of the existing analogy studies (Vogt et al., 2004; Vogt, 2013) for a nucleate bubble regime, the detailed analogy analysis between the CHF and CCD (anode effect) has not been performed sufficiently.

## Previous Study

The authors' research group conducted the CCD experiments using the hydrogen evolution electrode varying the orientation of electrode and channel gap size, previously (Ohk et al., 2019). The tendency of the CCD was compared with the existing CHF results using various working fluids. The correlation reflecting hydrodynamic parameters was also derived and well-agreed with the existing CHF results which generally follow $(\sin\theta)^{0.5}$ as in the **Figure 2**. It was concluded that the hydrogen evolving system can simulate the CHF tendency qualitatively with respect to the

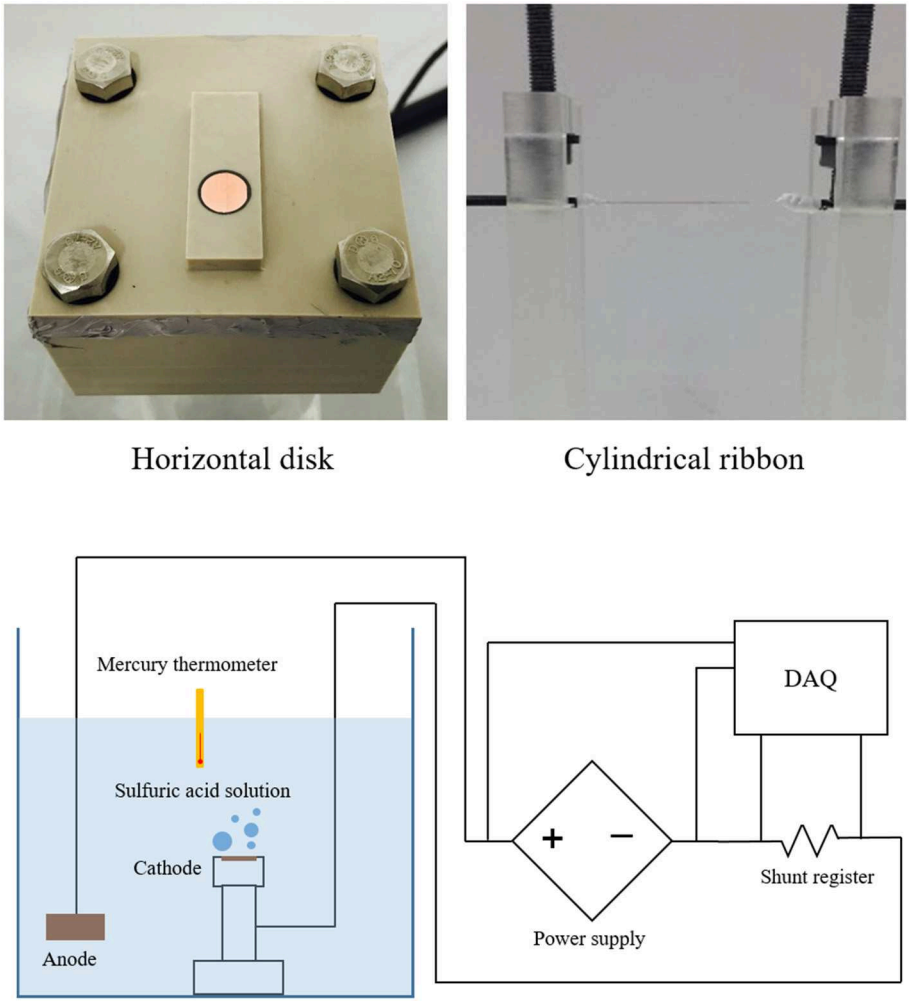


**FIGURE 3 |** Experimental apparatus and electric circuit.

surface orientation. However, the quantitative simulation of the CHF has still remained.

## EXPERIMENTAL SETUP

### Experimental Procedure and Test Apparatus

Two types of cathodes, disk of 0.01 m diameter and thin cylindrical ribbon of $2 \times 10^{-4}$ m thickness were employed for two independent experiments. One of these cathodes and the anode of 0.40 m × 0.50 m × 0.60 m block were located in the top-opened glass container filled with the aqueous solution of sulfuric-acid ($H_2SO_4$) of 1.5 M at atmospheric pressure and room temperature of 294 K. The mercury thermometer was located away from the cathode to measure bulk fluid temperature and the K-type thermocouple was set near the cathode surface to monitor the physical properties of the working fluid. The high-speed camera (Phantom Lab 111 6GMono, Komi) recorded the hydrogen evolution at the cathode surface. The electric current was controlled using power supply (N8952A, Keysight) simulating the typical heat flux controlled CHF experiments. The cell potential value was monitored and recorded by data acquisition system (34972A, Keysight) while the electric current was varied. To establish steady state condition at each current stage, time duration of about 20 s was maintained to get stabilized cell potential value. The CCD criterion was determined when cell potential was abruptly increased, which is similar to the abrupt temperature increase at the CHF condition as the cell potential of the present system is analogous to the superheat of the boiling system. The visual image of the hydrogen behavior around the CCD point was recorded. Three repeated experiments were conducted to measure the CCD and the discrepancy between minimum and maximum value was within 1.65%. The experimental apparatus, two types of the cathode and electric circuit were depicted in **Figure 3**.

The CHF value using the present hydrogen evolving system was calculated based on the gas generation rate at the CCD condition. The gas generation rate can be calculated by Equation

(8) suggested by Vogt et al. (2004). Equation (8) can be simplified at the CCD condition without any subreaction during the experiment as expressed in Equation (9) (Vogt, 1984), which is de facto the calculation of the number of moles of hydrogen reduced by the electric current together with the Boyle and Charles relations. Then the CHF at the saturated condition can be obtained by converting the gas generation rate with gas density and latent heat as in Equation (10).

$$\dot{V}_G = \dot{N} f_G \frac{R_m T}{p}\left(1 - \frac{p_{H2O}}{p}\right)^{-1} = \frac{I\varepsilon\nu}{nF} f_G \frac{R_m T}{p}\left(1 - \frac{p_{H2O}}{p}\right)^{-1}. \quad (8)$$

$$\dot{V}_{G,CCD} = \frac{I\nu}{nF} V_m \left(\frac{T}{273.15}\right). \quad (9)$$

$$q''_{CHF} = \frac{\dot{V}_{G,CCD}\rho_g h_{lg}}{A}. \quad (10)$$

## Uncertainty Analysis

Uncertainties in the proposed experimental methodology were analyzed using data reduction techniques (Coleman and Steele, 1999). As the final dependent variable was the CHF value using gas generation rate at the CCD, the uncertainty can be expressed as

$$q''_{CHF} = \frac{\dot{V}_G h_{lg}\rho_g}{A},$$
$$U_{q''_{CHF}}{}^2 = \left(\frac{\partial q''_{CHF}}{\partial \dot{V}_G} U_{\dot{V}_G}\right)^2 + \left(\frac{\partial q''_{CHF}}{\partial A} U_A\right)^2. \quad (11)$$

The measurement error of the cathode area, $A$ was assumed to be half of the resolution of the milling machine; $2.5 \times 10^{-4}$ m. Thus, the $U_A$ can be calculated as $3.93 \times 10^{-6}$ m$^2$. And then, the uncertainty of the gas generation rate at the cathode surface can be expressed as

$$\dot{V}_G = V_m\left(\frac{I\nu}{nF}\right)\left(\frac{T}{273.15}\right),$$
$$U_{\dot{V}G}{}^2 = \left(\frac{\partial \dot{V}_G}{\partial T} U_T\right)^2 + \left(\frac{\partial \dot{V}_G}{\partial I} U_I\right)^2. \quad (12)$$

The measurement error of the temperature, $T$ was estimated as standard accuracy of the K-type thermocouple, 2.2 K. However, the uncertainty of the current, $I$ was calculated using Ohm's law and thus

$$U_I{}^2 = \left(\frac{\partial I}{\partial R} U_R\right)^2 + \left(\frac{\partial I}{\partial V} U_V\right)^2, \quad (13)$$

where the uncertainties of $R$ and $V$ were stipulated in the manual of the product models, SCRD-R0001-5.0-H and Keysight 34972A, respectively. The calculated fractional maximum

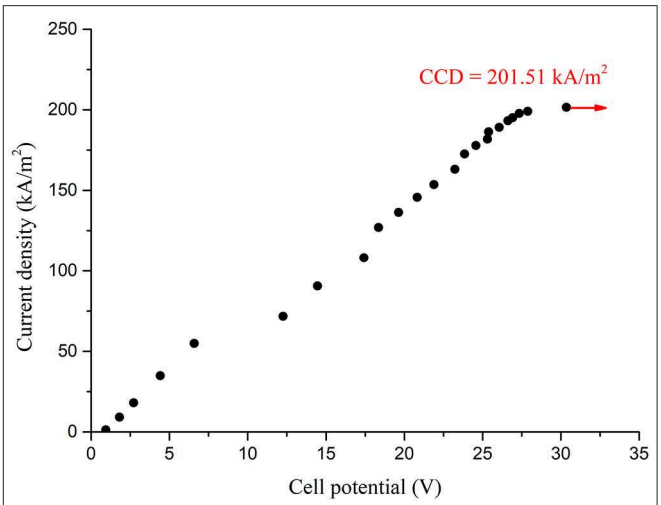


**FIGURE 5 |** Cell potential-current density curve.

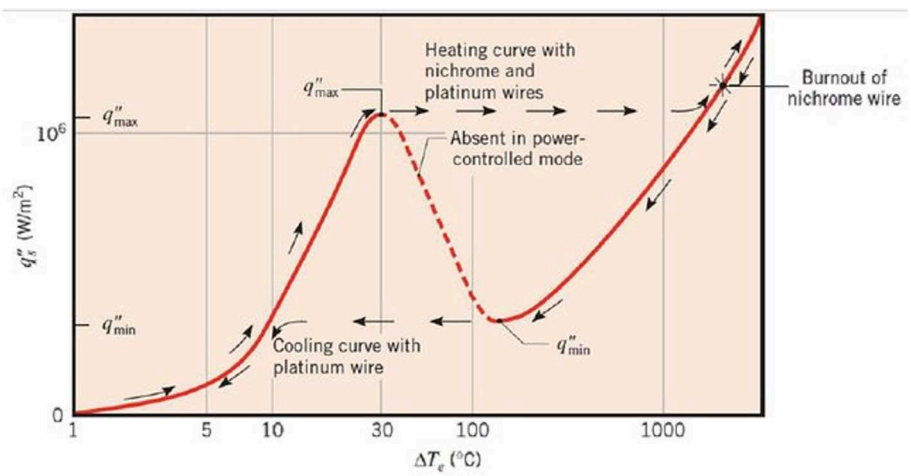


**FIGURE 4 |** Typical boiling curve (Nukiyama, 1966).

uncertainties were about 5.05%, showing the inherent accuracy of the experimental method. The largest uncertainties were caused by the tolerance of the shunt register, 5%.

# RESULTS AND DISCUSSION

## Analogous Curve

**Figures 4**, **5** compares the typical boiling curve by Nukiyama (1966) and the cell potential-current density curve measured using 10 mm copper disk. The cell potential increased as the applied current density increased up to the highest cell potential at the CCD, 201.51 kW/m$^2$, which shows resemblance to the nucleate boiling regime up to the CHF. In general, the CHF is detected by the rapid increase in the heater temperature. Similarly, the CCD was detected by the rapid increase in the cell potential in the present study. Therefore, this result has similarity with the CHF detection experiments in typical boiling system. The measured CCD was converted into the water CHF using Equations (9) and (10) as 37.1 kW/m$^2$. This value is much smaller than that of the existing CHF values, which used identical geometric condition with the present experiment (Katto and Yokoya, 1968; Haramura and Katto, 1983; Ahn and Kim, 2012). The similar curve with **Figure 5** was also obtained using the thin cylindrical ribbon and the comparisons with the boiling CHF was presented in **Table 1**. Though the current experimental results show much smaller CHF values than the CHF values with water boiling system, the ratios of the CHF values lie within 1.39–2.47%.

**TABLE 1 |** Comparison of the water CHF value between the present work and existing value.

| Surface geometry | CHF from the hydrogen evolving system (kW/m$^2$) | Existing CHF (kW/m$^2$) | Fraction from the existing CHF (%) |
|---|---|---|---|
| Horizontal disk plate | 37.1 | 1,861 (Katto and Yokoya, 1968) | 1.99 |
| | | 1,540 (Haramura and Katto, 1983) | 2.47 |
| | | 1,504 (Ahn and Kim, 2012) | 2.41 |
| Cylindrical ribbon | 16.1 | 1,053 (Sun and Lienhard, 1970) | 1.53 |
| | | 1,157 (Yeom et al., 2015) | 1.39 |

## Bubble Behaviors at the CHF and the CCD

**Figure 6** compares the bubble behaviors between the hydrogen evolving system and the water boiling system (**Figures 6A–C**) and (**Figures 6D–F**) (Ahn and Kim, 2012), respectively. The photographs were taken in series, from just before the CCD to after the CCD. Both systems had identical sizes of active surfaces and materials, 10 mm diameter of copper disks.

**Figures 6A,D** were taken at the nucleate bubble regime, just before the CCD and the CHF. The nucleate bubble on the edge of the surface maintained surface rewetting and thus kept its own regime in the both cases. **Figures 6B,E** depict the CCD and the CHF regime, respectively. The bubbles at the edge of the surface started to coalescence. Hence, the surface rewetting impeded due to the liquid inflow and thus a certain critical point was reached in the both cases. After that, the gaseous film covered the entire surface as shown in **Figures 6C,F**. In this regime, the

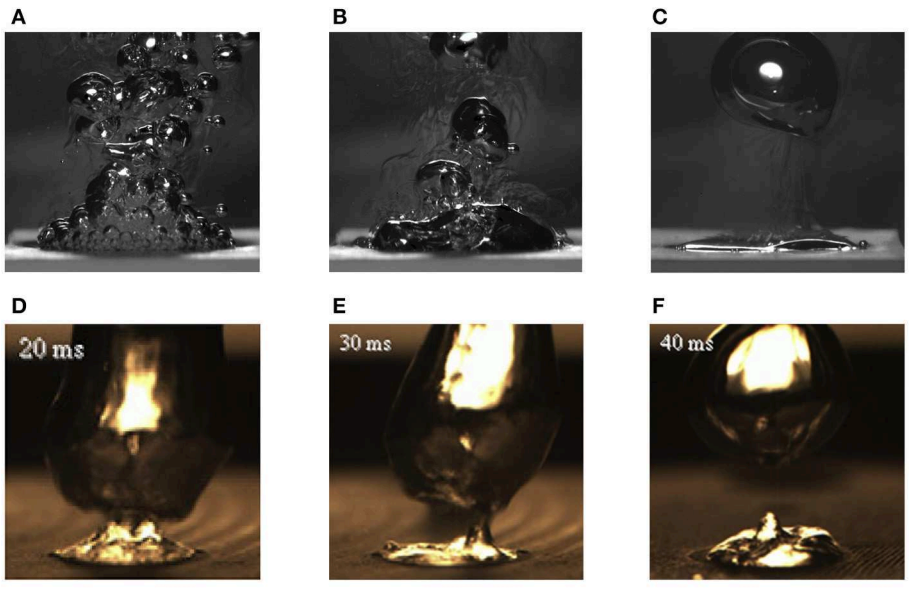


**FIGURE 6 |** Comparison of bubble behaviors between hydrogen evolving and water boiling system. **(A)** Just before CCD, **(B)** at CCD triggers, **(C)** after CCD, **(D)** just before CHF, **(E)** at CHF triggers, and **(F)** after CHF.

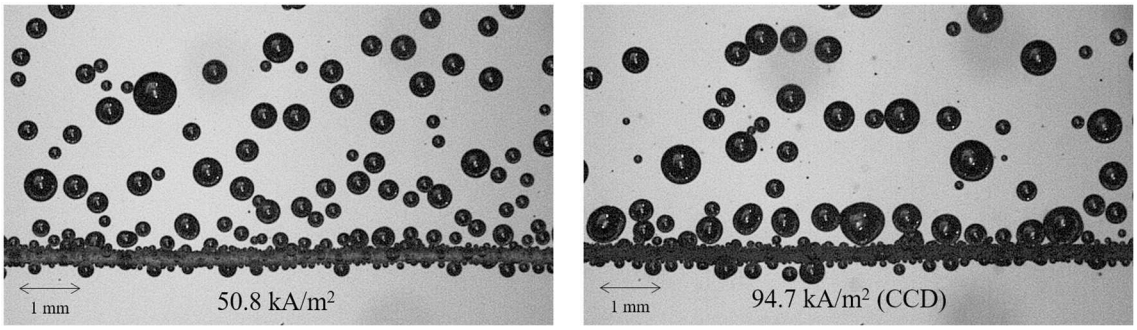


**FIGURE 7 |** Hydrogen bubble behaviors on thin cylindrical ribbon.

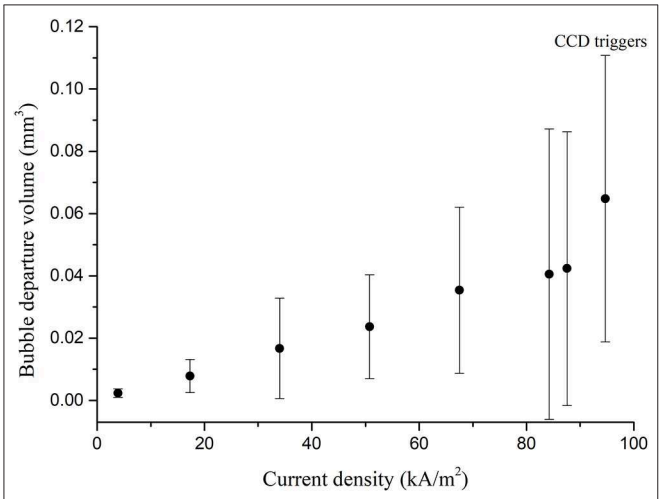


**FIGURE 8 |** Hydrogen departure volume according to the current density.

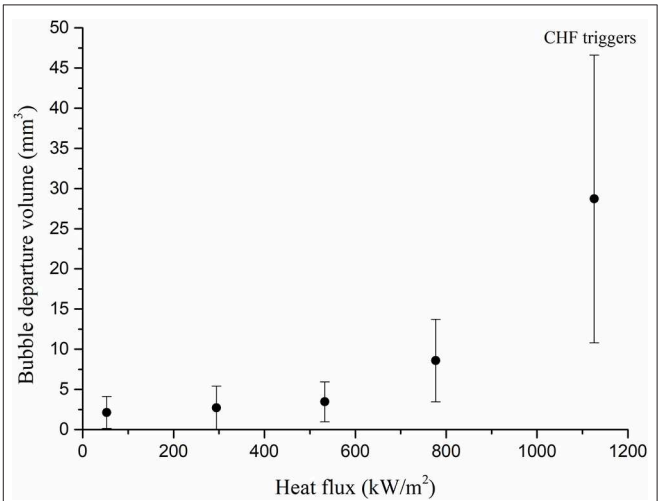


**FIGURE 9 |** Bubble departure volume according to the heat flux (Yeom et al., 2015).

cell-potential and the surface temperature greatly increased in the hydrogen evolving system and boiling system, respectively.

Based on the observation, it can be postulated that the macroscopic mechanism of the CCD and the CHF is similar except the bubble size. The relatively small hydrogen bubbles were observed compared with the vapor bubbles just before the CCD regime. In order to investigate more details of the bubble size, the hydrogen departure volumes were measured with respect to the current density using high speed camera. The thin cylindrical ribbon was used to capture the generalized bubble shapes. Fifty hydrogen bubbles were randomly selected and their diameters were measured to convert into volume assuming the bubbles had the perfect spherical shape due to its small size scale, as shown in **Figure 7**. Fifty data were averaged at each current density with standard deviations as shown in the **Figure 8**. The result was compared with those of water boiling experiment up to the CHF regime performed by Yeom et al. (2015) who also used the thin cylindrical ribbon as the heating surface as shown in the **Figure 9**. The hydrogen departure volume increased as the current density increased. Then the slope increased near the CCD point. It seems that the vigorous bubble coalescence on the surface impeded the liquid inflow and increased the cell-potential, the CCD. The trend of bubble volume with respect to the heat flux by Yeom et al. (2015) was similar to the present work. The vapor volume increased as heat flux increased and showed great increase in the CHF regime. However, the vapor volume at the CHF regime was about 440 times larger than that of the CCD regime. The size scale of hydrogen bubble was similar to the existing hydrogen evolving experiment (Vogt et al., 2004), and Vogt et al. (2004) referred that the increased cell potential affected the surface wettability. Based on these observations, the CCD of the hydrogen evolving system simulates the miniature scale of the water CHF.

## Water CHF Prediction

The water CHF was predicted by the measured CCD accounting for the differences in vapor/gas volume generation rates based on the miniature CHF assumption. For simplicity, the representative bubble concept at each CHF condition was postulated as shown in the **Figure 10**. As a result, the diameter and the lifetime of the bubbles in each system are same. Also, the bubble coalescence

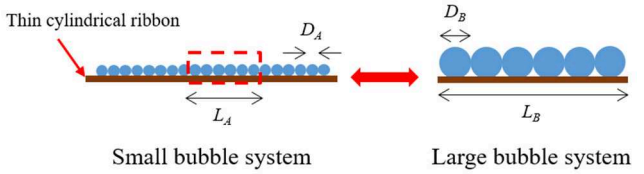


**FIGURE 10 |** Ideal configuration of bubble arrangement at CHF regime.

assumed to occur only for the 1-dimansional lateral direction because the cylindrical ribbon is thin enough to suppress the occurrence of 2-dimensional coalescence. Thus, heat flux ($W/m^2$) relationship between the two different system can be simplified as linear heat generation rate (W/m) as expressed in Equation (14) with a certain magnification factor, $C$.

$$C\frac{Q_A}{L_A} = \frac{Q_B}{L_B} \tag{14}$$

And the heat flow $Q$, can be substituted by the total bubble volume at saturated boiling condition since we assumed that the bubbles have the same lifetime, independent of the function of time.

$$C\frac{n_b V_A}{L_A} = \frac{n_b V_B}{L_B}. \tag{15}$$

The unit heater length, $L$ can be substituted by $n_b \times D$, and thus the magnification factor $C$ can be derived as

$$C = \left(\frac{\pi/6{D_B}^3}{\pi/6{D_A}^3}\right)\left(\frac{n_b D_A}{n_b D_B}\right) = \left(\frac{D_B}{D_A}\right)^2. \tag{16}$$

To apply the magnification factor for the present work, $D_A$ and $D_B$ in Equation (16) can be substituted to hydrogen departure diameter at the CCD triggers, 0.47 mm and bubble diameter measured by Yeom et al. (2015) at the CHF triggers, 3.79 mm, respectively. As a result, the magnification factor between two system was calculated as 65.03 and thus the CHF simulated by the present system can be corrected using relationship of Equation (14).

$$\begin{aligned} \mathrm{CHF}_{HES,C} &= C \times \mathrm{CHF}_{HES} = 65.03 \times 16.1 \\ &= 1,046.98\ \mathrm{kW/m^2} \end{aligned} \tag{17}$$

The measured CHF by the Yeom et al. (2015) was 1,157 $kW/m^2$. Finally, the discrepancy was largely reduced within 9.51%.

However, the proposed analogy approach using the hydrogen evolving system will not achieve full analogy with the boiling process by nature. There are several sacrificed factors such as conduction phenomenon, contact angle, buoyancy difference due to the different bubble size, change of interfacial tension including surface tension due to the surface charge in the electrode system, etc. These factors are important in boiling processes but many of them are not considered in most CHF modeling, which means that the limited number of these factors contributes to the CHF.

## CONCLUSION

Water pool boiling CHF at saturated condition was simulated using the hydrogen evolving system, which is essentially thermal free condition. The cell potential according to the current density curve, which is analogous to the typical boiling curve was obtained and the CCD was measured in analogous way to the boiling CHF, which by nature is much smaller than the water CHF values.

The superficial mechanism of the CHF and the CCD were compared using photographs. The CHF and the CCD triggered when the nucleate bubble on the edge of the surface started to coalescence. It is concluded that the similar bubble behaviors can be observed in both cases except the size of bubbles. The characteristics of hydrogen evolving system was tested using the thin ribbon electrode. The variation of bubble volume from nucleate bubble regime to the CHF and the CCD showed similar tendency in both systems. The hydrogen bubble volume was 440 times smaller than vapor volume measured in boiling heat transfer system near the CHF. Based on the observation, a miniature CHF model was postulated.

A magnification factor was derived by the miniature CHF model accounting for the differences in vapor/gas volume generation rates. The discrepancy between the existing CHF and the CHF from the hydrogen evolving system with magnification factor was <10%.

The possibility of simulating the CHF condition using a non-heating hydrogen evolving system was explored based on the fact that most CHF models were derived from the hydrodynamics. This work was partly successful in predicting the CHF value accounting for the volume generation rates. However, in order to achieve the full analogy between the hydrogen evolving system and the boiling heat transfer system, further works are needed regarding conduction, contact angle, surface tension and engineered surface such as roughness, porosity, and wettability.

## DATA AVAILABILITY STATEMENT

The datasets generated for this study are available on request to the corresponding author.

## AUTHOR CONTRIBUTIONS

All authors listed have made a substantial, direct and intellectual contribution to the work, and approved it for publication.

## FUNDING

This study was sponsored by Korean Ministry of Science and Information & Communication Technology and was supported by Nuclear Research & Development program grant funded by the National Research Foundation (NRF) (Grant code: 2017M2A8A4015283).

## REFERENCES


Ahn, H. S., and Kim, M. H. (2012). Visualization study of critical heat flux mechanism on a small and horizontal copper heater. *Int. J. Multiph. Flow* 41, 1–12. doi: 10.1016/j.ijmultiphaseflow.2011.12.006

Bang, I. C., Chang, S. H., and Baek, W. P. (2005). Visualization of a principle mechanism of critical heat flux in pool boiling. *Int. J. Heat Mass Transf.* 48, 5371–5385. doi: 10.1016/j.ijheatmasstransfer.2005.07.006

Carey, V. P. (2008). *Liquid-Vapor Phase-Change Phenomena*. Boca Raton, FL; London; New York, NY: CRC Press.

Chung, H. J., and No, H. C. (2007). A nucleate boiling limitation model for the prediction of pool boiling CHF. *Int. J. Heat Mass Transf.* 50, 2944–2951. doi: 10.1016/j.ijheatmasstransfer.2006.12.023

Coleman, H. W., and Steele, W. G. (1999). *Experimental and Uncertainty Analysis for Engineers*. New York, NY: John Wiley and Son.

Gaertner, R. F. (1965). Photographic study of nucleate pool boiling on a horizontal surface. *J. Heat Transf.* 87, 17–27. doi: 10.1115/1.3689038

Groeneveld, D. C., Ireland, A., Kaizer, J., and Vasic, A. (2018). An overview of measurements, data compilations and prediction methods for the critical heat flux in water-cooled tubes. *Nucl. Eng. Des.* 331, 211–221. doi: 10.1016/j.nucengdes.2018.02.031

Ha, S. J., and No, H. C. (1998). A dry-spot model of critical heat flux in pool and forced convection boiling. *Int. J. Heat Mass Transf.* 41, 303–311. doi: 10.1016/S0017-9310(97)00140-3

Ha, S. J., and No, H. C. (2000). A dry-spot model of critical heat flux applicable to both pool boiling and subcooled forced convection boiling. *Int. J. Heat Mass Transf.* 43, 241–250. doi: 10.1016/S0017-9310(99)00135-0

Haramura, Y., and Katto, Y. (1983). A new hydrodynamic model of critical heat flux, applicable widely to both pool and forced convective boiling on submerged bodies in saturated liquids. *Int. J. Heat Mass Transf.* 26, 389–399. doi: 10.1016/0017-9310(83)90043-1

Jeong, Y. H., Baek, W. P., and Chang, S. H. (2002). Non-heating simulation of pool-boiling critical heat flux. *Int. J. Heat Mass Transf.* 45, 3987–3996. doi: 10.1016/S0017-9310(02)00100-X

Kandlikar, S. G. (2001). A theoretical model to predict pool boiling CHF incorporating effects of contact angle and orientation. *J. Heat Transf.* 123, 1071–1079. doi: 10.1115/1.1409265

Katto, Y., and Yokoya, S. (1968). Principal mechanism of boiling crisis in pool boiling. *Int. J. Heat Mass Transf.* 11, 993–1002. doi: 10.1016/0017-9310(68)90005-7

Kellogg, H. H. (1950). Anode effect in aqueous electrolysis. *J. Electrochem. Soc.* 97, 133–142. doi: 10.1149/1.2777980

Kutateladze, S. S. (1950). A hydrodynamic model of the critical heat transfer in boiling liquids with free convection. *Zhurn. Tekhc. Fiz.* 20, 1389–1392.

Lienhard, J. H., and Dhir, V. K. (1973). Hydrodynamic prediction of peak pool-boiling heat fluxes from finite bodies. *J. Heat Transf.* 95, 152–158. doi: 10.1115/1.3450013

Lienhard, J. H., Dhir, V. K., and Riherd, D. M. (1973). Peak pool boiling heat-flux measurements on finite horizontal flat plates. *J. Heat Transf.* 95, 477–482. doi: 10.1115/1.3450092

Lloveras, P., Salvat-Pujol, F., Truskinovsky, L., and Vives, E. (2012). Boiling crisis as a critical phenomenon. *Phys. Rev. Lett.* 108:215701. doi: 10.1103/PhysRevLett.108.215701

Mazza, B., Pedeferri, P., and Re, G. (1978). Hydrodynamic instabilities in electrolytic gas evolution. *Electrochim. Acta* 23, 87–93. doi: 10.1016/0013-4686(78)80102-9

Nukiyama, S. (1966). The maximum and minimum values of the heat Q transmitted from metal to boiling water under atmospheric pressure. *Int. J. Heat Mass Transf.* 9, 1419–1433. doi: 10.1016/0017-9310(66)90138-4

O'Hanley, H., Coyle, C., Buongiorno, J., McKrell, T., Hu, L. W., Rubner, M., et al. (2013). Separate effects of surface roughness, wettability and porosity on the boiling critical heat flux. *Appl. Phys. Lett.* 103:024102. doi: 10.1063/1.4813450

Ohk, S. M., Park, H. K., and Chung, B. J. (2019). CHF experiments on the influence of inclination and gap size. *Int. J. Heat Mass Transf.* 132, 929–938. doi: 10.1016/j.ijheatmasstransfer.2018.12.076

Roday, A. P., and Jensen, M. K. (2009). A review of the critical heat flux condition in mini-and microchannels. *J. Mech. Sci. Technol.* 23, 2529–2547. doi: 10.1007/s12206-009-0711-y

Sadasivan, P., Chappidi, P. R., Unal, C., and Nelson, R. A. (1992). Possible mechanism of macrolayer formation. *Int. Commun. Heat Mass Transf.* 19, 801–815. doi: 10.1016/0735-1933(92)90016-B

Sakashita, H., and Ono, A. (2009). Boiling behaviors and critical heat flux on a horizontal plate in saturated pool boiling of water at high pressures. *Int. J. Heat Mass Transf.* 52, 744–750. doi: 10.1016/j.ijheatmasstransfer.2008.06.040

Saylor, J. R., and Simon, T. W. (1989). The effect of a dimensionless length scale on the critical heat flux in saturated, pool boiling. *Am. Soc. Mech. Eng. Heat Transf. Div.* 108, 71–80.

Sillen, C. W. M. P., Barendrecht, E., Janssen, L. J. J., and Van Stralen, S. J. D. (1982). Gas bubble behaviour during water electrolysis. *Int. J. Hydr. Energy* 7, 577–587. doi: 10.1016/0360-3199(82)90038-6

Sturgis, J. C., and Mudawar, I. (1999). Critical heat flux in a long, rectangular channel subjected to one-sided heating- I. flow visualization. *Int. J. Heat Mass Transf.* 42, 1835–1847. doi: 10.1016/S0017-9310(98)00274-9

Sun, K. H., and Lienhard, J. H. (1970). The peak pool boiling heat flux on horizontal cylinders. *Int. J. Heat Mass Transf.* 13, 1425–1439. doi: 10.1016/0017-9310(70)90178-X

Unal, C., Daw, V., and Nelson, R. A. (1992). Unifying the controlling mechanisms for the critical heat flux and quenching: the ability of liquid to contact the hot surface. *J. Heat Transf.* 117, 558–567. doi: 10.1115/1.2911909

Van Ouwerkerk, H. J. (1972). Burnout in pool boiling: the stability of boiling mechanisms. *Int. J. Heat Mass Transf.* 15, 25–34. doi: 10.1016/0017-9310(72)90163-9

Vogt, H. (1984). The rate of gas evolution at electrodes–I. an estimate of the efficiency of gas evolution from the supersaturation of electrolyte adjacent to a gas-evolving electrode. *Electrochim. Acta* 29, 167–173. doi: 10.1016/0013-4686(84)87043-7

Vogt, H. (2000). On the mechanism of the anode effect in aluminum electrolysis. *Metall. Mater. Trans. B-Proc. Metall. Mater. Proc. Sci.* 31, 1225–1230. doi: 10.1007/s11663-000-0009-z

Vogt, H. (2013). Heat transfer in boiling and mass transfer in gas evolution at electrodes – the analogy and its limits. *Int. J. Heat Mass Transf.* 59, 191–197. doi: 10.1016/j.ijheatmasstransfer.2012.12.018

Vogt, H., Aras, Ö., and Balzer, R. J. (2004). The limits of the analogy between boiling and gas evolution at electrodes. *Int. J. Heat Mass Transf.* 47, 787–795. doi: 10.1016/j.ijheatmasstransfer.2003.07.023

Williamson, C. R., and El-Genk, M. S. (1991). "High-speed photographic analysis of saturated nucleate pool boiling at low heat flux," in *ASME Winter Annual Meeting* (Atlanta, GA).

Yeom, H., Sridharan, K., and Corradini, M. L. (2015). Bubble dynamics in pool boiling on nanoparticle-coated surfaces. *Heat Transf. Eng.* 36, 1027–1027. doi: 10.1080/01457632.2015.979116

Zhang, W., Hibiki, T., Mishima, K., and Mi, Y. (2006). Correlation of critical heat flux for flow boiling of water in mini-channels. *Int. J. Heat Mass Transf.* 49, 1058–1072. doi: 10.1016/j.ijheatmasstransfer.2005.09.004

Zhuxian, Q., and Mingjie, Z. (1987). Studies on anode effect in molten salts electrolysis. *Electrochim. Acta* 32, 607–613. doi: 10.1016/0013-4686(87)87049-4

Zuber, N. (1959). *Hydrodynamic aspects of boiling heat transfer* (Dissertation). University of California, Los Angeles, CA, United States.


**Conflict of Interest:** The authors declare that the research was conducted in the absence of any commercial or financial relationships that could be construed as a potential conflict of interest.

# NOMENCLATURE

| | |
|---|---|
| $A$ | Area, $m^2$ |
| $A_h$ | Heated area, $m^2$ |
| $A_v$ | Vapor column area, $m^2$ |
| $C$ | Arbitrary coefficient |
| $D$ | Bubble departure diameter, m |
| $E$ | Cell potential, V |
| $f_G$ | Gas evolution efficiency |
| $F$ | Faraday constant, 96485 Coulomb/mol |
| $g$ | Gravitational acceleration, 9.8 $m/s^2$ |
| $h_{lg}$ | Latent heat, J/kg |
| $I$ | Current, A |
| $K$ | Dimensionless coefficient on CHF correlations |
| $L$ | Length, m |
| $n$ | Number of electrons in charge transfer reaction |
| $n_a$ | Expected number of isolated bubbles in a given area $A$ |
| $n_{ib}$ | Number of isolated bubbles without coalescence in a given area $A$ |
| $n_b$ | Number of bubbles |
| $\dot{N}$ | Flux of substance, mol/s |
| $p$ | Pressure, kg/m-$s^2$ |
| $q"$ | Heat flux, $W/m^2$ |
| $q"_{nb}$ | Nucleate boiling heat flux, $W/m^2$ |
| $q"_{CHF}$ | Critical heat flux, $W/m^2$ |
| $Q$ | Heat flow, W |
| $R$ | Electric resistance, Ω |
| $R_m$ | Gas constant, 8.3143 J/mol-K |
| $T$ | Temperature, K |
| $U_x$ | Uncertainty of $x$ |
| $V$ | Bubble departure volume, $m^3$ |
| $V_m$ | Molar volume, 0.022414 $m^3$/mol at 273.15 K, 1 atm |
| $\dot{V}_G$ | Gas generation rate, $m^3/s$ |
| **Greek symbols** | |
| $\delta_l$ | Thickness of the macrolayer |
| $\epsilon$ | Current efficiency |
| $\lambda_H$ | Kelvin-Helmholtz instability wavelength |
| $\lambda_{H,c}$ | Critical Kelvin-Helmholtz instability wavelength |
| $\lambda_{T,c}$ | Critical Rayleigh-Taylor instability wavelength |
| $\nu$ | Stoichiometric number |
| $\rho$ | Density, $kg/m^3$ |
| $\sigma$ | Surface tension, N/m |
| $\tau_d$ | Hovering period |
| **Subscripts** | |
| $CCD$ | Critical current density |
| $CHF$ | Critical heat flux |
| $g$ | Gas |
| $HES$ | Hydrogen evolving system |
| $l$ | Liquid |

frontiers in Energy Research

ORIGINAL RESEARCH
published: 13 December 2019
doi: 10.3389/fenrg.2019.00137

# Assessment of a Theoretical Model for Predicting Forced Convective Critical Heat Flux in Rod Bundles

*Yang Liu[1], Qian Yin[2], Jianqiang Shan[1]*, Bo Zhang[1], Wei Liu[3] and L. K. H. Leung[4]*

*[1] State Key Laboratory of Multiphase Flow in Power Engineering, Xi'an Jiaotong University, Xi'an, China, [2] Guangxi Fangchenggang Nuclear Power Co., Ltd, Fangchenggang, China, [3] State Key Laboratory of Reactor System Desgin Technology, Nuclear Power Institute of China, Chengdu, China, [4] Department of Engineering Physics, McMaster University, Hamilton, ON, Canada*

This study proposes a theoretical model for predicting forced convective critical heat flux (CHF) in rod bundles based on the bubble crowding phenomenon. The theoretical model applied to the rod bundle is based on Weisman-Pei's basic tube model. In order to make it suitable for rod bundles in Pressurized Water Reactors (PWR), the flow and heat transfer characteristics of rod bundles are considered, including velocity distribution, flow patterns, the grid effect on CHF, and turbulence intensity. The theoretical model is applied together with the subchannel code ATHAS to assess it against uniformly heated CHF data obtained from a 5 × 5 rod bundle, and good agreement is observed.

**Keywords: CHF, bundle, theoretical model, bubble crowding, PWR**

OPEN ACCESS

***Edited by:***
*Jun Wang,*
*University of Wisconsin-Madison, United States*

***Reviewed by:***
*Sipeng Wang,*
*Nanjing University of Aeronautics and Astronautics, China*
*Yuan Yuan,*
*Sun Yat-sen University, China*

***Correspondence:**
*Jianqiang Shan*
*jqshan@mail.xjtu.edu.cn*

***Specialty section:***
*This article was submitted to Nuclear Energy, a section of the journal Frontiers in Energy Research*

***Received:*** *08 October 2019*
***Accepted:*** *14 November 2019*
***Published:*** *13 December 2019*

***Citation:***
*Liu Y, Yin Q, Shan J, Zhang B, Liu W and Leung LKH (2019) Assessment of a Theoretical Model for Predicting Forced Convective Critical Heat Flux in Rod Bundles. Front. Energy Res. 7:137. doi: 10.3389/fenrg.2019.00137*

## INTRODUCTION

Effective and accurate prediction of critical heat flux (CHF) is essential to ensure the safe operation of forced convective equipment. It is of particular concern in the operation of water-cooled nuclear reactors, where cladding and core integrities must be maintained and a safe operating power envelope and margin must be established. Moreover, it is closely related to the economy of the reactors.

Theoretical models (Weisman, 1991; Celata et al., 1994; Bruder et al., 2015) have received the attention of some scholars because of their incorporation of physical mechanisms, accurate parameter trends, and wide application range, which provide flexibility in predicting CHF for new bundle concepts or configurations, such as those proposed for small modular reactors (SMRs).

The bubble crowding model (Weisman, 1991) is a successful theoretical model for predicting forced convective critical heat flux in a tube. The model was first proposed by Weisman and Pei (1983) based on bubble crowding. The main idea is that the bubbles generated on the heating wall hinder the radial flow of liquid from the bulk flow area to the near-wall bubble layer area. Ying and Weisman (1986) modified the model to accommodate the non-uniform void profile in a tube and extended the CHF prediction for void fractions up to 0.8. In addition, they revised the calculation for bubble diameters and included the slip ratio in the bubble layer to improve CHF prediction at low mass flow rates. Weisman and Illeslamlou (1988), on the other hand, extended the model to high subcooling conditions based on the energy balance at the outer edge of the bubble layer in round tubes. Chang and Lee (1989) revised the calculation of the lateral mass velocity from the core to the bubble layer at low qualities in uniformly heated tubes in their CHF model. Kwon and Chang (1999) introduced a drag force due to the roughness of wall-attached bubbles in the momentum balance, which determines the limiting transverse interchange of mass flux crossing the interface of the bubbly wall layer and the core. Furthermore, the bubbly layer was assumed to be a single

layer of wall-attached bubbles that acts as an equivalent of surface roughness. The critical void fraction at the bubble layer was represented with an exponential function related to the quality, which was determined from CHF data for round tubes. Kodama and Kataoka (2002) expressed the critical void fraction at the bubble layer in terms of the channel-average void fraction, which was also determined from CHF data for round tubes. Kinoshita et al. (2001) considered spherical bubbles in the bubble layer at high velocity and subcooling conditions. These bubbles were assumed to contact each other in a cubic configuration. The interference of bubbles was taken at the ratio of bubble diameter to bubble distance, equaling 0.5. The critical void fraction at the bubble layer was determined to be $\pi/12$.

Previous studies on bubble crowding models are based on a tube, which is not suitable for rod bundle structures. The objective of this study is to develop a generalized theoretical CHF model in rod bundles based on the bubble crowding concept (Weisman and Pei, 1983). The radial velocity distribution, grid enhancement effect, and flow pattern change in rod bundles are considered.

## DESCRIPTION OF THE THEORETICAL CHF MODEL

It is generally believed that the mechanism of CHF under subcooling and low quality is different from that under high quality. To distinguish between the two mechanisms, subcooled and low-quality CHF is called "departure from nucleate boiling" (DNB), and the other is termed dry-out.

### Physical Mechanism and Basic Equations

The derived prediction procedure of Weisman and Pei's tube CHF theoretical model (Weisman and Pei, 1983) is based on the bubble crowding concept. At the heating wall, bubbles will be generated. CHF will occur when there are too many bubbles to wet the heating wall effectively with cold liquid from the bulk flow area, as shown in **Figure 1**.

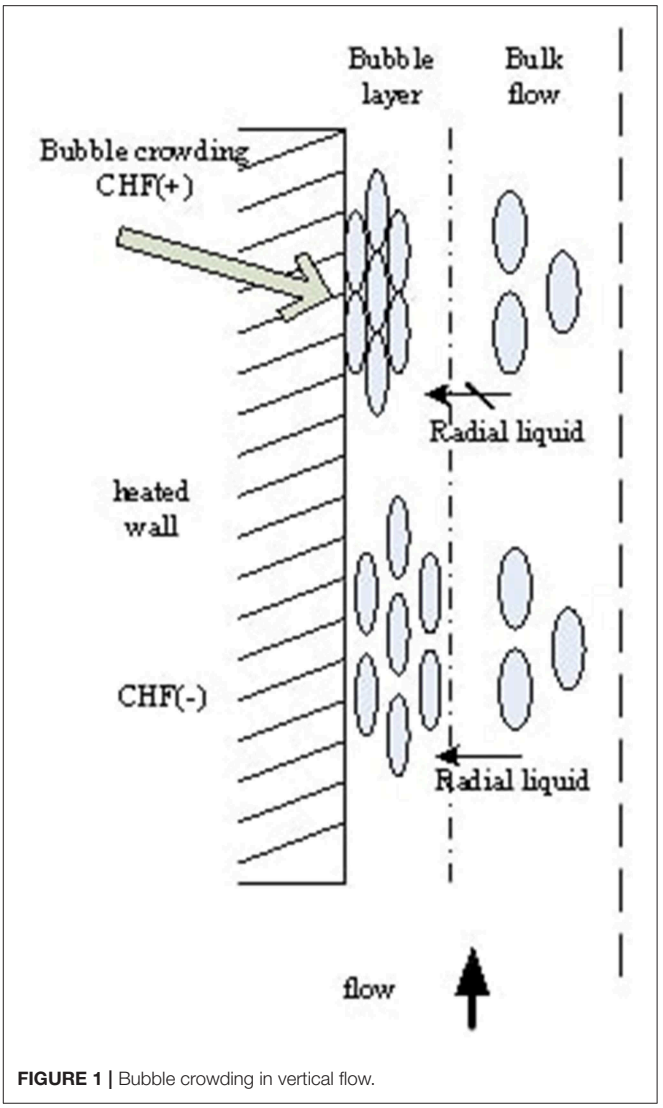


**FIGURE 1 |** Bubble crowding in vertical flow.

They divide the tube area into the bulk flow area and the near-wall bubble layer area. For these two areas, mass, and energy conservation equations are established to derive the CHF expression as follows:

$$q_{CHF}/(h_{fg}G_3) = (x_2 - x_1)(\frac{h_f - h_{ld}}{h_l - h_{ld}}) \quad (1)$$

where $q_{CHF}$ is the predicted value of CHF calculated by the model, $h_{fg}$ is the latent heat of evaporation, $x_2$ is the average quality at the bubble layer and $x_1$ is the average quality at the core layer, $h_f$ is the saturated liquid enthalpy, $h_l$ is the enthalpy of liquid, and $h_{ld}$ is the enthalpy at the point of bubble detachment.

$G_3$ is the lateral mass velocity from the core to the bubble layer due to turbulence, which is determined by:

$$G_3 = Gi_b\psi \quad (2)$$

in which $G_3$ is expressed in terms of the total axial mass velocity, G, the turbulence intensity at the interface between the bubbly layer and the core, $i_b$, and a miscellaneous function, $\psi$, which represents the share of liquid reaching the wall in the bulk flow. Weisman and Pei (1983) expressed $\psi$ as follows:

$$\psi = \left\{ \frac{1}{\sqrt{2\pi}} \exp\left[ -\frac{1}{2}(\frac{v_{1l}}{\sigma_{v'}})^2 \right] - \frac{1}{2}(\frac{v_{1l}}{\sigma_{v'}}) erfc(\frac{1}{\sqrt{2}}\frac{v_{1l}}{\sigma_{v'}}) \right\} \quad (3)$$

where v' is the radial fluctuating velocity, $\sigma_{v'}$ is the standard deviation of v, and $v_1 l$ is the radial velocity created by vapor generation.

$$v_{1l} = \frac{q_b}{h_{fg}\rho_g} \quad (4)$$

According to Lahey and Moody (1977), $q_b$, the portion of the total heat flux effective in generating vapor, has the following relationship with total heat flux, q:

$$q_b = q\left[\frac{h_l - h_{ld}}{h_f - h_{ld}}\right] \quad (5)$$

The following is the derivation of turbulence intensity $i_b$ in this study. Trupp and Azad's (1973) measurements of turbulent radial velocity fluctuations for a P/D of 1.35 (which is close to that of the PWR fuel assembly) are applied in establishing the radial turbulence fluctuation in the subchannel. Lee and Durst (1980) pointed out that the ratio $\left[\sqrt{\overline{(v')^2}}/U_\tau\right]/(l_e/r_0)$ does not depend on the Reynolds number and can be considered to be only a function of (r/r0). **Figure 2** compares the measurements of Trupp and Azad (1973) and those of a tube (Laufer, 1953). In addition, parabolic fits of all of and the near-wall (up to radius ratios, r/r0, of 0.5) measurements of Trupp and Azad (1973) are also shown. In view of the CHF occurrence at the wall, the near-wall velocity fluctuation (pink line) is of the most interest and is expressed as:

$$\frac{\sqrt{\overline{(v')^2}}}{U_\tau}/\left(\frac{l_e}{r_0}\right) = 2.318\left(\frac{r_0}{y}\right)^{0.538} \tag{6}$$

where $U_\tau$ is the frictional velocity, $l_e$ is the Prandtl mixing length, $r_0$ is the outer radius of the tube, and y is the radial distance from the wall. With the assumption that the ratio of two-phase to single-phase turbulence intensity is independent of radial position, we have Equation (7):

$$\frac{\sqrt{\overline{(v')^2}}}{U_\tau} = 2.318F_1\left(\frac{r_0}{y}\right)^{0.538}\left(\frac{l_e}{r_0}\right) \tag{7}$$

And the general relationship of $l_e$ is:

$$l_e = 0.4y \tag{8}$$

The frictional velocity $U_\tau$ is defined as:

$$U_\tau = \left(\frac{f}{2}\right)^{1/2}\frac{G}{\rho} \tag{9}$$

where f in the turbulent region is:

$$f = 0.046\mathrm{Re}^{-0.2} \tag{10}$$

From Equations (6) to (10), we have:

$$\frac{\sqrt{\overline{(v')^2}}}{G} = \frac{0.176}{\rho}F_1\mathrm{Re}^{-0.1}\left(\frac{y}{r_0}\right)^{0.538} \tag{11}$$

Weisman and Pei (1983) assumed the distance from the wall at which the bubbly layer–core interface occurs, $y_c$, is:

$$y_c = \left(kD_p\right)/(0.4F_2) \tag{12}$$

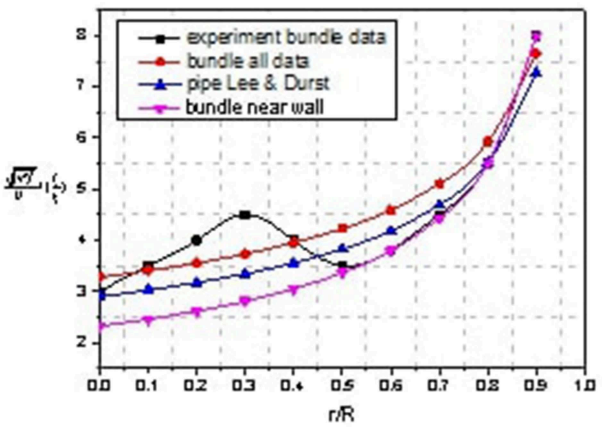


**FIGURE 2 |** Comparisons of radial turbulence fluctuations and fitted representations.

where k is an undetermined coefficient and $D_P$ is the bubble detachment diameter.

By replacing 'y' in Equation (11) with '$y_c$' in Equation (12), we have:

$$\sqrt{\overline{(v')^2}}\left(\frac{\rho}{G}\right) = 0.2962\left(\frac{F_1}{F_2^{0.6}}\right)(k)^{0.462}\mathrm{Re}^{-0.1}\times\left(\frac{D_p}{D}\right)^{0.462} = i_b \tag{13}$$

As indicated by Weisman and Pei, the two-phase factor $F_1$ represents the effect of bubble motion on turbulence intensity, and the two-phase factor $F_2$ accounts for the effect of bubble motion on the fluctuation velocity. Weisman and Pei assumed the ratio $F_1/F_2$ to be in the form:

$$(F_1/F_2^{0.6}) = \left[1 + a\left(\frac{\rho_l - \rho_g}{\rho_g}\right)\right] \tag{14}$$

The physical meaning of Equation (14) is the effect of two-phase flow on turbulence intensity.

## Constitutive Relations

### Bubble Detachment Point and Detachment Diameter

Reliable predictions of the onset of bubble departure and detached bubble diameter are essential for modeling in Equations (1) and (13). In a review in which an extensive amount of data was compared, Lee et al. (1992) found the Levy model (Levy, 1966) to achieve the best fit with the whole set of data of the many analytical models. Levy proposed the bubble departure enthalpy, which is defined as the liquid enthalpy at which vapor begins to break away from a heated surface as:

$$h_{ld} = h_f - \Delta T_{ld}C_{pf} \tag{15}$$

$$\begin{cases} 0 \le y_b^+ \le 5.0;\ \Delta T_{ld} = \frac{q}{H_{db}} - \frac{q}{G\left(\frac{f}{8}\right)^{1/2}}\mathrm{Pr}\,y_b^+ \\ 5.0 \le y_b^+ \le 30.0;\ \Delta T_{ld} = \frac{q}{H_{db}} - 5.0\frac{q}{G\left(\frac{f}{8}\right)^{1/2}}\left\{\mathrm{Pr} + In\left[1 + \mathrm{Pr}(y_b^+/5.0 - 1.0)\right]\right\} \\ y_b^+ \ge 30.0;\ \Delta T_{ld} = \frac{q}{H_{db}} - 5.0\frac{q}{G\left(\frac{f}{8}\right)^{1/2}}\left\{\mathrm{Pr} + In(1.0 + 5.0\,\mathrm{Pr}) + 0.5In(y_b^+/30.0)\right\} \end{cases} \tag{16}$$

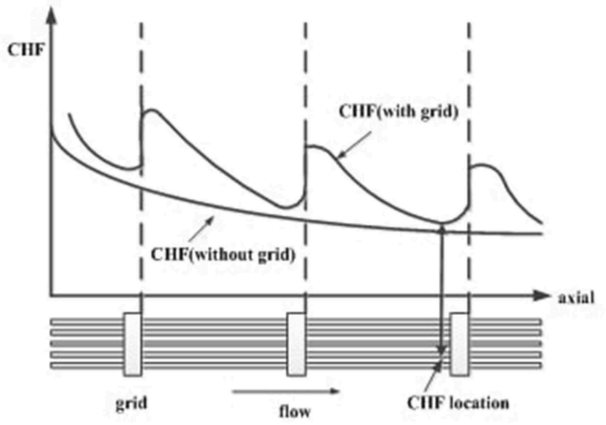


**FIGURE 3 |** Enhancement effect of grids on CHF.

where,

$$y_b^+ = \frac{0.015}{\mu_f}\sqrt{\frac{\sigma g_c D}{\nu_f}} \tag{17}$$

and $H_{db}$ is the single-phase heat transfer coefficient given by the Dittus-Boelter equation:

$$H_{db} = 0.023\mathrm{Re}^{0.8}\mathrm{Pr}^{0.4}k_f/D \tag{18}$$

Meanwhile, the bubble detachment diameter, $D_P$, which is determined from a balance of the fluid forces acting on the bubble and the surface force, was given by Levy (1966) as:

$$D_p = 0.015\left(\frac{8\rho\sigma D}{fG^2}\right) \tag{19}$$

## Grid Enhancement on Turbulence Intensity $i_b$

In rod bundles, grids enhance the turbulence intensity in the flow stream and, accordingly, the heat transfer. This enhancement effect is captured in the turbulence intensity factor, $i_b$, of the present model.

**Figure 3** schematically illustrates the enhancement effect of grids on CHF in a bundle with axially uniform heating. The local CHF is reduced monotonically along the bare bundle (i.e., without grids) due to the increase in flow quality and reaches a minimum at the end of the heated length. In the presence of grids, the local CHF is enhanced at the grid location but decays gradually with increasing distance downstream from the grid. The CHF decays until encountering the next grid, where the enhancement recovers, or it returns back to that of a bundle without grids if the distance between neighboring grids is long.

The enhancement effect of the grid on CHF is proportional to the enhancement in turbulence intensity at locations downstream of the grid. Nagayoshi and Nishida (1998) studied the radial turbulent velocity distribution of the straight-type grid and observed a decay in the radial turbulence intensity factor downstream of the grid. The normalized velocity fluctuation reached a maximum value at the grid and decayed with increasing distance from the grid. It approached the level for the bare bundle after a distance of approximately 10 times the hydraulic-equivalent diameter from the grid. Nagayoshi and Nishida (1998) expressed the change in radial turbulence intensity factor as:

$$\left(\frac{\sqrt{\overline{(v')^2}}}{U_\tau}\right)_{grid} \Big/ \left(\frac{\sqrt{\overline{(v')^2}}}{U_\tau}\right) = 1 + 6.5\varepsilon^2 \mathrm{e}^{-0.27\frac{x}{D}} \tag{20}$$

where x is the axial distance downstream from the grid, D is the hydraulics-equivalent, and $\varepsilon$ is the blockage-area ratio of the grid.

A grid correction factor, $F_{grid}$, was introduced into the radial turbulence intensity factor $i_b$ (Equation 13) in this study to include the enhancement effect, which is expressed as:

$$\begin{cases} i_{b-use} = i_b F_{grid} \\ F_{grid} = 1 + a_2\varepsilon^2 \mathrm{e}^{-b_2\frac{x}{D}} \end{cases} \tag{21}$$

The coefficients $a_2$ and $b_2$ depend on the type of grid. The experimental data of Yao et al. (1982) indicated that the heat-transfer enhancement due to a grid falls down to the reference value (i.e., a bundle without grids) at a distance of 25–30 times the hydraulics-equivalent diameter. Based on these data, the coefficient $b_2$ has been established as−0.13. A value of 6.5 has been derived for the coefficient $a_2$ from the data of Nagayoshi and Nishida (1998).

## Boiling Effect on Turbulence Intensity $i_b$

The turbulence intensity factor, $i_b$, expressed in Equation (13), is based primarily on single-phase parameters. Weisman and Pei (1983) introduced the ratio ($F_1/F_2$), the physical meaning of which is the effect of boiling or two phases on turbulence intensity, as shown in Equation (14), rewritten here as:

$$(F_1/F_2^{0.6}) = \left[1 + a\left(\frac{\rho_l - \rho_g}{\rho_g}\right)\right] \tag{22}$$

In Weisman and Pei's study, the coefficient "a" to account for the enhancement in turbulence intensity for two-phase flow, is expressed as:

$$a = 0.135\left(\frac{G}{G_{cr}}\right)^{a_1} \tag{23}$$

where Gcr is the reference mass flow rate at 970,000 kg/m2/h. Lim (1988) indicated a slight pressure dependency for the coefficient "a" based on their experimental data. The pressure effect is captured by associating it with the void fraction in this study. Therefore, we consider a function with a void fraction dependent variable to describe the effect of pressure. Through the analysis of the bundle CHF data in section assessment and analysis of the theoretical CHF model, we find that the two-phase factor has a

closer relationship with the void fraction, and the influence of the void fraction on the two-phase factor is obviously different between the high void fraction and the low void fraction, which is due to the change in flow pattern.

In the square rod bundle flow pattern experiments by Venkateswararao et al. (1982), they divided the flow pattern into bubbly flow, dispersed bubble flow, slug flow, churn flow, and annular flow when the ratio of the rod bundle spacing to the diameter (S/D) is about 1.38. They also defined the boundary between dispersed bubbly flow and churn flow as where void fraction "α" equals 0.52.

By comparing the experimental data and the flow pattern map given by Venkateswararao et al. (1982), we find that all of the bundle CHF data in section assessment and analysis of the theoretical CHF model are in the region of dispersed bubble flow and churn flow. Therefore, we can conclude that the boundary line due to the different flow patterns leads to different effects of the void fraction on the two-phase effect. The expression of Equation (22) can be simplified to:

$$(F_1/F_2^{0.6}) = 1 + a_3\left(\frac{G}{G_{cr}}\right)^{a_1}\alpha^{b_1} \tag{24}$$

According to the above boundary conditions, the boundary void fraction 'α' equals 0.52 between dispersed bubble flow and churn flow.

We used the CHF data in section assessment and analysis of the theoretical CHF model below to optimize the coefficients and found that $b_1$ equals 1.7 and $a_3$ equals 197.9 when α is greater than or equal to 0.52, and $b_1$ equals −0.06 and $a_3$ equals 69.65 when α is smaller than 0.52. For coefficient $a_1$, we still use the form of Weisman and Pei (1983).

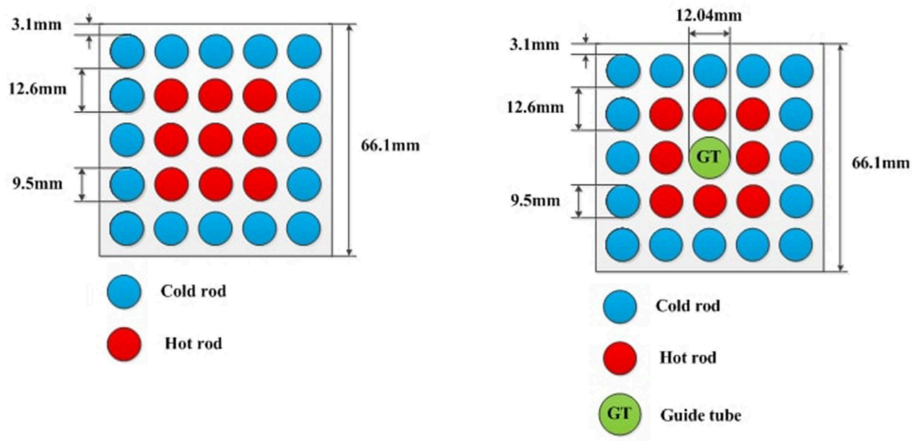


**FIGURE 4 |** Test bundle setup in the NPIC 5 × 5 rod-bundle experiment (rods setup).

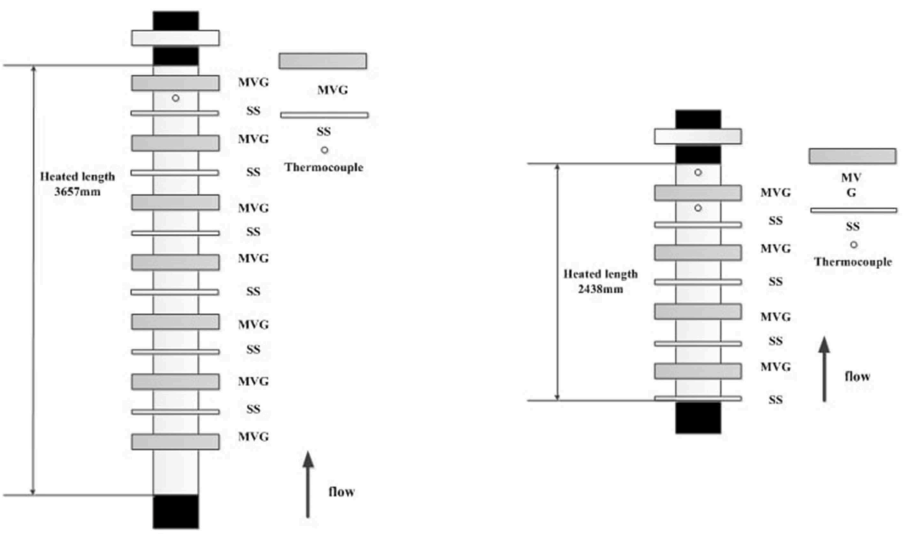


**FIGURE 5 |** Test bundle setup in the NPIC 5 × 5 rod-bundle experiment (grids setup).

## Other Relations

According to the assumption that there is homogeneous flow in both the bubble layer and the bulk flow region, this study follows Weisman and Pei's (1983) original idea that when CHF occurs, the void fraction in the bubble layer $\alpha_2$ equals 0.82, which was based on the maximum packing density of ellipsoids with an axis ratio of three to one. The two-phase flow parameters are calculated as follows:

$$\rho_2 = (1-\alpha_2)\rho_f + \alpha_2\rho_g \tag{25}$$

$$\rho_1 = \frac{r^2}{(r-s)^2}\rho - \rho_2\frac{2(r-\frac{s}{2})s}{(r-s)^2} \tag{26}$$

$$\alpha_1 = \frac{\rho_l - \rho_1}{\rho_l - \rho_g} \tag{27}$$

$$x_1 = \frac{\alpha_1 \times \rho_g}{\rho_1} \tag{28}$$

$$x_2 = \frac{\alpha_2 \times \rho_g}{\rho_2} \tag{29}$$

Subscript 1 denotes the parameters in the bulk flow, and subscript 2 denotes the parameters in the bubble layer. "r" is the channel radius and "s" is the bubbly layer thickness, which equals 5.5 times $D_P$, as recommended by Weisman and Pei (1983). The detailed calculation process of CHF model is shown in the **Appendix A**.

# ASSESSMENT AND ANALYSIS OF THE THEORETICAL CHF MODEL

## CHF Data Bank

The experiments were performed at the Nuclear Power Institute of China (NPIC) with water flow over a 5 × 5 rod bundle simulating a PWR fuel assembly with flat mixing vanes. Three test bundles were constructed for the experiments. Two of these bundles simulated a PWR fuel assembly with nine hot rods at the central locations and 16 cold rods at the peripheral locations inside a square frame 66.1 mm in width. Each rod had an outer diameter of 9.5 mm. The spacing between heated rods and between the cold rods and the frame was 3.1 mm (i.e., the rod pitch was 12.6 mm). One of these bundles was heated over a length of 2438 mm (or 8 ft) and the other over a length of 3657 mm (or 12 ft). **Figure 4** illustrates the rod configuration of the 5 × 5 rod bundle experiment. Eight grids were installed along the axial length of the short bundle [four of these grids were simple support grids without mixing vanes (SS), while four had mixing vanes installed in the grid (MVG)]. Thirteen grids were installed along the axial length of the long bundle at the locations shown in the figure (six SS grids and seven MVG grids). **Figure 5** illustrates the grid configurations of the long and short bundles. The span between grids with mixing vanes was 0.56 m. A set of thermocouples was installed at the location 56 mm upstream of the end of the heated length (10 mm upstream of the last grid with mixing vanes). The coolant traveled vertically upward from the bottom to the top.

The third test bundle in the experiments was equipped with a guide tube of 12.45 mm in outer diameter that replaced the hot rod at the central position (see **Figure 4**). The spacing between the hot rods and the guide tube was 1.625 mm. Thirteen grids were installed over the heated length of 3657 mm. The other geometric configurations of this bundle were the same as those of the long bundle described above. Six sets of data have been selected from the database to assess the prediction accuracy of the bubble-crowding-based mechanistic CHF model for subchannels in the test bundles. These data covered bundles of both short and long heated lengths with and without the guide tube (GT). **Table 1** lists the overall flow conditions covered by these data, which are 417 data under the PWR operations.

## Prediction Results of Bundle CHF Data

CHF is predicted using the bubble-crowding-based mechanistic CHF model with the local flow conditions at each subchannel along the axial distance of the bundle evaluated using the subchannel code ATHAS, which was developed by the Nuclear Safety and Operation Laboratory at Xi'an Jiao Tong University (Liu et al., 2014). The ATHAS code is based on the drift-flow basic model and can be used for core thermal-hydraulic analysis of PWRs and BWRs. Local flow conditions in the subchannel are directly applied in the model to evaluate the CHF. This is referred to as the Direct Substitution Method (DSM) for determining CHF, which is more commonly used in PWRs. The DSM method uses the experimental inlet mass rate flux, inlet temperature, and CHF value as the input of the subchannel code and calculates the real local parameters as the inputs of the

**TABLE 1 |** Range of CHF data selected in the assessment.

| Pressure (kPa) | Mass flux (t/m²/s) | Quality (subchannel) | Cross-sectional average void fraction | Inlet subcooling (°C) |
|---|---|---|---|---|
| 12400~16728 | 0.947~4.048 | <=0.3 | <=0.7 | 13.3-235.3 |

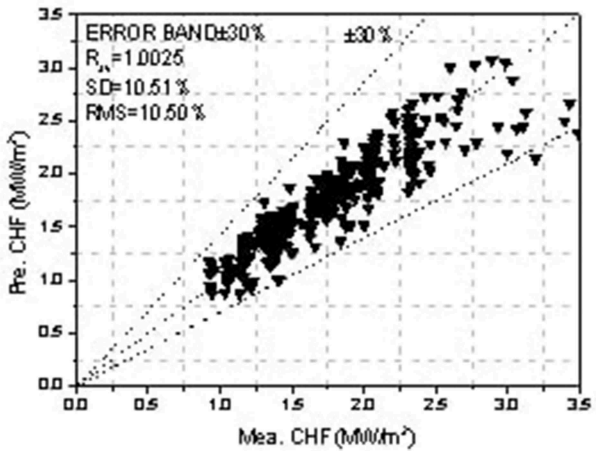


**FIGURE 6 |** Comparison of predicted and experimental CHF values by model.

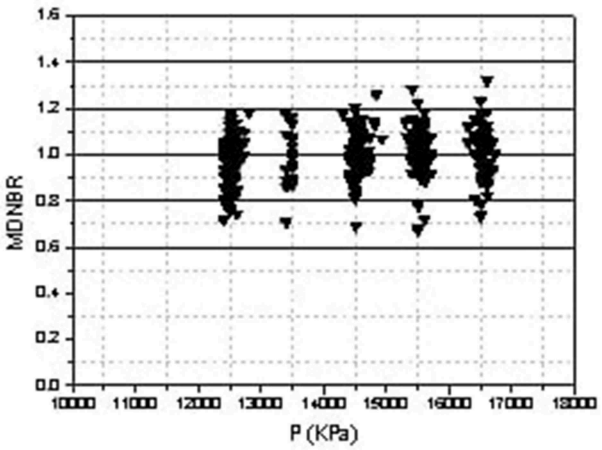


**FIGURE 7 |** Variation of predicted MDNBRs with pressure.

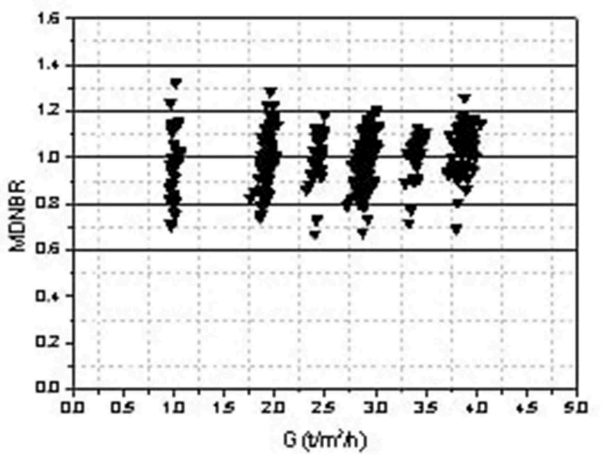


**FIGURE 8 |** Variation of predicted MDNBRs with mass flux.

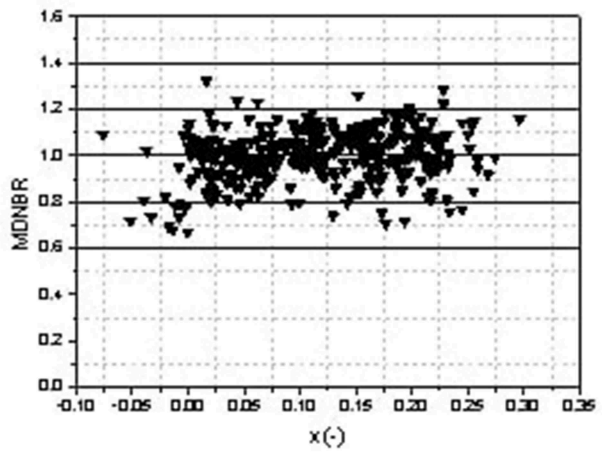


**FIGURE 9 |** Variation of Predicted MDNBRs with quality.

CHF model. A turbulent mixing coefficient of 0.066 is applied for the type of mixing grid installed in the tested bundles in ATHAS code.

The predicted CHF value is compared against the experimental heat flux to determine the DNBR in the subchannel. The location with the minimum DNBR (or MDNBR) is considered the initial CHF point. The prediction accuracy of the model is assessed from the average value of predicted MDNBRs, $R_{av}$, the standard deviation on MDNBR, SD, and the root-mean-square error on MDNBR, RMS, which are defined as:

$$DNBR = \frac{q_{pre}}{q_{\exp}} \tag{30}$$

$$R_{av} = \frac{1}{N}\sum_{i=1}^{N} MDNBR_i \tag{31}$$

$$SD = \left[\frac{1}{N}\sum_{i=1}^{N}(MDNBR_i - R_{av})^2\right]^{1/2} \tag{32}$$

$$RMS = \left[\frac{1}{N}\sum_{i=1}^{N}(MDNBR_i - 1)^2\right]^{1/2} \tag{33}$$

where MDNBRi is the MDNBR for each data point and N is the total number of data points.

**Figure 6** compares the predicted and experimental CHF values for 417 data points. The average value of MDNBRs, $R_{av}$, is 1.0025, with a standard deviation, SD, of 10.51%, and a root-mean-square error, RMS, of 10.50%. Almost all of the data are predicted within the ±30% error band. Applying the original model of Weisman and Pei (1983) leads to a $R_{av}$ of 0.88 with a standard deviation of 22% for the same set of data points. This demonstrates the improvement in prediction accuracy achieved by the current model.

Parametric trends of predicted MDNBR in the bundles are examined against the experimental conditions (i.e., pressure, mass flux, and quality) in **Figures 7**–**9**. There are no apparent trends of predicted MDNBRs with pressure (**Figure 7**), mass flux (**Figure 8**), and quality (**Figure 9**).

## CONCLUSIONS

A new mechanistic CHF model for subchannels in a bundle has been developed. It is based on the bubble-crowding concept for tubes but considers the effects of subchannel geometry on axial and radial velocity distributions and the effects of boiling characteristics and spacer grids on CHF. In the model, the turbulence intensity factor has been revised to capture the change in velocity profile between a tube and a subchannel. It also includes the enhancement effect due to a grid. Moreover, the influence of flow pattern change on CHF is also considered. This mechanistic CHF model has been assessed

against experimental data obtained with water flow through $5 \times 5$ rod bundles. Local flow conditions in subchannels of the bundle were calculated using the subchannel code "ATHAS." Experimental CHF values were predicted with an average value of 1.0025 and a standard deviation of 10.51% for 417 data points at PWR conditions of interest. The predicted MDNBRs appear independent of pressure, mass flux, and quality. More detailed local parameter distributions and evidence for CHF visualization need to be acquired for future optimization of this model.

## DATA AVAILABILITY STATEMENT

The datasets analyzed in this manuscript are not publicly available. Requests to access the datasets should be directed to The Nuclear Power Institute of China [Contact mail: liuwei0958@126.com].

## AUTHOR CONTRIBUTIONS

YL was responsible for the specific work of this paper. QY carried out some of the simulation work. JS guided the work of this article. BZ was responsible for the embedding of the model in the subchannel code. WL provided experimental data. LL optimized the structure and tone of this article.

## FUNDING

This work was financially supported by the National Key R&D Program of China (No. 2018YFB1900402).

## REFERENCES

Bruder, M., Bloch, G., and Sattelmayer, T. (2015). Critical heat flux in flow boiling-review of the current understanding and experimental approaches. *Heat Transf. Eng.* 38, 347–360. doi: 10.1080/01457632.2016.1189274

Celata, G. P., Cumo, M., Mariani, A., Simoncini, M., and Zummo, G. (1994). Rationalization of existing mechanistic models for the prediction of water subcooled flow boiling critical heat flux. *Int. J. Heat Mass Transf.* 37, 347–360. doi: 10.1016/0017-9310(94)90035-3

Chang, S. H., and Lee, K. W. (1989). A critical heat flux model based on mass, energy, and momentum balance for upflow boiling at low qualities. *Nucl. Eng. Des.* 113, 35–50. doi: 10.1016/0029-5493(89)90294-X

Kinoshita, H., Nariai, H., and Inasaka, F. (2001). Study of critical heat flux mechanism in flow boiling using bubble crowding model. *JSME Int. J.* 44, 81–89. doi: 10.1299/jsmeb.44.81

Kodama, S., and Kataoka, I. (2002). Study on analytical prediction of forced convective CHF in the wide range of quality. *Int. Conf. Nucl. Eng.* 62, 147–154. doi: 10.1115/ICONE10-22128

Kwon, Y. M., and Chang, S. H. (1999). A mechanistic critical heat flux model for wide range of subcooled and low-quality flow boiling. *Nucl. Eng. Des.* 188, 27–47. doi: 10.1016/S0029-5493(99)00025-4

Lahey, R. T., and Moody, F. (1977). *The Thermal Hydraulics of a Boiling Water Reactor*. La Grange Park: American Nuclear Society.

Laufer, J. (1953). *The structure of turbulence in fully developed pipe flow*. NACA Technical Note No. 2954.

Lee, S. C., Dorra, H., and Bankoff, S. G. (1992). A critical review of predictive models for the onset of significant void in forced-convection subcooled boiling, HTD, fundamentals of Subcooled Flow Boiling, *ASME* 217, 33–39. doi: 10.2172/10104504

Lee, S. L., and Durst, F. (1980). *On the motions of particles in turbulent flow*, U.S. Nuclear Regulatory Commission Report NUREG/CR-1556.

Levy, S. (1966). Forced convection subcooled boiling - prediction of Vapor volumetric fraction. *Int.J. Heat Mass Transf.* 10, 91–965. doi: 10.1016/0017-9310(67)90071-3

Lim, J. C. (1988). *Improvements in the theoretical prediction of the departure from nucleate boiling* (Ph.D. thesis). University of Cincinnati, Cincinnati, OH, United States.

Liu, W., Bai, N., Zhu, Y-B., Shan, J-Q., Zhang, B., Gou, J.-L et al. (2014). Study on reactor thermal-hydraulic sub-channel analysis code ATHAS. *Nucl. Sci. Eng.* 34, 59–66.

Nagayoshi, T., and Nishida, K. (1998). Spacer effect model for subchannel analysis. *J. Nucl. Sci. Technol.* 35, 399–405. doi: 10.1080/18811248.1998.9733881

Trupp, A. C., and Azad, R. S. (1973). The structure of turbulent flow in triangular array rod bundles. *Nucl. Eng. Des.* 32, 47–84. doi: 10.1016/0029-5493(75)90090-4

Venkateswararao, P., Semiat, R., and Dukler, A. E. (1982). Flow pattern transition for gas-liquid flow in a vertical rod bundle. *Int. J. Multiphase Flow* 8, 509–524. doi: 10.1016/0301-9322(82)90021-0

Weisman, J. (1991). The current status of theoretically based approaches to the prediction of the critical heat flux in flow boiling. *Nucl. Technol.* 9, 1–21. doi: 10.13182/NT92-A34699

Weisman, J., and Illeslamlou, S. (1988). Phenomenological model for prediction of critical heat flux under highly subcooled conditions. *Fusion Technol.* 13, 654–659. doi: 10.13182/FST88-A25140

Weisman, J., and Pei, B. (1983). Prediction of critical heat flux in flow boiling at low qualities. *Int. J. Heat Mass Transf.* 10, 1463–1477. doi: 10.1016/S0017-9310(83)80047-7

Yao, S. C., Hochreiter, L. E., and Leech., W. J. (1982). Heat-transfer augmentation in rod bundles near grid spacers. *Int. J. Heat Mass Transf.* 104, 76–81. doi: 10.1115/1.3245071

Ying, S. H., and Weisman, J. (1986). Prediction of critical heat flux in flow boiling at intermediate qualities. *Int. J. Heat Mass Transf.* 29, 1639–1648. doi: 10.1016/0017-9310(86)90105-5

**Conflict of Interest:** QY was employed by the company Guangxi Fangchenggang Nuclear Power Co., Ltd.

The remaining authors declare that the research was conducted in the absence of any commercial or financial relationships that could be construed as a potential conflict of interest.

## NOMENCLATURE

| Symbol | | Units |
|---|---|---|
| a | coefficient | / |
| D | hydraulic diameter of tube or bundle | m |
| $D_p$ | average bubble diameter | m |
| F | fraction of total heat flux for evaporation | / |
| G | total axial mass velocity | $kg/m^2s$ |
| $G_3$ | lateral mass velocity from core to bubbly layer due to turbulence | $kg/m^2s$ |
| $h_f$ | saturated liquid enthalpy | kJ/kg |
| $h_{fg}$ | latent heat of evaporation | kJ/kg |
| $h_l$ | enthalpy of liquid | kJ/kg |
| $h_{ld}$ | enthalpy at point of bubble detachment | kJ/kg |
| $i_b$ | turbulence intensity | / |
| k | coefficient | / |
| $l_e$ | Prandtl mixing length | m |
| Mea. CHF | experimental CHF value | $MW/m^2$ |
| Pre. CHF | predicted CHF value | $MW/m^2$ |
| $q_{CHF}$ | CHF value | $kW/m^2$ |
| $q_{exp}$ | experimental CHF value | $kW/m^2$ |
| r | outer radius of tube or bundle | m |
| $U_\tau$ | frictional velocity | m/s |
| v' | radial fluctuating velocity | m/s |
| $\overline{v'^2}$ | root mean square value of v' | / |
| $\overline{v'}$ | mean value of v' | m/s |
| x | average quality (across entire flow area) | / |
| $x_1$ | average quality in core layer | / |
| $x_2$ | average quality in bubble layer | / |
| y | distance from the wall | m |
| $\alpha_2$ | void fraction in bubble layer at CHF | / |
| $\delta$ | thickness of bubble layer | m |
| $\psi$ | miscellaneous function | / |
| $\rho_l$ | liquid density at bulk temperature | $kg/m^2$ |
| $\rho_g$ | vapor density | $kg/m^2$ |

## APPENDIX A: EVALUATION PROCEDURE OF THE MECHANISTIC BUBBLE-CROWDING MODEL

The calculation procedure is as follows:

$$q_{pre} = Gh_{fg}(x_2 - x_1)\psi i_{b-use}\frac{h_f - h_{ld}}{h_l - h_{ld}}$$

Calculate the bubble departure enthalpy $h_{ld}$

$$h_{ld} = h_f - \Delta T_{ld} C_{pf}$$

$$\begin{cases} 0 \le y_b^+ \le 5.0;\ \Delta T_{ld} = \frac{q}{H_{db}} - \frac{q}{G(\frac{f}{8})^{1/2}}\,\mathrm{Pr}\, y_b^+ \\ 5.0 \le y_b^+ \le 30.0;\ \Delta T_{ld} = \frac{q}{H_{db}} - 5.0\frac{q}{G(\frac{f}{8})^{1/2}}\left\{\mathrm{Pr} + In\left[1 + \mathrm{Pr}(y_b^+/5.0 - 1.0)\right]\right\} \\ y_b^+ \ge 30.0;\ \Delta T_{ld} = \frac{q}{H_{db}} - 5.0\frac{q}{G(\frac{f}{8})^{1/2}}\left\{\mathrm{Pr} + In(1.0 + 5.0\,\mathrm{Pr}) + 0.5In(y_b^+/30.0)\right\} \end{cases}$$

where,

$$y_b^+ = \frac{0.015}{\mu_f}\sqrt{\frac{\sigma g_c D}{\nu_f}}$$

$$H_{db} = 0.023\mathrm{Re}^{0.8}\mathrm{Pr}^{0.4}k_f/D$$

$$\mathrm{Re} = \frac{GD}{\eta_f}, \mathrm{Pr} = \frac{c_{pf}\eta_f}{k_f}$$

The turbulence intensity factor $i_b$ is calculated as

$$i_b = 0.2962 \times (k)^{0.462}\mathrm{Re}^{-0.1} \times (\frac{D_p}{D})^{0.462}[1 + a_3(\frac{G}{G_{\mathrm{cr}}})^{a_1}\alpha^{b_1}]$$

where k equals 0.58 and

$$\begin{aligned} a_1 &= 0.3, G > G_c;\ a_1 = -0.6, G < G_c;\ b_1 = 1.7, \\ &= a_3 197.9, \alpha \ge 0.52;\ b_1 = -0.06, a_3 = 69.65, \alpha < 0.52; \end{aligned}$$

$$F_{grid} = 1 + a_2\varepsilon^2 \mathrm{e}^{-b_2\frac{x}{D}}$$

$$i_{b-use} = i_b F_{grid}$$

where $a_2$ is 6.5, and $b_2$ is −0.13.

$$D_p = 0.015\left(\frac{8\rho\sigma D}{fG^2}\right)$$

Calculation of function $\psi$:

$$\psi = \left\{\frac{1}{\sqrt{2\pi}}\exp\left[-\frac{1}{2}(\frac{v_{1l}}{\sigma_{v'}})^2\right] - \frac{1}{2}(\frac{v_{1l}}{\sigma_{v'}})erfc(\frac{1}{\sqrt{2}}\frac{v_{1l}}{\sigma_{v'}})\right\}$$

$$\begin{aligned} v_{1l} &= \frac{q_b}{\rho_g h_{fg}} \\ q_b &= \frac{h_l - h_{ld}}{h_f - h_{ld}}q_{\exp} \\ \sigma_{v'} &= \frac{i_{b-use}G}{\overline{\rho}} = i_{b-use}\left[\frac{G}{\rho_l} + (\frac{G}{\rho_g} - \frac{G}{\rho_l})x_{avg}\right] \end{aligned}$$

To calculate the $x_1$ and $\rho_1$ based on $\alpha_2 = 0.82$:

$$\begin{aligned} s &= 5.5D_p \\ \rho_2 &= (1 - \alpha_2)\rho_f + \alpha_2\rho_g \\ \rho_1 &= \frac{r^2}{(r-s)^2}\rho_{avg} - \rho_2\frac{2(r - \frac{s}{2})s}{(r-s)^2} \\ \alpha_1 &= \frac{\rho_l - \rho_1}{\rho_l - \rho_g} \\ x_1 &= \frac{\alpha_1 \times \rho_g}{\rho_1}, x_2 = \frac{\alpha_2 \times \rho_g}{\rho_2} \end{aligned}$$

The predicted value is the result of the calculation on the left side of the first equation in Appendix A.

frontiers in Energy Research

ORIGINAL RESEARCH
published: 10 January 2020
doi: 10.3389/fenrg.2019.00161

# Numerical Simulation of Flow Boiling in Small Channel of Plate OTSG

*Xiaofei Yuan*[1,2], *Lixin Yang*[1,2]*, *Zihao Tian*[1,2], *Shuang Han*[1,2] *and Hongyan Lu*[1,2]

[1] *Institute of Thermal Engineering, School of Mechanical, Electronic and Control Engineering, Beijing Jiaotong University, Beijing, China,* [2] *Beijing Key Laboratory of Flow and Heat Transfer of Phase Changing in Micro and Small Scale, Beijing Jiaotong University, Beijing, China*

The plate OTSG (once-through steam generator) with channel diameter of 1–3 mm has high volume-power ratio and powerful resistance to high temperature and high pressure. It can well satisfy the needs of high heat transfer performance and good security of integrated pressure vessel in nuclear power. Heat transfer characteristics of flow boiling in the channel have aroused increasing concerns from scholars in this field. In this paper, based on the experimental results achieved by the researcher in our team, the drift flux model is applied to simulate the flow boiling heat transfer coefficients in the rectangular channel with equivalent diameter of 1.7 mm to further explore the flow boiling mechanism in the channel. The drift velocities and the distribution parameters of drift flux model are obtained by the empirical correlations of the horizontal flow. The simulation boundary conditions comply to the experimental conditions, the simulation resolutions are obtained by using STAR-CCM+. The simulation results indicate that the heat transfer coefficients trends along the flow direction are consistent with the trends of the experimental data. The drift velocities and the distribution parameters have little effect on the heat transfer coefficients of the horizontal small channel. When the drift velocity is 0 and the distribution parameter is 1, compared with the experimental data, the heat transfer coefficients in the single-phase liquid convective heat transfer region of the flow at high pressure are well higher, while those in the region that from bobble flow to the slug flow of the flow increase, even though they are still lower in annular flow region. The error between the predicted and the experimental is from −50 to +50%. Similarly, the model predicted heat transfer coefficients during subcooled flow boiling at low pressure are generally lower than experimental data. And the error between the predicted and the experimental is from −60 to +10%.

**Keywords: plate OTSG, rectangular channel, flow boiling, drift flux model, heat transfer coefficient**

OPEN ACCESS

***Edited by:***
*Liangming Pan,*
*Chongqing University, China*

***Reviewed by:***
*Rita Mastrullo,*
*Università degli Studi di Napoli Federico II, Italy*
*Zeyong Wang,*
*Converge Science, United States*

***Correspondence:**
*Lixin Yang*
*lxyang1@bjtu.edu.cn*

***Specialty section:***
*This article was submitted to Nuclear Energy, a section of the journal Frontiers in Energy Research*

***Received:*** *07 October 2019*
***Accepted:*** *11 December 2019*
***Published:*** *10 January 2020*

***Citation:***
*Yuan X, Yang L, Tian Z, Han S and Lu H (2020) Numerical Simulation of Flow Boiling in Small Channel of Plate OTSG. Front. Energy Res. 7:161. doi: 10.3389/fenrg.2019.00161*

## INTRODUCTION

After several severe accidents, the small modular reactor (SMR) design concepts are being developed for its good security and economic performance in recent years. The distinguishing feature of small modular reactor is that the pressurizer, the control rod drive mechanisms, all pumps and the steam generators are integrated into the reactor vessel. On the one hand, the small modular reactor can eliminate the coolant loss accident and enhance the safety in the process of accident. On the other hand, it can not only replace the traditional fossil fuel power plant, but also be used such as in underwater vehicle power system to increase the economy. Importantly,

the small module reactor can realize the overall off-site manufacturing and transportation to the site for assembly, which greatly reduces the construction cycle and construction time of the power plant and reduces the cost (Rowinski et al., 2015; Sun et al., 2018; Yin et al., 2018). Furthermore, increasing power density of small modular reactor is a way to make it more attractive for future deployment. And that power density can be increased by using more compact steam generators in the integral reactor vessel design (Shirvan et al., 2012). When the heat load and pressure drop are the same with those of traditional shell and tube heat exchanger, the volume of plate OTSG is decreased by 75%, while the heat transfer area density of plate OTSG is up to about 2,500 $m^2/m^3$, which can well meet the requirements of high volume power ratio, high heat transfer efficiency, high temperature resistance, and high pressure proof (Chen et al., 2016). But high volume power ratio of the plate OTSG will result in safety and design implications. So the studying of heat transfer characteristics in small channel of plate OTSG is the focus of research in the field of nuclear energy. At present, many researches focus on verification of the criterion correlations of single-phase convective heat transfer of the plate OTSG with different channel structures, etc. (Khan et al., 2015; Aneesh et al., 2018; Chen et al., 2019). Due to the complexity of the two-phase flow mechanism and the limitation of the experimental measurement methods (Banowski et al., 2017; Li et al., 2017), the two-phase flow characteristics of the small channel with diameter of about 3 mm are different from those of conventional channel. Shin and No (2017) suggested that experimental mass flow of flow boiling in small channel fluctuated greatly at low flow rates because of bubble disturbance and flow changed steadily as pressure increased. Yan et al. (2018) found that the bubble size during sliding in narrow rectangular channel are mainly affect by the liquid subcooling and wall superheat. Huang (2018) and Huang et al. (2018) found that the throat-annular flow pattern just generated in the horizontal small rectangular channel at high pressure and the heat transfer coefficients along the channel were higher than those of lower pressure with experimental conditions same. Kwon et al. (2018) proposed that film boiling occurred in the small semicircular channel because of the large temperature difference between the hot side and the cold side. As for flow boiling model, a mechanistic model for the wall heat flux partitioning during subcooled flow boiling developed and validated by Basu et al. (2005a,b) showed that the transient conduction component were the dominant mode of heat transfer at very high superheats. And an subcooled flow boiling modeling framework for CFD presented by Gilman and Baglietto (2017) revealed that the sliding (transient) conduction and augmented forced convection were the highest modes of heat removal from the surface. The predictions of an analytical model of transient heat transfer which developed by Wang and Podowski (2019) showed a good agreement with measurements. Sometimes the two-fluid model considering multiple effects between liquid and vapor phases have higher simulation accuracy, with closure models improved by experimental data for specific problems in a small range (Colombo and Fairweather, 2016; Sadaghiani and Koşar, 2016). However, due to lack of appropriate closure models describing all relevant phenomena and good numerical robustness for geometrically complex systems, applying two-fluid model to the engineering filed is very difficult now. It was noteworthy that within a certain operating range, the drift flux model predictions of the 2-D conventional scale channel were in good agreement with the experimental results (Rassame and Hibiki, 2018; Wei et al., 2018). And the empirical correlations of drift flow velocities and distribution parameters for different flow patterns in many drift flow models are available not only for conventional scale vertical channel (Hibiki and Ishii, 2003; Mei et al., 2018) but also for the horizontal flow of small channels (Bhagwat and Ghajar, 2014; Ran et al., 2018; Rassame and Hibiki, 2018). Therefore, based on the experimental data about heat transfer coefficients in the small rectangular channel of plate OTSG obtained by the researchers in our team (Huang, 2018; Huang et al., 2018), the drift flux model is applied to simulating the flow boiling heat transfer coefficients in the small rectangular channel of the plate OTSG in this paper. And the distribution parameters and the averaged drift velocities of drift flux model are illustrated in empirical correlations developed by Bhagwat and Ghajar (2014).

# EXPERIMENTAL SET-UP

## Test Loop

A test loop for the studying of flow boiling characteristics in small channel of plate OTSG had been built in our laboratory. Schematic diagram of the experimental apparatus is shown in **Figure 1**. The subcooled deionized water in the water tank is driven by the plunger pump into the preheater and then the test section. The 3 kW preheater is used to control the water temperature at the inlet of the test section. The voltage regulators having a total heating capacity of 9 kW make the preheated water turn into vapor in the channel of the test section. Then the liquid/vapor fluid mixture is condensed when mixture flows into the condenser. Finally the deionized water flow back to the tank. The mass flow in the loop is measured by the mass flowmeter. Temperature and pressure data are measured not only at inlet of the preheater but also at inlet and outlet of the test section. The system pressure is controlled by back pressure valve and safety valve. A high-speed camera is used to capture the flow pattern along the visualized area.

## Test Section

The schematic diagram of the test section is represented in **Figure 2**. The test section which horizontally placed in the test facility is 1,300 mm long, 90 mm wide, and 60 mm high. The rectangular small channel is machined in a stainless steel block. The high borosilicate glass is on the rectangular channel with asbestos pad under it. The rubber gasket is under the stainless steel cover of test section and the stainless steel cover is pressed against the glass by bolts. The rectangular channel is 2 mm in width and 1 mm in depth (the thickness of the asbestos gasket is 0.5 mm and so the total depth is 1.5 mm), thus resulting in an internal equivalent diameter of 1.7 mm. Its total length is 1,100 mm and the effective heating length is 900 mm. There are circular sumps with a diameter of 6 mm at each end of the

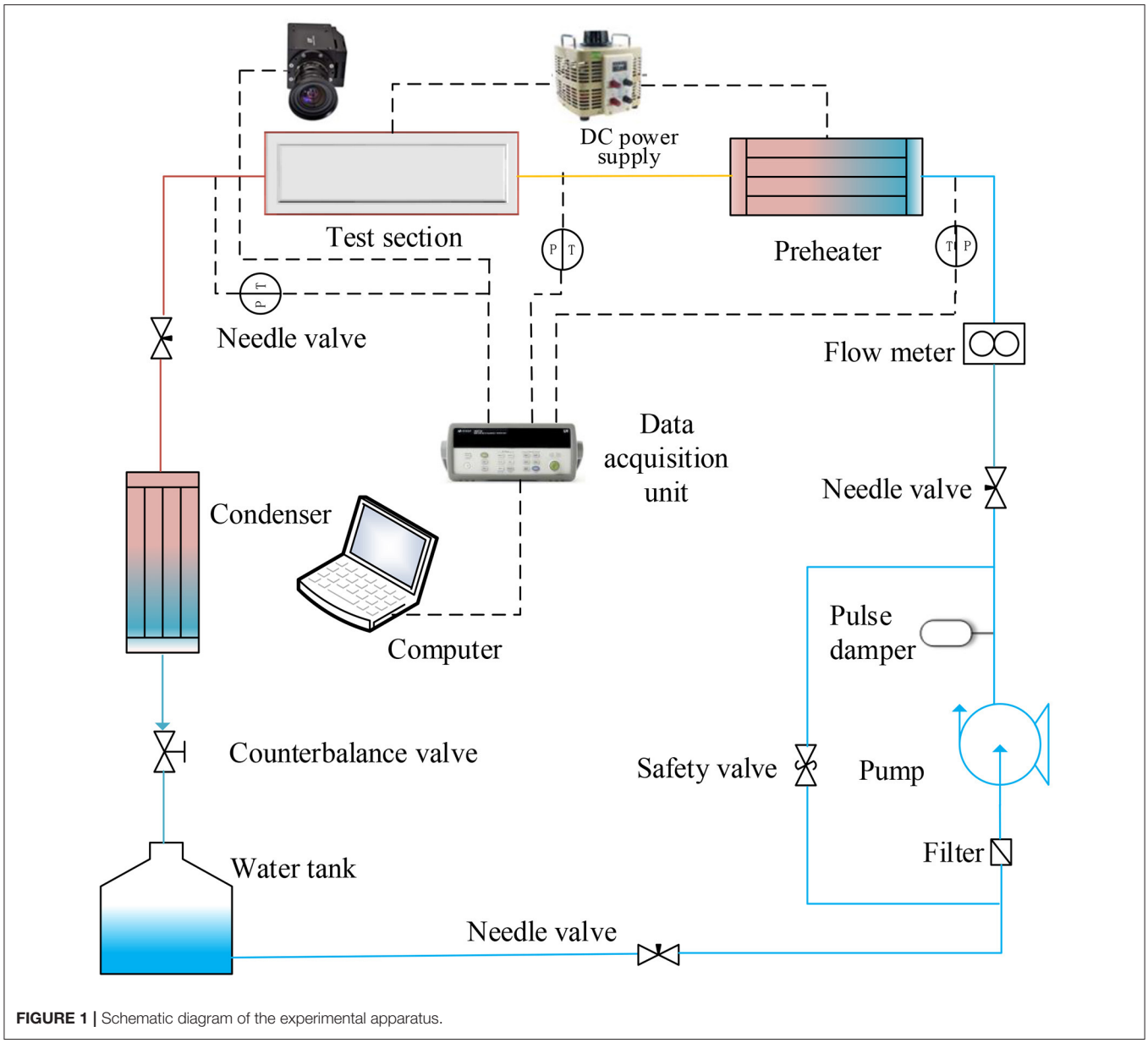


**FIGURE 1 |** Schematic diagram of the experimental apparatus.

rectangular channel. The two sumps extend 11 mm downward and connected with a circular passage of 8 mm in diameter and 86 mm in length, respectively. In order to facilitate the pipe connection, circular passages with a diameter of 13 mm and a length of 14 mm are machined at the inlet and outlet. At the bottom of the experimental section, there are two slots with a width of 5 mm and a depth of 39 mm near the inlet and outlet, so that the heat of the heated copper block is conducted upward, so as not to affect the liquid temperature measurement of the inlet and outlet. To measure the temperature along the test section, 27 thermocouples, three in each group, arranged right below the rectangular channel. Thirty-six barrel heaters with the diameter of 9 mm are placed in the copper base to provide heat power. The test section is covered with asbestos insulation material in order to minimize the heat losses.

## Experimental Data Reduction

The mass flux G inside the channel are calculated by the measured mass flow rate:

$$G = \frac{\dot{M}}{W \times H} \tag{1}$$

Subcooled section length:

$$L_{sub} = \frac{\dot{M} C_{p,l} \left(T_{sat} - T_{in}\right)}{(2 \times H + W)\, q} \tag{2}$$

The vapor quality $x$ at outlet can be calculated by the following formula:

$$x = \frac{1}{h_{lv}} \left( \frac{Q}{\dot{M}} - C_{p,l} \left(T_{sat} - T_{inlet}\right) \right) \tag{3}$$

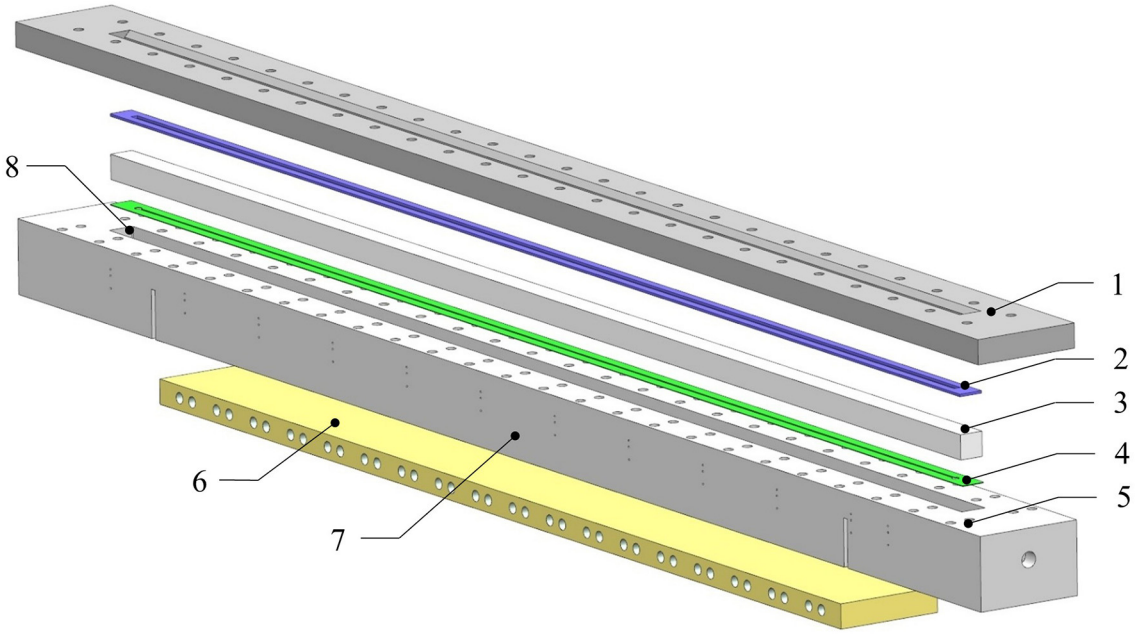


1. Stainless-cover; 2. Rubber gasket; High borosilicate glass; 4. Asbestos pad; 5. Stainless foundation; 6. Thermocouple position; 7. Brass heat block; 8. Small channel

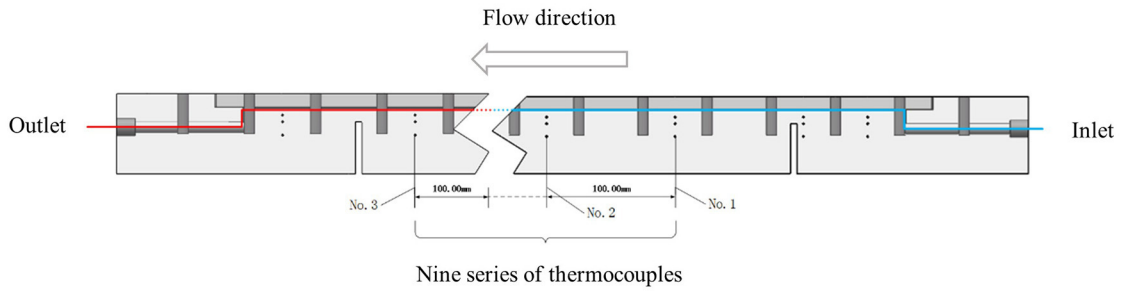


**FIGURE 2 |** The schematic diagram of the test section.

The heat transfer coefficient at the measurement point is obtained as follows:

$$h_{exp} = \frac{q_i}{T_{w,i} - T_{water,i}} \tag{4}$$

The subscript $i$ refers to the $i$th point. Whereas, $T_{water,i}$ represents the temperature of the water. The temperature of the water rises linearly from the inlet temperature to the saturation temperature in the flow direction when the water is in subcooled state. In the boiling state, the temperature of the water represents the saturation temperature. Assuming that the pressure along the path decreases linearly from the inlet pressure to the outlet pressure and the corresponding saturation temperature evaluated by the software REFPROP 9.0.

The heat flux and channel wall temperature are evaluated by the one-dimensional Fourier heat conduction law in the direction perpendicular to the channel cross section, respectively:

$$q_i = k\frac{\Delta T_i}{\Delta y_i} \tag{5}$$

$$T_{w,i} = T_i - \frac{q_i \Delta y_i}{k} \tag{6}$$

Whereas, $q_i$ is the heat flux and $T_{w,i}$ is the channel wall temperature. Where $k$ is thermal conductivity of stainless material. $\Delta T_i$ and $\Delta y_i$ represent the temperature difference and vertical distance between the thermocouples, respectively. $T_i$ refers to the thermocouple temperature.

Huang (2018) and Huang et al. (2018) conducted the subcooled flow boiling experiments in the rectangular small channel with the above introduced test loop. The heat transfer coefficients along the flow direction were reported with the

uncertainty of ±6.98%. The flow patterns in the rectangular small channel at a low pressure and a high pressure from Huang (2018) and Huang et al. (2018) are shown in **Figure 3**. As shown seven flow patterns were defined along the path in the experimental visualization and the proportion of every flow patterns in the flow path was described in the literature. To deeply understand the heat transfer mechanism in the small rectangular channel of plate OTSG, the drift flux model is applied to simulate the heat transfer coefficients in this paper based on the experimental data reported. The experimental conditions applied in this simulation are listed in **Table 1.** The vapor qualities at outlet of the channel for all these cases are lower than 1 and critical heat flux (CHF) does not occurred during Huang's experiments.

# NUMERICAL MODEL

## Drift Flux Mathematical Model

Assumption:

(a) The gas-liquid two-phase mixture is considered as a single fluid;
(b) The gas-liquid two phases are in thermal equilibrium;
(c) The gas-liquid two phases can move relative to each other.

Vapor quality:

$$x = \max\left[0, \min\left(1, \frac{h_m - h_{ls}}{h_{vs} - h_{ls}}\right)\right] \tag{7}$$

Vapor volume fraction:

$$\alpha = \frac{x}{x + (1-x)\frac{\rho_{vs}}{\rho_{ls}}} \tag{8}$$

Mixture continuity:

$$\frac{\partial \rho_m}{\partial t} + \nabla \cdot (\rho_m \mathbf{v}_m) = 0 \tag{9}$$

Mixture momentum:

$$\frac{\partial (\rho_m \mathbf{v}_m)}{\partial t} + \nabla \cdot (\rho_m \mathbf{v}_m \mathbf{v}_m) = -\nabla p + \nabla \cdot \mathbf{T}_m + \mathbf{f}_v - \nabla \cdot \left[\frac{\alpha}{1-\alpha}\frac{\rho_v \rho_l}{\rho_m}\bar{\mathbf{v}}_{vj}\bar{\mathbf{v}}_{vj}\right] \tag{10}$$

Mixture energy:

$$\frac{\partial (\rho_m E_m)}{\partial \mathrm{t}} + \nabla \cdot (\rho_m H_m \mathbf{v}_m) = -\nabla \cdot \dot{\mathbf{q}} + \nabla \cdot (\mathbf{T}_m \cdot \mathbf{v}_m) + (\mathbf{f}_v \cdot \mathbf{v}_m) - \nabla \cdot \left[\frac{\alpha \rho_v \rho_l}{\rho_m}\left(h_{vs} - h_{ls}\right)\bar{\mathbf{v}}_{vj}\right] \tag{11}$$

Solid equation:

$$\frac{\partial \left(\rho \mathrm{C}_p \mathrm{T}\right)}{\partial t} = -\nabla \cdot \dot{\mathbf{q}}' \tag{12}$$

Flow-solid interface equation:

$$\dot{\mathbf{q}} = \dot{\mathbf{q}}' \tag{13}$$

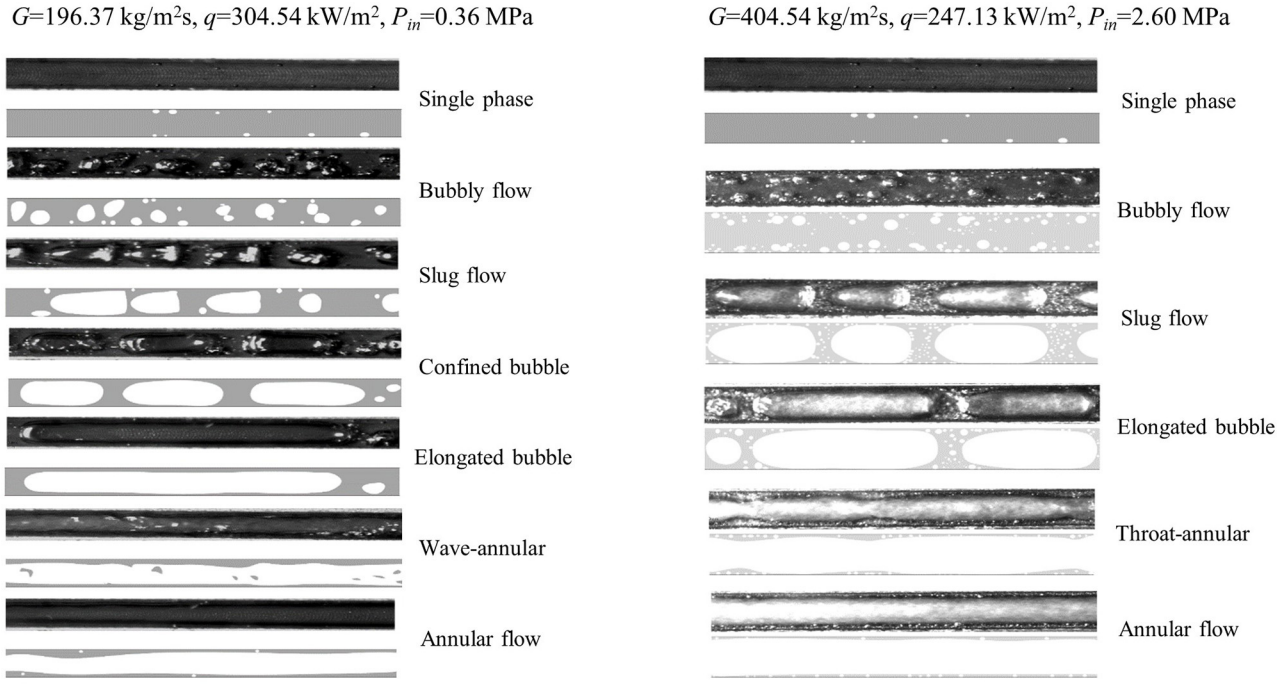


**FIGURE 3 |** The flow patterns in the rectangular small channel at a low pressure and a high pressure.

**TABLE 1 |** Simulation cases based on experimental conditions.

| Case | $P_{in}$ (MPa) | Mass flux [kg/(m$^2$·s)] | Average heat flux of channel wall (kW/m$^2$) | $M_{in}$ (kg/s) | $T_{in}$ (K) | $T_{sat}$ (K) | $P_{out}$ (MPa) | $Q$ (W) |
|---|---|---|---|---|---|---|---|---|
| 1 | 2.73 | 500 | 397.36 | 0.001444 | 450.12 | 501.77 | 2.727 | 1462.28 |
| 2 | 2.53 | 500 | 349.36 | 0.001462 | 447.09 | 497.55 | 2.521 | 1285.64 |
| 3 | 2.20 | 500 | 294.91 | 0.001476 | 445.86 | 490.32 | 2.193 | 1085.27 |
| 4 | 2.83 | 400 | 350.00 | 0.001207 | 474.56 | 503.7 | 2.826 | 1288.00 |
| 5 | 2.83 | 400 | 298.31 | 0.001207 | 474.56 | 503.7 | 2.826 | 1097.76 |
| 6 | 2.66 | 400 | 247.13 | 0.001212 | 460.12 | 500.21 | 2.650 | 909.44 |
| 7 | 2.63 | 300 | 292.94 | 0.000988 | 439.70 | 499.65 | 2.617 | 1078.02 |
| 8 | 0.21 | 500 | 299.40 | 0.00149 | 317.99 | 391.70 | 0.165 | 1101.78 |
| 9 | 0.34 | 400 | 297.94 | 0.001198 | 329.25 | 409.43 | 0.309 | 1096.44 |
| 10 | 0.38 | 300 | 295.57 | 0.000931 | 337.20 | 413.79 | 0.351 | 1087.71 |

$$T_m = T_s \tag{14}$$

The stress tensor:

$$\mathbf{T}_m = \mu_m \left[ \left( \nabla \mathbf{v}_m + \nabla \mathbf{v}_m{}^{\mathrm{T}} \right) - \frac{2}{3} \left( \nabla \cdot \mathbf{v}_m \right) \mathbf{I} \right] \tag{15}$$

Heat flux:

$$\dot{\mathbf{q}} = -k_{eff,m} \cdot \nabla T \tag{16}$$

$$\dot{\mathbf{q}}' = -k_{\mathrm{s}} \cdot \nabla T_s \tag{17}$$

The effective thermal conductivity:

$$k_{eff,m} = k_m + \frac{\mu_{t,m} C_{p,m}}{\sigma_{t,m}} \tag{18}$$

The mixture density:

$$\rho_m = \sum_{i=1}^{2} \alpha_i \rho_i \tag{19}$$

The mixture velocity:

$$\mathbf{v}_m = \frac{\sum_{i=1}^{2} \alpha_i \rho_i \mathbf{v}_i}{\rho_m} \tag{20}$$

The mixture viscosity:

$$\mu_m = \sum_{i=1}^{2} \alpha_i \mu_i \tag{21}$$

The mixture thermal conductivity:

$$k_m = \sum_{i=1}^{2} \alpha_i k_i \tag{22}$$

The mixture-specific static enthalpy:

$$h_m = \frac{\sum_{i=1}^{2} \alpha_i \rho_i h_i}{\rho_m} \tag{23}$$

The mixture total energy:

$$E_m = H_m - \frac{p}{\rho_m} \tag{24}$$

The mixture total enthalpy:

$$H_m = h_m + \frac{|\mathbf{v}_m|^2}{2} \tag{25}$$

The mean drift velocity of the vapor phase:

$$\bar{\mathbf{v}}_{vj} = \mathbf{v}_v - \mathbf{j} \tag{26}$$

The volume-weighted mixture velocity:

$$\mathbf{j} = \alpha \mathbf{v}_v + (1 - \alpha) \mathbf{v}_l \tag{27}$$

The velocity of vapor phase:

$$\mathbf{v}_v = \mathbf{v}_m + \frac{\rho_l}{\rho_m} \bar{\mathbf{v}}_{vj} \tag{28}$$

The velocity of liquid phase:

$$\mathbf{v}_l = \mathbf{v}_m - \frac{\alpha}{1 - \alpha} \frac{\rho_v}{\rho_m} \bar{\mathbf{v}}_{vj} \tag{29}$$

The averaged drift velocity is formulated in a functional form as:

$$\bar{\mathbf{v}}_{vj} = \frac{\left[ (C_0 - 1) \mathbf{v}_m + \mathbf{v}_{vj} \right] \rho_m}{C_0 \alpha \rho_v + (1 - C_0 \alpha) \rho_l} \tag{30}$$

The distribution parameter:

$$C_0 = \frac{\langle \alpha j \rangle}{\langle \alpha \rangle \langle j \rangle} \tag{31}$$

The subscripts $v$, $l$, $m$, and $s$ represent gas phase, liquid phase, mixing, and solids, respectively. $T_{sat}$ is the saturation

temperature. $\rho_{vs}$ and $\rho_{ls}$ are the densities of vapor and liquid at saturation temperature, respectively. $h_{vs}$ and $h_{ls}$ refer to the enthalpies of vapor and liquid at saturation temperature, respectively. $\mathbf{f}_v$ is the force due to gravity.

The empirical correlations of the distribution parameter and the averaged drift velocity developed by Bhagwat and Ghajar (2014) with experimental methods can be modeled as follow.

The distribution parameter:

$$C_0 = \frac{2 - \left(\frac{\rho_v}{\rho_f}\right)^2}{1 + \left(\frac{\mathrm{Re}_m}{1000}\right)^2} + \frac{\left[\left(\sqrt{1 + \left(\frac{\rho_v}{\rho_f}\right)^2}\right)(1-\alpha)\right]^{0.4}}{1 + \left(\frac{1000}{\mathrm{Re}_m}\right)^2} \quad (32)$$

$$\mathrm{Re}_m = \frac{j\rho_f D_h}{\mu_f} \quad (33)$$

The averaged drift velocity:

$$\mathbf{v}_{vj} = 0.45\sqrt{\frac{(\rho_f - \rho_v)\, gD_h}{\rho_f}}(1-\alpha)^{0.5} \quad (34)$$

## Numerical Model Settings

The numerical model and boundary conditions is shown in **Figure 4**. UG is used for the construction of the 3-D numerical model. Numerical solutions are obtained by using STAR-CCM+. As shown the numerical model is almost the same to that experimental test section studied by Huang (2018).Thermocouple holes and bolt holes have little effects on heat transfer in the channel. They are removed to simplify the numerical model so as to reduce the number of grids and increase computational efficiency. The uniform heating power is provided on the barrel heaters wall in the copper base. The other solid walls are adiabatic. The mass flow inlet and pressure outlet boundary conditions are selected for the flow liquid, respectively. All the data of simulation boundary conditions are taken from Huang's experimental data as shown in **Table 1**. The temperature of fluid thermo-physical properties is defined as saturation temperature at the average pressure of the inlet and outlet of test section. The fluid thermo-physical properties are obtained from the software REFPROP 9.0. The turbulence model is the K-Epsilon model. The thermo-physical properties of the solid materials are presented in **Table 2**. Steady-state simulations are conducted for all cases.

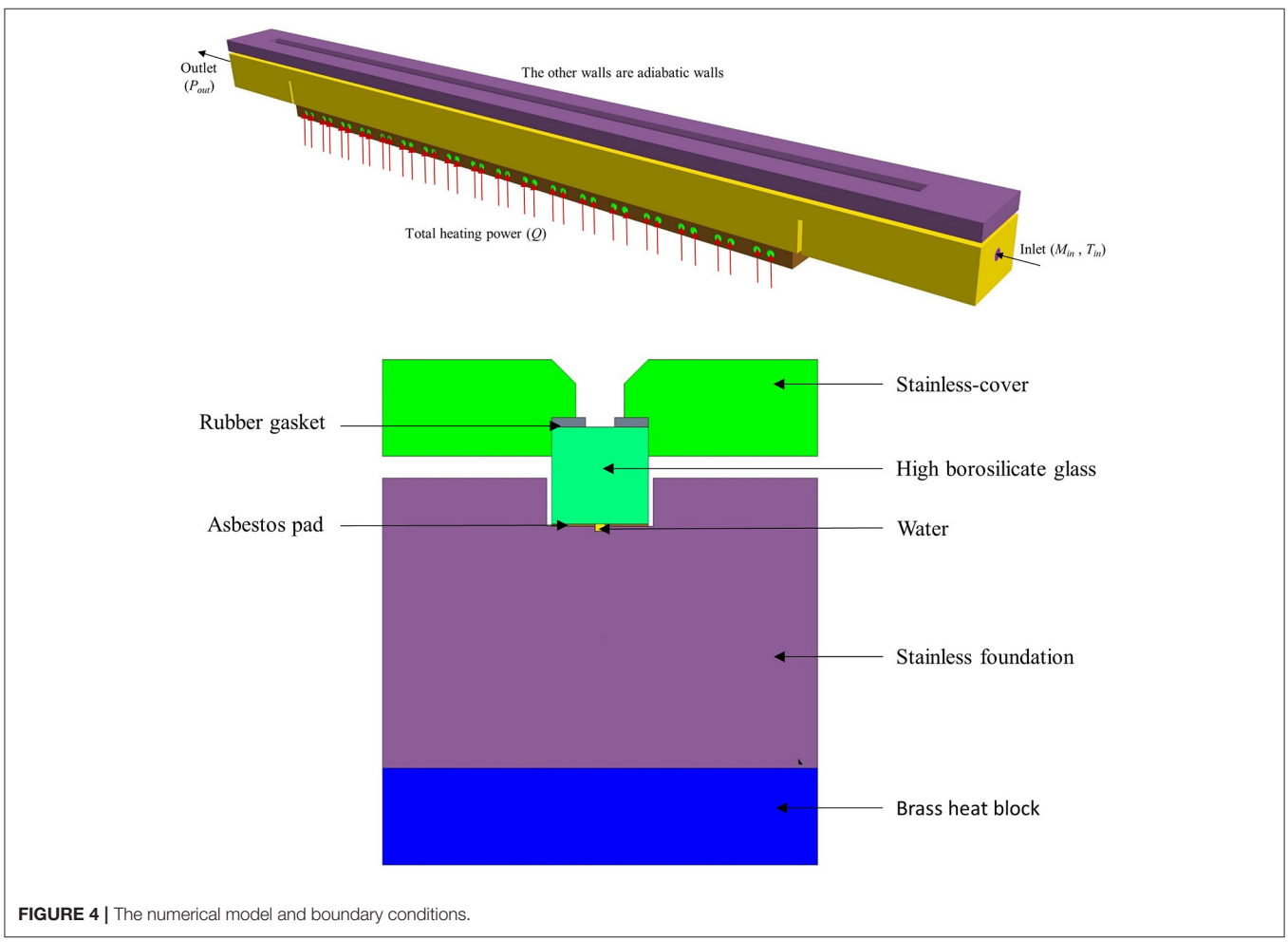


**FIGURE 4 |** The numerical model and boundary conditions.

**TABLE 2 |** The thermo-physical properties of the solid materials.

| | Brass | Stainless steel | Asbestos | High borosilicate glass | Rubber |
|---|---|---|---|---|---|
| $\rho$ (kg/m$^3$) | 8,530 | 8,055 | 2,490 | 2,230 | 1,100 |
| $C_p$[J/(kg·K)] | 375 | 480 | 816 | 900 | 692 |
| $k$ [W/(m·K)] | 120 | 15 | 0.15 | 1.2 | 0.9 |

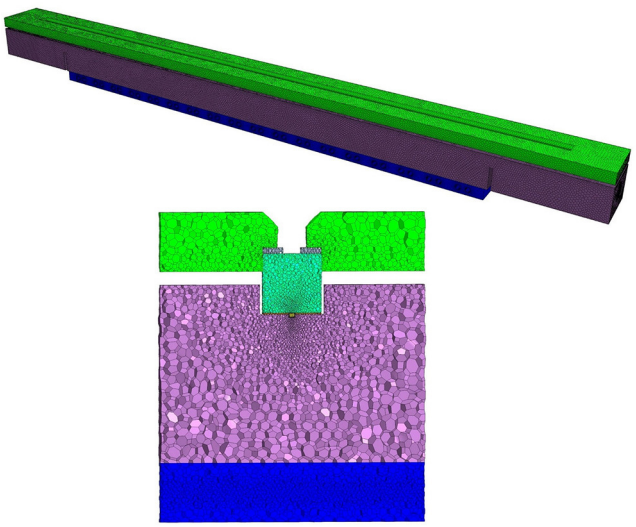

**FIGURE 5 |** The mesh of numerical model.

## Grid Independence Verification

The mesh of numerical model is shown in **Figure 5**. The mesh consists of a polyhedral mesh and a near wall prism layer mesh. The prism layer mesh is used at the interface between the solid and the fluid. The first layer is 0.1 mm. And three rows are constructed with a growth factor of 1.2 so that the wall y+ value remains at ∼30. Four different base size polyhedral meshes are used for mesh independence test, including mesh with grid numbers of 2373485, 2814973, 3370942, and 3722110. The results of grid independent validation test, illustrated in **Figure 6**, confirm that the average heat transfer coefficients do not change too much as a function of number of elements when the grid beyond 3370942 elements. Therefore, the grid number of 3370942 is sufficient to obtain a grid independent result.

# RESULTS AND DISCUSSION

The data reduction method of simulation is presented in **Figure 7**. The numerical heat transfer coefficients along the path can be calculated with the same formula used in the experiment. To reduce the error that maybe be caused by limit local data in the simulation, the small rectangular channel is divided into nine sections and each is 100 mm long. The heat flux and temperature of the channel wall of each section in the formula are regarded as the area average value, respectively. The fluid temperature of each section is defined as the average temperature at the centerline. Simply, the homogeneous flow model is abbreviated as HM, the drift flux model, as DFM, the experiment, as Exp.

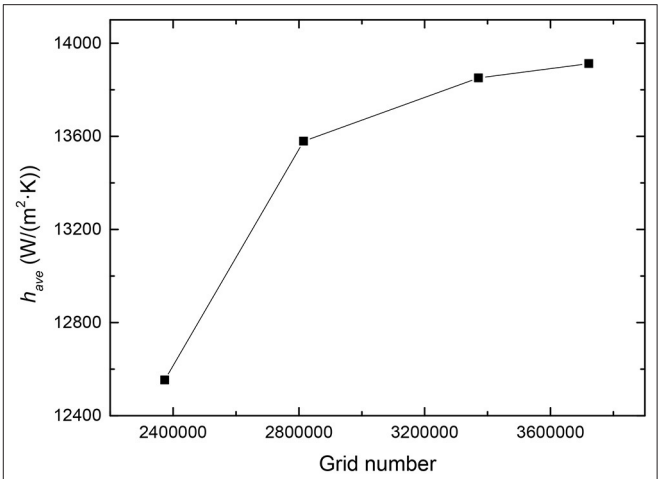


**FIGURE 6 |** The results of grid independent validation test.

The relative error can be calculated as follow:

$$\mathrm{RE} = \frac{h_{HM} - h_{Exp}}{h_{Exp}} \times 100\% \tag{35}$$

It should be noted that the proportions of different flow patterns mentioned in this results discussion are all taken from literatures of Huang (2018) and Huang (2018).

## Results Analysis of Drift Flux Model

**Figure 8** shows the effects of the distribution parameters and the averaged drift velocities on the heat transfer coefficients for case 1 [$G$ = 500 kg/(m$^2$·s), $q$ = 397.36 kW/m$^2$]. The distribution parameters and drift velocities calculated by Bhagwat and Ghajar (2014) have little change with gas fraction. So they are each evaluated by the average value ($C_0$ = 1.02, $v_{vj}$ = 0.05$m$/s) in the simulation. Also other typical values for the drift velocities and the distribution parameters are also applied in the simulation. An acceptable prediction is observed in the middle section of the channel, while simulated heat transfer coefficient is somewhat over-predicted in the inlet section and under-predicted in the outlet section. Obviously the drift velocities and the distribution parameters have little effects on the heat transfer coefficients during subcooled flow boiling. In short, the effects of two parameters of drift flux model can be neglected and that is homogeneous flow model.

## Results Analysis of Homogeneous Flow Model

### Results at High Pressure

The comparisons between experimental and numerical heat transfer coefficients at three heat fluxes of 294.91, 349.36, and

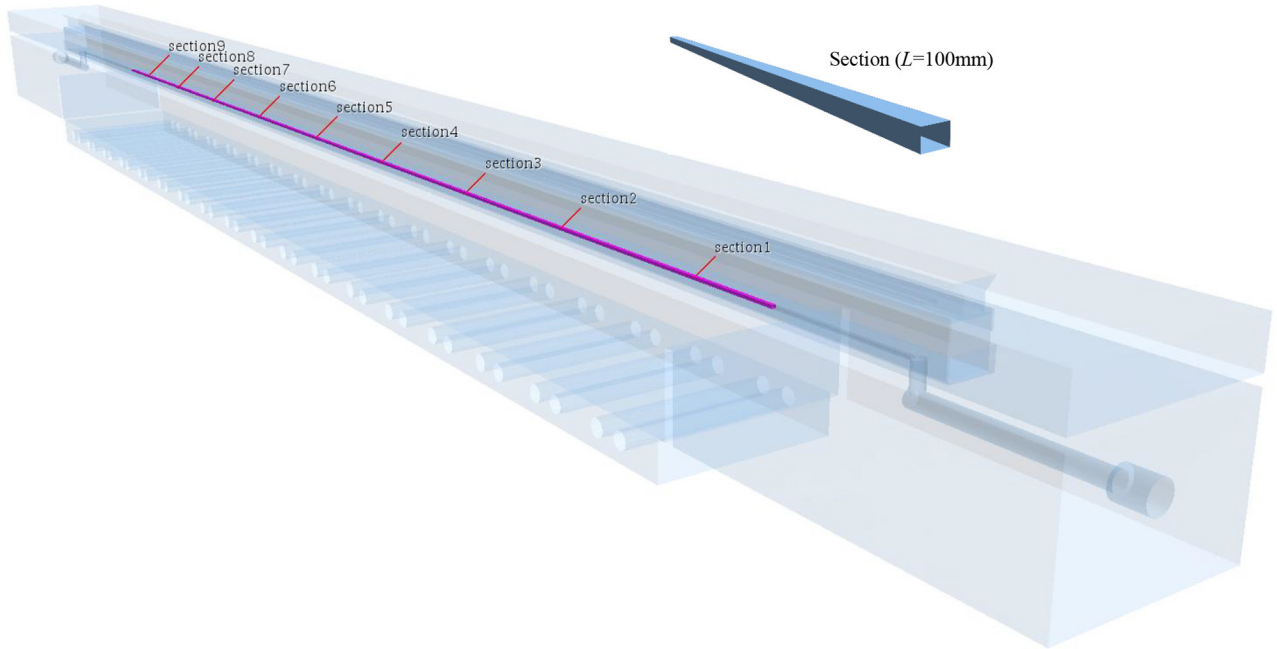


**FIGURE 7 |** The data reduction method of simulation.

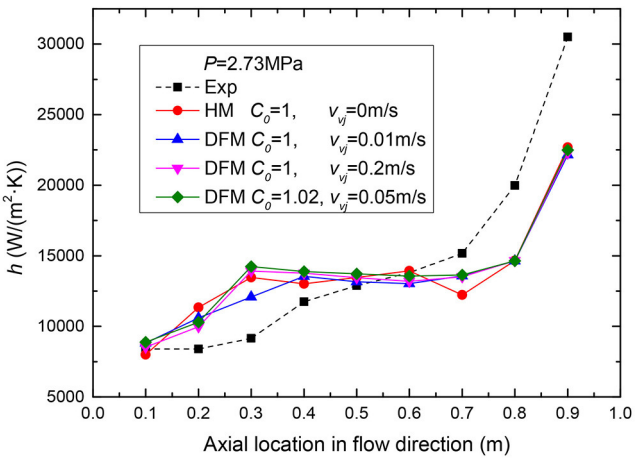


**FIGURE 8 |** The effects of the distribution parameters and the averaged drift velocities on the heat transfer coefficients.

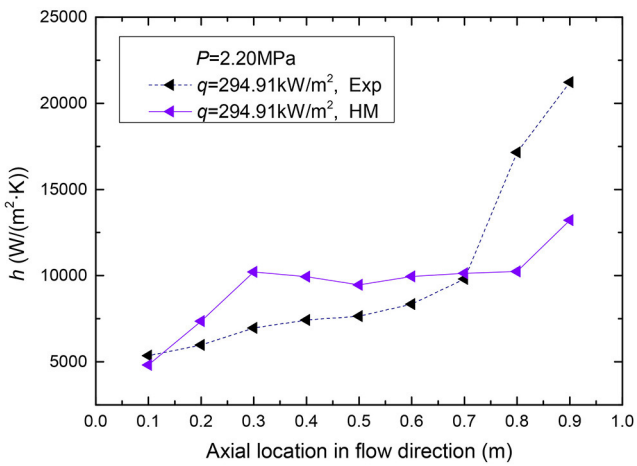


**FIGURE 9 |** The comparisons between experimental and numerical heat transfer coefficients for $q$ = 294.91 kW/m$^2$ and $G$ = 500 kg/(m$^2$·s).

397.36 kW/m$^2$, a mass flux of 500 kg/(m$^2$·s) are shown in **Figures 9–11** respectively. As can be found in the simulation results, the heat transfer coefficients increase along the flow path and the trends of simulation results match well with that of the experimental data. Compare with the experimental data, the heat transfer coefficients of simulation are well higher in the single-phase liquid convective heat transfer region and the higher the heat flux, the higher the simulated heat transfer coefficients. The differences among the heat transfer coefficients of simulation and those of experiment are mainly caused by the differences of thermo-physical properties. The temperature of the simulated fluid thermo-physical properties is defined as saturation temperature corresponding to the average pressure of the inlet and outlet of test section. The inlet pressure are slightly higher than the average pressure of inlet and outlet and also the inlet temperature are lower than the saturation temperature at the average pressure. And the values of specific heat of water in inlets of experiments are smaller than those at saturation temperatures which are applied to the simulation. Therefore, more heat is taken

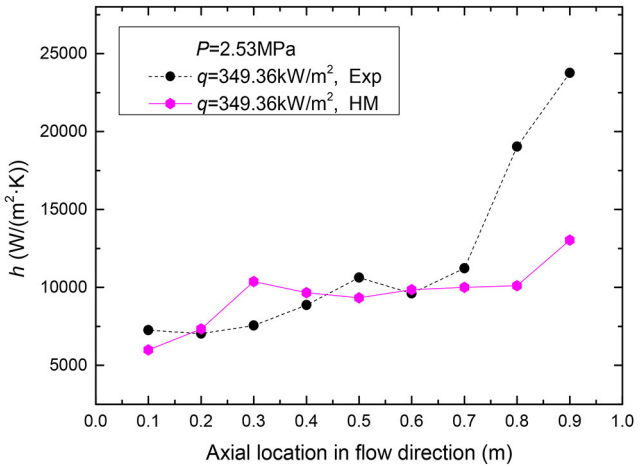


**FIGURE 10 |** The comparisons between experimental and numerical heat transfer coefficients for $q = 349.36$ kW/m$^2$ and $G = 500$ kg/(m$^2$·s).

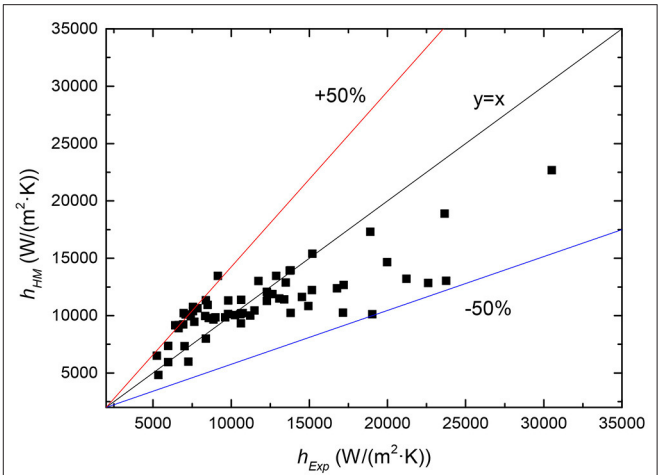


**FIGURE 12 |** The relative error at high pressure.

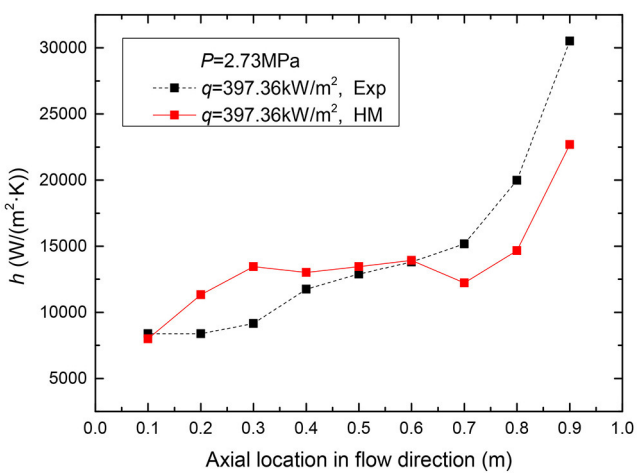


**FIGURE 11 |** The comparisons between experimental and numerical heat transfer coefficients for $q = 397.36$ kW/m$^2$ and $G = 500$ kg/(m$^2$·s).

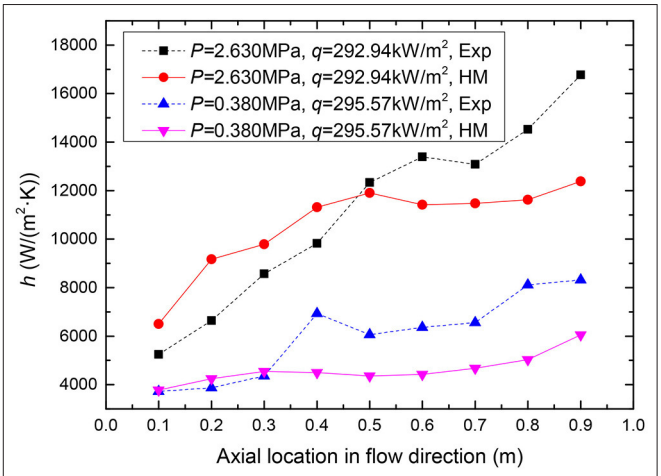


**FIGURE 13 |** The influences of the pressures on the heat transfer coefficients for $q = 300$ kW/m$^2$ and $G = 300$ kg/(m$^2$·s).

away from the inlet section in the simulation and the numerical heat transfer coefficients are higher than those of experiment. As the fluid enters the nucleate boiling region, the numerical heat transfer coefficients tend to approach the experimental results, and this trend continues in the region that from bobble flow to the slug flow. This is because of the phenomenon that the bubbles separated from the wall and sufficiently mixed with the water. Then the homogeneous flow model can well predict the heat transfer coefficients of plate OTSG. As flow boiling develops, the flow pattern is converted from a slug flow to an annular flow. The heat transfer coefficients continued to increase, even though they are still lower than those of experiment, It is considered that the small bubbles in the thin liquid layer near the wall disturb the thermal boundary layer and enhance the convective heat transfer in the experiment. But the homogeneous model can't give this phenomena a reasonable description. **Figure 12** indicates the relative error at high pressure. The relative error between simulation and experiment is from −50 to +50%.

## Results Comparisons at Different Pressures

The influences of the pressures on the heat transfer coefficients for mass fluxes of 300 and 400 kg/(m$^2$·s), heat flux of 300 kW/m$^2$ are illustrated in **Figures 13**, **14**, respectively. Compare with the experimental data, the simulation results trends at high pressures match better than those at low pressures. The numerical heat transfer coefficients in the single-phase liquid convective heat transfer region are basically consistent with the experimental results at low pressure. While simulation results are lower than the experimental data in the flow boiling region. It is taken into consideration that the gas density is lower at low pressure and thus the bubble disturbance to the liquid can significantly increase heat transfer in the experimental. The relative error at low pressure

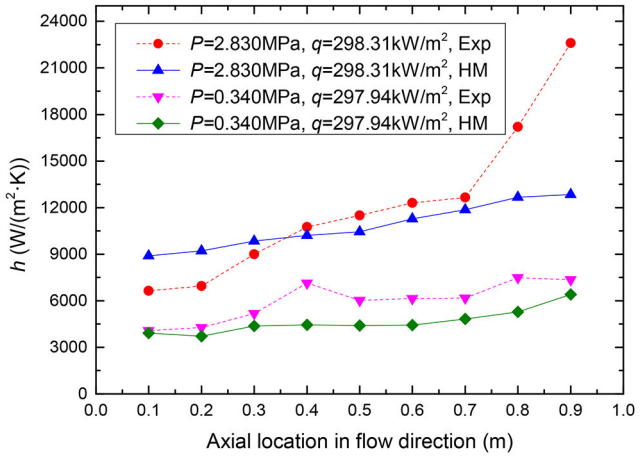


**FIGURE 14 |** The influences of the pressures on the heat transfer coefficients for $q = 300$ kW/m$^2$ and $G = 400$ kg/(m$^2$·s).

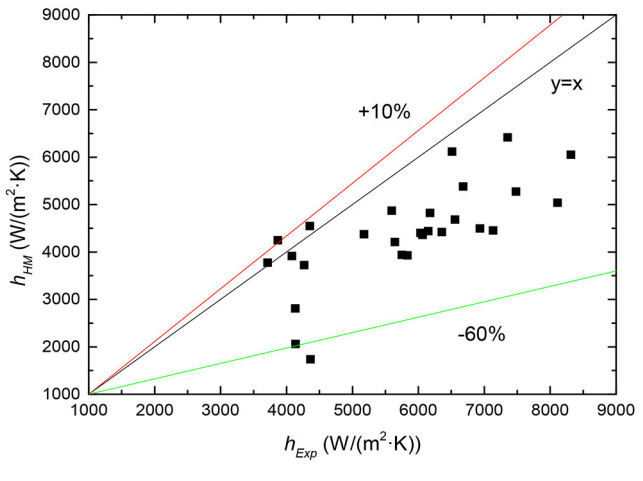


**FIGURE 15 |** The relative error at low pressure.

indicated in **Figure 15**, shows that the relative error between model predicted results and experimental data is from −60 to +10%.

## CONCLUSIONS

In this research, the drift flux model and homogeneous flow model are adopted to simulate the flow boiling heat transfer coefficients in small rectangular channel, The simulation software is STAR-CCM+. Conclusions are drawn as follows:

(1) The drift velocities and the distribution parameters have little effects on the heat transfer coefficients of the plate OTSG and the effects can be neglected.
(2) The homogeneous flow model under-predicts the heat transfer coefficients during subcooled flow boiling at low pressures. And the predictions of the homogeneous flow model at high pressures match better with the experimental results.
(3) At high pressure, the relative error between prediction and experiment is from −50 to +50%. At low pressure, the relative error between prediction and experiment is from −60 to +10%.
(4) According to the fluid-solid coupled 3-D simulations, the homogeneous flow model can predict the trends of heat transfer coefficients along the path at both high and low pressures. And at high pressure, the homogeneous flow model can well predict the heat transfer coefficients of plate OTSG in the region that from bobble flow to the slug flow. It is shown that the homogeneous flow model will be useful for evaluating the heat transfer characteristics of the plate OTSG.

## DATA AVAILABILITY STATEMENT

All datasets generated for this study are included in the article/supplementary material.

## AUTHOR CONTRIBUTIONS

XY carried out the establishment of boiling numerical model, geometric model, mesh models, the sampling of boundary conditions from experimental data, the results analysis as well as the writing of paper. LY provided the guideline of the research and modified the language of manuscript. ZT help finish the geometric modeling. SH and HL also provide guidance and assistance in the process. All authors worked together to define the methodology and procedures.

## REFERENCES

Aneesh, A. M., Sharma, A., Srivastava, A., and Chaudhury, P. (2018). Effects of wavy channel configurations on thermal-hydraulic characteristics of printed circuit heat exchanger (PCHE). *Int. J. Heat Mass Transf.* 118, 304–315. doi: 10.1016/j.ijheatmasstransfer.2017.10.111

Banowski, M., Hampel, U., Krepper, E., Beyer, M., and Lucas, D. (2017). Experimental investigation of two-phase pipe flow with ultrafast X-ray tomography and comparison with state-of-the-art CFD simulation. *Nucl. Eng. Des.* 336, 90–104. doi: 10.1016/j.nucengdes.2017.06.035

Basu, N., Warrier, G. R., and Dhir, V. K. (2005a). Wall heat flux partitioning during subcooled flow boiling: part 1—model development. *J. Heat Transfer* 127, 131–140. doi: 10.1115/1.1842784

Basu, N., Warrier, G. R., and Dhir, V. K. (2005b). Wall heat flux partitioning during subcooled flow boiling: partII—model validation. *J. Heat Transfer* 127, 141–148. doi: 10.1115/1.1842785

Bhagwat, S. M., and Ghajar, A. J. (2014). A flow pattern independent drift flux model based void fraction correlation for a wide range of gas-liquid two phase flow. *Int. J. Multiphase Flow* 59, 186–205. doi: 10.1016/j.ijmultiphaseflow.2013.11.001

Chen, M., Sun, X., and Christensen, R. N. (2019). Thermal-hydraulic performance of printed circuit heat exchangers with zigzag flow channels. *Int. J. Heat Mass Transf.* 130, 356–367. doi: 10.1016/j.ijheatmasstransfer.2018.10.031

Chen, M., Sun, X., Christensen, R. N., Shi, S., Skavdahl, I., Utgikar, V., et al. (2016). Experimental and numerical study of a printed circuit heat exchanger. *Ann. Nucl. Energy* 97, 221–231. doi: 10.1016/j.anucene.2016.07.010

Colombo, M., and Fairweather, M. (2016). Accuracy of eulerian–eulerian, two-fluid cfd boiling models of subcooled boiling flows. *Int. J. Heat Mass Transf.* 103, 28–44. doi: 10.1016/j.ijheatmasstransfer.2016.06.098

Gilman, L., and Baglietto, E. (2017). A self-consistent, physics-based boiling heat transfer modeling framework for use in computational fluid dynamics. *Int. J. Multiphase Flow* 95, 35–53. doi: 10.1016/j.ijmultiphaseflow.2017.04.018

Hibiki, T., and Ishii, M. (2003). One-dimensional drift-flux model and constitutive equations for relative motion between phases in various two-phase flow regimes. *Int. J. Heat Mass Transf.* 46, 4935–4948. doi: 10.1016/S0017-9310(03)00322-3

Huang, Q. (2018). *Experimental study on flow boiling in large diameter ratio of small channel* [master's thesis]. Beijing Jiaotong University, Beijing, China.

Huang, Q., Jia, L., Dang, C., and Yang, L. X. (2018). Experimental study on flow boiling of deionized water in a horizontal long small channel. *J. Therm. Sci.* 27, 157–166. doi: 10.1007/s11630-018-0996-1

Khan, H. H., M, A. A., Sharma, A., Srivastava, A., and Chaudhuri, P. (2015). Thermal-hydraulic characteristics and performance of 3d wavy channel based printed circuit heat exchanger. *Appl. Therm. Eng.* 87, 519–528. doi: 10.1016/j.applthermaleng.2015.04.077

Kwon, D., Jin, L., Jung, W. S., and Jeong, S. (2018). Experimental investigation of heat transfer coefficient of mini-channel pche (printed circuit heat exchanger). *Cryogenics* 92, 41–49. doi: 10.1016/j.cryogenics.2018.03.011

Li, H. W., Li, J. W., Su, Q., Liu, J. P., and Sun, B. (2017). Analysis of the characteristics of two-phase flow pattern in y-shape mixed microchannel based on double coupled duffing vibration simulation detection system. *Exp. Therm. Fluid Sci.* 91, 432–442. doi: 10.1016/j.expthermflusci.2017.10.039

Mei, Y., Gong, S. J., Gu, H. Y., and Ma, W. M. (2018). A study on steam-water two phase flow distribution in a rectangular channel with di?erent channel orientations. *Exp. Therm. Fluid Sci.* 99, 219–232. doi: 10.1016/j.expthermflusci.2018.07.022

Ran, K., Qingzi, Z., Seungjin, K., Mamoru, I., Stephen, B., and Kirk, T., et al. (2018). Void fraction prediction and one-dimensional drift-flux analysis for horizontal two-phase flow in different pipe sizes. *Exp. Therm. Fluid Sci.* 99, 433–445. doi: 10.1016/j.expthermflusci.2018.08.019

Rassame, S., and Hibiki, T. (2018). Drift-flux correlation for gas-liquid two-phase flow in a horizontal pipe. *Int. J. Heat Mass Transf.* 69, 33–42. doi: 10.1016/j.ijheatfluidflow.2017.11.002

Rowinski, M. K., White, T. J., and Zhao, J. Y. (2015). Small and medium sized reactors (SMR): a review of technology. *Renew. Sustain. Energy Rev.* 44, 643–656. doi: 10.1016/j.rser.2015.01.006

Sadaghiani, A. K., and Koşar, A. (2016). Numerical and experimental investigation on the effects of diameter and length on high mass flux subcooled flow boiling in horizontal microtubes. *Int. J. Heat Mass Transf.* 92, 824–837. doi: 10.1016/j.ijheatmasstransfer.2015.09.004

Shin, C. W., and No, H. C. (2017). Experimental study for pressure drop and flow instability of two-phase flow in the PCHE-type steam generator for SMRs. *Nucl. Eng. Des.* 318, 109–118. doi: 10.1016/j.nucengdes.2017.04.004

Shirvan, K., Hejzlar, P., and Kazimi, M. S. (2012). The design of a compact integral medium size PWR. *Nucl. Eng. Des.* 243, 393–403. doi: 10.1016/j.nucengdes.2011.11.023

Sun, H., Wang, C., Liu, X., Tian, W., Qiu, S., and Su, G. (2018). Reactor core design and analysis for a micronuclear power source. *Front. Energy Res.* 6:14. doi: 10.3389/fenrg.2018.00014

Wang, Z. Y., and Podowski, M. Z. (2019). Analytical modeling of the effect of heater geometry on boiling heat transfer. *Nucl. Eng. Des.* 144, 122–130. doi: 10.1016/j.nucengdes.2018.12.020

Wei, N., Xu, C. Y., Meng, Y. F., Li, G., Ma, X., and Liu, A. Q. (2018). Numerical simulation of gas-liquid two-phase flow in wellbore based on drift flux model. *Appl. Math. Comput.* 338, 175–191. doi: 10.1016/j.amc.2018.03.067

Yan, M., Ren, T., Chen, K., Yan, C., Yang, Y., Tian, C., et al. (2018). Visualized experiment of bubble behaviors in a vertical narrow rectangular channel under natural circulation condition. *Front. Energy Res.* 6:105. doi: 10.3389/fenrg.2018.00105

Yin, S., Tian, Y., Qiu, S., Tian, Y., Fang, H., Huang, W., et al. (2018). Accident process and core thermal response during a station blackout initiated study for small modular reactor. *Front. Energy Res.* 6:43. doi: 10.3389/fenrg.2018.00043

**Conflict of Interest:** The authors declare that the research was conducted in the absence of any commercial or financial relationships that could be construed as a potential conflict of interest.

## NOMENCLATURE

| | |
|---|---|
| Re | Reynolds number |
| $H$ | Height |
| $W$ | Width |
| $L$ | Length |
| $L_{sub}$ | Subcooled section length |
| $D_h$ | Equivalent diameter |
| $T$ | Temperature |
| $\Delta T_i$ | Temperature difference between the thermocouples |
| $\Delta y_i$ | Vertical distance between the thermocouples |
| $x$ | Vapor quality |
| $g$ | Gravitational acceleration |
| $k$ | Thermal conductivity |
| $C_p$ | Constant pressure specific heat |
| $Q$ | Total heating power |
| $M$ | Mass flow |
| $G$ | Mass flux |
| $q$ | Heat flux |
| $E$ | Total energy |
| $H$ | Total enthalpy |
| $h$ | Specific static enthalpy |
| $C_0$ | Distribution parameter |
| $\mathbf{v}_{vj}$ | Drift velocity |
| $j$ | The volume-weighted mixture velocity |
| **Greek symbols** | |
| $\alpha$ | Vapor volume fractions |
| $\rho$ | Densities |
| $\mu$ | Dynamic viscosity |
| **Subscripts and acronyms** | |
| Exp | Experimental parameter |
| DFM | Drift flux model |
| *RE* | Relative error |
| HM | Homogeneous flow model |
| *AL* | Aluminum |
| *w* | Wall |
| *sat* | Saturation condition |
| *l* | Liquid |
| *v* | Vapor |
| *s* | Solid |
| *m* | Mixture |
| *ave* | Average |
| *i* | ith point or ith phase |

frontiers in Energy Research

ORIGINAL RESEARCH
published: 17 January 2020
doi: 10.3389/fenrg.2019.00167

# Thermoelectric Conversion Performance of Combined Thermoions System for Space Nuclear Power Supply

*Haochun Zhang[1]*, Dezhuang Yin[1], Xiaoming Chai[2], Boran Kong[1] and Xiuting Liu[1]*

*[1] School of Energy Science and Engineering, Harbin Institute of Technology, Harbin, China, [2] Key Laboratory of Reactor System Design Technology, Nuclear Power Institute of China, Chengdu, China*

Thermoelectric conversion system, as one of the keys of space nuclear power supply system, is of great significance to the development and application of space nuclear power source. Thermion thermoelectric conversion system is a kind of thermoelectric conversion technology with potential for development, it has simple equipment and compact structure, but its conversion efficiency is limited by the inherent characteristics of the heat ion Energy converter, in order to improve the conversion efficiency of the thermionic energy converter, the thermionic energy converter and thermoelectric generator are coupled. In this paper, the thermionic-thermoelectric generator is taken as the research object, and the thermodynamic analysis and calculation of the thermionic-thermoelectric generator model is carried out by using the existing formula, on the basis of which the appropriate parameters are selected to optimize the system performance.

**Keywords: space nuclear power source, thermionic-thermoelectric, generator system performance, quality factor, optimization**

OPEN ACCESS

***Edited by:***
*Ki-Yong Choi,*
*Korea Atomic Energy Research Institute (KAERI), South Korea*

***Reviewed by:***
*Luteng Zhang,*
*Chongqing University, China*
*Huali Wu,*
*University of Wisconsin System, United States*

****Correspondence:***
*Haochun Zhang*
*zhc5@vip.163.com*

***Specialty section:***
*This article was submitted to Nuclear Energy, a section of the journal Frontiers in Energy Research*

***Received:*** *31 October 2019*
***Accepted:*** *24 December 2019*
***Published:*** *17 January 2020*

***Citation:***
*Zhang H, Yin D, Chai X, Kong B and Liu X (2020) Thermoelectric Conversion Performance of Combined Thermoions System for Space Nuclear Power Supply. Front. Energy Res. 7:167. doi: 10.3389/fenrg.2019.00167*

## INTRODUCTION

Space nuclear power is very important for deep space exploration, and the thermoelectric conversion efficiency of space nuclear power devices has a very important impact on the whole system. Thermoelectric conversion is divided into static conversion and dynamic conversion. Dynamic conversion mainly includes Stirling cycle, Rankine cycle, and Brayton cycle. Static conversion includes thermionic conversion, alkali metal conversion, temperature difference conversion, and MHD power generation.

Thermion thermoelectric conversion is a kind of static thermoelectric convention device that can conveniently convert the heat energy at relatively high temperatures into electricity (Yarygin, 2012). At present, only thermionic conversion and temperature difference conversion are used in nuclear power plants. Thermionic conversion has the advantages of small system volume and light weight, but short service life and low efficiency (Albertoni et al., 2013). Since the beginning of the last century, research on space nuclear thermionic thermoelectric conversion has been carried out. The thermoelectric conversion method adopted by the power supply of the two TOPAZ space nuclear reactors successfully launched by Russia is thermionic thermoelectric conversion. TOPAZ-I was in orbit for 6 months until cesium was consumed. TOPAZ-II uses a single section of thermionic original, and can be electrically heated on the test bench before launching. But its efficiency is not ideal. In order to improve the efficiency of thermoelectric conversion, the

energy conversion efficiency of thermion conversion is closely dependent on the materials of the cathode working at higher temperatures and the space charge effect (Bellucci et al., 2016). El-Genk et al. established a thermionic transient analysis model (TITAM) to analyze the steady state and transient state of the power system of a thermionic nuclear reactor. The research has reference value for space nuclear power thermionic conversion (El-Genk et al., 1993). Covas Nickoff proved that adding barium vapor to cesium vapor can ensure the emitter to reach the best work function, thus improving the conversion efficiency. NASA developed program code to analyze flowing fluid in space radiators (Hainley, 1991). GRC has developed LERCHP code, which can determine the operating temperature of radiator under specific conditions (Tower et al., 1992). El-Genk proposed that micro-nano technology can be used to reduce the work function on the emitter surface, thus improving the conversion efficiency (Paramonov and El-Genk, 1997). Jensen proposed a micro-ridge arrangement of electrodes, which is beneficial for electrons to face the receiving electrode and can improve the overall current density (Jensen et al., 2006). Mannhart suggests that graphene or related 2D materials can be treated as gate electrodes because electrons with energies between 2 and 40 eV have a transparency of up to 60% (Hassink et al., 2015; Wanke et al., 2016). Koeck and Nemanich have developed nitrogen doped nano diamond films with effective work function as low as 1.99eV (Koeck and Nemanich, 2006). Zhang et al. have done a lot of work on the design and performance analysis of liquid metal heat pipe radiators for space nuclear energy systems (Zhang et al., 2016a,b). Wang et al. modified and applied the system analysis code RELAP5 to provide more detailed transient thermal-hydraulic characteristics of space nuclear energy systems (Tang et al., 2019).

Research has proved that there is not much room to improve the efficiency of thermionic conversion due to its working principle. However, the electrode still has a high temperature after thermionic thermoelectric conversion. These energies are directly discharged into space and are not well-utilized. In this paper, thermionic conversion and thermoelectric generation are combined to utilize waste heat after thermionic conversion and improve conversion efficiency.

## THERMIONIC THERMOELECTRIC CONVERSION DEVICE

The direct conversion of heat energy into electrical energy is called thermion conversion by the phenomenon of transmitting electrons at high temperature of metal. At a non-0 temperature, when the metal is immersed in rare gas vapor, charged particles, such as electrons, ions, emitted from the metal surface like vapor are called thermion emission (Hatsopoulos and Gyftopoulos, 1973).

Thermoelectric conversion devices based on the principle of thermion emission are called thermionic energy converters. The thermionic energy converter consists of a emitter that emits electrons, a receiving stage that receives electrons, and a metal ceramic seal that separates two electrodes. The thermionic energy converter is insulated and sealed (Liao et al., 2016; Chen et al., 2017). At work, the emitter is heated to a very high temperature. The free electrons on the metal surface get enough energy and leap the electrode clearance, then reach the receiving stage. The electrons work on the load through the outer circuit connected to two electrodes, then return to the emitter, forming an electrical circuit. The residual heat is discharged through the receiving stage. The principle of thermionic energy converter is shown in **Figure 1**.

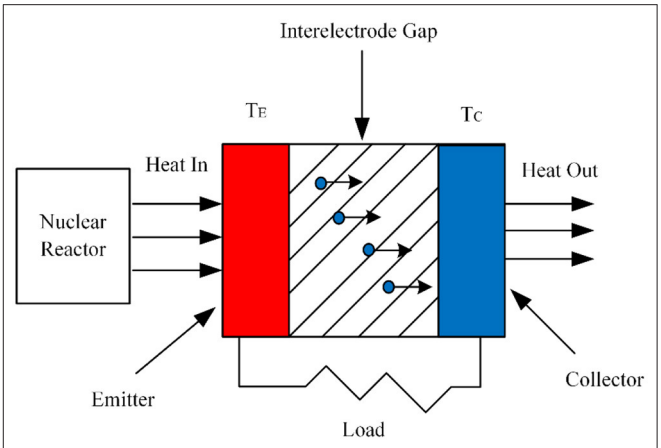


**FIGURE 1 |** The principle of thermionic energy converter.

## THERMIONIC THERMOELECTRIC GENERATOR

### Model of Thermionic-Thermoelectric Generator

In order to use the temperature of the anode discharge of the thermion thermoelectric conversion, the thermion thermoelectric conversion, and the thermoelectric generator are coupled. Without significantly affecting the performance of thermion thermoelectric conversion, the thermoelectric generator is driven by a large temperature difference between the anode temperature and the room temperature to generate additional power (Meng et al., 2014). Model of thermionic-thermoelectric generator is shown in **Figure 2**.

### Formula of Thermionic-Thermoelectric Generator Model

Thermionic generator consists of two components: emitter and collector, which are separated by a small space (Zhang et al., 2014). After the emitter of the thermionic generator is heated by the heat source, part of the electrons in the interior of the thermionic generator will have kinetic energy greater than the work function. The electrons escape from the surface of the emitter to form thermionic ions and they are accelerated by the collector. Then run to the collector and create the formation of current. When the current flows through the load, part of the emitter′s heat energy is consumed by the load. The current density from the emitter and collector can be approximated by

the Richardson equation:

$$Jc = AT_{c^2} \exp\left(-q\Phi_c/K_B Tc\right) \quad (1)$$

$$Ja = AT_a{}^2 \exp\left(-q\Phi_a/K_B Ta\right) \quad (2)$$

$$J = J_c - J_a \quad (3)$$

The heat flow rate away from the emitter due to the transmission of electrons is $Q_1$, the heat flow rate received of the receiver due to the transmission of electrons is $Q_2$. The radiant current from emitter to receiver is $Q_R$.

$$Q_1 = A\left[\left(\Phi_{c+}2K_B T_c/q\right)Jc\text{-}\left(\Phi_c{+}2K_B T_a/q\right)J_a\right] \quad (4)$$

$$Q_2 = A\left[\left(\Phi_{a+}2K_B T_c/q\right)Jc\text{-}\left(\Phi_{a+}2K_B T_a/q\right)J_a\right] \quad (5)$$

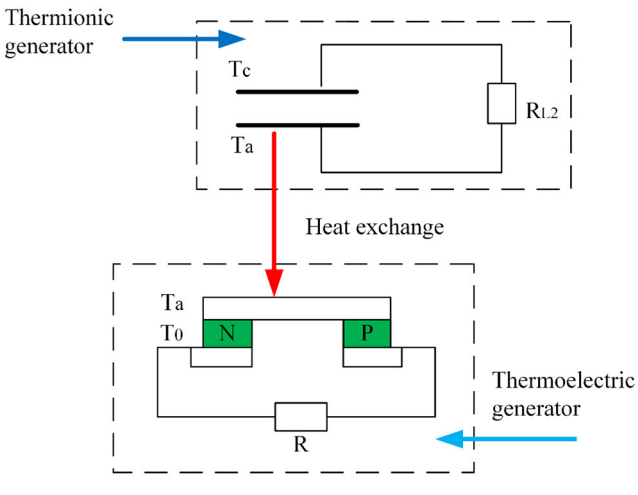


**FIGURE 2 |** Model of thermionic-thermoelectric generator.

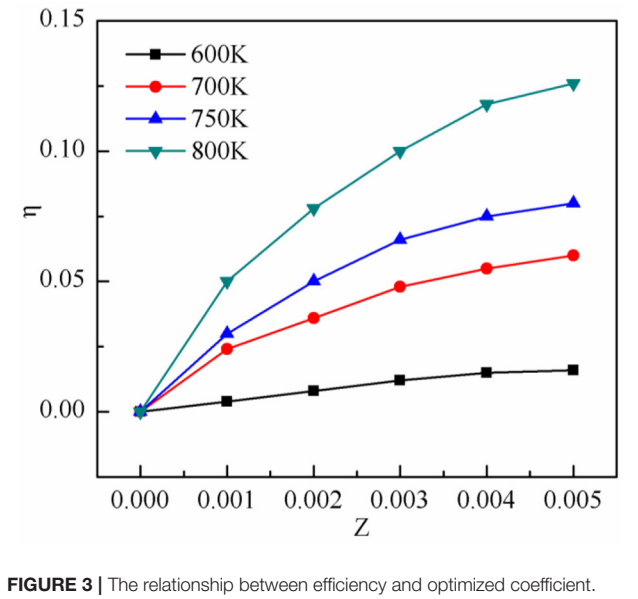


**FIGURE 3 |** The relationship between efficiency and optimized coefficient.

$$Q_R = \varepsilon_0 \sigma A\left(T_c^4\text{-}T_{a^4}\right) \quad (6)$$

The total heat flow away from the emitter is $Q_C$, the total heat flow received of the receiver is $Q_A$.

$$Q_C = Q_1{+}Q_R \quad (7)$$

$$Q_A = Q_2{+}Q_R \quad (8)$$

Finally, the power density of the thermionic convertor can be calculated:

$$P_{TH}{=}Q_C\text{-}Q_A{=}VJA \quad (9)$$

The heat absorbed from hot junction is $Q_H$, the heat released by cold junction is $Q_L$.

$$Q_H = \alpha I T_a\text{-}\frac{1}{2}I^2 R\text{-}K\left(T_a\text{-}T_0\right) \quad (10)$$

$$Q_L = \alpha I T_{0+}\frac{1}{2}I^2 R{+}K\left(T_a\text{-}T_0\right) \quad (11)$$

In the equation: α, I, R, K is the Bessel coefficient, current, resistance, heat transfer coefficient of the semi-conductor.

$$\alpha = N\left(\alpha_p\text{-}\alpha_n\right) \quad (12)$$

**TABLE 1 |** The parameters of the semi-conductor.

| Item | Value |
|---|---|
| The ratio of area over length $A_p/l_p = A_n/l_n$ | 10 mm |
| Thermal conductivity $K_p{+}K_n$ | 4.83 W/m·K |
| Heat resistance $\rho_p{+}\rho_n$ | $4.17 \times 10^{-6}\Omega$·m |
| Bessel coefficient $\alpha_{p-}\alpha_n$ | 830 uV/K |
| The number of the conductor | 33 |

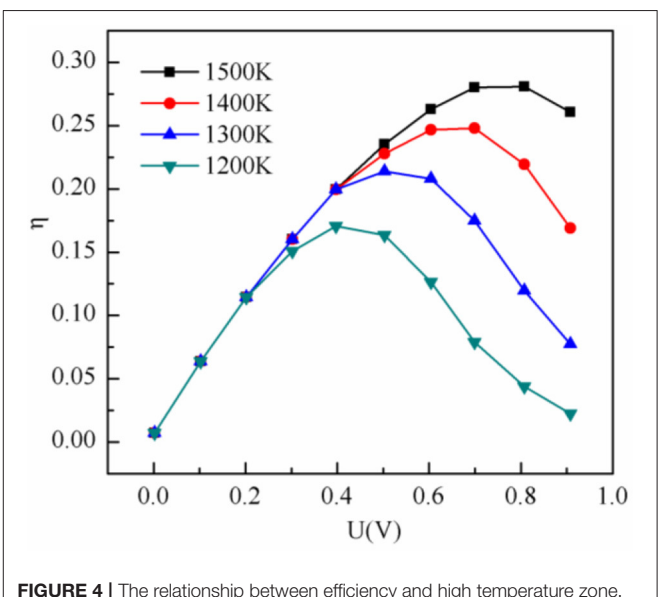


**FIGURE 4 |** The relationship between efficiency and high temperature zone.

$$R = N\left(\rho_p 1_p/A_p + \rho_n l_n/A_n\right) \quad (13)$$

$$K = N\left(k_p A_p/l_p + k_n A_n/l_n\right) \quad (14)$$

In the equation, the lower mark means whether it is n side or the p side of the semi-conductor. And then get the thermoelectric conductor power formula:

$$P_{TE} = \frac{ZK(T_a\text{-}T_0)^2}{(1+R_{L2}/R)^2}\frac{R_{L2}}{R} \quad (15)$$

$$P_{TOTAL} = P_{TH}+P_{TE}=VJA+\frac{ZK(T_a\text{-}T_0)^2}{(1+R_{L2}/R)^2}\frac{R_{L2}}{R} \quad (16)$$

The final efficiency formula is:

$$\eta=\frac{P_{TH}+P_{TE}}{Q_{in}}=\frac{VJA+\frac{ZK(T_a\text{-}T_0)^2}{(1+R_{L2}/R)^2}\frac{R_{L2}}{R}}{Q_1+Q_R} \quad (17)$$

## Optimization of Thermoionic-Thermoelectric Generator

For the whole thermoelectric conversion device, the optimization coefficient Z is an important parameter of the thermoelectric conversion device, and the value of the optimization coefficient Z needs to be determined first. Therefore, it is necessary to find the relationship between

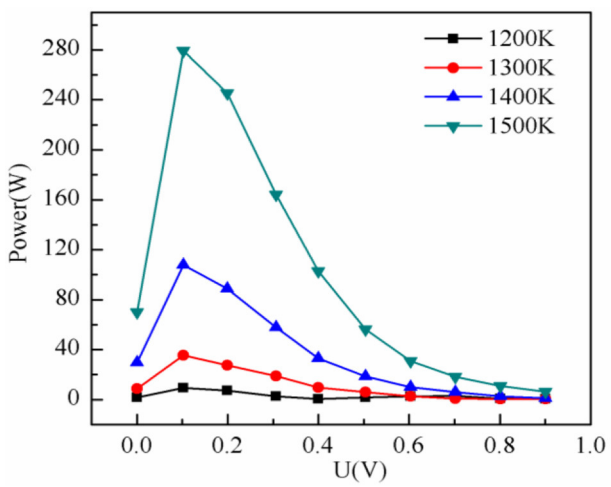


**FIGURE 5 |** The relationship between power and high temperature zone.

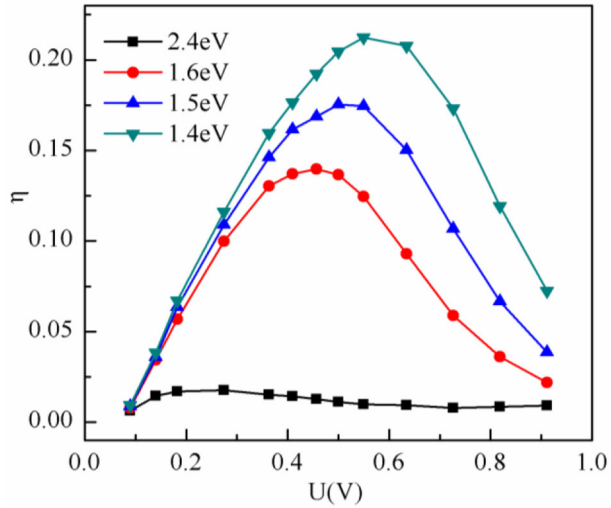


**FIGURE 6 |** The relationship between efficiency and rare vapor pressure.

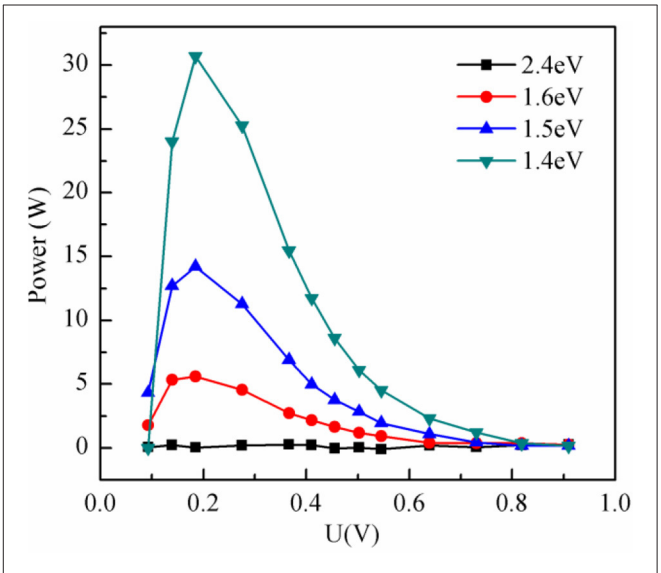


**FIGURE 7 |** The relationship between power and rare vapor pressure.

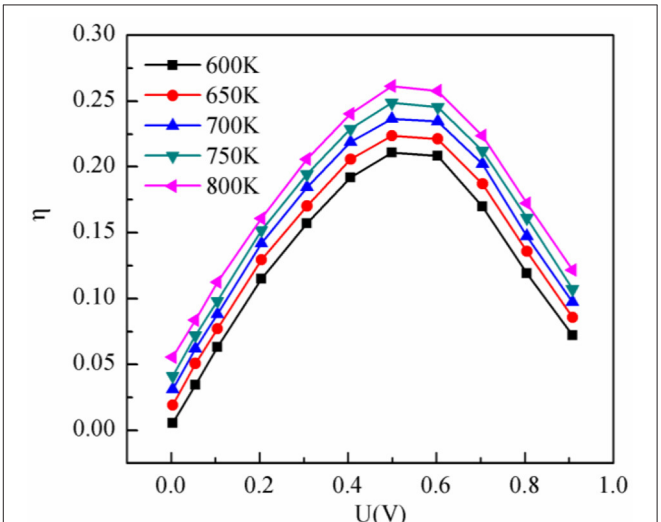


**FIGURE 8 |** The relationship between efficiency and low temperature zone.

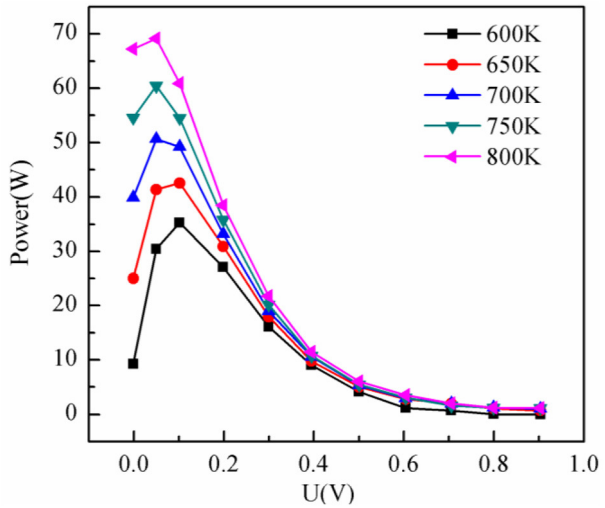


**FIGURE 9 |** The relationship between power and low temperature zone.

**TABLE 2 |** The parameters of the model.

| Items | Value |
|---|---|
| $T_c$ | 1,500 K |
| $T_a$ | 800 K |
| Z | 0.00336 |
| Rare vapor pressure | 1.4 eV |
| $A$ | $2.5 \times 10^{-4} m^2$ |
| $R_{L2}/R$ | 1.01 |
| The number of the convertor | 33 |

efficiency and optimization coefficient Z, as shown in **Figure 3**.

It can be seen from the figure that with the increase of the $Z$, the efficiency of the thermoelectric is higher, so it is better to choose a higher $Z$. The part makes a choice between the price and the mass, and finally find a semi-conductor that is relative high optimized coefficient. And the final $Z$ is 0.00336. The parameters of the semi-conductor are listed in **Table 1**.

After determining the optimized coefficient Z and the parameters of the semi-conductor, we need to find the relationships between efficiency, power and high temperature zone Tc. The output voltage is U. The relationships between efficiency, power and high temperature zone Tc are shown in **Figures 4**, **5**.

From the figures, it can be seen that with the increase of the high temperature zone, the peak power and the efficiency are all higher. Here choose Tc = 1,500 K. The relationships between efficiency, power and rare vapor pressure are shown in **Figures 6**, **7**.

It can be seen that if the rare vapor pressure is smaller, the efficiency and the power will be higher. The pressure is related with the material properties. Cs is chosen of which the pressure is 1.4 eV.

The items of the thermoelectric convertor have been gotten. It is needed to determine the relationships between efficiency, power, and low temperature zone. As are shown in **Figures 8**, **9**.

As can be seen from **Figures 8**, **9**, when the output voltage is constant, the higher the temperature in the low temperature zone, the higher the corresponding efficiency and power. There is little difference in peak efficiency when the temperature is different. As the output voltage increases, both the output power and efficiency first increase and then decrease. Under actual conditions, the temperature in the low temperature zone is generally not higher than 800 K. When the output voltage is constant, the peak power at 800 K in the low temperature zone is about 15–20% higher than that at other temperatures. The temperature in the low temperature zone is 800 K. The parameters of the whole model are listed in **Table 2**.

## CONCLUSIONS

In the paper, the performance analysis and optimization of thermionic-thermoelectric generators are mainly studied. Combined with actual working conditions, appropriate constraint parameters are selected, and the following conclusions are drawn. The efficiency of the thermionic-thermoelectric generator is 12% higher than that of the thermoelectric generator alone. According to past experience, the temperature of the transmitting stage is not higher than 1,800 K, and the temperature of the receiving stage is not higher than 800 K. In this range increasing the temperature of emitter and receiver can improve the output power and efficiency of the system. In fact, when the quality factor Z is about 0.00336, the economy and efficiency of the whole system is the best. Comparing several common rare vapor pressure, the lower the rare vapor pressure, the greater the efficiency of the system.

## DATA AVAILABILITY STATEMENT

All datasets generated for this study are included in the article/supplementary material.

## AUTHOR CONTRIBUTIONS

HZ conceived and designed the research. DY analyzed the data. XC, BK, and XL made the assistance.

## FUNDING

This work was supported by the Key Laboratory of Reactor System Design Technology (Grant Nos. SQKFKT-02-2016005 and HT-KFKT-10-2018004).

## REFERENCES


Albertoni, R., Pedrini, D., Paganucci, F., and Andrenucci, M. (2013). A reduced-order model for thermionic hollow cathodes. *IEEE Trans. Plasma. Sci.* 41, 1731–1745. doi: 10.1109/TPS.2013.2266512

Bellucci, A., Girolami, M., and Calvani, P. (2016). Buried boron doped layer for CVD diamond photo-thermionic cathodes. *IEEE Trans. Nanotechnol.* 15, 862–866. doi: 10.1109/TNANO.2016.2566674

Chen, L., Ding, Z., Zhou, J., Wang, W., and Sun, F. (2017). Thermodynamic performance optimization for an irreversible vacuum thermionic generator. *Eur. Phys. J. Plus*. 132:293. doi: 10.1140/epjp/i2017-11561-2

El-Genk, M. S., Xue, H., and Paramonov, D. (1993). Start-up simulation of a thermionic space nuclear reactor system. *AIP Conf. Proc*. 271:935. doi: 10.1063/1.43119

Hainley, D. C. (1991). *User's Manual for the Heat Pipe Space Radiator Design and Analysis Code (HEPSPARC). Report No. NASA-CR-187067*. Brook Park, OH: Sverdrup Technology, Inc.

Hassink, G., Wanke, R., Rastegar, I., Braun, W., Stephanos, C., Herlinger, P., et al. (2015). Transparency of graphene for low-energy electrons measured in a vacuum-triode setup. *APL Mater.* 3:076106. doi: 10.1063/1.4927406

Hatsopoulos, G. N., and Gyftopoulos, E. P. (1973). Thermionic energy conversion. *Process. Devices* 1:4362-4366.

Jensen, K. L., Lau, Y. Y., and Jordan, N. (2006). Emission nonuniformity due to profilimetry variation in thermionic cathodes. *Appl. Phys. Lett.* 88:164105. doi: 10.1063/1.2197605

Koeck, F. A., and Nemanich, R. J. (2006). Emission characterization from nitrogen-doped diamond with respect to energy conversion. *Diam. Relat. Mater*. 15, 217–220. doi: 10.1016/j.diamond.2005.08.045

Liao, T., Chen, X., Lin, B., and Chen, J. (2016). Performance evaluation and parametric optimum design of a vacuum thermionic solar cell. *Appl. Phys. Lett*. 108:39. doi: 10.1063/1.4940195

Meng, J. H., Zhang, X. X., and Wang, X. D. (2014). Multi-objective and multi-parameter optimization of a thermoelectric generator module. *Energy* 71, 367–376. doi: 10.1016/j.energy.2014.04.082

Paramonov, D. V., and El-Genk, M. S. (1997). A review of cesium thermionic converters with developed emitter surfaces. *Energy Convers. Manag.* 38, 533–549. doi: 10.1016/S0196-8904(96)00067-2

Tang, S., Sun, H., Wang, C., Tian, W., Qiu, S., Su, G. H., et al. (2019). Transient thermal-hydraulic analysis of thermionic space reactor TOPAZ-II with modified RELAP5. *Prog. Nucl. Energy*. 112, 209–224. doi: 10.1016/j.pnucene.2018.12.016

Tower, L. K., Baker, K. W., and Marks, T. S. (1992). *Nasa Lewis Steady-State Heat Pipe Code Users Manual*. Cleveland, OH: National Aeronautics and Space Administration. doi: 10.2172/10181275

Wanke, R., Hassink, G. W. J., Stephanos, C., Rastegar, I., Braun, W., and Mannhart, J. (2016). Magnetic-field-free thermoelectronic power conversion based on graphene and related two-dimensional materials. *J. Appl. Phys*. 119:244507. doi: 10.1063/1.4955073

Yarygin, V. I. (2012). Experimental studies of properties of excited states of cesium in the interelectrode plasma of a low-temperature thermal to electric energy thermionic converter. *J. Clust. Sci.* 23, 77–93. doi: 10.1007/s10876-012-0443-5

Zhang, J., Xuan, Y., and Yang, L. (2014). Performance estimation of photovoltaic-thermoelectric hybrid systems. *Energy* 78, 895–903. doi: 10.1016/j.energy.2014.10.087

Zhang, W., Wang, C., Chen, R., Tian, W., Qiu, S., and Su, G. H. (2016a). Preliminary design and thermal analysis of a liquid metal heat pipe radiator for TOPAZ-II power system. *Ann. Nucl. Energy* 97, 208–220. doi: 10.1016/j.anucene.2016.07.007

Zhang, W., Zhang, D., Tian, W., Qiu, S., and Su, G. H. (2016b). Thermal-hydraulic analysis of the improved TOPAZ-II power system using a heat pipe radiator. *Nucl. Eng. Des.* 307, 218–233. doi: 10.1016/j.nucengdes.2016.07.020


**Conflict of Interest:** The authors declare that the research was conducted in the absence of any commercial or financial relationships that could be construed as a potential conflict of interest.

frontiers in Energy Research

ORIGINAL RESEARCH
published: 15 April 2020
doi: 10.3389/fenrg.2020.00051

# Experimental Study of Bubbly-Slug Flow Transition Criteria in an Vertical Circular Tube by Using WMS

*Shimo Yu, Xiao Yan*, Lei Zhou, Aiwei Xu, Junyi Zhang, Suijun Gong and Yuanfeng Zan*

*China National Nuclear Corporation (CNNC) Key Laboratory on Nuclear Reactor Thermal Hydraulics Technology, Nuclear Power Institute of China, Chengdu, China*

Two-phase flow is an important and common phenomenon in reactor systems, and there are significant differences in the heat and mass transfer characteristics of two-phase flow under different flow patterns. Researchers have proposed a variety of flow pattern transition mechanisms to predict the two-phase flow. But limited by the means of measurement, the critical void fraction for flow pattern transition can't be determined. Two types of bubbly-slug flow transition criteria in vertical circular tubes are studied in this paper and a wire mesh sensor (WMS) was manufactured to measure the critical void fraction for bubbly-slug transition. One hundred forty-seven visualization tests were carried out for validation.

**Keywords: two-phase flow, bubbly-slug flow, transition mechanism, vertical tube, WMS**

OPEN ACCESS

***Edited by:***
*Liangming Pan,*
*Chongqing University, China*

***Reviewed by:***
*Bruno Panella,*
*Politecnico di Torino, Italy*
*Fenglei Niu,*
*North China Electric Power University, China*
*Keyou S. Mao,*
*Purdue University, United States*
*Victor Petrov,*
*University of Michigan, United States*

****Correspondence:***
*Xiao Yan*
*yanxiao_npic@163.com*

***Specialty section:***
*This article was submitted to Nuclear Energy, a section of the journal Frontiers in Energy Research*

***Received:*** *16 August 2019*
***Accepted:*** *12 March 2020*
***Published:*** *15 April 2020*

***Citation:***
*Yu S, Yan X, Zhou L, Xu A, Zhang J, Gong S and Zan Y (2020) Experimental Study of Bubbly-Slug Flow Transition Criteria in an Vertical Circular Tube by Using WMS. Front. Energy Res. 8:51. doi: 10.3389/fenrg.2020.00051*

## INTRODUCTION

In nuclear reactor system, two-phase flow is a common and important phenomenon. The structure of gas liquid interface is very complex because of the interaction between the phases and it varies as the velocity changes of the two phases. In a vertical circular tube, two phase flow is divided into four typical flow patterns including bubbly flow, slug flow, churn flow, and annular flow. The thermal hydraulic characteristics of two phase flow strongly depend on the flow pattern. Many flow pattern transition mechanisms are put forward in order to predict the two phase flow (Weisman and Kang, 1981; Barnea et al., 1982; Mcquillan and Whalley, 1985). The derivation process of flow pattern transition mechanism can be divided into two categories: the first ones are the empirical criteria based on a large number of experimental data, the second ones analyze the transition mechanism based on the physical process. Two widely used flow pattern transition mechanisms of the second category were proposed by Mishima and Ishii (1984) and Taitel et al. (1980). This paper focuses on the bubbly-slug flow transition criteria of the Mishima-Ishii and Taitel transition mechanisms. These two criteria base on different mechanism and take different critical void fraction. Electrical probes and optical probes have been widely used to measure the void fraction in two phase flow (Hibiki and Ishii, 1998; Kim et al., 2000; Euh et al., 2001) for several decades, but they can commonly only measure a spatial point at one time. Recent years' the WMS developed by Prasser (Prasser et al., 2005; Prasser, 2007; Pietruske and Prasser, 2007; Beyer et al., 2010; Banowski et al., 2016) can measure the void fraction of the whole cross section instantaneously with a high spatial and temporal resolution. A comprehensive evaluation of WMS proposed by Tompkins et al. (2018) shows that the WMS is a good choice for this study. The authors of the present paper manufactured a WMS to measure the critical void fraction for bubbly-slug flow transition. The detailed analysis results are given and visualization experiment are carried out for the validation of the results.

## BUBBLY-SLUG FLOW TRANSITION CRITERIA

For the adiabatic air water two phase flow in vertical circular tubes, the most widely used bubbly-slug flow transition criteria were proposed by Mishima and Ishii (1984) and Taitel et al. (1980). The two transition criteria are based on different physical mechanisms and take different critical void fractions for bubbly-slug transition.

Mishima-Ishii bubbly-slug flow transition mechanism is based on the drift flow model, and the superficial velocity of the two phases given by Equation (1).

$$\frac{J_g}{\alpha} = C_0 J + \sqrt{2}\left(\frac{\sigma g\left(\rho_l - \rho_g\right)}{\rho_l^2}\right)^{1/4} (1-\alpha)^{1.75} \tag{1}$$

Where $J$ is the two phase mixture superficial velocity shown as Equation (2), $C_0$ is the distribution parameter, $C_0$ in Equation (3) is for circular tube.

$$J = J_g + J_l \tag{2}$$

$$C_0 = 1.2 - 0.2\sqrt{\frac{\rho_g}{\rho_l}} \tag{3}$$

The key parameter to determine the transition criterion is the critical void fraction α in Equation (1). To obtain the critical void fraction, Mishima and Ishii (1984) proposed a model of the bubble distribution structure as shown in **Figure 1**. The effective range of the interaction between bubbles are 1.5 times the diameter of the bubble $r_b$ and the probability of bubble coalescence will sharply increase when the distance between bubbles is less than or equal to $2r_b$. As a result, the critical void fraction for bubbly-slug flow transition can be derived by Equation (4).

$$\alpha = \left(\frac{2}{3}\right)^3 = 0.296 \approx 0.3 \tag{4}$$

The Mishima-Ishii transition criterion based on the drift flow model can be derived by combining Equations (1) and (4). It is shown in Equation (5).

$$J_l = \left(\frac{3.33}{C_0} - 1\right) J_g - \frac{0.76}{C_0}\left(\frac{\sigma g(\rho_l - \rho_g)}{\rho_L^2}\right)^{1/4} \tag{5}$$

Taitel bubbly-slug flow transition mechanism is based on the raising velocity of big bubbles in two phase flow. Harmathy (1960) proposed the raising velocity of big bubbles relative to the liquid phase flow field. The velocity is shown in Equation (6) which is independent of bubble size.

$$U_0 = U_g - U_l = 1.53\left[\frac{g(\rho_l - \rho_g)\sigma}{\rho_l^2}\right]^{1/4} \tag{6}$$

The relationships between real velocity and superficial velocity of the two phases are shown in Equations (7) and (8).

$$J_g = \alpha U_g \tag{7}$$

$$J_l = (1-\alpha)\, U_l \tag{8}$$

And different from Mishima-Ishii criterion, Taitel chose 0.25 to be the bubbly-slug transition critical void fraction. The Taitel bubbly-slug transition criterion as shown in Equation (9) can be obtained by combining Equations (6)–(8).

$$J_l = 3.0 J_g - 1.15\left(\frac{g(\rho_l - \rho_g)\sigma}{\rho_l^2}\right)^{1/4} \tag{9}$$

## EXPERIMENT SET UP

According to the analysis in the previous section, the critical void fraction for flow pattern transition is the key parameter for deriving the transition criterion. But it was difficult to measure the void fraction accurately limited by the measurements when Mishima and Ishii (1984) and Taitel et al. (1980). put forward the flow pattern transition mechanisms. Benefitting from the advance in measurement, the void fraction of two phase flow can be measured accurately. Different from traditional single point measurement (conductivity/optical probe) (Hibiki and Ishii, 1998; Kim et al., 2000; Euh et al., 2001), The WMS can measure the void fraction of the whole cross section instantaneously (Prasser et al., 2005; Pietruske and Prasser, 2007; Prasser, 2007; Beyer et al., 2010; Banowski et al., 2016). The authors of this paper built an experimental loop and manufactured a WMS to obtain the critical void fraction for bubbly-slug transition.

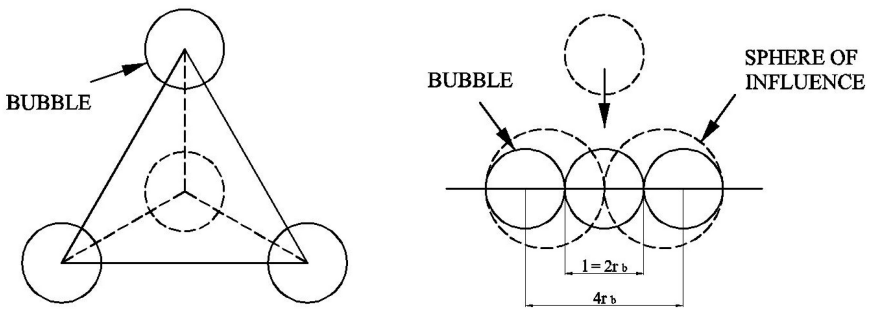


**FIGURE 1 |** Bubble packing and coalescence pattern.

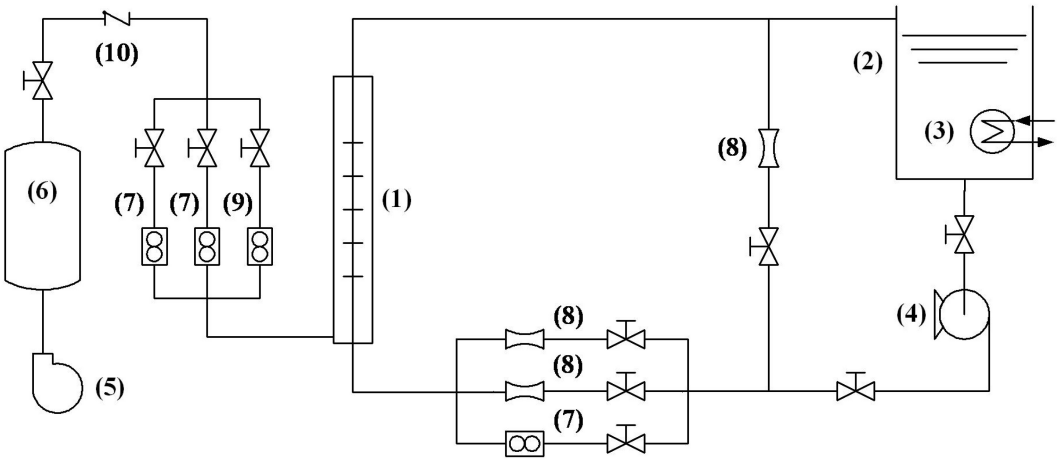


**FIGURE 2 |** Scheme of the experiment set-up. (1) test section, (2) water tank, (3) heat exchanger, (4) pump, (5) air compressor, (6) air storage tank, (7) Coriolis meter, (8) Venturi meter, (9) Thermal meter, (10) check valve.

## Experiment Loop

The experiment loop consists of a water loop part and an air loop part as shown in **Figure 2**. A by-pass loop is applied for smoothly adjusting the flow rate of water flowing through the test section. The experiment was carried out at the room temperature (∼20°C), and a heat exchanger was used in the water tank to take the heat generated by the pump for stabilizing the temperature. The water tank is 1.5 m high and 0.8 m in diameter, and it is opening to the atmosphere, so the system pressure is around 1 atm except the outlet of the pump which is a little higher than the atmosphere pressure. The compressed air is generated by the air compressor and stabilized by the 1 $m^3$ air storage tank. The maximum water mass flow rate is 40 t/h and the maximum air volume flow rate is 2,400 NL/min. The Coriolis/Thermal mass flow meter and Venturi flow meter were used to measure the flow rate of water and air as shown in **Table 1**.

## Test Section

The test section is a transparent plexiglass round tube with 3 m height and 50 mm inner diameter as shown in **Figure 3A**. The test section is placed vertically. Water and air mix at the bottom of the test section and flow out from the top of the test section. The WMS is placed on the top of test section to ensure that the two phase flow is fully developed. The water/air mixture is separated in the water tank. Referring to Prasser's (2007) work on TOPFLOW facility, the air injector applies a uniform injecting structure consisting of 24 orifices of 1 mm diameter drilled around the tube wall as shown in **Figure 3B**.

**TABLE 1 |** Specifications of the flow meters applied in this study.

| Phase | Meter type | Range | Precision |
|---|---|---|---|
| Water | Coriolis meter | 0.1–2 t/h | ±0.25% |
| | Venturi meter | 0.75–15 t/h | ±1.00% |
| | Venturi meter | 7–50 t/h | ±1.00% |
| Air | Thermal meter | 2–80 NL/min | ±2.00% |
| | Coriolis meter | 80–800 NL/min | ±0.25% |
| | Coriolis meter | 800–2,400 NL/min | ±0.25% |

## Wire Mesh Sensor

The WMS contains three layers of electrode wires as shown in **Figure 4**. Each layer is made up of 16 parallel wires and the distance between the wires is 3 mm. The axial distance between two adjacent layers is 2.5 mm. The middle layer is the transmitter electrode and the up and down layers are the receiver electrodes as shown in **Figure 4B**. The three layers structure

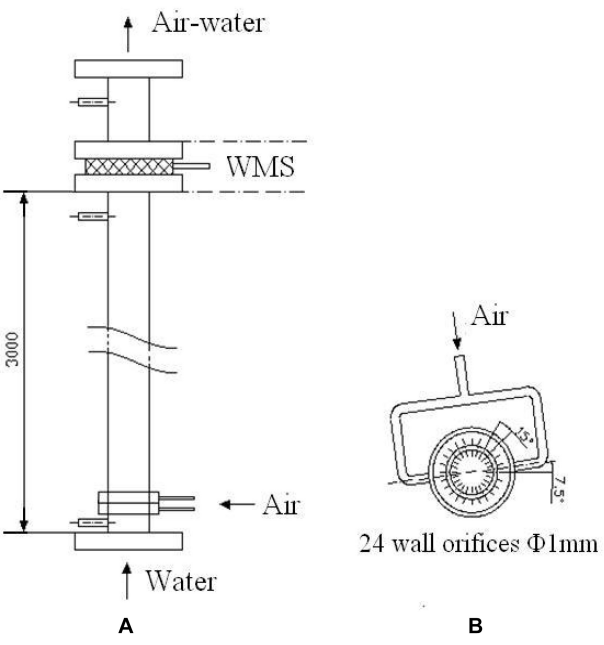


**FIGURE 3 | (A)** Scheme of the experiment set-up, **(B)** air injector.

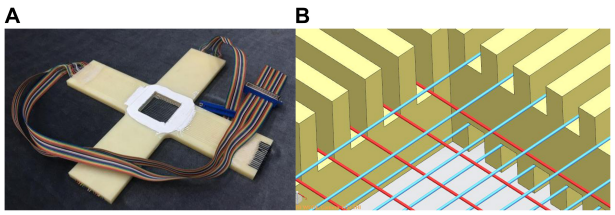


**FIGURE 4 | (A)** The picture of WMS. **(B)** The detail of the three layers structure.

forms two effective two layers WMS located up and down which can measure the bubble velocity. Actually, the bubble velocity isn't studied in this paper, so just one effective two layers WMS is applied to measure the void fraction.

When the WMS is working, ±5 V pulsed square waves generated by the transmitter circuit pass through each transmitter electrode in turn, then pass through the fluid and received by the receiver electrode. The received original signal is filtered and amplified by the receiver circuit, and it is converted into digital signal by a 16 bits ADC. The conductivity of the fluid is between 420 and 450 $\mu S/cm$ which is adjusted by salt. The scan frequency is 6,500 Hz. A three-dimensional voltage matrix $V(i, j, k)$ can be obtained in each measurement. The void fraction can be calculated by Equation (10). The $(i, j)$in Equation (10) is the space coordinate and $k$ is the time coordinate. The local reference voltage $V_l(i, j)$ and $V_g(i, j)$ for liquid phase and gas phase is measured in every test.

$$\alpha(i, j, k) = \frac{V(i, j, k) - V_L(i, j)}{V_g(i, j) - V_l(i, j)} \tag{10}$$

In every test, sampling begins after the experimental state is stable and lasts for 10 s. So a $16 \times 16 \times 65{,}000$ void fraction matrix will be obtained in every test. Then the average void fraction of the cross section is calculated by Equation (11).

$$\overline{\alpha} = \frac{\sum \alpha(i, j, k)}{\sum i, j, k} \tag{11}$$

## CALIBRATION EXPERIMENT

Before the critical void fraction experiment, calibration experiment including single bubble and multi bubbles tests is carried out to evaluate the measuring error of the WMS. For single bubble tests (Yu et al., 2018), 95% of the bubble velocity data's relative error is in ±15 and 93% of the bubble volume data's relative error is in ±15%, Yu et al. (2018) gives the analysis process and detailed results of the single bubble test.

In this paper, the multi bubbles measuring error is more concerned because the critical void fraction is a macro parameter for multiple bubbles two phase flow. The available data shows that the WMS has a uncertainty of ±10.5% for void fraction measurement, but the accuracy is largely based on the practical application (Tompkins et al., 2018). So a calibration experiment is needed for this study. This paper uses the differential pressure

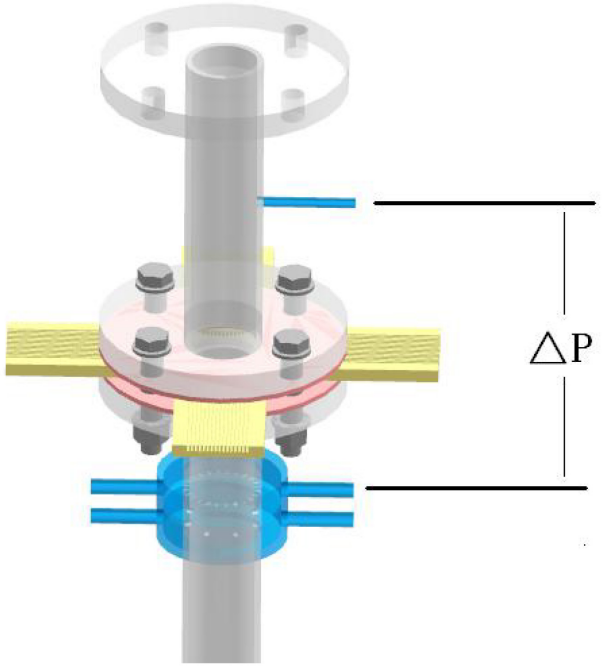


**FIGURE 5 |** Differential pressure measuring.

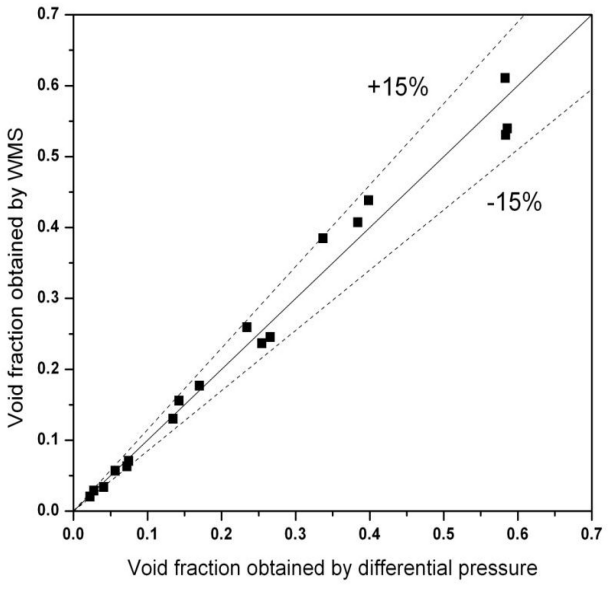


**FIGURE 6 |** Comparison result of void fraction calculation.

method to evaluate the measuring error of the WMS. The pressure measuring points are located near the WMS as shown in **Figure 5**. The distance between the two measuring points is 265 mm. A Honeywell ST3000 differential pressure gauge whose precision is 0.1% is applied to measure the differential pressure. And the average void fraction is calculated by Equation (12) which is derived by the conservation of momentum. The term

**TABLE 2 |** Void fraction experimental results.

| Test No. | $J_l$ m/s | $Jg$ m/s | α | Flow pattern |
|---|---|---|---|---|
| B3 | 0.040 | 0.047 | 0.177 | Bubbly |
| B4 | 0.041 | 0.096 | 0.245 | Slug |
| C3 | 0.082 | 0.047 | 0.130 | Bubbly |
| C4 | 0.082 | 0.097 | 0.286 | Slug |
| D3 | 0.161 | 0.066 | 0.156 | Bubbly |
| D4 | 0.161 | 0.132 | 0.309 | Slug |
| E4 | 0.361 | 0.126 | 0.202 | Bubbly |
| E5 | 0.364 | 0.250 | 0.333 | Slug |
| F5 | 0.634 | 0.264 | 0.237 | Bubbly |
| F6 | 0.636 | 0.529 | 0.335 | Slug |

on the left hand side of Equation (12) is the differential pressure per meter which is calculated by the differential pressure data. The first term in the right hand side of Equation (12) is the friction pressure drop which is calculated by Lockhart-Matinelli separated flow model (Lockhart and Martinelli, 1949) in this paper. The second term on the right hand side is the gravity differential pressure, and $\sin\theta = 1$ for the vertical tube.

In the multiple bubbles calibration tests, the superficial liquid velocity varies from 0.040 to 0.160 m/s and the superficial gas liquid varies from 0.014 to 0.530 m/s. the average void fraction of the cross section measured by WMS varies from 0.034 to 0.611 while the average void fraction calculated by Equation (12) varies from 0.041 to 0.583. The comparison result of void fraction obtained by WMS and differential pressure is shown in **Figure 6**. Ninety-four percentage of the data's relative error is in ±15%.

$$-\frac{dp}{dz} = \left(-\frac{dp}{dz}\right)_f + \left[\alpha\rho_g + (1-\alpha)\rho_l\right] g \sin\theta \qquad (12)$$

## EXPERIMENTAL STUDY OF THE CRITICAL VOID FRACTION

After calibration experiment, 48 tests with different velocity combination of the two phases are carried out. The superficial

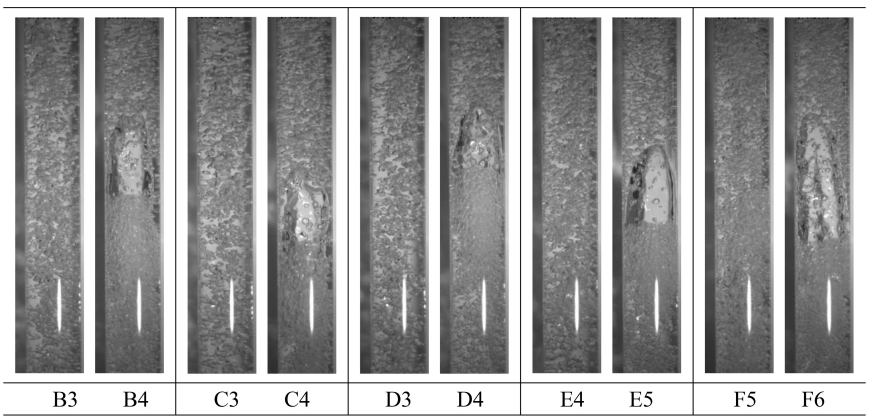


**FIGURE 7 |** Pictures of 10 tests before and after bubbly-slug flow transition.

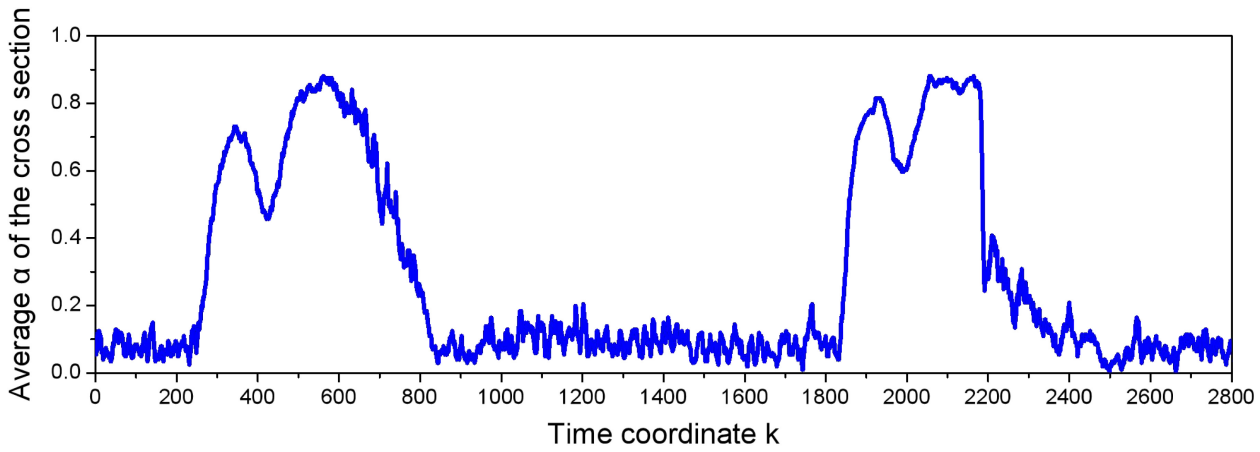


**FIGURE 8 |** The instantaneous void fraction of the cross section in test E5.

liquid velocity varies from 0.040 to 3.272 m/s and the superficial gas liquid varies from 0.011 to 0.960 m/s. The flow patterns include bubbly flow, slug flow, and churn flow. To study the critical void fraction for bubbly-slug flow transition, 10 tests before and after the flow pattern transition are chosen which are shown in **Table 2**. The pictures of these 10 tests are shown in **Figure 7**. The slug flow is defined as having stable gas slugs that occupy almost all of the cross section of the tube. The void fraction of each test is measured by WMS. **Figure 8** shows the instantaneous void fraction of the cross section in test E5. The time average void fraction is calculated by Equation (11) where the time coordinate k varies from 0 to 64,999. The experimental result of these 10 tests shown in **Table 2** indicates that the critical void fraction of bubbly-slug transition is between 0.237 and 0.245 which is closer to the Taitel model.

## VISUALIZATION VALIDATION EXPERIMENT

The experimental study of the critical void fraction shows that shows that the critical void fraction of bubbly-slug flow transition is closer to the Taitel model. For further validation, an visualization validation experiment with 147 tests was carried out. The PCO dimax high speed camera was applied. The superficial velocity of the liquid phase is between 0.02 and 3.55 m/s and the superficial velocity of the gas phase is between 0.0075 and 1.92 m/s. The superficial velocity interval between adjacent tests is smaller. The flow pattern of the visualization validation experiment includes bubbly flow, slug flow, churn flow, and dispersed bubbly flow.

The Taitel bubbly-slug transition formula as shown in Equation (13) is obtained by substituting the parameters $\rho_g = 1.18kg/m^3$, $\rho_l = 997.05kg/m^3$, $\sigma = 0.072N/m$which are under the experimental condition into Equation (9). **Figure 9** shows the comparison between Taitel criterion and experimental results.

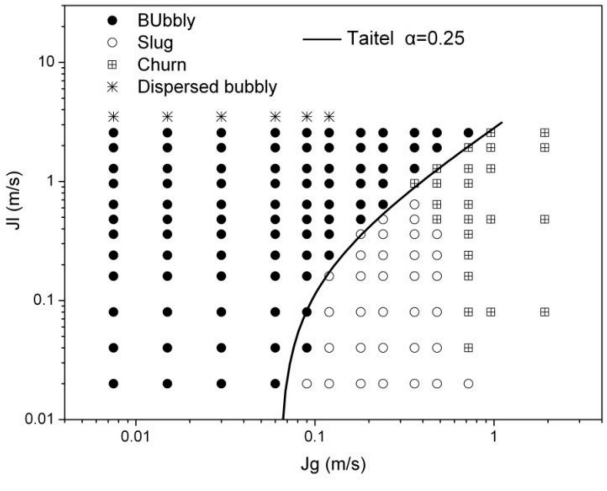


**FIGURE 9 |** Comparison between Taitel criterion and experimental results.

From the figure, it can be seen that the criterion agrees well with the experimental results at both low and high liquid velocity.

$$J_l = 3.0J_g - 0.1875 \tag{13}$$

In the same way, the Mishima-Ishii bubbly-slug transition formula as shown in Equation (14) can be obtained by substituting the physical parameters and the circular tube distribution parameter. **Figure 10** shows the comparison between Mishima-Ishii criterion and experimental results. In the low superficial liquid velocity region (0.02–0.08 m/s), Mishima-Ishii criterion agrees well with the experimental results, while in the high superficial liquid velocity region (0.16–2.56 m/s),

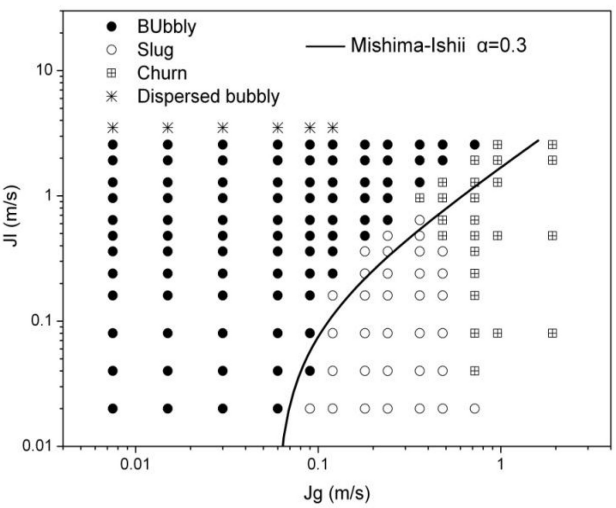


**FIGURE 10 |** Comparison between Mishima-Ishii criterion and experimental results.

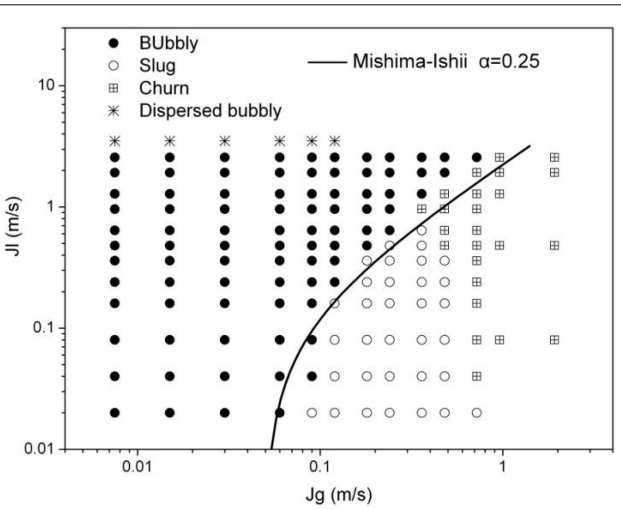


**FIGURE 11 |** Comparison between modified Mishima-Ishii criterion and experimental results.

the superficial gas velocity given by Mishima-Ishii criterion is higher than the experimental results.

$$J_l = 1.791J_g - 0.104 \quad (14)$$

For the deviation of the Mishima-Ishii criterion, this paper considers whether it is caused by the inappropriate critical void fraction. So a modified Mishima-Ishii criterion is given by choosing 0.25 as the bubbly-slug transition critical void fraction. The formula is shown in Equation (15). **Figure 11** shows the comparison between modified Mishima-Ishii criterion and experimental results. In the high superficial liquid velocity region (0.16–2.56 m/s), the modified Mishima-Ishii criterion is more accurate than the original Mishima-Ishii criterion. But the deviation becomes greater in the low superficial liquid velocity region (0.02–0.08 m/s), the superficial gas velocity given by modified Mishima-Ishii criterion is lower than the experimental results.

$$J_l = 2.353J_g - 0.117 \quad (15)$$

## CONCLUSION

Two bubbly-slug flow transition criteria in vertical circular tubes proposed by Mishima and Ishii (1984) and Taitel et al. (1980). are studied in this paper. They are basing on different transition mechanism and apply different critical void fraction. A WMS was manufactured to measure the critical void fraction for bubbly-slug transition. Experimental result shows that the critical void fraction is closer to 0.25. For further validation, an visualization validation experiment including 147 tests were carried out. The validation experimental result shows that the Taitel bubbly-slug transition criterion basing on big bubble raising velocity model is more suitable for bubbly-slug flow transition in a vertical circular tube with 50 mm diameter.

## DATA AVAILABILITY STATEMENT

The datasets generated for this study are available on request to the corresponding author.

## AUTHOR CONTRIBUTIONS

SY gave substantial contributions to the conception or design of the work, and the acquisition, analysis, or interpretation of data for the work. XY provided approval for publication of the content. LZ, AX, JZ, SG, and YZ have given some help during the experiment.

## REFERENCES


Banowski, M., Beyer, M., Szalinski, L., Lucasa, D., and Hampel, U. (2016). Comparative study of ultrafast X-ray tomography and wire-mesh sensors for vertical gas–liquid pipe flows. *Flow Meas. Instrum.* 53, 95–106. doi: 10.1016/j.flowmeasinst.2016.02.001

Barnea, D., Shoham, O., and Taitel, Y. (1982). Flow pattern transition for vertical downward two phase flow. *Chem Eng Sci.* 37, 741–744. doi: 10.1016/0009-2509(82)85034-3

Beyer, M., Lucas, D., and Kussin, J. (2010). Quality check of wire-mesh sensor measurements in a vertical air/water flow. *Flow Meas. Instrum.* 21, 511–520. doi: 10.1016/j.flowmeasinst.2010.09.001

Euh, D. J., Yun, B. J., Song, C. H., Kwon, T. S., Chung, M. K., Lee, U. C., et al. (2001). Development of the five-sensor conductivity probe method for the measurement of the interfacial area concentration. *Nucl. Eng. Des.* 205, 35–51. doi: 10.1016/s0029-5493(00)00376-9

Harmathy, T. Z. (1960). Velocity of large drops and bubbles in media of infinite or restricted extent. *Aiche* 6:281. doi: 10.1002/aic.690060222

Hibiki, T., and Ishii, M. (1998). Effect of flow-induced vibration on local flow parameters of two-phase flow. *Nucl. Eng. Des.* 185, 113–125. doi: 10.1016/s0029-5493(98)00241-6

Kim, S., Fu, X. Y., Wang, X., and Ishii, M. (2000). Development of the miniaturized foursensor conductivity probe and the signal processing scheme. *Int. J. Heat. Mass. Transf.* 43, 4101–4118. doi: 10.1016/s0017-9310(00)00046-6

Lockhart, R. W., and Martinelli, R. C. (1949). Proposed correlation of data for isothermal two-phase, two-component flow in pipes. *Chem. Eng. Prog.* 45, 39–48.

Mcquillan, K. W., and Whalley, P. B. (1985). Flow patterns in vertical two-phase flow. *Int. J. Multiphase Flow* 11, 161–175. doi: 10.1016/0301-9322(85)90043-6

Mishima, K., and Ishii, M. (1984). Flow regime transition criteria for upward two-phase flow in vertical tubes. *Int. J. Heat Mass Transfer.* 27, 723–737. doi: 10.1016/0017-9310(84)90142-x

Pietruske, H., and Prasser, H. M. (2007). Wire-mesh sensors for high-resolving two-phase flow studies at high pressure and temperatures. *Flow Meas. Instrum.* 18, 87–94. doi: 10.1016/j.flowmeasinst.2007.01.004

Prasser, H.-M. (2007). Evolution of interfacial area concentration in a vertical air–water flow measured by wire–mesh sensors. *Nucl. Eng. Des.* 237, 1608–1617. doi: 10.1016/j.nucengdes.2007.02.024

Prasser, H. M., Misawa, M., and Tiseanu, I. (2005). Comparison between wire-mesh sensor and ultra-fast X-ray tomograph for an air–water flow in a vertical pipe. *Flow Meas. Instrum.* 16, 73–83. doi: 10.1016/j.flowmeasinst.2005.02.003

Taitel, Y., Bornea, D., and Dukler, A. E. (1980). Modelling flow pattern transitions for steady upward gas-liquid flow in vertical tubes. *Aiche J.* 26, 345–354. doi: 10.1002/aic.690260304

Tompkins, C., Prasser, H.-M., and Corradini, M. (2018). Wire-mesh sensors: a review of methods and uncertainty in multiphase flows relative to other measurement techniques. *Nucl. Eng. De.* 337, 205–220. doi: 10.1016/j.nucengdes.2018.06.005

Weisman, J., and Kang, S. Y. (1981). Flow pattern transitions in vertical and upwardly inclined line. *Int. J. Multiphase Flow.* 7, 271–291. doi: 10.1016/0301-9322(81)90022-7

Yu, S., Yan, X., Zhao, D., et al. (2018). *Three-Layers Wire-Mesh System for Air Bubble Measurement in a Rectangular Channel[C].* Orlando, FL: American Nuclear Society, 937–944.


**Conflict of Interest:** The authors declare that the research was conducted in the absence of any commercial or financial relationships that could be construed as a potential conflict of interest.

## NOMENCLATURE

| | |
|---|---|
| $C_0$ | Distribution parameter |
| $g$ | Gravitational constant, N/kg |
| $i$ | Space coordinate on X direction |
| $j$ | Space coordinate on Y direction |
| $J$ | Superficial velocity, m/s |
| $k$ | Time coordinate |
| $p$ | Pressure, Pa |
| $U$ | Velocity, m/s |
| $V$ | Voltage, V |
| $z$ | Distance along the tube, m |
| **Greek symbols** | |
| α | Void fraction |
| ρ | Density, kg/m$^3$ |
| σ | Surface tension, N/m |
| **Subscripts** | |
| $f$ | Friction |
| $g$ | Gas phase |
| $l$ | Liquid phase |

frontiers in Energy Research

ORIGINAL RESEARCH
published: 28 April 2020
doi: 10.3389/fenrg.2020.00057

# Integral Effect Test on Top-Slot Break Scenario With 4 Inches Cold Leg Break LOCA in ATLAS Facility

*Jongrok Kim, Byoung-Uhn Bae, Jae Bong Lee, Yusun Park, Seok Cho and Kyoung-Ho Kang**

*Innovative System Safety Research Division, Korea Atomic Energy Research Institute, Daejeon, South Korea*

An experimental simulation for a loss of coolant accident with a 4-in cold leg top-slot break was performed using ATLAS, an integral effect test facility at the Korea Atomic Energy Research Institute (KAERI), South Korea. The aims of this test are to resolve a safety issue and to validate the thermal hydraulic safety analysis codes for the activity of the 4th ATLAS-Domestic Standard Problem. The related safety issue for this test is that a loop seal clearing and loop seal reformation of APR1400 can lead to a core temperature excursion because of the characteristics of the loop seal geometry. In the experimental results, the core heater temperature slowly increased after loop seal reformation. This increase is attributed to the accumulated steam at the upper head. The accumulated steam increased the pressure and saturated the temperature in the core. The core heater temperature then increased due to the increased saturated temperature. This temperature increase, therefore, was not a core temperature excursion. Sensitivity analysis results using Multidimensional Analysis of Reactor Safety KINS Standard (MARS-KS), which is a best-estimate thermal hydraulic system analysis code, are also presented in this study. In the 4th ATLAS-Domestic Standard Problem, 15 participants performed calculations and sensitivity analyses using various thermal hydraulic safety analysis codes (MARS-KS, SPACE, RELAP5, and TRACE). From this exercise, several parameters that affect the calculation results are brought out. The sensitivity analysis results using MARS-KS with some of these parameters are also presented. The MARS-KS calculation results are similar to the experimental data. The effects of critical flow model, break line modeling, and fine node modeling are also discussed.

**Keywords: ATLAS, thermal hydraulics, APR1400, top-slot break, cold leg break, loop seal clearing, loop seal reformation**

OPEN ACCESS

***Edited by:***
*Jun Wang,*
*University of Wisconsin-Madison,*
*United States*

***Reviewed by:***
*Genglei Xia,*
*Harbin Engineering University, China*
*Victor Petrov,*
*University of Michigan, United States*

****Correspondence:***
*Kyoung-Ho Kang*
*khkang@kaeri.re.kr*

***Specialty section:***
*This article was submitted to Nuclear Energy, a section of the journal Frontiers in Energy Research*

***Received:*** *05 November 2019*
***Accepted:*** *25 March 2020*
***Published:*** *28 April 2020*

***Citation:***
*Kim J, Bae B-U, Lee JB, Park Y, Cho S and Kang K-H (2020) Integral Effect Test on Top-Slot Break Scenario With 4 Inches Cold Leg Break LOCA in ATLAS Facility. Front. Energy Res. 8:57. doi: 10.3389/fenrg.2020.00057*

## INTRODUCTION

An issue of the APR1400 loop seal and its impact on long-term cooling during a postulated loss-of-coolant accident (LOCA) was raised (Lu, 2014). In particular, a top-slot break at a cold leg (CL) with a medium- or small-size break was concerned. A possible scenario is as follows:

i. Top-slot break at CL (medium/small break size maybe the concern)
ii. Loop seal clearing (LSC) and empty intermediate leg (IL)
iii. Primary steam condensation by steam generator (SG) heat transfer or safety injection water flooding (reverse flow to loop seal)

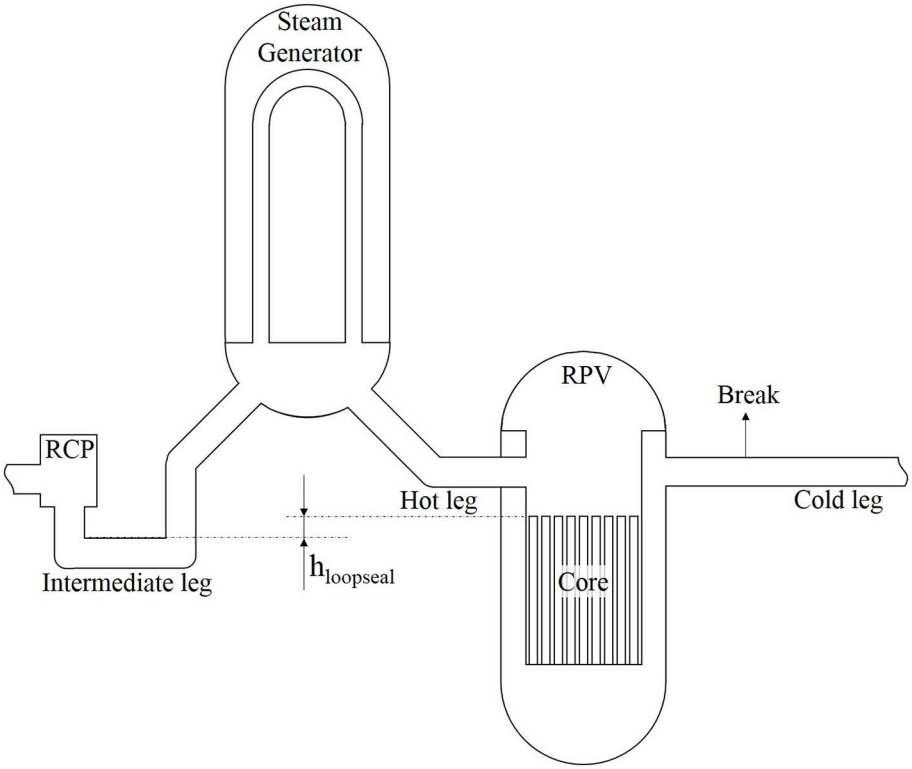


**FIGURE 1 |** Geometry of pressurized water reactors (PWRs).

**TABLE 1 |** Uncertainty level of instruments.

| Items | Unit | Uncertainty |
|---|---|---|
| Static pressure | MPa | 0.039 |
| Differential pressure | kPa | 0.23 |
| Collapsed water level | % | 0.18 (core)<br>2.6 (downcomer)<br>8.6 (RCP suction side of the intermediate leg) |
| Temperature | °C | Maximum 2.4 |
| Flowrate | kg/s | 0.053 |
| Loop flowrate | % | 15 (two-phase flow)<br>13 (liquid-phase flow) |
| Break flow | kg/s | 0.07 (by the load cell-based measuring)<br>(by the RCS inventory change) |

iv. Loop seal reformation (LSR)
v. Pressure increase at the top core region due to the steam released from core
vi. Core water level decrease
vii. Partial core uncovery and core temperature excursion may occur.

**Figure 1** shows a schematic diagram of a pressurized water reactor. The height of the loop seal in **Figure 1** indicates the depth of the loop seal, and the APR1400 has 0.608 m depth while the US EPR has 0.030 m depth (Wells, 2009). The APR1400 has a deeper loop seal, and the impact of the loop seal can be more serious than in other pressurized water reactors (PWRs) because the deeper loop seal necessitates longer time to clear the loop seal and partial core uncovery can occur during this time.

Considering the importance of the loop seal of APR1400, experimental investigations for the top-slot break at a CL have been performed as a test item of the 4th ATLAS-Domestic Standard Problem (DSP) (Kang et al., 2018). A top-slot break scenario was simulated in ATLAS, an integral effect test facility. This experiment was aimed at investigating the thermal hydraulic transient in the top-slot break at the CL and analyzing the effect of the LSC and LSR on the APR1400. In the experiment, the break shape was assumed as a circular hole because simulation of a slot break is difficult. To simulate the top break, a break line was installed on the top side of the CL. From the experimental results, the effect of the loop seal during the long-term phase of a LOCA was evaluated.

## EXPERIMENTAL TEST FACILITY

ATLAS is an integral effect test facility designed to simulate transient scenarios for thermal hydraulics of a PWR (Baek et al., 2005). The reference reactor of ATLAS is APR1400. ATLAS was designed with the same component system as APR1400. The RCS system of ATLAS has simulation systems for primary, secondary, safety injection, containment, auxiliary, and break simulation. The primary system has a reactor pressure vessel (RPV), a pressurizer, two hot legs (HLs), four

CLs, two SGs, and four reactor coolant pumps (RCPs). The three-level scaling methodology (Ishii and Kataoka, 1983) was applied for the ATLAS design to simulate accident scenarios realistically. ATLAS was scaled down to 1/2 for height and 1/288 for volume (Choi et al., 2014). To simulate an accident realistically, ATLAS was developed to be able to operate at the same pressure and temperature as APR1400 (Kim et al., 2008). To measure multidimensional thermal hydraulic behavior, ∼1,500 measuring instruments were installed. The uncertainty level of each instrument is summarized in **Table 1**. ATLAS data can be used to analyze the thermal hydraulic behavior for a whole plant or the subcomponents during anticipated transients and postulated accidents. Detailed information of ATLAS facility is provided in the facility description report (Lee et al., 2018).

**Figure 2** shows a schematic diagram of ATLAS and the position where a break line was installed. **Figure 3** shows the break line that was installed on the top side of CL1A of ATLAS to simulate a top-slot break at a CL. The break nozzle, which has 7.12 mm inner diameter, was installed at the break line system to simulate a 4-in break of APR1400.

## TEST CONDITION

During the test, four safety injection tanks (SITs) and four safety injection pumps (SIPs) were utilized as a safety injection system during the test period, and operation of the main steam safety valves (MSSVs) and supply of the auxiliary feed water were available. The initial and boundary conditions were defined in compliance with the scaling ratios.

In the present test, the maximum SIP flowrate and relatively cold emergency core cooling (ECC) water temperature

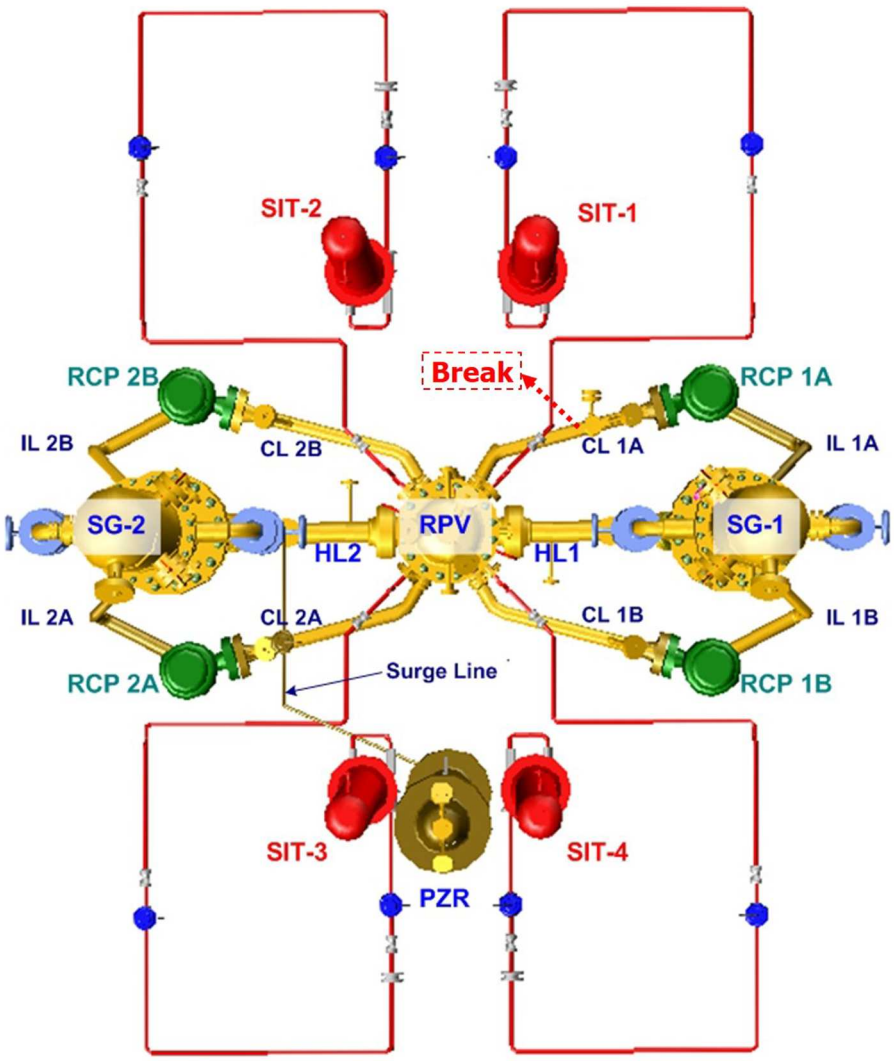


**FIGURE 2 |** ATLAS bird eye view.

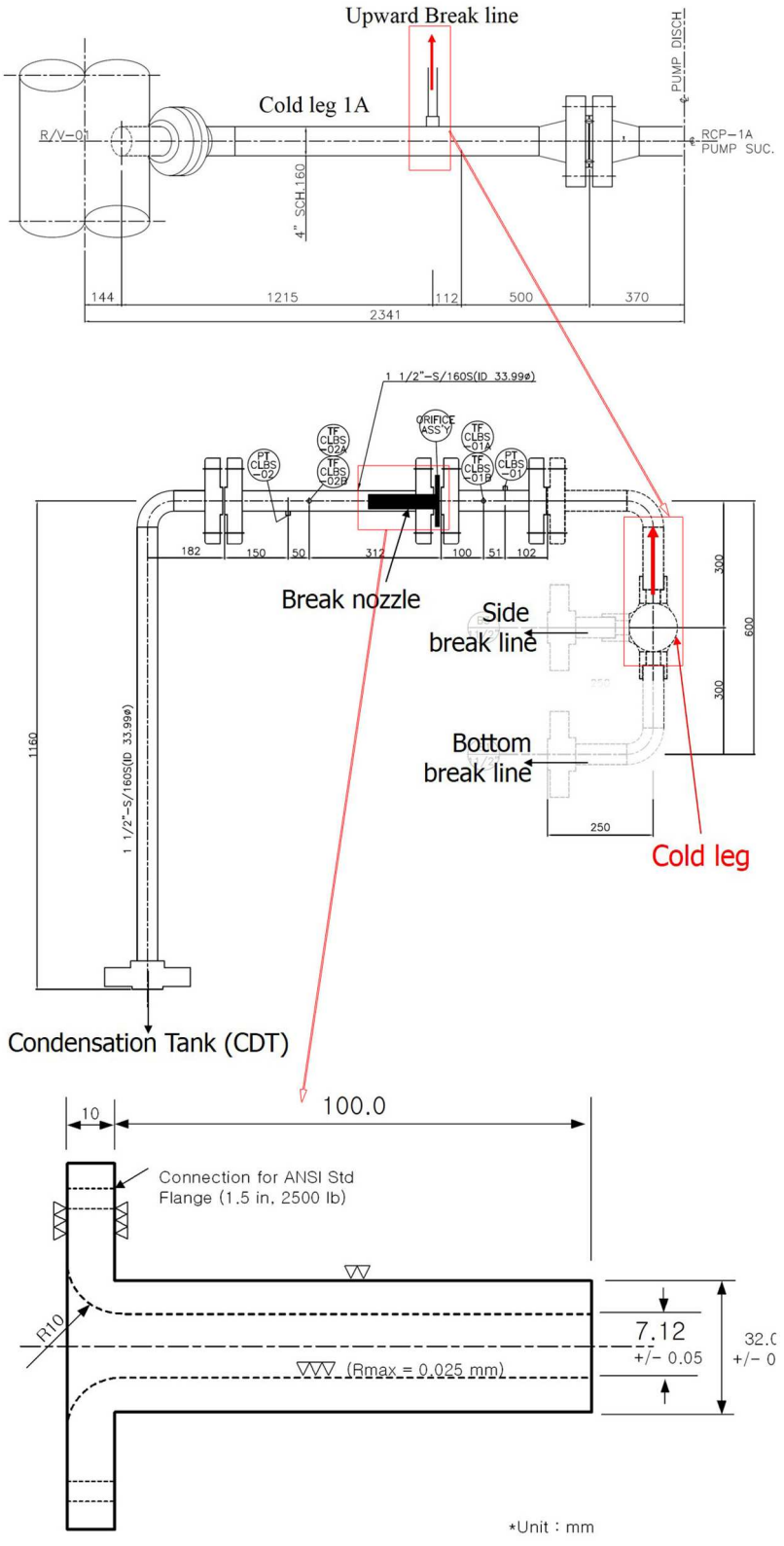


**FIGURE 3 |** Break simulation system.

were assumed to promote repeatable LSC and LSR. The SIP flowrate was dependent on the pressure difference between the SIT and the primary system. ECC water (0.32 kg/s) was injected to the RPV through the direct vessel injection (DVI) nozzles. For the present experiment, the ECC water was stored in the RWT, and the temperature was around 10–17°C.

To simulate a conservative condition, a power table that was 1.2 times the ANS-73 decay curve of the decay heat was applied. The initial heater power was 1.64 MW, and then, the heater power was controlled to follow the power table after 31.7 s from the break valve opening. After the system parameters reached a steady-state condition, the systems were maintained for more than 30 min. The experiment then begun by the break valve opening.

**TABLE 2 |** Actual sequence of events of the experiment.

| Events | Timing (non-dimensional time) | Remarks |
|---|---|---|
| Break start | 0.033 | MFW terminated |
| MSSV | 0.037/0.038 | SG pressure |
| LPP trip | 0.037 | Low pressurizer pressure |
| SIP on | 0.042 | |
| SIT on | 0.118 | |
| Loop seal clearing | 0.081–0.410 | Loop 1A (broken loop) |
| | 0.084–0.413 | Loop 2A |
| | 0.455–0.461 | Loop 1A (broken loop), 1B |
| | 0.455–0.462 | Loop 2B |
| | 0.554–0.571 | Loop 1A (broken loop) |
| | 0.553–0.572 | Loop 2A |
| | 0.814–0.828 | Loop 1A (broken loop) |

## TEST RESULTS AND DISCUSSION

### Transient Results of Experiment

According to the agreement of the ATLAS-DSP, the test data should be confidential. All of the test results in this paper

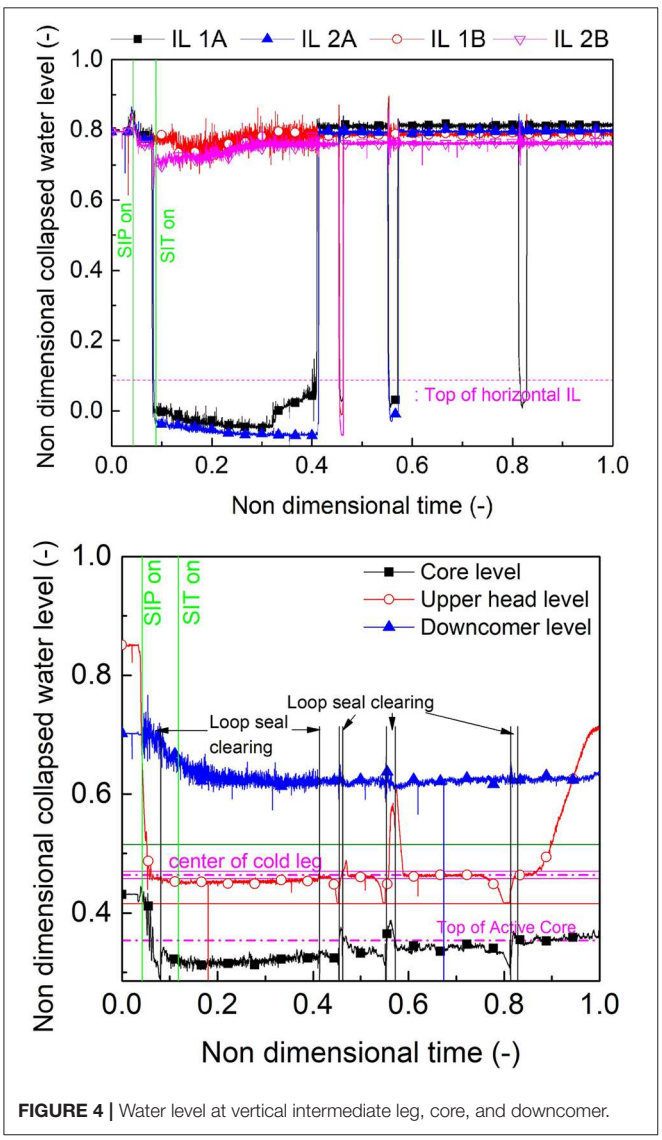


**FIGURE 4 |** Water level at vertical intermediate leg, core, and downcomer.

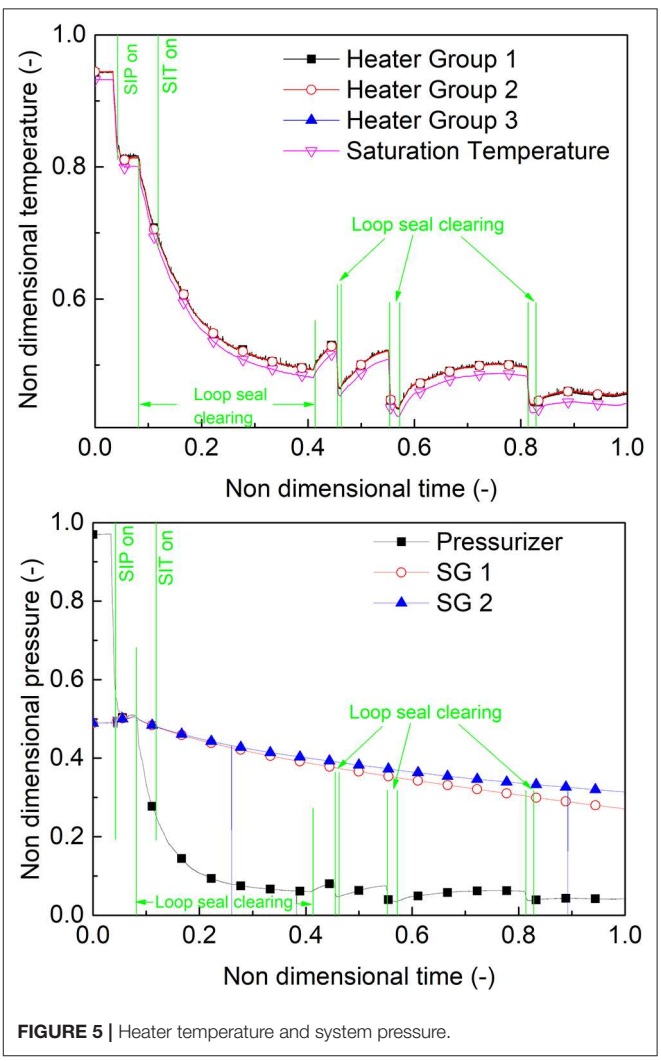


**FIGURE 5 |** Heater temperature and system pressure.

including the time frame were thus divided by an arbitrary value and plotted on a non-dimensional axis.

**Table 2** summarizes the sequence of major events. After break valve opening, the sequence of experiment was controlled by control logic that defined the set value and related time for this scenario. When the pressure of the pressurizer (sensor ID: PT-PZR-01) dropped below a certain pressure, a low pressurizer pressure (LPP) signal was issued. After the LPP signal, the reactor, RCP, and pressurizer heater were tripped immediately. The main feed water isolation valves were closed with the LPP signal. The actuation of the SIPs was set to occur with a 28-s delay from the LPP signal.

LSC and LSR are recognized with the water level of the IL of the primary loop. For an LSC, the water level at the vertical IL (sensor IDs: LT-ILj-03) becomes lower than the height of the horizontal IL. On the other hand, the water level at the vertical IL becomes higher than the height of the horizontal IL for the LSR. **Figure 4** shows the water levels measured by LT-ILj-03, core, and downcomer. For the short-term phase, the duration of the LSC is long because a large amount of generated stream due to high heater power kept the steam flow path through the loop seal. For the long-term phase, the heater power decreased and the stream generation rate also decreased, and then, the force that drives the steam flow became weak and the loop seal was reformed easily. During the LSC, the coolant at the ILs flowed to the core, and the core water level increased. After the LSR, the steam that was produced by core decay heat was accumulated at the upper head of the RPV and increased the

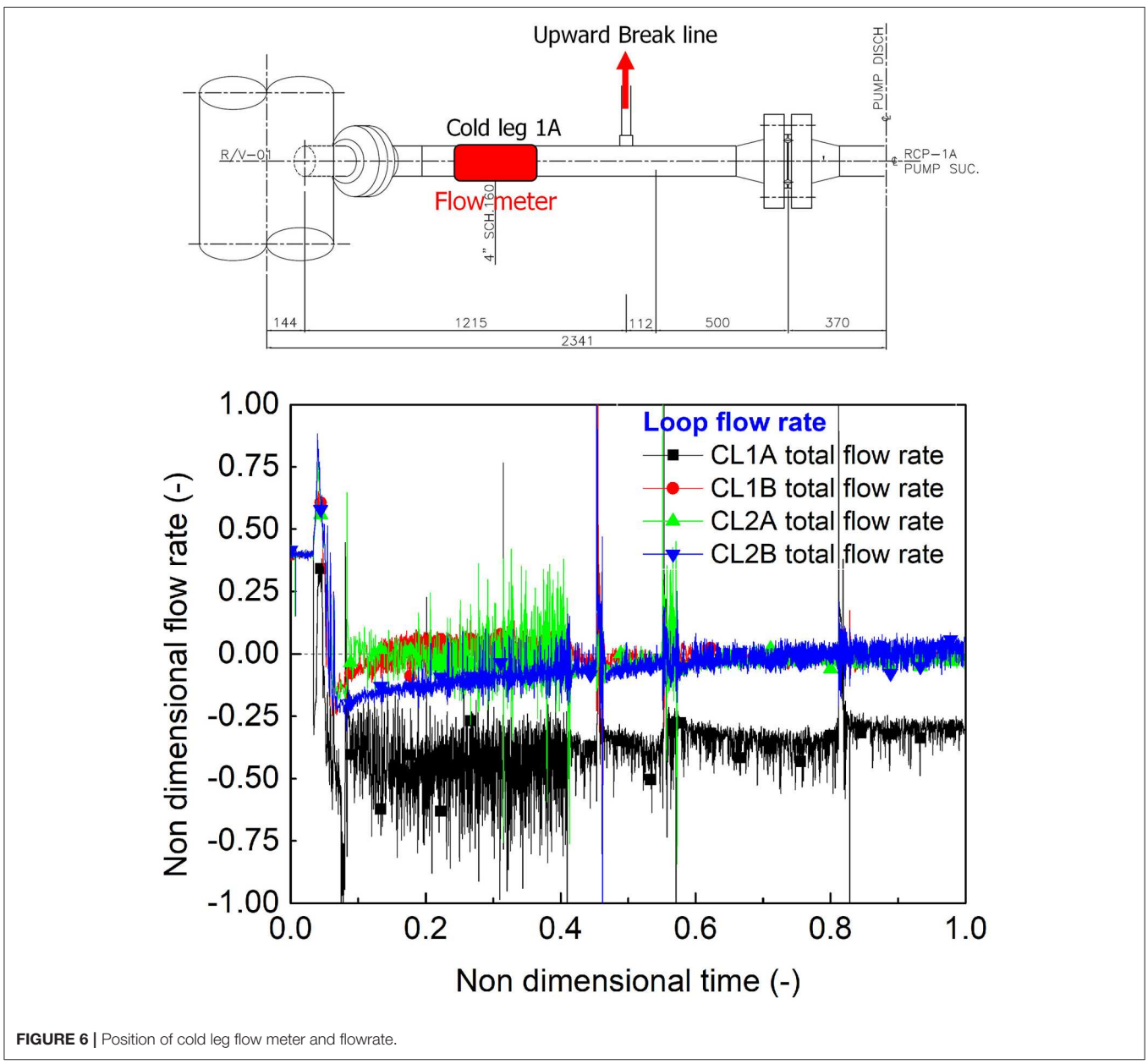


**FIGURE 6 |** Position of cold leg flow meter and flowrate.

upper head pressure. The increased pressure pushed down the core water level.

**Figure 5** shows the heater temperature and the pressure of the pressurizer and SGs. The primary pressure gradually decreased during the test, and some peaks were observed at the LSC and LSR. After the LSR, the heater temperatures slowly increased. This increase can be attributed to the accumulated steam at the upper head. It increased the pressure and saturated temperature in the core. The core heater temperature then increased due to the increased saturated temperature. Therefore, these temperature increases were not a core temperature excursion. In addition, the coolability of the reactor coolant system was available during the test. The pressure of the SGs increased after isolation of the feed and steam line. Furthermore, the MSSVs operated because of the increase in the SG pressure. The pressure of the SGs then gradually decreased by heat transfer from the secondary side to the primary side at the SGs because the temperature of the primary system was lower than that of the secondary system.

**Figure 6** shows the position of the flow meter at the CL1A and CL flowrates. The flowrate of the CL1A was negative after the break. For the normal condition, the coolant in the CL flows from the SG to the RPV. During the present test, however, the flow direction in CL1A was opposite because the coolant flew out through the break line from both the RPV and the SG. Therefore, the flow meter at CL1A indicated negative value.

## MARS-KS Code Calculation

### Nodalization for ATLAS

The experiment shows that the LSC and LSR do not affect the coolability of the reactor cooling system. In the fourth DSP, 15 participants performed several sensitivity analyses using thermal hydraulic safety analysis codes (Kim et al., 2020). From this exercise, several parameters that affect the calculation results were brought out. In this section, sensitivity analysis results using Multidimensional

**TABLE 3 |** Sensitivity analysis matrix.

| Case | Critical flow model | Break line modeling | Number of loop seal nodes |
|---|---|---|---|
| Base | Ransom–Trapp | O | 5 |
| HF | Henry–Fauske | O | 5 |
| No Break line | Ransom–Trapp | X | 5 |
| Fine node | Ransom–Trapp | O | 14 |

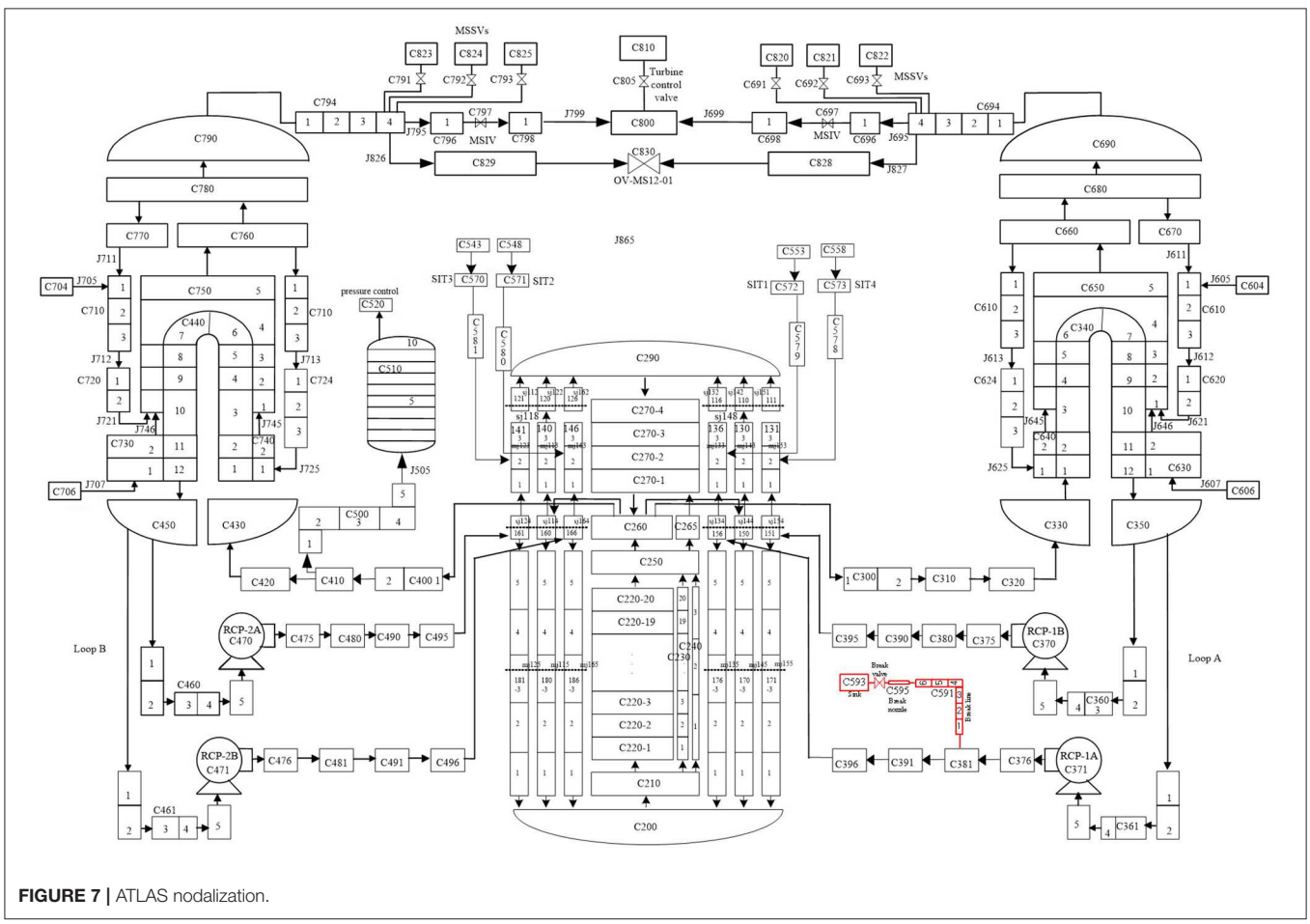


**FIGURE 7 |** ATLAS nodalization.

Analysis of Reactor Safety KINS Standard (MARS-KS) with some major parameters of the brought parameters are described.

The MARS-KS code is a best-estimate thermal hydraulic system analysis code that treats the two-phase flow phenomena based on the two-fluid model with six transport equations for the mass, momentum, and energy of each phase (Jeong et al., 1999). KAERI has developed a standard input of MARS-KS for ATLAS. The calculation input for the present test was modified from the standard input for ATLAS. The nodalization for the standard input of the ATLAS facility is shown in **Figure 7** (black blocks). In order to simulate a break system at a CL, a break line was added on the top of component 381, which is located between RPV and RCP of CL-1A. The nodalization of the break line is shown in **Figure 7** (red blocks). In order to accurately predict the break flow, modeling of the break line should be similar to the test configuration. The developed 1-D break line consisted of the main break line, break nozzle, break valve (trip valve), and sink volume. During the test, choking occurs at the smallest area of the break line. The break line had a pipe with an inner diameter of 33.99 mm, and the break nozzle and break valve had inner diameter of 7.12 mm, which is the smallest diameter. Thus, critical flow is expected to occur at the valve or break nozzle. In the case of the valve, there was a diverging area, and it prevented chocking. Therefore, modeling of the break nozzle was the most important aspect in this simulation, and a choking option was applied only to the break nozzle with the Ransom–Trapp model (subcooled discharge coefficient = 0.8, two-phase discharge coefficient = 1.2, superheated discharge coefficient = 1.0). In addition, an upward facing break was applied with the off-take model for a junction from node C381

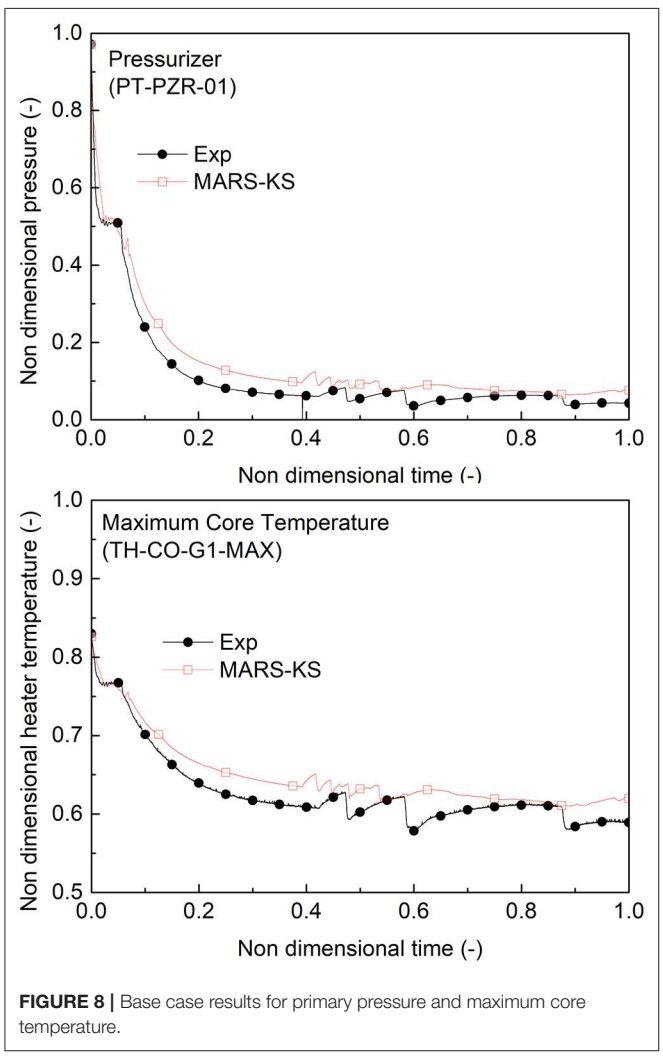


**FIGURE 8 |** Base case results for primary pressure and maximum core temperature.

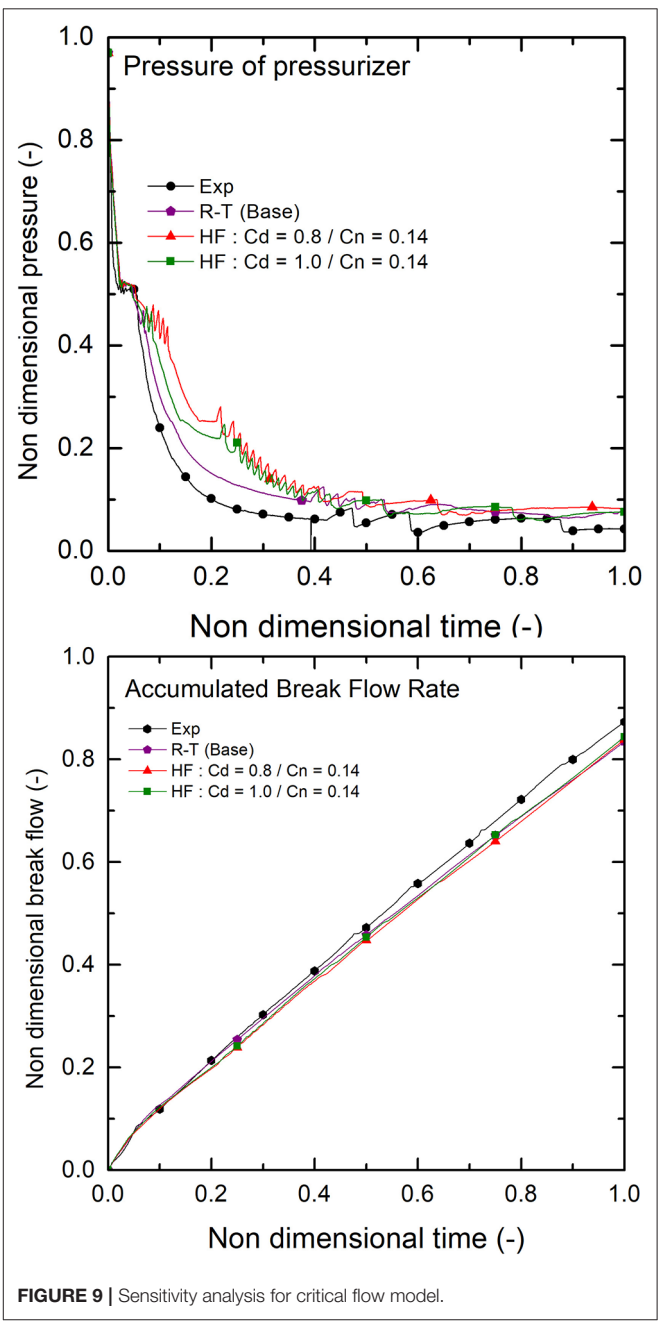


**FIGURE 9 |** Sensitivity analysis for critical flow model.

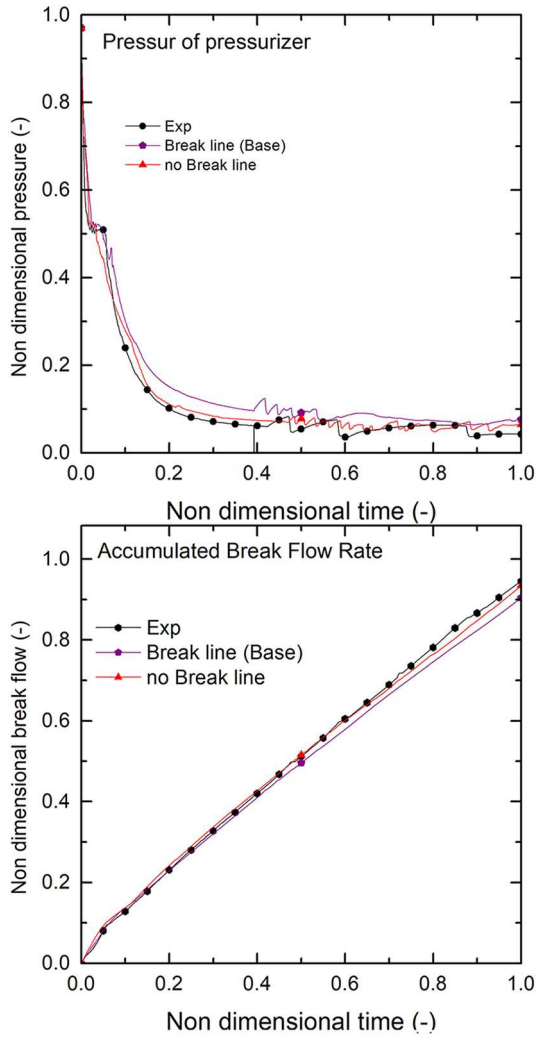


**FIGURE 10 |** Sensitivity analysis for break line model.

to break line. At the loop seal and break junction, the Wallis CCFL model was applied. A heat loss model was not applied for this simulation.

## Sensitivity Analysis

A sensitivity analysis was performed for the critical flow model, break line modeling, and loop seal node number. The analysis matrix is summarized in **Table 3**.

The base case was compared with the experimental results. The MARS-KS calculation was comparable with the test results, as presented in **Figure 8**. The predicted times of the first and the second pressure drop were similar with the test data during the early stage. After the second pressure drop, MARS-KS calculated relatively higher pressure because the break flowrate of the calculation was lower than that of the experiment. The maximum core temperature for both data has peaks after LSRs. It could be found from the MARS-KS calculation that an LSR does not induce an excursion of the cladding temperature, which is also observed in the ATLAS test.

**Figure 9** shows the effect of the critical flow model. Two Henry–Fauske models with Cd = 0.8/Cn = 0.14 and Cd = 1.0/Cn = 0.14 were applied. Cd = 1.0 is default coefficient in MARS-KS, and it predicted earlier first loop seal clearing and shorter plateau than experiment because break flowrate was larger for very short-term period. To predict similar first loop seal clearing time of experiment, Cd = 0.8 was applied. For the short-term period, the Henry–Fauske models calculated a smaller break flowrate, and the primary pressures were higher than those of the base case. For the long-term period, however, the calculations showed a similar trend.

**Figure 10** compares the base case and a No Break line case. In the case of the No Break line, the break line was simplified. The break line included only the break valve and the sink volume. The No Break line case shows a fast pressure decrease for the primary system because a

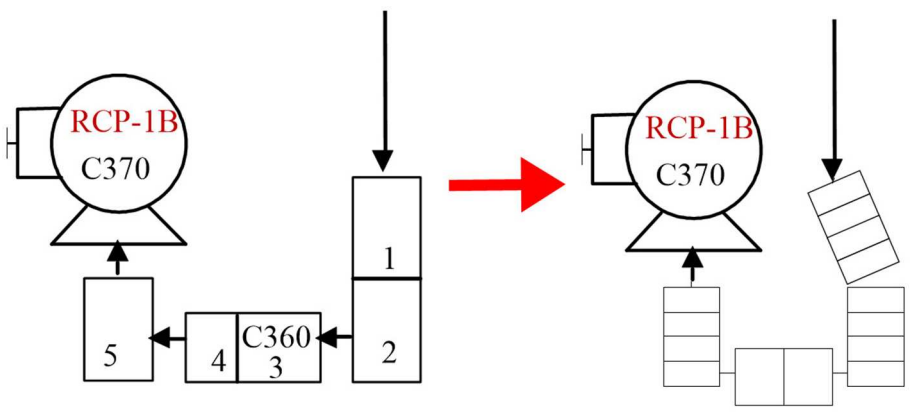


**FIGURE 11 |** Nodalization for fine node.

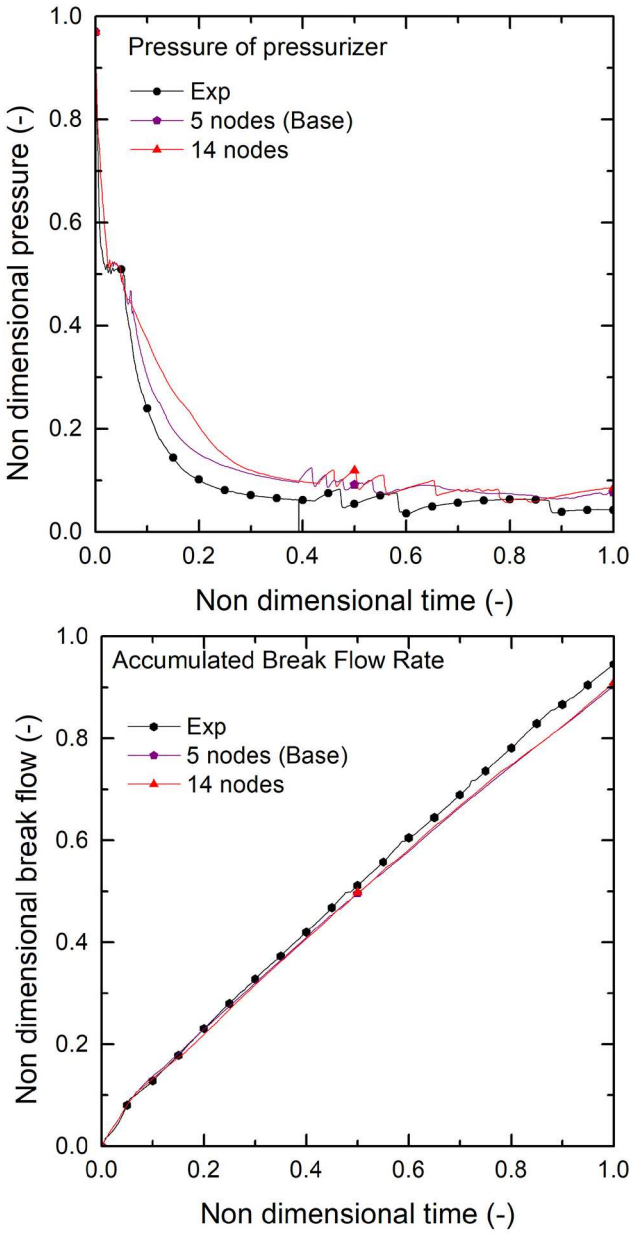


**FIGURE 12 |** Sensitivity analysis for fine node.

simple break line has lower pressure resistance for a break flow, and this leads to a higher break flowrate and fast pressure drop.

For the fine node case, the node number at the loop seal was increased to 14, as presented in **Figure 11**. **Figure 12** shows the difference between the base case and the fine node case. The fine node case calculated a smaller break flowrate during the break flow condition that was two phased. The primary pressure was thus higher than that of the base case. After the two-phase break flow condition, the break flowrate was almost the same, and the pressure trend was similar for the two cases.

## CONCLUSION

An ATLAS test for a 4-in cold leg top-slot break LOCA was performed to resolve an issue that the LSC and LSR of APR1400 can lead to a core temperature excursion. In the experimental results, the core heater temperature slowly increased after the LSR. This increase is attributed to the accumulated steam at the upper head. This increased the primary pressure and saturated temperature. The core heater temperature then increased due to the saturated temperature. Therefore, this temperature behavior was not a core temperature excursion, and the coolability of the reactor coolant system was available during the transient.

The experimental results were compared with the MARS-KS 1.4 code calculation results. The MARS-KS calculation results show reasonable agreement with the ATLAS test data. The LSC and LSR also did not lead to excursion of the cladding temperature during the transient in the MARS-KS calculation. A sensitivity analysis was performed with the MARS-KS calculation. The effects of the critical flow model, break line modeling, and fine node modeling were discussed, and the results show that these parameters affected the break flowrate and thermal hydraulic behaviors in the system.

## DATA AVAILABILITY STATEMENT

The datasets generated for this study will not be made publicly available. These datasets are products for ATLAS-Domestic Standard Problem project. Distribution of datasets is prohibited by MOU for this project.

## AUTHOR CONTRIBUTIONS

JK analyzed experimental data, calculated sensitivity analysis and wrote the first draft. K-HK advised and managed direction of study. All authors contributed to conception and design of the experiment, performed experiment. All authors also contributed to manuscript revision, read, and approved the submitted version.

## FUNDING

The National Research Foundation of Korea (NRF) grant funded by the Korea government (Ministry of Science and ICT) (NRF-2017M2A8A4015026).

## REFERENCES


Baek, W. P., Song, C. H., Yun, B. J., Kwon, T. S., Moon, S. K., and Lee, S. J. (2005). KAERI integral effect test program and the ATLAS design. *Nuclear Technol.* 152, 183–195. doi: 10.13182/NT05-A3669

Choi, K. Y., Kang, K. H., Kwon, T. S., Kim, Y. S., Kim, J.-R., Moon, S. K., et al. (2014). *Scaling Analysis Report of the ATLAS Facility, Kaeri Report, KAERI/TR-5465/2014*. Daejeon: KAERI.

Ishii, M., and Kataoka, I. (1983). *Similarity Analysis and Scaling Criteria for LWRs Under Single Phase and Two-Phase Natural Circulation*. NUREG/CR-3267, ANL-83-32. Argonne: Argonne National Laboratory. doi: 10.2172/6312011

Jeong, J. J., Ha, K. S., Chung, B. D., and Lee, W. J. (1999). Development of a multi-dimensional thermal-hydraulic system code, MARS 1.3.1. *Ann. Nuclear Energy* 26, 1611–1642. doi: 10.1016/S0306-4549(99)00039-0

Kang, K. H., Park, Y., Bae, B. U., Kim, J. R., Choi, N. H., and Choi, K. Y. (2018). Code assessment of ATLAS integral effect test simulating main steam-line break accident of an advanced pressurized water reactor. *J. Nuclear Sci. Technol.* 55, 104–112. doi: 10.1080/00223131.2017.1383212

Kim, J., Kang, K. H., Bae, B. U., Park, Y. S., Yun, B. S., Lim, S. K., et al. (2020). *Comparison Report of Calculations for ATLAS Domestic Standard Problem (DSP-04). KAERI Report, KAERI/TR-7335/2018*. Daejeon: KAERI.

Kim, Y. S., Choi, K. Y., Park, H.-S., Cho, S., Kim, B. D., Choi, N. H., et al. (2008). Commissioning of the ATLAS thermal-hydraulic integral test facility. *Ann. Nuclear Energy* 35, 1791–1799. doi: 10.1016/j.anucene.2008.05.010

Lee, J. B., Bae, B. U., Park, Y., Kim, J., Kim, Y. S., Cho, S., et al. (2018). *Description Report of ATLAS Facility and Instrumentation (Second Revision). KAERI Report, KAERI/TR-7218/2018*. Daejeon: KAERI.

Lu, S. (2014). *APR-1400 Loop Seal and Its Impact on Long. Term Cooling During A Postulated Loss-of-Coolant Accident*. ML14134A347. Washington, DC: U.S.NRC.

Wells, R. D. (2009). *Response to Request for Additional Information No. 241, Supplement 1*. ML093330003. Washington, DC: U.S.NRC; U.S. EPR Design Certification Application AREVA NP Inc.


**Conflict of Interest:** The authors declare that the research was conducted in the absence of any commercial or financial relationships that could be construed as a potential conflict of interest.

frontiers in Energy Research

REVIEW
published: 10 July 2020
doi: 10.3389/fenrg.2020.00119

# Review of Regime Maps of Steam-Submerged Direct Contact Condensation

*Yu Du, Xiao Yan*, Jinguang Zang and Yan Zhang*

*CNNC Key Laboratory on Nuclear Reactor Thermal Hydraulics Technology, Nuclear Institute of China, Chengdu, China*

Steam-submerged direct contact condensation is widely applied in industry fields. As it has the enormous capacity of heat and mass transfer, the phenomenon is widely used in nuclear engineering equipment which are related to safety, such as the suppression pool in the boiling water reactor (BWR). It is important to understand the regime map when we study this phenomenon because the characteristics of heat and mass transfer vary with the regime, including the characteristic of the interface of steam and water. Lots of researchers have investigated the regime of steam-submerged direct contact condensation. Different researchers have developed different regime maps with their own or other people's experimental data. This article reviews the present research on the regime maps and discusses further efforts on the important phenomenon.

**Keywords: submerged, direct contact condensation, regime map, two-phase flow, steam jet**

OPEN ACCESS

***Edited by:***
*Liangming Pan,*
*Chongqing University, China*

***Reviewed by:***
*Jinbiao Xiong,*
*Shanghai Jiao Tong University, China*
*Keyou S. Mao,*
*Oak Ridge National Laboratory (DOE), United States*

****Correspondence:***
*Xiao Yan*
*yanxiao_npic@163.com*

***Specialty section:***
*This article was submitted to Nuclear Energy, a section of the journal Frontiers in Energy Research*

***Received:*** *06 October 2019*
***Accepted:*** *19 May 2020*
***Published:*** *10 July 2020*

***Citation:***
*Du Y, Yan X, Zang J and Zhang Y (2020) Review of Regime Maps of Steam-Submerged Direct Contact Condensation. Front. Energy Res. 8:119. doi: 10.3389/fenrg.2020.00119*

## INTRODUCTION

Direct contact condensation (DCC) is the phenomenon where steam condenses when it gets into contact with the same liquid directly. The DCC is widely used in industrial applications, as it has a remarkable advantage on heat transfer. In applications in nuclear engineering, steam-submerged DCC is an important phenomenon in safety-related equipment, such as the pressure suppression pool and in-containment refueling water storage tank (IRWST), in which the steam is discharged into the water pool. In researches of steam-submerged DCC, the characteristics of heat and mass transfer are always based on the regime. As a result, the regime map is the foundation of understanding the steam-submerged DCC.

## RESEARCH OF REGIME MAPS OF STEAM-SUBMERGED DCC

Arinobu (1980) conducted experiments to study the steam-submerged DCC and developed a regime map with his experimental data. The steam mass flux was in the range of 5–100 kg/m$^2$ s, while the temperature of water varied from 20 to 92°C. To study the influence of water depth, the submerged depths of the pipe were 0.2 and 0.4 m. And Arinobu proposed that the submerged depths of the pipe have little to do with the regime. The diameters of the pipe used in the experiment were 0.0161 and 0.0276 mm. The regime map is shown in **Figure 1**. Arinobu defined the regime with shape and position of the steam–water interface and optimized it with pressure oscillation.

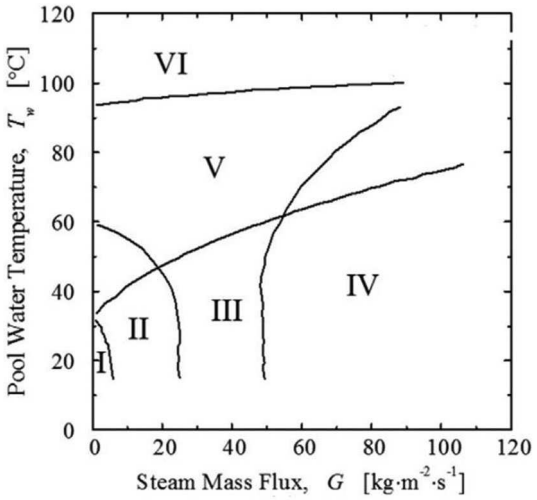


**FIGURE 1 |** The regime map developed by Arinobu (1980).

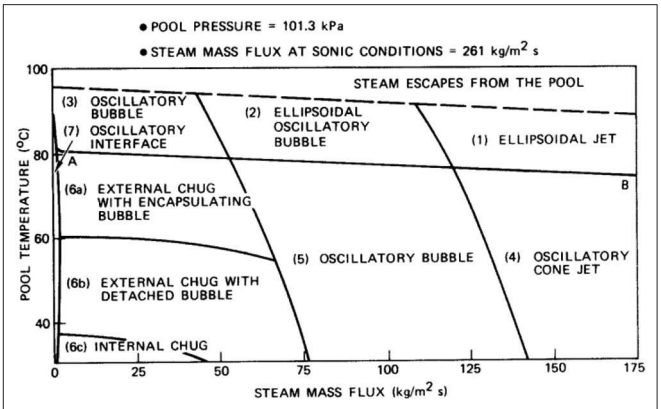


**FIGURE 2 |** The regime map developed by Chan and Lee (1982).

The characteristics of every regime are described as follows.

Region I: The steam condenses in the pipe, while the steam–water interface and pressure are both oscillating.

Region II: The steam mass flux is larger than the condensation rate, so there is a steam region forming at the pipe exit. Water will rush into the pipe as soon as the stream region collapses. And then the steam in the pipe will push the water out, because the smaller heat transfer area makes the condensation weaker when the interface is in the pipe. As a result, a new steam region will form, and the progress repeats. This regime is always called chugging by almost all researchers.

Region III: The water does not rush into the pipe anymore as the steam flux is large enough. There is no obvious pressure oscillation in this regime.

Region IV: The pressures in the pipe and pool are oscillating periodically, and violent oscillation of the steam–water interface is observed. This regime is called condensation oscillation (CO).

Region V: The steam surrounds the pipe and condenses. As a result, obvious oscillation was observed.

Region VI: The water temperature is high and the condensation capacity gets weaker, so the area of the steam–water interface becomes larger. The steam could escape from the water because it cannot be condensed completely.

Lahey and Moody (1993) named these regimes of Arinobu's map as follows. Chugging, CO, quasi-steady oscillation, transition region, and incomplete condensation. It is worth mentioning that Lahey called region III as CO. But the characteristic of CO was observed in region IV in Arinobu's research.

Chan and Lee (1982) conducted an experiment and developed a regime map of steam-submerged DCC, in which the steam mass flux varied from 1 to 175 kg/m$^2$ s and the water temperature was in the range of 40 to 90°C. The pipe diameter in the experiment was 0.0508 m. The regime map is shown in **Figure 2**. Chan used two parameters to identify regimes: the axial location of the steam region relative to the pipe exit and the location where bubbles detach from the steam region. Though Chan identified seven regimes in his research, he classified them into three categories: chugging (<50 kg/m$^2$ s), oscillatory bubbles (median flux), and oscillatory jet (>125 kg/m$^2$ s). Chan describes the characteristics of each regime as follows.

*Region l (ellipsoidal jet)*: In this regime, the water temperature is high, and the steam flux is large. The steam encapsulates the pipe as an ellipsoid, the small diameter of which is about eight pipe diameters. There is no bubble detachment observed in this regime.

*Region 2 (ellipsoidal oscillatory bubble)*: The steam flux is lower. Though the steam region is still an ellipsoid, there is an obvious bubble detachment. The frequency of the detachment is about 11 Hz.

*Region 3 (Oscillatory bubble)*: The steam flux is even lower. The steam region moves up and encapsulates more of the pipe. The bubble detaches above the pipe exit. The separated steam would condense as it floats up toward the water surface. The lower steam region still encapsulates the pipe and begins to grow into another column. The progress repeats. The detachment frequency of the bubble is about 7 Hz.

*Region 4 (oscillatory cone jet)*: In this regime, the water temperature is low, and the steam mass flux is high. The steam region exists below the pipe exit. The bubble detaches at the point about one to two pipe diameters below the exit. Chan described this progress as an interface instability, which grows as the steam region moves away from the exit. And a volume of steam would detach when the instability grows large enough. The frequency of the detachment is about 40 Hz.

*Region 5 (oscillatory bubble)*: The initial position of instability mentioned above is closer to the pipe exit. The detachment point moves up to about one pipe diameter below the exit. The detachment frequency is about 26 Hz. The detachment point and the initial position of instability will be closer to the exit when the

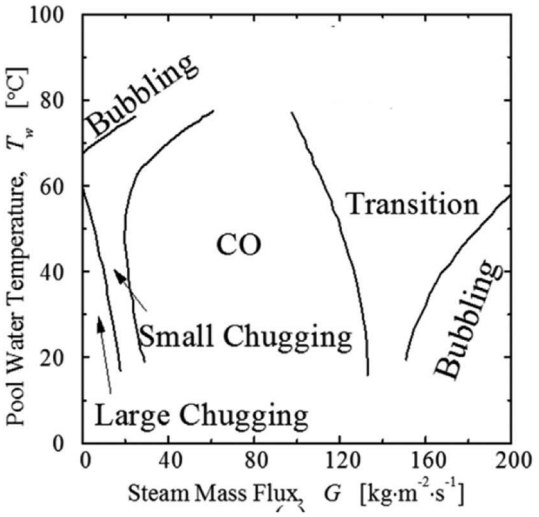


**FIGURE 3 |** The regime map by Aya et al. (1980, 1983) and Nariai and Aya (1986).

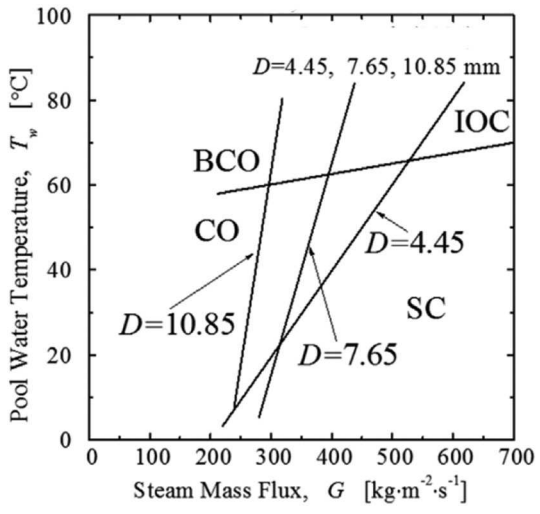


**FIGURE 4 |** The regime map developed by Chun et al. (1996).

steam flux becomes lower. It is the boundary of the oscillatory bubble and chugging when the detachment happens just at the exit, because the steam could only exist periodically in the pool and the water would enter the pipe periodically if the steam flux becomes lower. Chan separated the chugging into three regimes with the shape and pressure oscillation: internal chug, external chug with detached bubble, and external chug with encapsulating bubble (shown in **Figure 2**).

*Region 7 (oscillatory interface)*: No bubble detachment was observed in this regime. The steam–water interface is right at the pipe exit. The steam flux is so low that we cannot measure accurate data.

If the water temperature is above the dashed line at the top of **Figure 2**, steam would escape from the water surface.

Aya et al. (1980, 1983) and Nariai and Aya (1986) developed a regime map in the 1980s with his experiment, as shown in **Figure 3**. In his experiment, the steam flux varied from 0 to 200 kg/m$^2$ s, and the water temperature is in the range of 10 to 100°C. The diameters of pipes used in the experiment were 18 and 29 mm. Aya identified the regime with the amplitude and frequency of the pressure and the temperature in the pipe. The characteristics of each regime are described as follows.

*Large chugging/intermittent growth (La-C)*: Pressure oscillations with high amplitude and frequency are observed, which results from the level of water rushing into the pipe.

*Small chugging/beat (Sm-C)*: The steam–water interface oscillates near the pipe exit.

*CO*: A bubble grows and shrinks at the pipe exit. The frequency of pressure oscillation is just the same as that of steam–water interface oscillation.

*Bubbling (B)*: In this regime, the water temperature or high steam mass flux is high, and the steam velocity is close to the sonic velocity. Bubble growth and detachment were both observed.

*Transition (T)*: The behaviors of the steam–water interface are the transition from CO to bubbling.

Chun et al. (1996) conducted experiments and developed the regime map, as shown in **Figure 4**. The steam flux in the experiment varied from 200 to 700 kg/m$^2$ s, while the water temperature varied from 12 to 83°C. The diameters of the pipe varied from 4.45 to 10.85 mm. Chun classified the regimes in which the steam–water interface is almost stable into three categories: conical, ellipsoidal, and divergent shapes. Chun thought that the diameter of steam region is related to the diameter of the pipe and indicated that the shape of the steam region is related to the steam flux and water subcooling. And the steam region shape would be divergent when the subcooling is small enough. Chun identified six regimes, summarized as follows.

*Chugging (C)*: The steam flux and water temperature are both low. The steam plume forms and collapses periodically. The water rushes into the pipe when the steam plume collapses and then is pushed out by the steam. The amplitude of pressure oscillation is large and irregular.

*Transition region from chugging to CO (TC)*: The water cannot enter the pipe. A crowd of small bubbles forms near the pipe exit.

*CO*: The steam–water interface and pressure oscillate violently in a high frequency.

*Bubble CO (BCO)*: The water temperature is high, and the steam flux is the same as that in CO. The steam bubble detaches with an irregular shape and condenses or escapes from the water surface.

*Stable condensation (SC)*: The steam condenses rapidly. The sound of condensation and amplitude of pressure oscillation are both mild.

*Interfacial oscillation condensation (IOC)*: The water temperature and steam flux are high. The steam condenses unstably. The steam–water interface oscillates violently.

Chun conducted experiments with pipes of different diameters. We can easily find that in the diameter range Chun have chosen, the steam flux would be smaller when we get a stable condensation, if the pipe diameter is lager. But this rule

is not always applicative when the pipe diameter varies. In the regime map of Chun, the pipe diameter is 18 or 29 mm, and the steam region did not become stable even when the steam flux got to 200 kg/m$^2$ s.

And when the pipe diameter turns to 50.8 mm, which is the pipe diameter used in Chan's experiments (Chan and Lee, 1982), the regime map is much different. In Chan's regime map (Chan and Lee, 1982), the detachment and oscillation are usual. This could be explained by the fact that when the pipe diameter is large enough, the condensation rate is not enough to consume the tail of the steam and the tail could detach from the main region. And the limited condensation could not affect the main steam region, the condensation and the momentum of the steam make the oscillation happen.

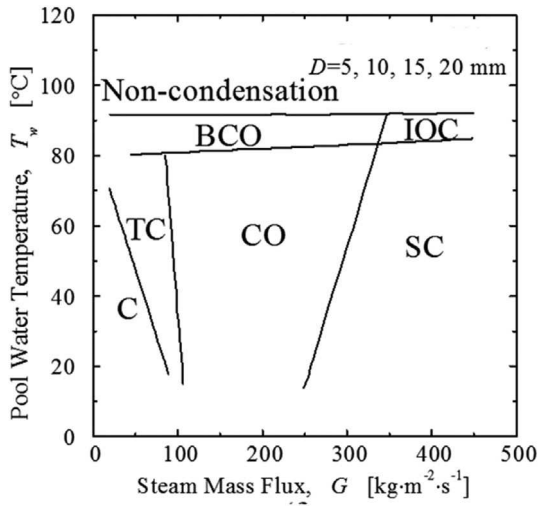


**FIGURE 5 |** The regime map developed by Cho et al. (1998).

Cho et al. (1998) conducted experiments and proposed a regime map including six regimes, shown in **Figure 5**. The definitions of these regimes are similar with Chun's, while the boundaries are not all the same. The difference in regime maps may be the result of the different pipe diameters.

Petrovic De With et al. (2007) researched the steam-submerged DCC regime map with data from the literature. De With proposed that the previous planar regime maps could predict the regime under a certain condition, but it would not work when the diameter of pipe varies. De With proposed a three-dimensional regime map, shown in **Figure 6**. He conducted experiments to validate the regime map. He classified the regimes into three categories: chugging, jetting, and bubbling, similar with Chan and Lee (1982). And he also agreed with Chun et al. (1996) that there are three typical plume shapes in the jetting regime: conical, ellipsoidal, and divergent.

Wu et al. (2007, 2009a,b,c) has begun an experimental research on the steam-submerged DCC since 2007. His experiments included sonic and supersonic steam jets. Wu observed six typical regimes under the supersonic condition and four typical regimes under the sonic condition. He explained the causes of formation of different shapes under sonic and supersonic conditions with the expand–compress wave theory. And he developed a three-dimensional regime map, as shown in **Figure 7**. In the regime map, the pressure ratio (the ratio of the

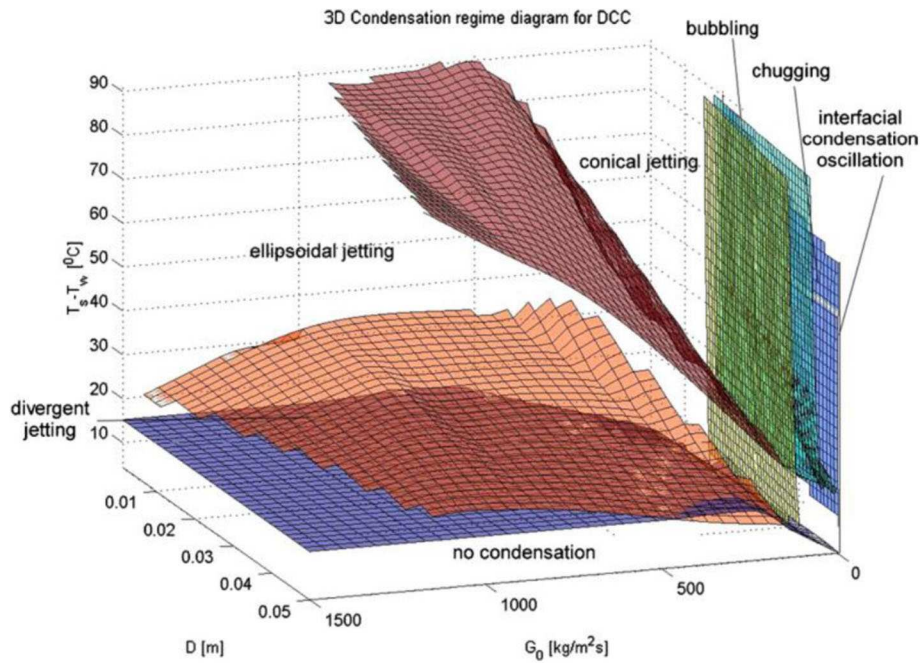


**FIGURE 6 |** The regime map developed by Petrovic De With et al. (2007).

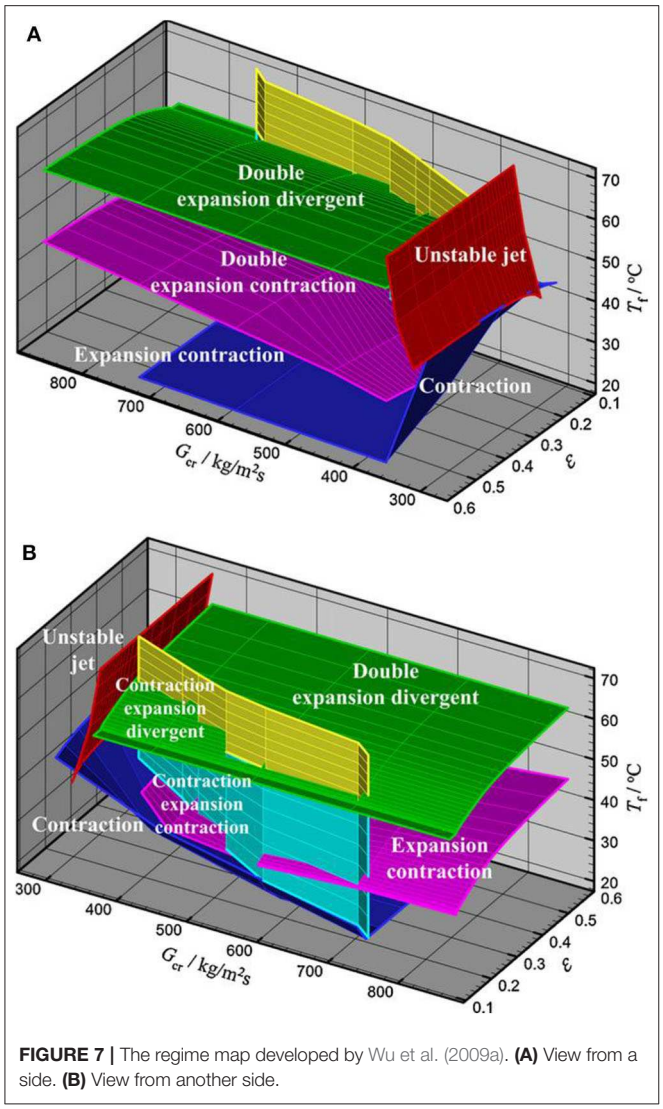


**FIGURE 7 |** The regime map developed by Wu et al. (2009a). **(A)** View from a side. **(B)** View from another side.

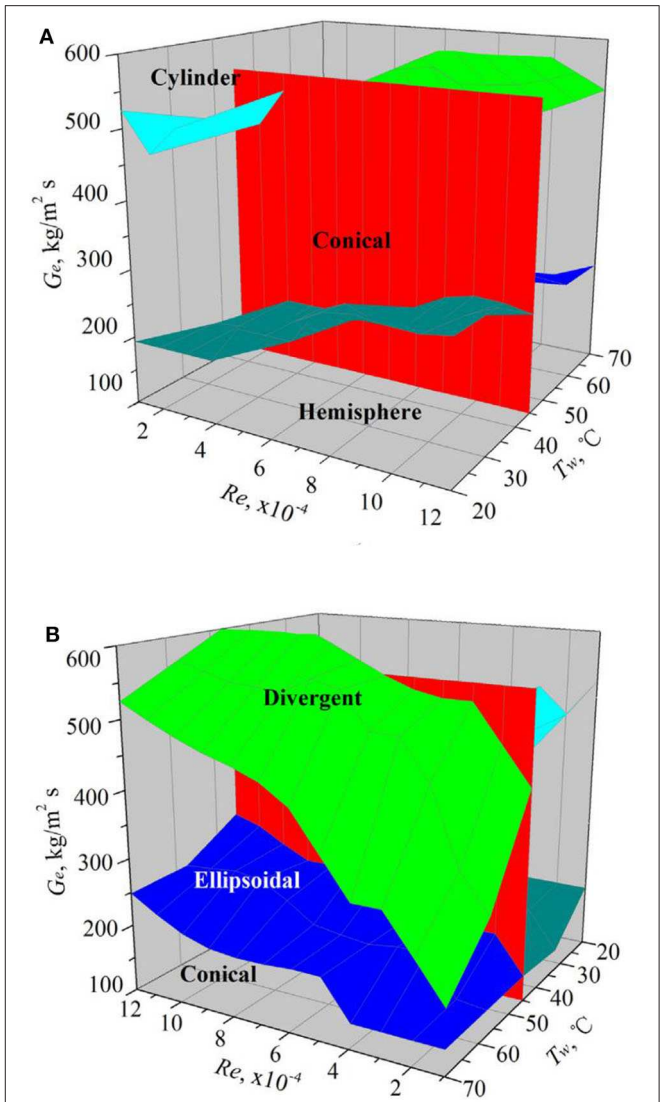


**FIGURE 8 |** The regime map developed by Xu et al. (2013). **(A)** View from a side with low water temperature. **(B)** View from a side with high water temperature.

pressure of the pipe exit and pressure of the pipe inlet) is a factor which is related to the steam plume shape. The classifications of regimes are based on the compressing and expanding of the steam plume.

Wu focused his attention on the stable condensation regime. In his research, different pipe exit diameters were used, but no obvious differences were observed between regimes of different diameters. It seems that the diameter does not affect the stable regime as efficiently as it does when the regime is unstable.

Xu et al. (2013) performed experiments to study the steam-submerged DCC regime map, in which the steam meets with the water flow in a vertical pipe. The regime map is shown in **Figure 8**. In his regime map, the regime is related to the steam flux, water temperature, and the *Re* of the water. Xu acquired a stable jetting regime, and there are five typical shapes: cylinder, conical, hemisphere, ellipsoidal, and divergent. In 2016, Xu and Guo (2016) conducted an experiment to study the regime map when the steam jet is oblique when it enters the pipe. The regime maps are shown in **Figure 9**.

Gregu et al. (2017) conducted experiments focusing on the chugging regime and further subdivided the chugging regime into four regimes, as shown in **Figure 10**. The characteristics of each regime are described as follows.

*Small encapsulating bubbles (SEB)*: A small bubble encapsulates the pipe exit.

*Big encapsulating bubbles (BEB)*: A large bubble encapsulates the pipe exit.

*Big encapsulating elongated bubbles (BEEB)*: A large elongated bubble encapsulates the pipe exit.

*Nonencapsulating bubbles (NEB)*: no bubble encapsulates the pipe exit.

Zhao and Hibiki (2018) reviewed the condensation maps of steam-submerged jet condensation in 2018, but some of the

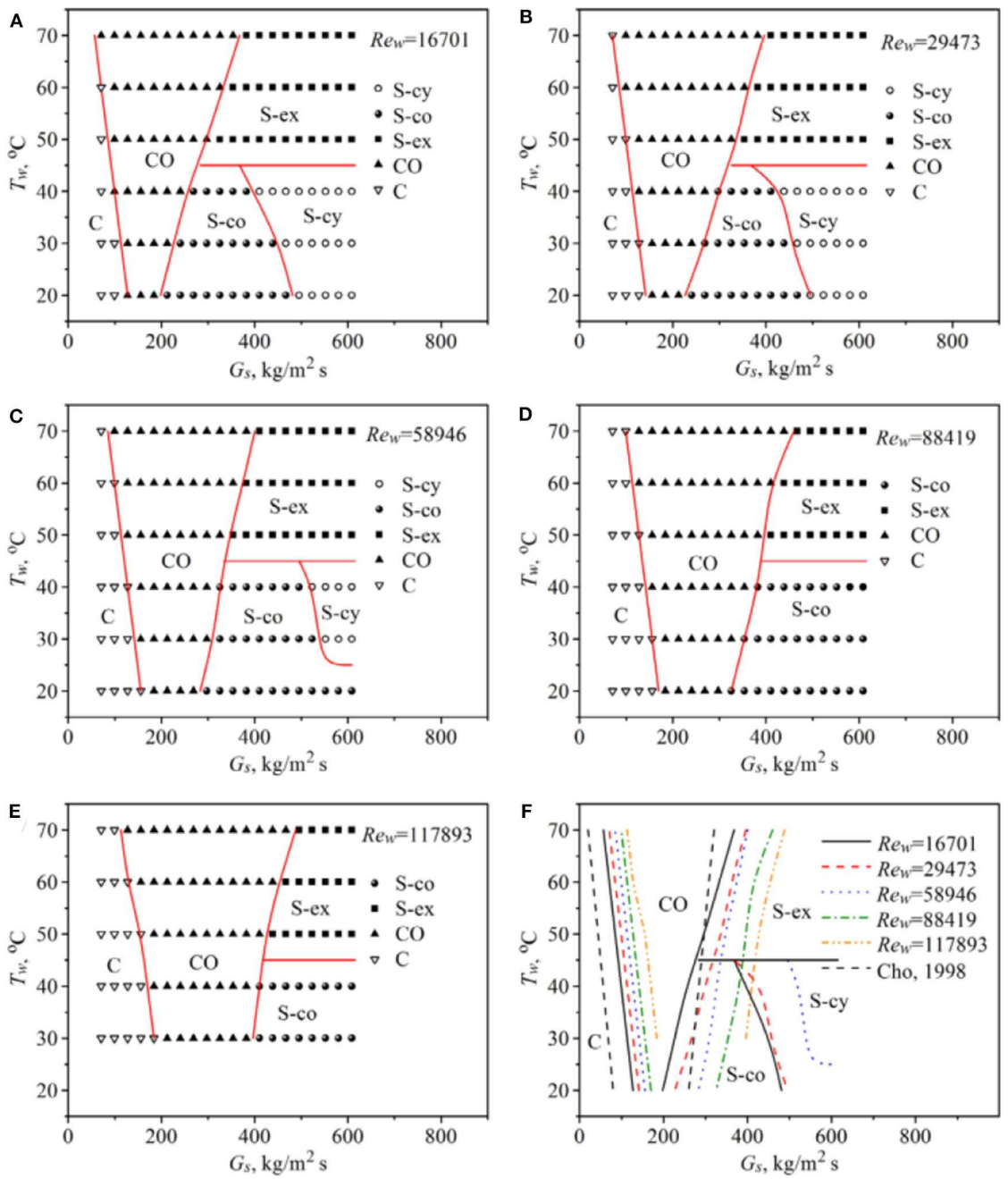


**FIGURE 9 |** The planar regime maps developed by Xu and Guo (2016). **(A)** Re = 16,701; **(B)** Re = 29,473; **(C)** Re = 58,946; **(D)** Re = 88,419; **(E)** Re = 117,893; **(F)** transition lines for different Re.

information is inaccurate, such as the diameter of the pipe in Chan's experiment (Chan and Lee, 1982) and the range of water temperature in Chan's research (Chun et al., 1996).

## SHAPE AND LENGTH OF THE STEAM PLUME

The steam plume is stable when the steam flux is large and steady enough. Many researchers pay attention to the length of the steam plume, which is an important parameter of a stable regime. It is significant to know the length because it has an important effect on the heat transfer characteristics. Kerney et al. (1972) conducted experiments to study the length of a stable regime and acquired a semiempirical correlation to predict the dimensionless steam plume length. The pipes of different external structures with the same flow areas were used in Kerney's experiments. And it proved that the external structure has little to do with the dimensionless length. The correlation

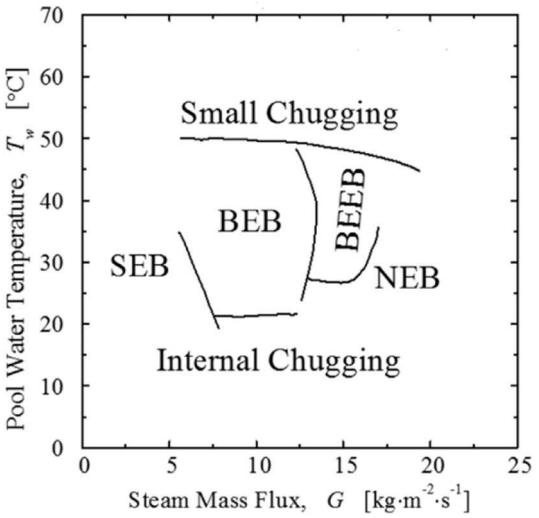


**FIGURE 10 |** The regime maps developed by Gregu et al. (2017).

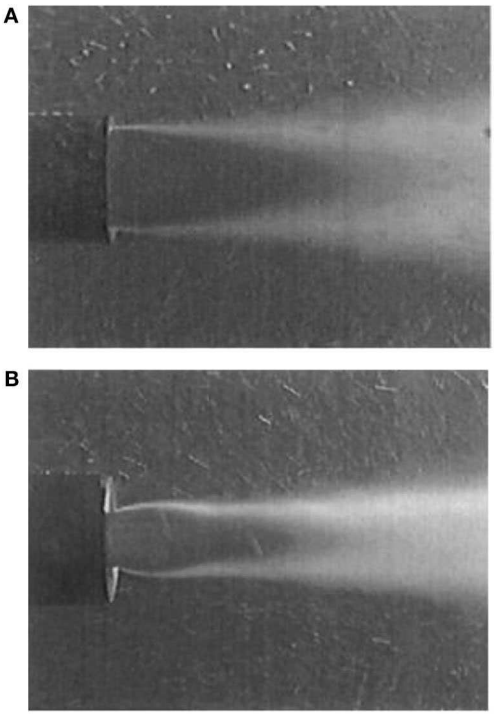


**FIGURE 11 |** The typical shapes observed by Hwan Kim et al. (2001). **(A)** Conical shape (nozzle ID: 20mm, mass flux: 280 kg/m2-s). **(B)** Ellipsoidal shape (nozzle ID: 10.15mm, mass flux: 600 kg/m$^2$-s).

Kerney proposed was based on the dimensionless condensation driving potential and the steam flux, as shown in **Equation (2)**. The condensation driving potential, *B*, which represents the condensation capacity, is defined in **Equation (1)**. Most of the correlations of dimensionless steam plume proposed by the latecomers have a similar form with Kerney's correlation. But Weimer et al. (1973) proposed a correlation adding the ratio of densities between liquid and steam as a factor.

$$B = C_p\,(T_v - T_l)\,/h_{lv} \tag{1}$$

$$l/d = 0.7166B^{0.1689}(G_0/G_m)^{0.6446} \tag{2}$$

Hwan Kim et al. (2001) conducted experiments to study the length of a stable steam plume in 2011. He has observed conical and ellipsoidal steam plumes in the experiment, as shown in **Figure 11**. And Kim proposed a correlation of dimensionless steam plume length with his experimental data, as shown in **Table 1**.

De With (2009) analyzed the data from the literatures and indicated that the length of the steam plume is related to the Reynolds number of the steam, which could reflect the inertia of the steam. De With used all the data collected from literatures to developed a diagram of steam plume length with the condensation potential and the Reynolds number of the steam, as shown in **Figure 12**. The diagram was produced through interpolation using existing data from literatures to create the integrated surface. De With filtered the data that have large deviations in colors from the surrounding colors, for the reason that he assumed that the large deviations are the result of inaccuracies in the measurements and variations in measurement techniques and setups during experiments.

Wu et al. (2007, 2009b,c), Xu et al. (2013, 2017), and Xu and Guo (2016) also conducted experiments to study the steam plume length. They observed different plume shapes in their experiments and proposed correlations to predict dimensionless steam plume length. One of the correlations proposed by Wu took the effects of steam inlet pressure and pool pressure into account. In Xu's study, the steam is jetted into the vertical

**TABLE 1 |** Summary sheet of correlations for dimensionless length of steam plume.

| Authors | Correlation |
|---|---|
| Kerney | $l/d = 0.7166B^{0.1689}(G_0/G_m)^{0.6446}$ |
| Weimer | $l/d = 17.72B^{-1}(G_0/G_m)^{0.5}(\rho_v/\rho_l)^{-0.5}$ |
| Chun | $l/d = 0.5923B^{-0.66}(G_0/G_m)^{0.3444}$ |
| Kim | $l/d = 0.503B^{-0.70127}(G_0/G_m)^{0.47688}$ |
| Wu | $l/d = 0.868B^{-0.6}(G_0/G_m)^{0.5}(p_v/p_l)^{0.2}$ |
| Wu | $l/d = 0.597B^{-0.8}(G_0/G_m)^{0.5}(p_v/p_l)^{0.2}$ |
| Wu | $l/d = 0.1B^{-1.37}(G_0/G_m)^{1.86}$ |
| Xu | $l/d = 2.03B^{-0.72}(G_0/G_m)^{1.71}Re^{-0.19}$, 2456<*Re*<29473<br>$l/d = 11925B^{-0.62}(G_0/G_m)^{1.61}Re^{-1.01}$, 29473<*Re*<117893 |
| Xu | $l/d = 0.1B^{-2.249}(G_0/G_m)^{1.941}Re^{-0.165}$ |
| Xu | $l/d = 0.14B^{-1.354}(G_0/G_m)^{1.737}Re^{-0.1}(p_v/p_l)^{-1.415}$ |
| Symbol | *l*: steam plume length, mm; *d*: pipe diameter, mm; B: condensation driving potential, $B = c_p(T_v - T_l)/h_{lv}$; $G_0$: steam flux, kg/m$^2$ s; $G_m$: critical steam flux, kg/m$^2$ s; $\rho$: density, kg/m$^3$; *p*: pressure, MPa; Re: water Reynolds number; *T*: temperature, K; subscripts: 1, liquid; v, vapor |

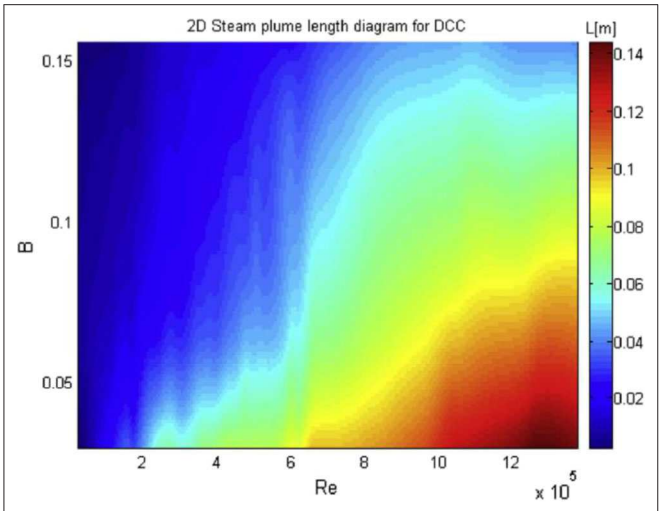


**FIGURE 12 |** The new diagram of steam plume length developed by De With (2009).

pipe. All the correlations for the steam plume length are shown in **Table 1**.

## CONCLUSIONS

There are nine regime maps developed for the submerged-steam condensation by different researchers depending on different experiments. But the regime boundaries are quite different in each of their regime maps. There are even some contradictions between the regime maps. An important reason is that almost all researchers did not take the diameter of the pipe into account when they the developed regime maps, except Cho and De With. And the pipe diameter has a remarkable influence on the regime.

Though Chun took the pipe diameter into account, the regime boundaries in his regime map are almost linear and not exact enough. De With's regime map may need more experimental data to ensure accuracy, because the limited data may be not enough to draw a continuous regime map. Wu and Xu researched the stable regime minutely but did not research the unstable regime. There are many correlations to predict the dimensionless steam plume length, but they are all semiempirical correlations, and none of them could reveal the mechanism.

In the future, we may pay more attention to the effect of the pipe diameter on the regime map. The regime map could be developed when the diameter is certain. And the comparison of regime maps of different pipe diameters needs to be done to help us know the impacting mechanism of the pipe diameter.

On the other hand, almost all the experiments were conducted under atmospheric pressure, and experiments under other pressures should be performed to satisfy the needs on much wider applications.

## AUTHOR CONTRIBUTIONS

YD wrote this article. XY, JZ, and YZ gave the suggestions to revise this article. All authors contributed to the article and approved the submitted version.

## FUNDING

This work was supported by Postdoctoral Science Foundation of China (2018M643528) and Natural Science Foundation of Sichuan Province of China (2019YJ0298).

## REFERENCES

Arinobu, M. (1980). "Studies on the dynamic phenomena caused by steam condensation in water," in *Proceedings of the ANS/ASME/NRC International Topical Meeting on Nuclear Reactor Thermal-hydraulics* (New York, NY), 293-302.

Aya, I., Kobayashi, M., and Nariai, H. (1983). Pressure and fluid oscillations in vent system due to steam condensation (II). *J. Nuclear Sci. Technol.* 20, 213–227 doi: 10.1080/18811248.1983.9733383

Aya, I., Nariai, H., and Kobayashi, M. (1980). Pressure and fluid oscillations in vent system due to steam condensation. *J. Nuclear Sci. Technol.* 17, 499–515. doi: 10.1080/18811248.1980.9732617

Chan, C. K., and Lee, C. K. B. (1982). A regime map for direct contact condensation. *Int. J. Multiphase Flow* 8, 11–20. doi: 10.1016/0301-9322(82)90003-9

Cho, S., Song, C. H., Park, C. K., Yang, S. K., and Chung, M. K. (1998). "Experimental study on dynamic Pressure Pulse in direct contact condensation of steam discharging into subcooled water" in *1st Korea-Jopan Symposium on Nuclear Thermal Hydraulics and Safety (NTHASl)* (Pushan).

Chun, M. H., Kim, Y. S., and Park, J. W. (1996). An investigation of direct condensation of steam jet in subcooled water. *Int. Commit. Heat Mass Transf.* 23, 947–958. doi: 10.1016/0735-1933(96)00077-2

De With, A. (2009). Steam plume length diagram for direct contact condensation of steam injected into water. *Int. J. Heat Fluid Flow* 30, 971–982. doi: 10.1016/j.ijheatfluidflow.2009.06.001

Gregu, G., Takahashi, M., Pellegrini, M., and Mereu, R. (2017). Experimental study on steam chugging phenomenon In a vertical sparger. *Int. J. Multiphase Flow* 88, 87–98. doi: 10.1016/j.ijmultiphaseflow.2016.09.020

Hwan Kim, H. Y., Yoo Bae, Y., Chul Song, H., Jong Park, K., and Sang Choi, M. (2001). Experimental study on stable steam condensation in a quenching tank. *Int. J. Energy Res.* 25, 239–252 doi: 10.1002/er.675

Kerney, P. J., Faeth, G. M., and Olson, D. R. (1972). Penetration characteristics of a submerged steam jet. *AlChE J.* 8, 548–553. doi: 10.1002/aic.690180314

Lahey, R. T., and Moody, F. J. (1993). The thernal-hydraulics of a boiling water nuclear reactor. *Am. Nuclear Soc.* 284, 581–583.

Nariai, H., and Aya, I. (1986). Fluid and pressure oscillations occurring at direct contact condenstaion of steam flow with cold water. *Nuclear Eng. Design* 95, 35–45. doi: 10.1016/0029-5493(86)90034-8

Petrovic De With, A., Calay, R. K., and De With, G. (2007). Three-dimensional condensation regime diagram for direct contact condensation of steam injected into water. *Int. J. Heat Mass Transf.* 50, 1762–1770. doi: 10.1016/j.ijheatmasstransfer.2006.10.017

Weimer, J. C., Faeth, G. M., and Olson, D. R. (1973). Penetration of vapor jets submerged in subcooled liquids. *AlChE J.* 19, 552–558. doi: 10.1002/aic.690190321

Wu, X. Z., Pan, D. D., Liu, G. Y., and Li, W. J. (2009a). Condensation regime diagram for supersonic/sonic steam jet in subcooled water.

*Nuclear Eng. Design* 239, 3142–3150. doi: 10.1016/j.nucengdes.2009.08.010

Wu, X. Z., Yan, J. J., Li, W. J., Pan, D. D., and Chong, D. T. (2009c). Experimental study on sonic steam jet condensation in quiescent subcooled water. *Chem. Eng. Sci.* 64, 5002–5012. doi: 10.1016/j.ces.2009.08.007

Wu, X. Z., Yan, J. J., Li, W. J., Pan, D. D., and Liu, G. Y. (2009b). Experimental investigation of over-expanded supersonic steam jet submerged in quiescent water. *Exp. Thermal Fluid Sci.* 34, 10–19. doi: 10.1016/j.expthermflusci.2009.08.006

Wu, X. Z., Yan, J. J., Shao, S. F., Cao, Y., and Liu, J. (2007). Experimental study on the condensation of supersonic steam jet submerged in quiescent subcooled water: steam plume shape and heat transfer. *Int. J. Multiphase Flow* 33, 1296–1307. doi: 10.1016/j.ijmultiphaseflow.2007.06.004

Xu, Q., and Guo, L. (2016).Direct contact condensation of steam jet in crossflow of water in a vertical pipe. Experimental investigation on condensation regime diagram and jet penetration length. *Int. J. Heat Mass Transf.* 94, 528–538. doi: 10.1016/j.ijheatmasstransfer.2015.02.036

Xu, Q., Guo, L., and Chang, L. (2017). Interfacial characteristics of steam jet condensation in crossflow of water in a vertical pipe. *Appl. Thermal Eng.* 113, 1266–1276. doi: 10.1016/j.applthermaleng.2016.11.094

Xu, Q., Guo, L., Zou, S., Chen, J., and Zhang, X. (2013). Experimental study on direst contact condensation of stable steam jet in water flow in a vertical pipe. *Int. J. Heat Mass Transf.* 66, 808–817. doi: 10.1016/j.ijheatmasstransfer.2013.07.083

Zhao, Q., and Hibiki, T. (2018). Review: condensation regime maps of steam submerged jet condensation. *Prog. Nuclear Energy* 107, 31–47. doi: 10.1016/j.pnucene.2017.12.014

**Conflict of Interest:** The authors declare that the research was conducted in the absence of any commercial or financial relationships that could be construed as a potential conflict of interest.

frontiers in Energy Research

ORIGINAL RESEARCH
published: 14 July 2020
doi: 10.3389/fenrg.2020.00123

# Study on Natural Circulation Heat Transfer Characteristics of Different Liquid Metals Based on Factor Analysis

*Feng Xiang*[1,2,3]*, *Zhou Tao*[2,3,4]*, *Zhang Jialei*[1,2,3], *Zhang Boya*[1,2,3] and *Chen Juan*[1,2,3]

[1] School of Nuclear Science and Engineering, North China Electric Power University, Beijing, China, [2] Institute of Nuclear Thermal-Hydraulic Safety and Standardization, North China Electric Power University, Beijing, China, [3] Beijing Key Laboratory of Passive Safety Technology for Nuclear Energy, North China Electric Power University, Beijing, China, [4] Southeast University, Nanjing, China

The study of the commonness and differences of natural circulation of different liquid metals plays an important role in improving the safety of reactors. The numerical simulation of liquid metal natural circulation heat transfer was carried out by CFX, and its heat transfer coefficient, flow, and outlet temperature were studied. The factor analysis method was used to analyze the influence of the interaction between factors and the contribution rate of each factor. It can be found that the commonality of heat exchange between different liquid metals is that the heat transfer coefficient is mainly affected by the power, the contribution rate of power to the heat transfer coefficients of liquid sodium, sodium-potassium alloy, lead, and lead-bismuth alloy reached 40.16, 78.16, 97.95, and 92.19%, respectively; the flow rate and outlet temperature of the liquid metal increase with the increase of power; the flow rate and outlet temperature are hardly affected by pressure. The difference is that the heat transfer coefficients of liquid metals have different trends with the change of power; in addition, the interaction between the factors of heat transfer coefficient is different; the heat transfer coefficient of liquid sodium and sodium-potassium alloy is affected by pressure, the pressure affects the heat transfer coefficient by coupling with power or inlet temperature. In general, the heat transfer performance of sodium is the best, with a much higher heat transfer coefficient than the other three liquid metals; the natural circulation ability of sodium-potassium alloy is the strongest, and its flow velocity is greater than other liquid metals.

**Keywords: liquid metal, natural circulation, heat transfer coefficient, factor analysis, interaction**

OPEN ACCESS

***Edited by:***
*Yanping Huang,*
*Nuclear Power Institute of China (NPIC), China*

***Reviewed by:***
*Zhitong Bai,*
*University of Michigan, United States*
*Han Bao,*
*Idaho National Laboratory (DOE), United States*

***Correspondence:**
*Feng Xiang*
*number5654@163.com*
*Zhou Tao*
*101012636@seu.edu.cn*

***Specialty section:***
*This article was submitted to Nuclear Energy, a section of the journal Frontiers in Energy Research*

***Received:*** *29 January 2020*
***Accepted:*** *25 May 2020*
***Published:*** *14 July 2020*

***Citation:***
*Xiang F, Tao Z, Jialei Z, Boya Z and Juan C (2020) Study on Natural Circulation Heat Transfer Characteristics of Different Liquid Metals Based on Factor Analysis. Front. Energy Res. 8:123. doi: 10.3389/fenrg.2020.00123*

## INTRODUCTION

Natural circulation has a very broad application prospect in reactor safety, and it is also widely used in other industries. The passive natural circulation (Ma et al., 2017; Wang et al., 2018; Yagov et al., 2019) can simplify the system in the reactor and reduce the system's dependence on the reliability of the external power supply, which greatly improves the inherent safety of the reactor. The safety performance of the third generation AP1000 (Hashim et al., 2014) is 100 times higher than that of the second generation nuclear power plant. One of its features is that the safety system adopts the passive natural circulation principle

in many places. GM's SBWR reactor (Duncan, 1988) and the Swedish PIUS reactor all use natural circulation to ensure reactor safety. The US S5G, S6G, and S8G nuclear submarine reactors (Liu, 2015) are natural circulation pressurized water reactors. The initial interest in the study of liquid metals was in the design of fast neutron reactors. This is mainly because the liquid metal (Xie et al., 2016) has a high power density active zone, excellent thermal, and nuclear physical properties, which enables efficient energy extraction from the reactor. At present, the coolant of the fast breeder reactor developed by various countries is mainly sodium or sodium-potassium alloy. The chemical properties of sodium and sodium-potassium alloy are particularly active. They are easily reacted with water, oxygen, etc., causing combustion or even explosion. Therefore, the study of coolant heat transfer characteristics is a very important technical and safety issue during the operation, maintenance, and decommissioning of sodium-cooled fast reactor. Liquid lead and lead-bismuth alloy (Gaiying et al., 2012) are the main candidate materials for ADS coolant, which has excellent thermal properties, such as high density, chemical inertia, and natural circulation ability similar to water. In view of the heat transfer characteristics of the natural circulation of liquid metal, scholars from various countries have done some research in recent years. Chang and Hahn (2002) used SSC-K software to calculate the sodium boiling under KALIMER severe accident, and obtained the curves of interface heat transfer, liquid film thickness and heat transfer coefficient. Ma et al. (2007) studied the natural circulation steady state of heavy metal loops, and concluded that the temperature difference between the system geometry and the hot and cold sections have an effect on the natural circulation flow of heavy metal fluids. Based on the NACIE experimental bench, Tarantino et al. (2008) conducted a related study on the flow of lead-bismuth alloy natural circulation, and analyzed the experimental results. Gao et al. (2015) measured the diffusion coefficient of Ni and Cr in liquid lead-bismuth alloy by using a capillary tube, and obtained the diffusion coefficient of LBE from the experimental data of nickel concentration. Watanabe et al. (2015) studied the evaluation method of the residual heat removal system of the natural circulation of sodium cooled fast reactor. The reliability of the safety analysis of sodium cooled fast reactor was verified by comparison with the three-dimensional analysis of the turbulence model. Borgohain et al. (2016) conducted a natural circulation experiment in a non-uniform diameter lead-bismuth circuit. The natural circulation of steady state and transient is performed under different power conditions. Factorial analysis is a multi-factor and multi-level experimental design. It can test not only the differences between levels of each factor, but also the interactions between factors. When the level of one factor changes, the effect of another factor or multiple factors changes, which indicates that there is an interaction; otherwise, it implies that there is no interaction and it is independent. Among the above research results, only the natural circulation of a single liquid metal has been studied, and the interaction between factors affecting natural circulation heat transfer has not been analyzed. By comparing the natural circulation flow and heat transfer characteristics of different liquid metals, the commonalities and differences of heat transfer rules are obtained, which has guiding significance for improving the safety of the reactor.

# RESEARCH OBJECT

## Geometric Model

The natural circulation model is established by ANSYS ICEM, which mainly includes preheating section, heating inlet section, heating section, heating outlet section, cooling section, and descending section. The specific structure of the model is shown in **Figure 1**.

As can be seen from **Figure 1**, the natural circulation model of different liquid metals is 2.5 m high, 3.5 m wide, and the pipe diameter is 4 mm. The length of the preheating section is 3.5 m, the length of the heating inlet section is 0.25 m, the length of the heating section is 2 m, the length of the heating outlet section is

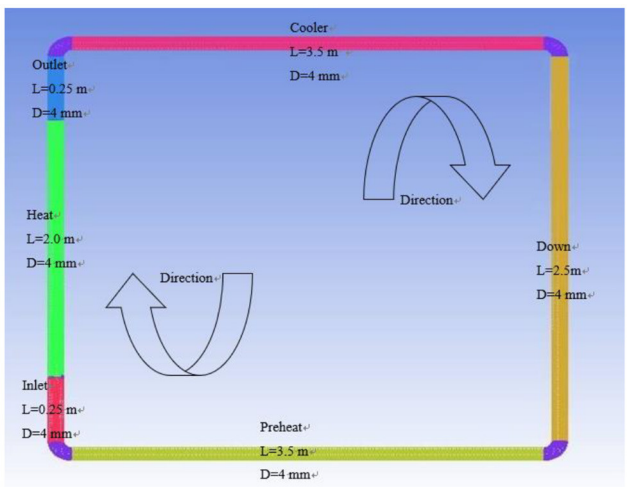


**FIGURE 1 |** Natural circulation loop.

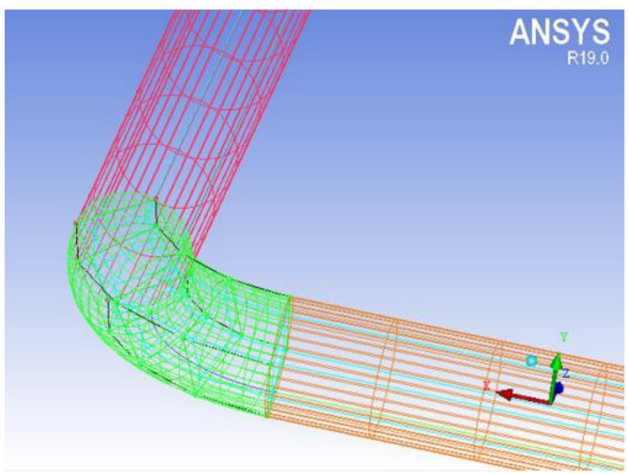


**FIGURE 2 |** Grid partitioning.

0.25 m, the cooling section is 3.5 m, and the descending section is 2.5 m. The preheating section is used to preheat the working fluid in the pipeline to a predetermined temperature. The heating section is used to continue heating the working fluid and reach the operating temperature. The cooling section is used to cool the working medium in the pipeline, and finally the working fluid forms a natural circulation in the pipeline. In order to ensure that the difference in flow and heat transfer is not affected by conditions such as loop size and height, the geometric models of different liquid metals are consistent.

## Meshing

The natural circulation loop is meshed, and part of the grid structure is shown in **Figure 2**.

As can be seen from **Figure 2**, the natural circulation loop model is meshed with o-type grid. In order to improve the accuracy of the calculation, the boundary layer is encrypted in the grid setting, and the number of grids is 823674. The related information of the specific node division at each position is shown in **Table 1**.

## Boundary Conditions

The boundary conditions are consistent when studying the natural circulation heat transfer characteristics of different liquid metals. Since the melting point of lead is high, the initial temperature of the fluid domain is set to 610 K. When the power is too large, the fluid outlet temperature is very high. Compared with lead and lead-bismuth alloy, the sodium, and sodium-potassium alloy have a lower boiling point. In order to keep the metal in a single-phase liquid state, the maximum power control is 30 kW/m$^2$. In the liquid range, the natural circulation heat transfer characteristics of the four metals were studied. The initial parameters are shown in **Table 2**.

For the convenience of analysis, the power, pressure, and temperature are represented by the letters A, B, and C, respectively. Then, the effect of interaction between power and pressure is AB, the effect of interaction between power and temperature is AC, the effect of interaction between pressure and temperature is BC, and the effect of total interaction of power, pressure, and temperature is ABC.

## Convergence Standard Information

In the control settings of the solver, the specific solver settings, and convergence criteria information are shown in **Table 3**.

## Grid Sensitivity Analysis

The effect of the number of grids on the calculation results was studied to test the grid sensitivity. The number of grids is 21640, 548262, 823674, and 1041780, respectively. Taking lead-bismuth alloy as an example, the change of the mainstream temperature with the axial position of the heating section is shown in **Figure 3**.

It can be seen from **Figure 3** that the mainstream temperatures at different axial positions are basically the same when the number of grids is 823674 and 1041780. Therefore, it is more suitable to divide the mesh number into 823674 based on the economical and accurate calculation process.

# FACTORIAL ANALYSIS CALCULATION MODEL

Factorial analysis (Jingjing et al., 2014) is a method of experimental design, which can be used to study the influence of individual factors and the interaction between factors. When the level and number of factors are small, and the relationship between factors and effects is more complicated, then factorial analysis is a good analytical tool. The two-level factorial test of k factors is recorded as a $2^k$ factorial analysis (representing k factors, each factor has 2 levels). This is the most commonly used analysis method, which can use a relatively small sample to obtain more information, especially factor interactive analysis. The comparison of effect $AB\cdots K$ is as shown in Equation (1).

$$(\text{Contrast})_{AB\ldots K} = (a \pm 1)(b \pm 1)\cdots(k \pm 1) \tag{1}$$

(1) In the formula (1), $(\text{Contrast})_{\text{AB...K}}$ represents a comparison of effects; a, b, and k represent respective factors. In Expansion (1), use the method of elementary algebra to expand it, and replace "1" with [1], which means that all factors take a low level. The

**TABLE 1 |** Grid node division information.

| Node setting item | Node value | Node setting item | Node value |
|---|---|---|---|
| Heating section | 250 | Heating outlet section | 20 |
| Cooling section | 150 | Heating inlet section | 20 |
| Down section | 50 | Pipe center | 20 |
| Preheating section | 100 | Pipe edge | 20 |

**TABLE 3 |** Convergence standard information.

| Basic settings | Setting content | Basic settings | Setting content |
|---|---|---|---|
| Advection scheme | High resolution | Timescale factor | 1.0 |
| Heat transfer model | Thermal energy | Maximum iterations | 5,000 |
| Timescale control | Auto timescale | Residual type | RMS |
| Length scale option | Conservation | Residual target | 1e-6 |

**TABLE 2 |** Parameter range.

| Pressure (Mpa) | Heating section power (kW/m$^2$) | Preheating section temperature (K) | Cooling section temperature(K) | Pipe diameter(mm) | Other wall |
|---|---|---|---|---|---|
| 1–5 | 2–30 | 620–710 | 610 | 4 | Adiabatic condition |

negative sign in the parentheses indicates that the factor is taken, and the positive sign indicates that the factor is not taken. Once the effects are calculated, their estimated effects and their sum of squares can be calculated separately.

$$AB\cdots K = \frac{2}{2n}^{k}(\text{Contrast}_{AB\cdots K}) \quad (2)$$

$$SS_{AB\cdots K} = \frac{1}{2n}^{k}(\text{Contrast}_{AB\cdots K})^2 \quad (3)$$

Among them, $AB\ldots K$ represents the effect estimate, $SS_{\text{AB...K}}$ represents the sum of squares of effects, $n$ is the number of repeated experiments.

y is the response value, $x_{\text{i}}$ $(i = 1, 2, 3)$ represents each factor, and the fitting formula is as shown in (4).

$$y = \alpha_0 + \sum \alpha_{\text{i}} x_{\text{i}} + \sum \alpha_{\text{ij}} x_{\text{i}} x_{\text{j}} + \alpha_{123} x_1 x_2 x_3 \quad (4)$$

Among them, $\alpha_0$,$\alpha_i$,$\alpha_{ij}$,$\alpha_{123}$ are, respectively, the mean, the effect of factor i, the effect of the interaction of factors i and j, the effect of the interaction of three factors.

# CALCULATION RESULTS

## Influence of Heating Power on Flow Heat Transfer

### Effect of Power on Heat Transfer Coefficient

The working fluids are liquid sodium, sodium-potassium alloy, lead and lead-bismuth alloy. The preset system pressure is 1 Mpa, the preheating section temperature is 620 K, the cooling section temperature is 610 K, and the power density ranges from 2 to 30 kW/m$^2$. The change trend of heat transfer coefficient of four liquid metals with power is shown in **Figure 4**.

It can be seen from the **Figure 4** that the heat transfer coefficient of liquid sodium decreases with the increase of heating power, and the heat transfer coefficient of sodium-potassium alloy increases first and then decreases with the increase of power. The heat transfer coefficient of lead and lead-bismuth increases as power increases. Although the liquid sodium heat transfer coefficient is negatively correlated with power, the heat transfer coefficient of sodium is much larger than that of sodium-potassium alloy, lead, and lead-bismuth alloy. Because liquid metal has a common physical property, its molecular thermal conductivity is large, and the molecular Prandtl number is much smaller than that of ordinary fluid. Therefore, the molecular thermal diffusion capacity is far better than the momentum diffusion ability, the molecular thermal conduction is stronger than the turbulent heat transport, and the thermal conductivity

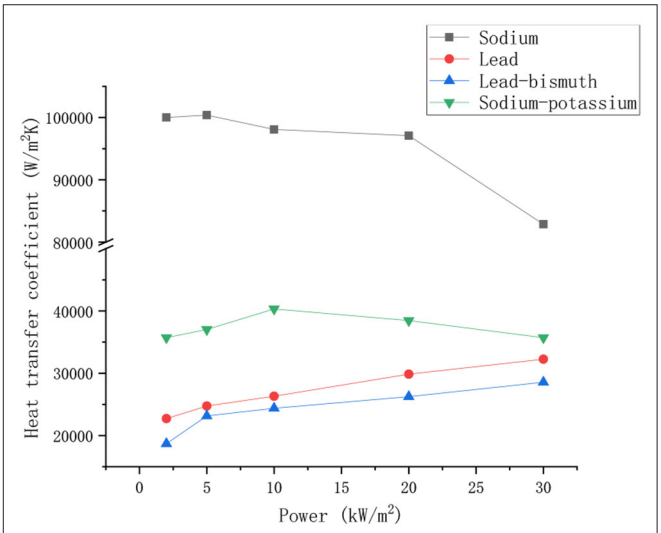


**FIGURE 4 |** Effect of heating power on heat transfer coefficients of different liquid metals.

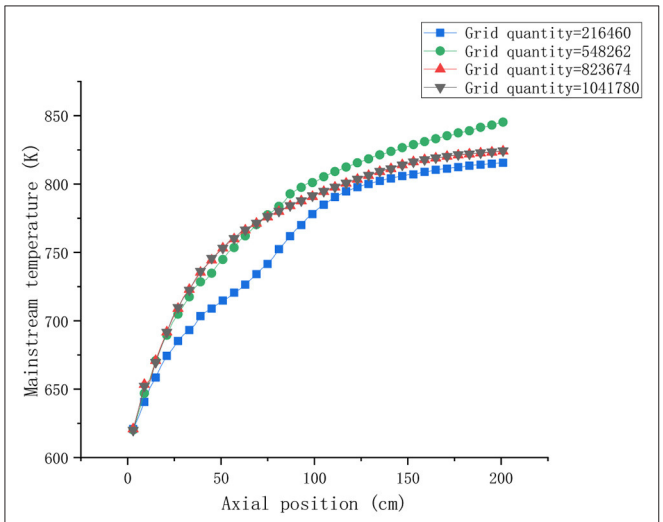


**FIGURE 3 |** Grid sensitivity analysis.

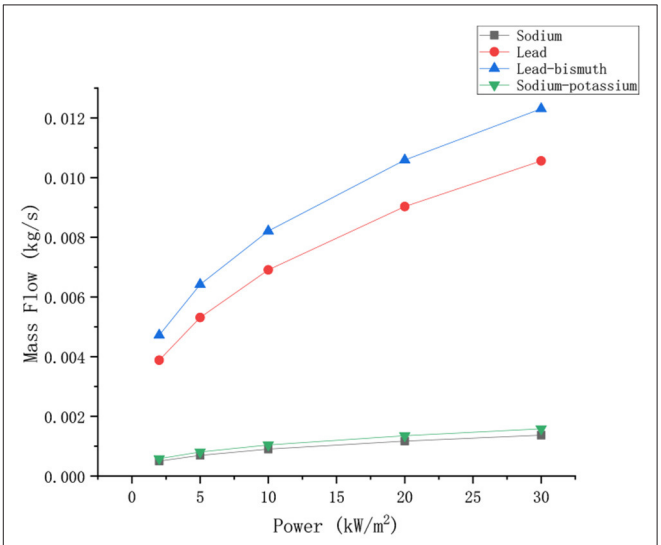


**FIGURE 5 |** Effect of heating power on mass flow of different liquid metals.

plays a role in promoting heat transfer. The thermal conductivity of liquid sodium is greater than that of the other three liquid metals, and its specific heat at constant pressure is higher than that of other metals. So the heat transfer performance is better under the same power conditions. The change trend of the heat transfer coefficient of the four metals with the power is mainly affected by the thermal conductivity and the temperature difference between the hot and cold sections. As the power increases, the temperature of the fluid increases. The thermal conductivity of liquid sodium decreases with increasing temperature. At the same time, with the increase of power, the temperature difference between the cold and hot sections of the fluid increases, and the thermal driving force of the fluid also increases, so the heat transfer of the fluid is enhanced. Compared with the other three liquid metals, the thermal conductivity of liquid sodium is greatly affected by the power. The thermal conductivity occupies a dominant position, and the heat transfer enhancement caused by temperature difference can be ignored. Therefore, the change trend of heat transfer coefficient is consistent with that of thermal conductivity. For lead and lead-bismuth, the thermal conductivity is less affected by temperature, and the increase in temperature difference caused by power increases the heat transfer capacity. As a result, the heat transfer coefficient of lead and lead-bismuth increases with the increase of power. The heat transfer coefficient of sodium-potassium alloy increases first and then decreases with the increase of power. Therefore, it is promoted by the thermal conductivity coefficient and the temperature difference when the power is small. The heat transfer coefficient increases first with the increase of power, and the increase rate is fast. When the power is large, the thermal conductivity decreases with the increase of power, and the inhibiting effect of thermal conductivity on heat transfer is greater than the promoting effect of temperature difference on heat transfer. So the heat transfer coefficient of sodium-potassium alloy decreases with the increase of power, and the decreasing speed is slow.

## Influence of Power on Mass Flow

Keeping the boundary conditions unchanged, the mass flow of the four liquid metals changes with power as shown in **Figure 5**.

As can be seen from the **Figure 5**, the mass flow rates of liquid sodium, sodium-potassium alloy, lead, and lead-bismuth alloy increase with increasing power. The mass flow of lead and lead-bismuth alloy is greater than that of sodium and sodium-potassium alloy. This is mainly because the density of lead and lead-bismuth is much higher than the density of sodium and sodium-potassium. Even if the flow velocity of lead and lead-bismuth is slow, the mass flow will be higher than that of sodium and sodium-potassium. Therefore, it is usually more accurate by comparing the flow velocity when comparing the circulation capacities of different liquid metals.

## Effect of Power on Velocity

Keeping the boundary conditions constant, and the velocity changes with power as shown in **Figure 6**.

It can be seen from the **Figure 6** that the velocity of different liquid metals increases with the increase of power. The velocity

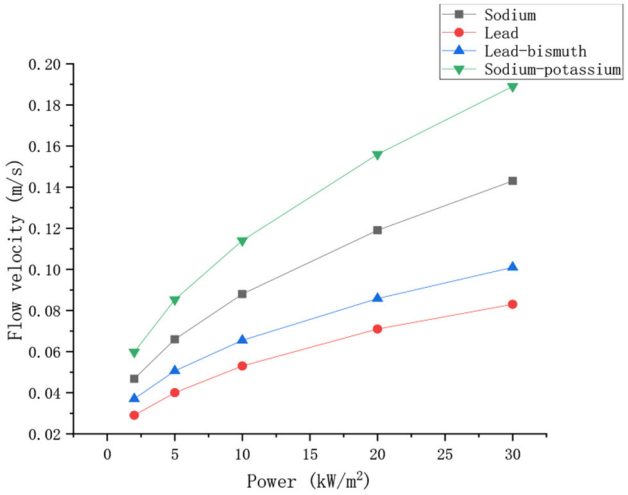


**FIGURE 6 |** Effect of heating power on velocity of different liquid metals.

of sodium potassium was the highest, followed by that of sodium, and the velocity of lead bismuth was the lowest. At the beginning, the velocity difference between the four liquid metals is small. As the power increases, the gap between the velocity increases. This is mainly because the temperature of the fluid increases as the power increases, the thermal expansion of the fluid causes an increase in the density difference between the hot and cold sections, which leads to the increase of the driving head and the increase of the velocity. Compared to the other three liquid metals, the density of sodium-potassium alloy changes more violently with temperature, so its velocity increases most dramatically with power. Among the four liquid metals, the ability of sodium-potassium alloy to naturally circulate is the strongest.

## Effect of Power on Outlet Temperature

The boundary conditions are kept constant, and the changes in the outlet temperature of the four liquid metals with power are shown in **Figure 7**.

As can be seen from the **Figure 7**, the outlet temperatures of different liquid metals increase with increasing power. At the same power, the sodium-potassium alloy has the highest outlet temperature. At lower heating powers, the lead and lead-bismuth outlet temperatures are below the sodium outlet temperature. When the power reaches about 5 Kw/m$^2$, the outlet temperature of lead and lead-bismuth exceeds that of sodium, and kept the trend of exceeding. This is because the specific heat capacity of sodium is larger than that of lead and lead-bismuth alloy. Therefore, the temperature rise caused by lead and lead-bismuth is greater when the same heat is absorbed. At lower power, the thermal conductivity is absolutely superior to the specific heat capacity of liquid sodium. As a result, liquid sodium can absorb more heat at the same power, and heat transfer performance is better. Therefore, its outlet temperature is greater than that of lead and lead-bismuth as a whole. When the power is further

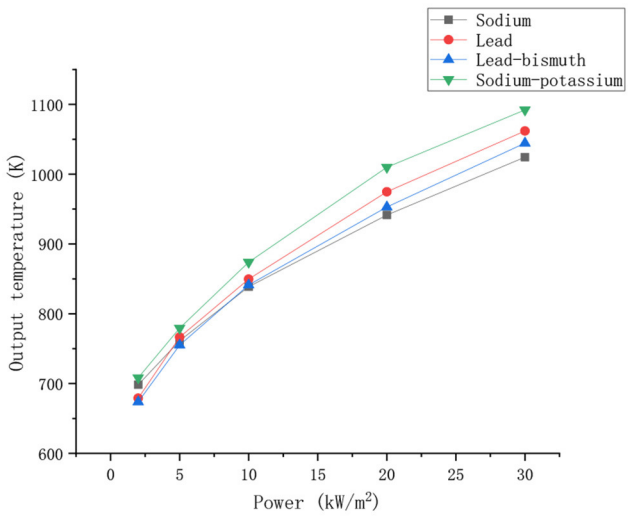


**FIGURE 7 |** Effect of heating power on outlet temperatures of different liquid metals.

increased, the thermal conductivity of sodium decreases with increasing power, the thermal conductivity of lead and lead-bismuth increases with increasing power. So the advantage of the thermal conductivity of sodium is weakened, and the difference of heat transfer performance between sodium and lead, lead-bismuth alloy decreases. At this time, the difference in specific heat capacity occupies a dominant position, which leads to a higher output temperature of lead and lead-bismuth.

## Influence of Pressure on Flow Heat Transfer

The working fluids are liquid sodium, sodium-potassium alloy, lead and lead-bismuth alloy. The preheating section temperature is 620 K, the cooling section temperature is 610 K, the power density is 20 kW/m$^2$, and the values of pressure are 1, 2, 3, 4, and 5 Mpa, respectively. The heat transfer coefficient, mass flow, velocity, and outlet temperature of four liquid metals change with pressure as shown in **Figure 8**.

As can be seen from the **Figure 8**, the heat transfer coefficient of liquid sodium tends to decrease slightly with increasing pressure, while the sodium-potassium alloy, on the other hand, tends to increase. It can be seen from section Influence of Factors on Heat Transfer Coefficient that the heat transfer coefficient of sodium is mainly affected by the power-pressure interaction and the contribution rate is about 32.73%. Therefore, the pressure affects the heat transfer coefficient by coupling with the power. For sodium-potassium alloys, the heat transfer coefficient is affected by the interaction of inlet temperature-pressure. The pressure affects the heat transfer coefficient by coupling with the inlet temperature. For lead and lead-bismuth, there is no interaction between pressure and power or temperature, so its heat transfer coefficients have little change with pressure. In general, the effect of pressure on the heat transfer coefficient of liquid metals is not obvious. The mass flow, velocity, and outlet temperature of the liquid metal are hardly affected by the pressure. At the same pressure, the velocity of sodium-potassium alloy, sodium, lead-bismuth alloy, and lead are successively decreased. The velocity does not change with pressure because the density of the liquid metal is less affected by the pressure. The increase in pressure does not cause a change in the density difference between the hot and cold section. The driving head of the system tends to be stable, so there is no change in the flow velocity of the liquid metal. The influence of pressure on the physical properties of liquid metal is small, so the outlet temperature of different liquid metals tends to be stable.

## Influence of Inlet Temperature on Flow Heat Transfer

The working fluids are liquid sodium, sodium-potassium alloy, lead, and lead-bismuth alloy. The cooling section temperature is 610 K, the power density is 20 kW/m$^2$, and the preheating section temperature is the inlet temperature of the heating section, and the values are 620, 650, 680, 710, and 740 K, respectively. The heat transfer coefficient, mass flow, velocity, and outlet temperature of the four liquid metals vary with the inlet temperature as shown in **Figure 9**.

As can be seen from the **Figure 9**, the heat transfer coefficient of liquid sodium decreases as the inlet temperature increases. The inlet temperature has no effect on the heat transfer coefficient of sodium-potassium alloy, lead, and lead-bismuth. This is mainly because the thermal conductivity of liquid sodium changes significantly with temperature, while the thermal conductivity of sodium-potassium alloys, lead, and lead-bismuth has a smaller trend with temperature. The mass flow, velocity, and outlet temperature of liquid metal increase with the increase of inlet temperature. The density of lead and lead-bismuth alloy is much larger than that of sodium and sodium-potassium alloy, so the increase of mass flow is more obvious than that of the latter. However, the increase in the velocity of sodium-potassium alloy and sodium was slightly greater than that of lead and lead-bismuth alloy. At a certain power, an increase in the inlet temperature of the liquid metal causes an increase in the outlet temperature, which causes the temperature difference between the hot and cold sections to increase. At the same time, it increases the driving force of the system. So the velocity of the liquid metal increases as the inlet temperature increases. The rate of increase of the outlet temperature of lead-bismuth alloy is greater than that of lead. Therefore, when the inlet temperature increases to a certain value, the lead-bismuth outlet temperature is higher than the lead outlet temperature. This is mainly because the specific heat capacity of lead increases as the temperature increases, and the specific heat capacity of lead-bismuth decreases as the temperature increases, so when the same amount of heat is absorbed, the tendency of the temperature increase of the lead-bismuth is more obvious.

## Validation of Simulation Results

Ma et al. (2007) conducted an experimental study on the mass flow and velocity of lead-bismuth natural circulation. The

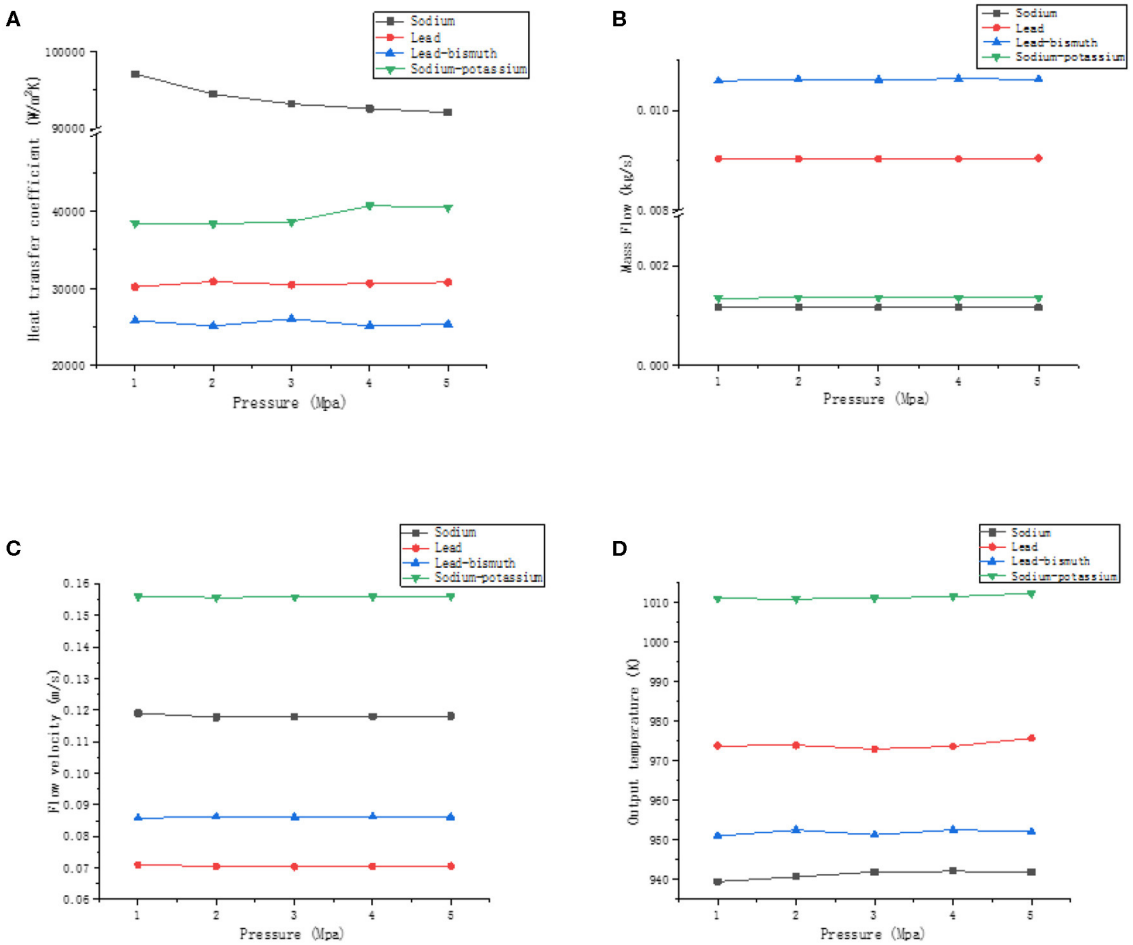


**FIGURE 8 |** The effect of pressure. **(A)** Effect of pressure on the heat transfer coefficient, **(B)** effect of pressure on mass flow, **(C)** effect of pressure on velocity, and **(D)** effect of pressure on outlet temperature.

comparison between simulation results and experimental data is shown in **Figure 10**.

In **Figure 10**, due to the difference in model size between the experiment and the simulation, the mean dimensionless method is used to deal with temperature difference, mass flow and flow velocity. $\Delta T$ is the temperature difference between the hot and cold section, $\Delta T_{ave}$ is the average temperature difference, W is the mass flow, $W_{ave}$ is the average mass flow, U is the flow velocity, and $U_{ave}$ is the average flow velocity. The calculated data are compared with the experimental data by dimensionless method. The variation trend of experimental and simulation results is basically the same, so the adaptability of the established simulation model can be determined.

## FACTORIAL ANALYSIS

### Effect of Interaction on Heat Transfer Coefficient

By using the method of factor analysis, the interaction between the factors is analyzed. The effect of the interaction on the heat transfer coefficients of different liquid metals is shown in **Figure 11**.

It can be seen from **Figure 11** that the interaction of factors on the natural cycle heat transfer coefficient of liquid metal. When the effect of one factor changes with other factors, and the difference between them exceeds the range of random fluctuations, the interaction between them is indicated. In **Figure 11**, if the two lines intersect, it indicates that there is an interaction between the two factors; if the two lines are nearly parallel, it implies that the interaction between the two factors can be ignored. Among the factors affecting the heat transfer coefficient of liquid sodium, there is an interaction between power and pressure. Among the factors affecting the heat transfer coefficient of sodium-potassium alloys, there is an interaction between pressure and inlet temperature. There is no interaction between the factors influencing the heat transfer coefficient of liquid lead. For the factors affecting the heat transfer coefficient of lead-bismuth, there is an interaction between power and inlet temperature; while for power and pressure, although the two straight lines have a certain inclination, they are nearly

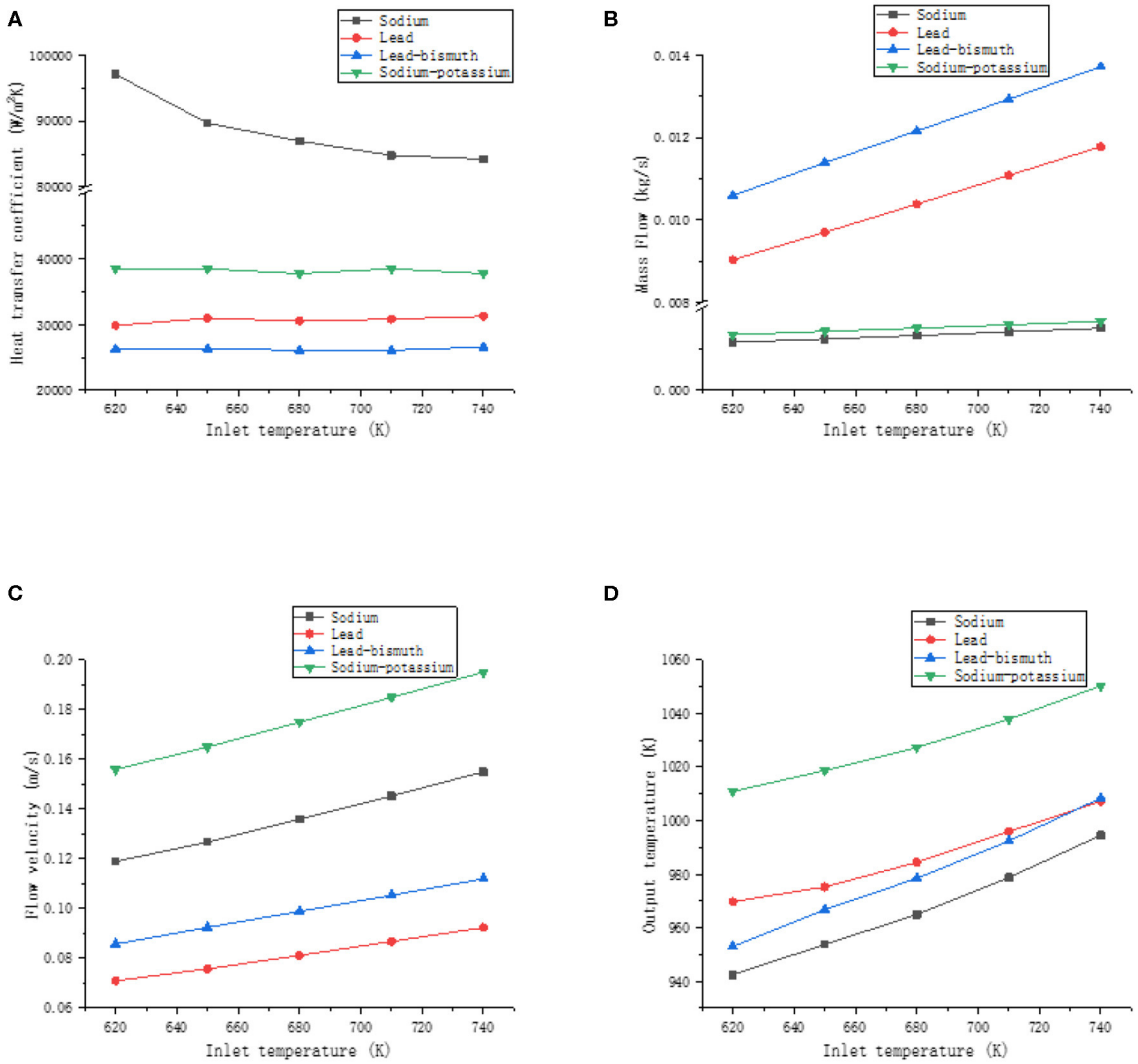


**FIGURE 9 |** The effect of inlet temperature. **(A)** Effect of inlet temperature on heat transfer coefficient, **(B)** effect of inlet temperature on mass flow, **(C)** effect of inlet temperature on flow velocity, and **(D)** effect of inlet temperature on outlet temperature.

parallel, and it can be seen that the interaction is small and can be ignored.

## Influence of Factors on Heat Transfer Coefficient

By substituting the calculation data in section Calculation Results into formulas (1)–(3), the estimated effect and interaction among factors can be obtained. The semi-normal probability of the effect of heat transfer coefficient is shown in **Figure 12**.

In **Figure 12**, the negligible effect is normally distributed and will generally fall near a line on the graph. The effect farther from the straight line indicates that the factor is statistically significant and has the greatest influence on the heat transfer coefficient. The effect percentage contribution rate is obtained by the ratio of the sum of the squares of the effects to the total sum of squares, indicating the degree of dependence between the influencing factors and the heat transfer coefficient. For liquid sodium, except for the effect A, effect AB, and effect C, other effects are negligible. Effect A deviates furthest from the line, indicating that it has the greatest influence on the heat transfer coefficient, and its contribution rate is about 40.16%; the contribution rate of effect AB is about 32.73%, indicating that there is interaction between power and pressure; the contribution rate of effect C is about 6.79%. For sodium-potassium alloy, effect A has the greatest influence on heat transfer coefficient, and the contribution rate is about 78.16%; the contribution rate of effect BC to heat transfer coefficient is about 7.70%, which indicates that there is interaction between pressure and inlet temperature; other effects are negligible for sodium—potassium alloys. For liquid lead, except for effect A, other effects are negligible, and the contribution rate of effect A to the heat transfer coefficient is about 97.95%. For lead-bismuth alloys, the

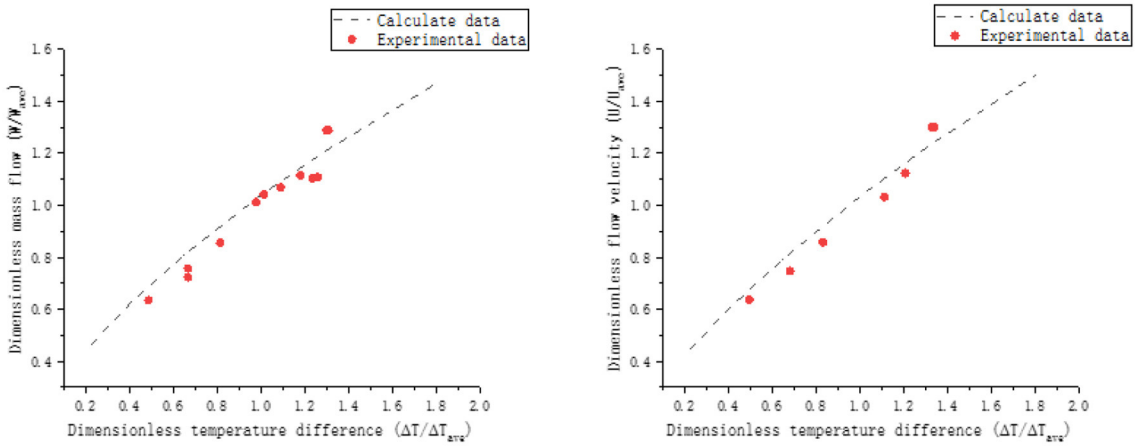


**FIGURE 10 |** Comparison of experimental and simulation results.

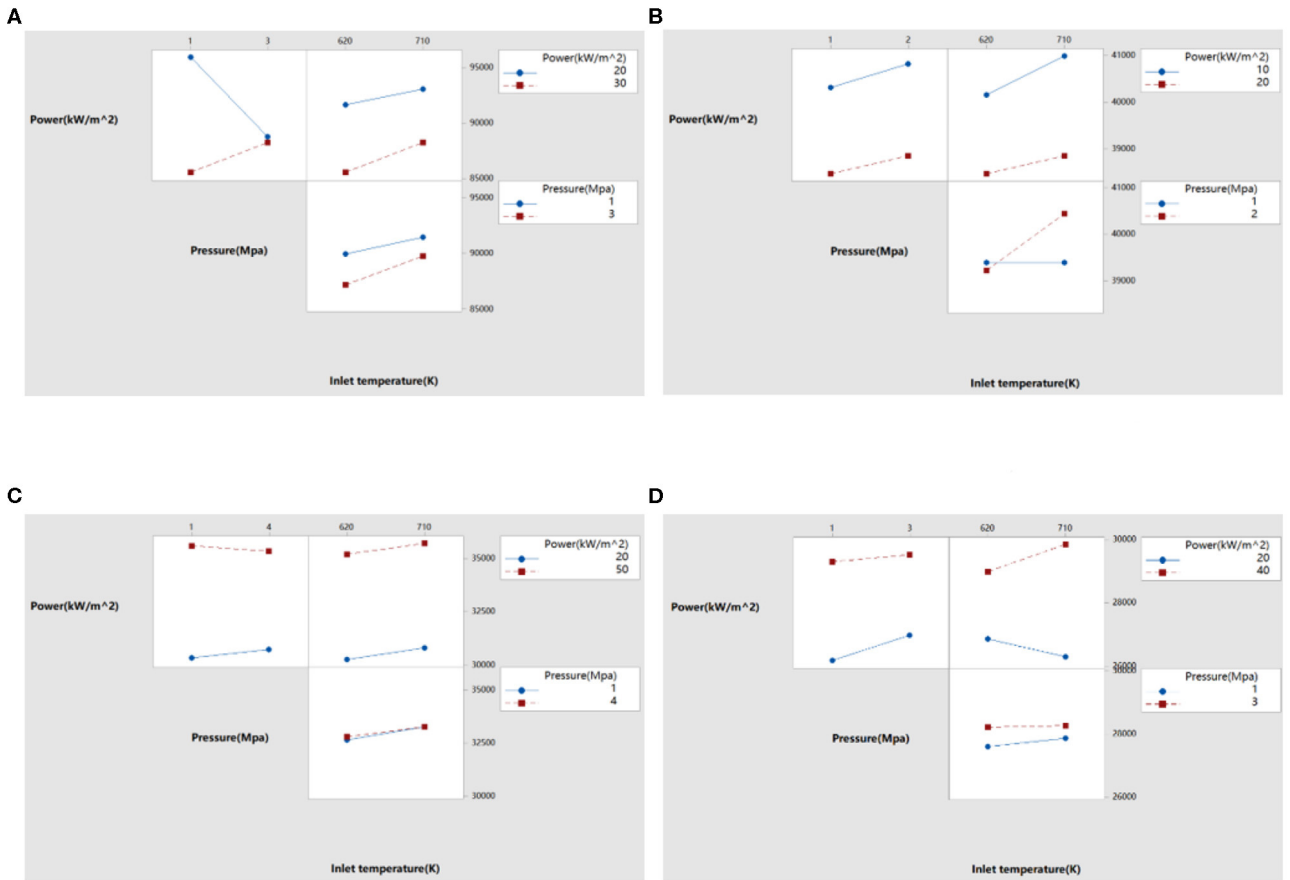


**FIGURE 11 |** Effect of interaction on heat transfer coefficients of different liquid metals. **(A)** Effect on heat transfer coefficient of sodium, **(B)** effect on heat transfer coefficient of sodium-potassium alloy, **(C)** effect on heat transfer coefficient of lead, and **(D)** effect on heat transfer coefficient of lead-bismuth.

contribution rate of effect A is about 92.19%; the contribution rate of effect AC is about 5.62%, so there is an interaction between power and inlet temperature; other effects are negligible for lead-bismuth alloys.

## CONCLUSION

The flow and heat transfer of liquid metal natural circulation was numerically simulated by CFX. The influencing factors were

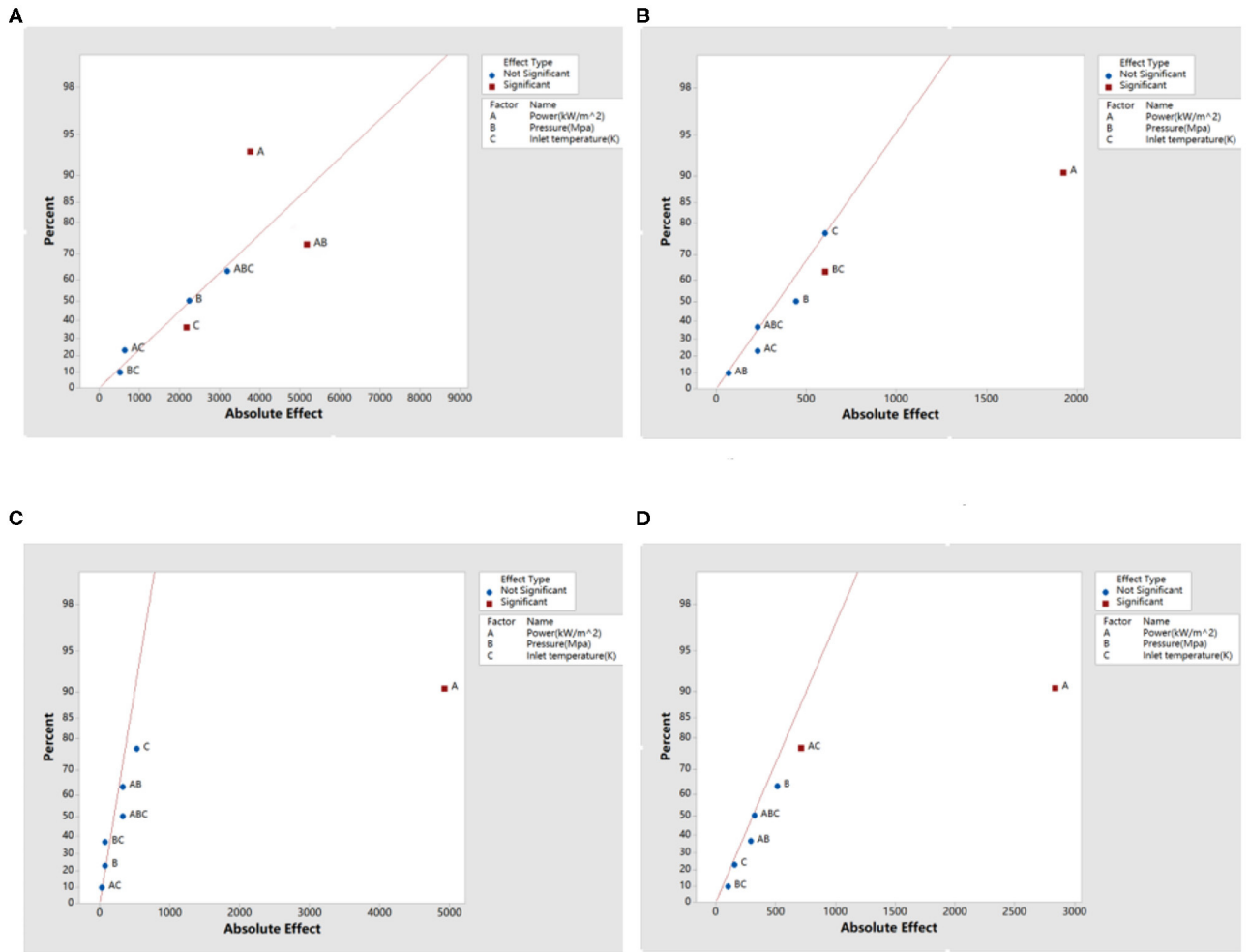


**FIGURE 12 |** Semi-normal probability of the effect of heat transfer coefficient. **(A)** Effect of heat transfer coefficient of sodium, **(B)** effect of heat transfer coefficient of sodium-potassium alloy, **(C)** effect of heat transfer coefficient of lead, and **(D)** effect of heat transfer coefficient of lead-bismuth.

compared by using factor analysis. The effects of power, pressure, and inlet temperature on the heat transfer coefficient of liquid metal were obtained.

(1) The heat transfer coefficient of liquid sodium decreases with the increase of power, while the heat transfer coefficient of liquid lead and lead-bismuth increases with the increase of power, and the heat transfer coefficient of sodium-potassium alloy increases first and then decreases with the increase of power. Under the same conditions, sodium has the best heat transfer performance, and its heat transfer coefficient is much larger than that of the other three liquid metals. The sodium-potassium alloy has the strongest natural circulation ability, and its flow velocity is higher than other liquid metals.

(2) The flow rate and outlet temperature of liquid metal are hardly affected by pressure. The heat transfer coefficient of liquid sodium and sodium-potassium alloy is affected by pressure. The heat transfer coefficient of sodium is affected by the power-pressure interaction and the contribution rate is about 32.73%. Therefore, the pressure affects the heat transfer coefficient by coupling with the power. For sodium-potassium alloys, the pressure affects the heat transfer coefficient by coupling with the inlet temperature. For lead and lead-bismuth alloy, there is no interaction between pressure and power or temperature, so their heat transfer coefficients have little change with pressure.

(3) For the heat transfer coefficient of four liquid metals, the power is the factor that contributes the most. The contribution rate of power to the heat transfer coefficients of liquid sodium, sodium-potassium alloy, lead and lead-bismuth alloy reached 40.16, 78.16, 97.95, and 92.19%, respectively. In addition to lead, the heat transfer coefficients of sodium, sodium-potassium alloy, and lead-bismuth alloy are affected by the interaction between the factors. Therefore,

in improving the heat transfer coefficient of sodium, sodium-potassium alloy, and lead-bismuth alloy, it is not possible to simply analyze the influence of one of the factors, and it is necessary to comprehensively consider the coupling between the factors.

## DATA AVAILABILITY STATEMENT

All datasets generated for this study are included in the article/supplementary material.

## AUTHOR CONTRIBUTIONS

All authors listed have made a substantial, direct and intellectual contribution to the work, and approved it for publication.

## FUNDING

This project was supported by Natural Science Foundation of Beijing Municipality (3172032).

## REFERENCES

Borgohain, A., Maheshwari, N. K., and Vijayan, P. K. (2016). Natural circulation experiments in a non-uniform diameter lead bismuth loop and validation of LeBENC code. *Progress Nuclear Energy* 91, 68–82. doi: 10.1016/j.pnucene.2016.03.005

Chang, W. P., and Hahn, D. (2002). "Development of sodium two phase flow model for Kalimer core analysis," in *International Conference on Nuclear Engineering* (Washington, DC: American Society of Mechanical Engineers), 333–341.

Duncan, J. D. (1988). SBWR, a simplified boiling water reactor. *Nuclear Eng. Design.* 109, 73–77. doi: 10.1016/0029-5493(88)90143-4

Gaiying, W., Qing, B., Sheng, G., Min, Z., and Qunying H. (2012). Preliminary study on liquid lead bismuth oxygen concentration measurement technology. *Nuclear Sci. Eng.* 32, 165–169. doi: 10.3969/j.issn.0258-0918.2012.02.012

Gao, Y., Takahashi, M., and Nomura, M. (2015). Experimental study on diffusion of Ni in lead-bismuth eutectic (LBE). *Energy Proc.* 71, 313–319. doi: 10.1016/j.egypro.2014.11.884

Hashim, M., Yoshikawa, H., Matsuoka, T., and Yang, M. (2014). Quantitative dynamic reliability evaluation of AP1000 passive safety systems by using FMEA and GO-FLOW methodology. *J. Nuclear Sci. Technol.* 51, 526–542. doi: 10.1080/00223131.2014.881727

Jingjing, L., Tao, Z., Qijun, H., and Zejun, X. (2014). Study on the stability of supercritical water natural circulation flow based on factorial analysis. *Nuclear Power Eng.* 35, 66–69. doi: 10.13832/j.jnpe.2014.05.0066

Liu, X. (2015). Analysis of the construction of overseas land model reactors and their contribution to the development of nuclear power equipment for ships. *Chin. Ship Res.* 10, 84–91. doi: 10.3969/j.issn.1673-3185.2015.03.014

Ma, D., Zhou, T., Chen, J., Qi, S., Shahzad, M. A., and Xiao, Z. (2017). Supercritical water heat transfer coefficient prediction analysis based on BP neural network. *Nuclear Eng. Des.* 320, 400–408. doi: 10.1016/j.nucengdes.2017.06.013

Ma, W., Karbojian, A., and Sehgal, B. R. (2007). Experimental study on natural circulation and its stability in a heavy liquid metal loop. *Nuclear Eng. Design* 237, 1838–1847. doi: 10.1016/j.nucengdes.2007.02.023

Tarantino, M., Grandis, S. D., Benamati, G., and Oriolo, F. (2008). Natural circulation in a liquid metal one-dimensional loop. *J. Nuclear Mater.* 376, 409–414. doi: 10.1016/j.jnucmat.2008.02.080

Wang, L., Chen, P., Zhou, Y., Li, W., Tang, C., Miao, Y., et al. (2018). Experimental study on the condensation of steam with air out of the vertical tube bundles. *Front. Energy Res.* 6:32. doi: 10.3389/fenrg.2018.00032

Watanabe, O., Oyama, K., Endo, J., Doda, N., Ono, A., Kamide, H., et al. (2015). Development of an evaluation methodology for the natural circulation decay heat removal system in a sodium cooled fast reactor. *J. Nuclear Sci. Technol.* 52, 1102–1121. doi: 10.1080/00223131.2014.994049

Qiu, Z., Lan, Z., Ma, Z., Qiu, S., Zan Y., Xing D., et al. (2016). Theoretical study on heat transfer characteristics of liquid metal sodium boiling two-phase flow. *Nuclear Power Eng.* 37, 124–127. doi: 10.13832/j.jnpe.2016.S2.0121

Yagov, V. V., Zubov, N. O., Kaban'kov, O. N., and Sukomel, L. A. (2019). Experimental and calculated investigation of a natural circulation loop's thermal-hydraulic characteristics. *Thermal Eng.* 66, 477–490. doi: 10.1134/S0040601519070103

**Conflict of Interest:** The authors declare that the research was conducted in the absence of any commercial or financial relationships that could be construed as a potential conflict of interest.

frontiers in Energy Research

ORIGINAL RESEARCH
published: 08 October 2020
doi: 10.3389/fenrg.2020.521233

# A Critical Flow Model for Supercritical Pressures

*Yufeng Lv*, Minfu Zhao and Kaiwen Du*

*China Institute of Atomic Energy, Beijing, China*

The investigation of critical flow model for supercritical pressure condition is relatively rare. Based on isentropic flow and thermal equilibrium assumptions, a model is derived to calculate discharge flow rate and critical pressure. Considering the influence of friction and local resistance, a correction coefficient is added which can be calculated from CFX analysis software. The model avoids the calculation of quality and is applicable to wide range which covering the subcooled water, two-phase mixture, steam critical flow under subcritical pressure and supercritical pressure. Reasonable agreement is shown between model predicted results and experiment data, illustrating the accuracy of the proposed model.

**Keywords: critical flow, supercritical water cooled reactor, loss of coolant accident, thermal equilibrium effect, resistance coefficient**

OPEN ACCESS

***Edited by:***
*Jun Wang,*
*University of Wisconsin–Madison,*
*United States*

***Reviewed by:***
*Jinbiao Xiong,*
*Shanghai Jiao Tong University, China*
*Keyou S. Mao,*
*Oak Ridge National Laboratory (DOE),*
*United States*
*Cheng Liu,*
*University of Wisconsin–Madison,*
*United States*

****Correspondence:***
*Yufeng Lv*
*nuclear15@163.com*

***Specialty section:***
*This article was submitted to Nuclear Energy, a section of the journal Frontiers in Energy Research*

***Received:*** *18 December 2019*
***Accepted:*** *14 September 2020*
***Published:*** *08 October 2020*

***Citation:***
*Lv Y, Zhao M and Du K (2020) A Critical Flow Model for Supercritical Pressures. Front. Energy Res. 8:521233. doi: 10.3389/fenrg.2020.521233*

## INTRODUCTION

During a postulated loss of coolant accident of a pressurized water reactor, the critical flow occurs at the break. An accurate estimation of the critical flow rate is very important for the evaluation of reactor safety, because the critical flowrate controls heat transfer in the core and the rate of system depressurization, thus has a significant effect on the accident consequence. The loss of coolant accident is particularly of a concern for the supercritical water cooled reactor reactor safety, because the coolant inventory in supercritical water cooled reactor is much smaller than that in the current pressurized water reactor for same power output, and thus the transient response of the reactor would be dominated by the discharge flow rate more strongly.

Under subcritical pressures, various theoretical models to predict discharge flowrates have been advanced, such as homogeneous equilibrium model (HEM) (Starkman et al., 1964), hydrodynamic non-homogenous model (Fauske, 1962; Moody, 1965), and thermal non-equilibrium model (Henry and Fauske, 1971; Richter, 1983). Still more elaborate mechanistic models have been recently developed which can account for both thermal and hydrodynamic non-equilibrium between phases (Richter, 1983; Dobran, 1987). Although still poorly understood, mechanistic models that attempt to follow the nucleation and growth of the vapor bubbles require specification of initial conditions at the onset of flashing. Abdollahian (1982) did comprehensive and excellent reviews on the existing models. Many researchers adopt HEM model or modified HEM model to predict the critical flow rate under supercritical pressure. Guillaume Mignot et al. (2008) found that the HEM model predicts higher than United Kingdom Atomic Energy Authority experimental data due to the isentropic flow assumption. Chen et al. (2012) considered the local resistance effect and proposed a modified HEM which showed good agreement in the region of near and beyond pseudo-critical temperature. For the inlet temperature well below the pseudo-critical point, Bernoulli equation gave an upper envelope of the test data. He suggested that from the reactor safety point of view the combination of the HEM with Bernoulli equation gave a conservative estimation for the break discharge flow rate. But there exists discontinuity at the intersection of the two models.

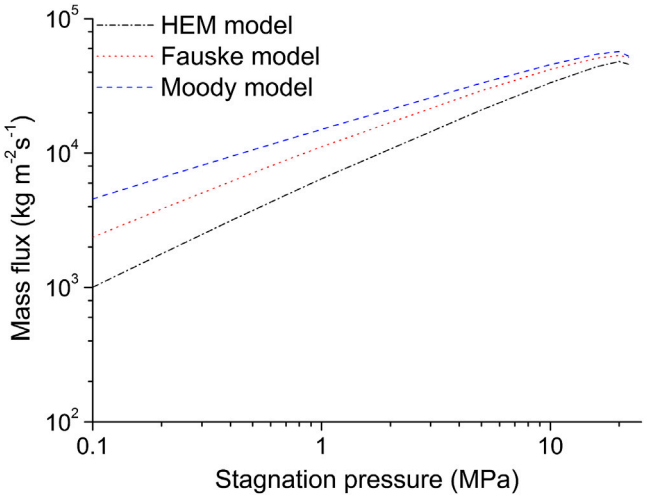


**FIGURE 1 |** Variation of mass flux with stagnation pressure for saturated water.

In the present study, we focus on conducting a more general critical flow model which can be applicable for inlet temperature well below the pseudo-critical point and temperature beyond the pseudo-critical point under supercritical pressure. First, the hydrodynamic non-homogeneous and thermal non-equilibrium have been proved having little effect on critical flow rate and a model is put forward based on isentropic flow and thermal equilibrium assumptions. Then considering the local resistance and friction, an empirical coefficient $C$ which can be obtained through the Computational Fluid Dynamics (CFD) simulation is added to the model. The model accuracy is validated by supercritical water blowdown test data conducted by the United Kingdom Atomic Energy Authority and China Institute of Atomic Energy (CIAE).

## THERMAL AND HYDRODYNAMIC NON-EQUILIBRIUM EFFECT

Usually slip ratio is introduced to account for the two phase relative motion effect, which is defined as the ratio of gas velocity to liquid velocity. Fauske (1962) led the field in developing a model which allows for hydrodynamic effects. For critical flow, the slip ratio at the critical location is given by $S = (v_g/v_l)^{1/2}$ and the critical mass flux subject to $G_c^2 = -(\partial p/\partial v_m)$, both isentropic and isenthalpic processes were considered. Moody (1965) developed a critical flow model starting from the continuity and energy equations. The slip ratio is determined by maximizing the kinetic energy flow rate and is expressed as $S = (v_g/v_l)^{1/3}$.

The HEM model, Fauske model and Moody model are adopted to calculate the critical mass flux for saturated water flowing in nozzles under different stagnation pressures (0.1–20 MPa). The nozzle outlet pressure (critical pressure) is calculated accordingly for different models. The value of outlet pressure may be different for each model, but the main principle is the mass flux reaches a maximum value at the critical pressure. The comparison for different models is shown in **Figure 1** and **Table 1**. It can be seen that, at lower pressure, the slip ratio has great effect on critical mass flux; but at higher pressure, the slip ratio effect decreases. For example, when stagnation pressure is 22 MPa, the mass flux calculated by Moody model is 52,700 kg m$^{-2}$ s$^{-1}$ and the mass flux calculated by HEM model is 45,892kg m$^{-2}$ s$^{-1}$, the deviation is only 12.9%. Therefore, it is concluded that under supercritical pressures, the hydrodynamic effect is small and can be neglected.

Thermal non-equilibrium decreases as pressure increasing, and in the region of supercritical pressure the thermal equilibrium is dominant (Chen et al., 2008; Chen et al., 2009). This trend is reasonable, because higher pressure corresponds to higher vapor density and thermal conductivity and smaller droplet, associated with more efficient interfacial heat exchange. Same finding was achieved in the similar experiments of supercritical water (Lee and Swinnerton, 1983) and $CO_2$ (Mignot et al., 2008).

## THE PRESENT MODEL

### Model Derivation

Based on the above discussion, the thermal equilibrium and hydrodynamic homogeneous effect is dominant for critical flow under supercritical pressure. Therefore, in the model developed here, the following assumptions are made:

(1) Steady-state flow.
(2) The friction effect is ignored and the flow is considered isentropic.
(3) The vapor phase and liquid phase are in thermal equilibrium state.
(4) Liquid and vapor velocity are the same.
(5) The flow is considered to be one-dimensional.

The mass flux at the nozzle outlet is defined as:

$$G = \rho_e u_e \tag{1}$$

**TABLE 1 |** Comparison of critical mass flux with homogeneous equilibrium model, Fauske model and Moody model.

| Mass flux (kg m$^{-2}$ s$^{-1}$) | $p_0$ | | | | | | | | | | |
|---|---|---|---|---|---|---|---|---|---|---|---|
| | 0.1 | 0.2 | 0.4 | 0.7 | 0.9 | 1 | 5 | 10 | 16 | 20 | 22 |
| G-Homogeneous equilibrium model | 1,004 | 1779 | 3,135 | 4,878 | 5,937 | 6,441 | 20,941 | 33,385 | 43,999 | 48,122 | 45,892 |
| G-Fauske | 2,367 | 3,837 | 6,130 | 8,852 | 10,405 | 11,128 | 29,219 | 41,936 | 50,911 | 53,351 | 51,547 |
| G-Moody | 4,563 | 6,573 | 9,412 | 12,526 | 14,225 | 15,002 | 33,138 | 45,503 | 54,580 | 56,992 | 52,700 |

where $\rho_e$ is the fluid density at the nozzle outlet, is the velocity at the nozzle outlet.

Because it is assumed that there is no heat exchange between fluid and environment, and the energy equation is simplified as:

$$h_1 + \frac{u_1^2}{2} = h_2 + \frac{u_2^2}{2} = \text{Constant} \tag{2}$$

As the nozzle upstream stagnation velocity is zero, the relationship between inlet stagnation enthalpy and outlet enthalpy can be expressed as follows:

$$h_0 = h_e + \frac{u_e^2}{2} \tag{3}$$

Because the friction effect is ignored, the outlet velocity can be obtained by energy conservation equation:

$$u_e = \sqrt{2(h_0 - h_e)} \tag{4}$$

Substituting **Eq. 4** to **Eq. 1**, the outlet mass flow rate can be obtained:

$$G = \rho_e\sqrt{2(h_0 - h_e)} = \rho(p_e, s_0)\sqrt{2[h_0 - h(p_e, s_0)]} \tag{5}$$

where $h_0$ is the specific enthalpy at the nozzle inlet, $s_0$ is the specific entropy at the nozzle inlet, $h_e$ is the specific enthalpy at the nozzle outlet, $p_e$ is the nozzle outlet pressure.

For ideal gas and superheated vapor, the relationship between inlet density, outlet density, inlet pressure and outlet pressure can be expressed as:

$$p_0\left(\frac{1}{\rho_0}\right)^k = p_e\left(\frac{1}{\rho_e}\right)^k, \quad p_e = p_0\beta_{cr} = p_0\left(\frac{2}{k+1}\right)^{\frac{k}{k-1}} \tag{6}$$

The following expression can be obtained:

$$\rho_e = \rho_0\left(\frac{2}{k+1}\right)^{\frac{1}{k-1}} \tag{7}$$

$$u_e = \sqrt{2(h_0 - h_2)} = \sqrt{2c_p(T_0 - T_2)} = \sqrt{2\frac{k}{k-1}R_g(T_0 - T_2)}$$

$$= \sqrt{2\frac{k}{k-1}R_gT_0\left[1 - \left(\frac{P_2}{P_0}\right)^{\frac{k-1}{k}}\right]} = \sqrt{2\frac{k}{k-1}\frac{p_0}{\rho_0}\left[1 - \left(\frac{p_2}{p_0}\right)^{\frac{k-1}{k}}\right]} \tag{8}$$

$$= \sqrt{\frac{2k}{k+1}\frac{p_0}{\rho_0}}$$

By substituting **Eqs 7** and **8** to **Eq. 1**, the mass flux can be evaluated as:

$$G = \sqrt{kp_0\rho_0\left(\frac{2}{k+1}\right)^{\frac{k+1}{k-1}}} \tag{9}$$

**Equation 9** is exactly the same with the critical flow equation in gas dynamics. In other words, the proposed critical flow model is applicable to critical flow for ideal gas and superheated vapor.

For room temperature water, the density $\rho$ is almost constant, combining the definition of entropy, during the isentropic process, we can obtain:

$$ds = \frac{dh}{T} - \frac{1}{\rho T}dp = 0 \Rightarrow dh = \frac{1}{\rho}dp \Rightarrow h_0 - h_e = \frac{p_0 - p_e}{\rho} \tag{10}$$

Thus, **Eq. 5** may be simplified to:

$$G = \rho_e\sqrt{2(h_0 - h_e)} = \sqrt{2\rho^2\left(\frac{p_0 - p_e}{\rho}\right)} = \sqrt{2\rho(p_0 - p_e)} \tag{11}$$

**Equation 11** is identical to the Bernoulli Equation, where the back pressure equals the atmosphere pressure. It can be concluded that **Eq. 8** is a general model which is applicable to both subcooled water and superheated steam.

Based on isentropic assumptions with thermal equilibrium and equal velocities of two-phases, a HEM model (Starkman et al., 1964) was proposed as follows,

$$G = \frac{\left\{2\left[h_0 - (1-x)h_l - xh_g\right]\right\}^{\frac{1}{2}}}{(1-x)/\rho_l + x/\rho_g} \tag{12}$$

where $h$ is the enthalpy, $\rho$ is density, $x$ the equilibrium quality at the critical plane, and the subscripts $l$ and $g$ refer to the liquid and vapor, respectively, and 0 the stagnation (inlet) condition.

In fact, the current model **Eq. 5** may be converted to **Eq. 12** by substituting $\rho$ and $h(p_e, s_0)$ in the two-phase expression.

Considering the actual discharge flow is not isentropic due to the friction and local resistance effect, Chen et al. (2012) modified the HEM model as

$$G = \left[\frac{2\left(h_0 - (1-x)h_l - xh_g\right)}{\frac{C}{\bar{\rho}^2} + \left(\frac{1-x}{\rho_l} + \frac{x}{\rho_g}\right)^2}\right]^{\frac{1}{2}} \tag{13}$$

where $C$ is the local resistance factor, and $\bar{\rho}$ the average density at the inlet.

Similarly, taking the friction and local resistance effect into account, a resistance factor $C$ is multiplied to **Eq. 5** and it becomes:

$$G = C\rho(p_e, s_0)\sqrt{2(h_0 - h(p_e, s_0))} \tag{14}$$

## Calculation of Resistance Factor *C*

Usually, an empirical coefficient $C$ is used for the critical mass flux calculation. For example, in Chen's previous work, different empirical coefficients are used in the modified HEM model: for sharp-edge nozzle (nozzle A), the recommended $C$ is 0.6; for round-edge nozzle (nozzle B), $C = 0.4$. But the choice of $C$ is totally empirical and based on the user's experience. Actually, the resistance factor $C$ is not only affected by nozzle inlet geometry, but also related with nozzle length and fluid state.

In this section, a method of using the CFD software to calculate resistance factor is proposed. The commercial CFD code ANSYS CFX 14.0 is employed. To illustrate the analysis method to calculate resistance factor $C$, the nozzle configuration employed is a round-edge nozzle taken from literature (Chen et al., 2012), as shown in **Figure 2**.

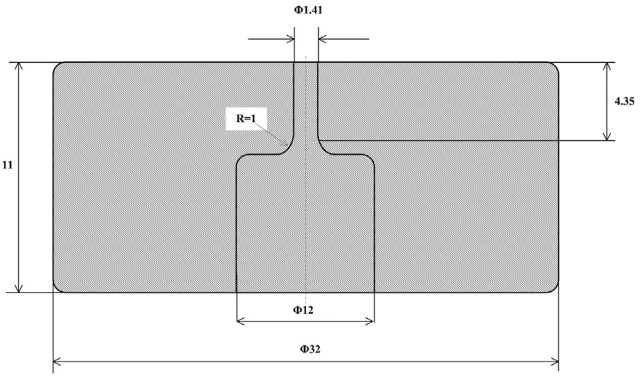


**FIGURE 2 |** Schematic of nozzle A in literature (Chen et al., 2012).

The test section adopts high pressure lens pad orifice, and is fitted onto the main loop through threaded flange. To ensure the accuracy and reproducibility of the test, the finishing process is used and the tolerance of the nozzle diameter is 2 μm. The schematic diagram is shown in **Figure 2**. The total length of the test section is 11 mm, the outer and inner diameter of the lens pad orifice is 32 and 12 mm, respectively. The diameter of the nozzle is 1.41 mm and the length of the nozzle is 4.35 mm with rounded edge inlet, the radius of which is 1.0 mm.

The involved problem is room temperature water flowing through the nozzle. The region inside the nozzle is chosen as the numerical analysis region. The inlet of analysis region is set as Pressure Inlet at which the pressure, temperature are specified. The outlet is set as the Pressure Outlet with relative pressure 0 Pa. In this simulation, the initial pressure $p_0$ = 25 MPa, initial temperature $T_0$ = 20°C, and the standard $k$–$\varepsilon$ model is employed. Then the mass flux $G$ can be calculated by the simulation, thus the resistance factor $C$ can be calculated by the following expression:

$$C = \frac{G}{\sqrt{2\rho(p_0 - p_e)}} \tag{15}$$

where $G$ is the mass flux calculated by CFX, $\rho$ is fluid density, $p_0$ is initial pressure, $p_e$ is the atmosphere pressure.

For example, for supercritical water of initial pressure $p_0$ = 25 MPa, initial temperature $T_0$ = 20°C flowing in a round-edge nozzle (Nozzle A), the geometry of which is chosen from literature (Chen et al., 2012), as shown in **Figure 2**. The calculated mass flux is 175,000 kg m$^{-2}$ s$^{-1}$), substituting the value into **Eq. 15**, the resistance factor can be obtained. For this case, the resistance factor $C$ equals 0.8.

For a given upstream condition and nozzle of certain geometry, the calculation procedure of the present model is as following:

Firstly, set a series of outlet pressure $p_e$ which decreases from stagnation pressure $p_0$ to atmosphere pressure at a constant interval, for example, 0.1 MPa, then the corresponding density $\rho$ and enthalpy $h$ can be obtained by water physical property lookup software. Secondly, using the CFD software to calculate the coefficient $C$ based on the actual nozzle geometry. Thirdly, using **Eq. 6** the corresponding mass flux can be calculated. It should be noted that the calculated mass flux first increases and then decreases as the outlet pressure decreases, and the maximum mass flux is the critical mass flux and the corresponding pressure is the critical pressure.

# VERIFICATION OF THE MODEL

## Supercritical Pressure Condition

The supercritical pressure critical flow experiment performed by Chen et al. (2012) adopts nozzle of 1.41 mm in diameter and 4.35 mm in length with rounded-edge, with inlet pressure range of 22.1–31 MPa, subcooling range of −88–82°C. Under supercritical pressures, the subcooling is defined as the

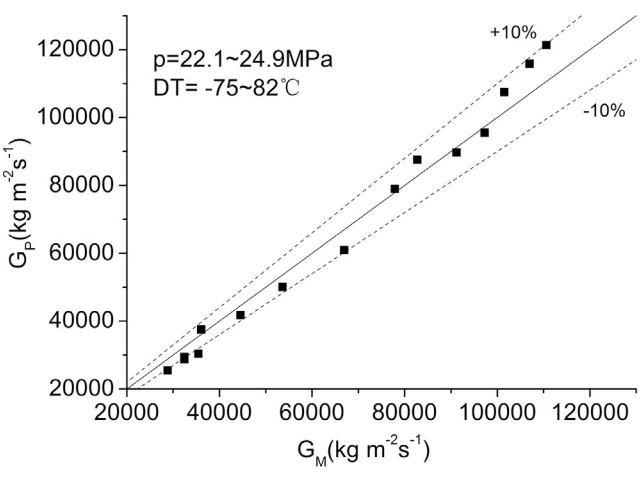


**FIGURE 3 |** Comparison to the result of Chen ($p$ = 22.1–24.9 MPa).

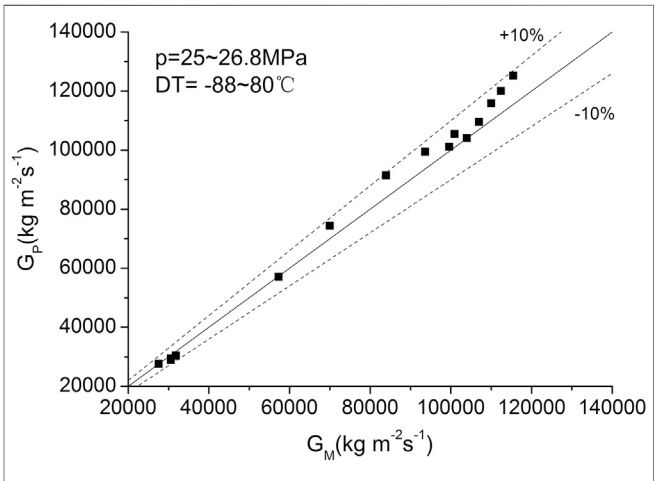


**FIGURE 4 |** Comparison to the result of Chen ($p$ = 25–26.8 MPa).

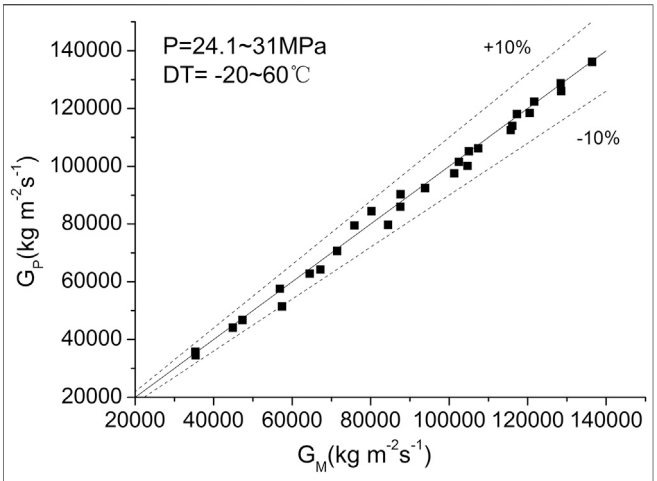


**FIGURE 5 |** Comparison to the result of Lee and Swinnerton.

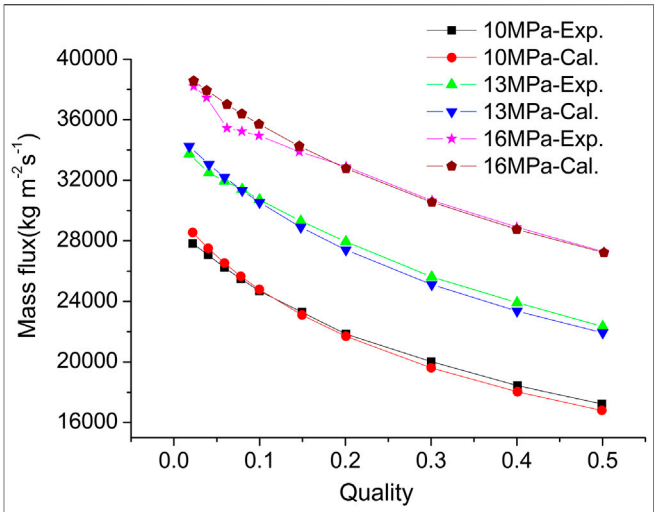


**FIGURE 7 |** Comparison of model prediction with experiment data (saturated condition).

pseudo-critical temperature corresponding to the nozzle inlet pressure minus the inlet temperature ($DT_{pc} = T_{pc} - T_{in}$). The pseudo-critical temperature, $T_{pc}$, is evaluated by the following expressions in ℃ (Lee and Swinnerton, 1983):

$$T_{pc} = \begin{cases} 3.0p + 307.6 & 22.1\ \text{MPa} < p < 24.1\ \text{MPa} \\ 3.767p + 289.0 & 24.1\ \text{MPa} < p < 31.0\ \text{MPa} \end{cases} \quad (16)$$

**Figure 3** shows the comparison between the present correlation with the test data for inlet pressure of 22.1–24.9 MPa, subcooling of −75–82°C. In the calculation, the initial pressure is set as 23 MPa for convenience. According to the calculation method of resistance coefficient in "Calculation of Resistance Factor *C*" section, the coefficient *C* is chosen as 0.8. As can be seen, the model gives the agreement basically within ±10%.

**Figure 4** shows the comparison between the present model with test data for inlet pressure of 25–26.8 MPa, subcooling of −88–80°C. The initial pressure is set as 26 MPa and the resistance factor remains unchanged. The calculated mass flux matches with the test data within 10% relative error.

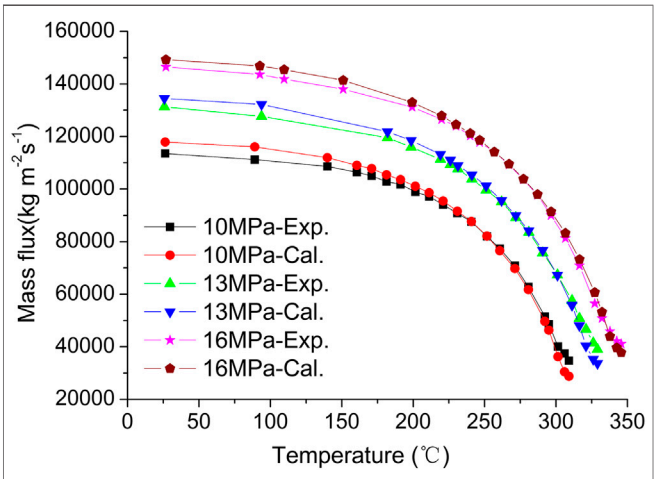


**FIGURE 6 |** Comparison of model prediction with experiment data (subcooled condition).

The critical flow experimental data of supercritical water were obtained by Lee and Swinnerton (1983) with four different nozzle test sections. In this study, test data of nozzle B is used to validate the proposed critical flow model. The nozzle diameter is 1.78 mm, length to diameter is 3, the range of inlet pressure is of 24.1–31 MPa, and the range of subcooling is of −20–60°C. The resistance coefficient is 0.9 in this calculation. The comparison of model predicted mass flux and measured data is shown in **Figure 5**. It can be concluded that calculated mass flux and experimental results agree within 10% of relative error, which validates the accuracy of the proposed model.

## Subcritical Pressure Condition

CIAE has conducted a series of steady state critical flow tests with long nozzle, the diameter of which is 2 mm and the length of which is 40 mm, the test parameter covers a wide range: initial temperature ranges from 20 to 350°C, inlet quality ranges from 0.0 to 0.5, the upstream pressure is 10, 13, and 16 MPa, respectively (Zhao et al., 2015). According to the CFD calculation, choose the resistance coefficient $C$ = 0.82 for subcooled condition and $C$ = 0.9 for the saturated condition. The results are displayed in **Figures 6** and **7**. As can be observed, the model predicted results and long nozzle experiment results are in good agreement.

It can be seen from **Figure 6** that at low temperature, the calculated mass flux is a bit higher than the measured data; while at high temperature, especially near the saturation temperature region, the calculated mass flux is lower than the test data. The error is closely related to the value of resistance coefficient *C*. In the current model, $C$ = 0.82 is obtained at the room temperature condition ($T_{in}$ = 20°C) and this value is used for all the subcooled region condition. Considering the error in numerical simulation, the

calculated mass flux is a little higher than the measured value for the low temperature region and the maximum error between model prediction with test data is within 5%. As mentioned above, $C = 0.9$ is chosen for saturated region and this value is obtained for the saturated vapor condition. Therefore, there is a discontinuity between subcooled condition and saturated condition. Essentially, the resistance coefficient $C$ should gradually increase from 0.82 to 0.9 for the transition from subcooled condition to saturated condition. This is why the calculated mass flux is lower than the test data for the near saturated condition. Caution is needed for the calculation of critical mass flux near saturated condition.

It should be mentioned that the current model is derived with the thermal equilibrium assumption, and is not applicable for two-phase critical flow condition where thermal non-equilibrium effect is dominant. For instance, inlet water with low subcooling or low quality and flowing through short nozzle condition. It is suggested that critical flow model considering thermal non-equilibrium effect is used in the above situation.

## CONCLUSIONS

(1) With the isentropic and thermal equilibrium assumption, a critical flow model for supercritical pressure is proposed which can calculate critical pressure and critical mass flow rate. This model is also applicable for room temperature water discharge, two phase mixture, superheated steam critical flow.
(2) Considering friction and local resistance, the actual process is not isentropic; a resistance coefficient $C$ is added in the model can be calculated from the CFD simulation.
(3) The maximum error between model prediction results and experiment data are within 10% under supercritical pressure and within 5% under low temperature region at subcritical pressure, illustrating that the model is accurate.
(4) Though the model gives satisfactory result at supercritical flow condition, it is not applicable for two-phase critical flow condition where thermal non-equilibrium effect is dominant.

## DATA AVAILABILITY STATEMENT

All datasets generated for this study are included in the article.

## AUTHOR CONTRIBUTIONS

YL was mainly responsible for critical flow model derivation and verification, data collection, and paper drafting. MZ mainly contributed to the model derivation design, critical flow test conduction under sub-critical pressure. KD was mainly responsible for paper review and modification.

## ACKNOWLEDGMENTS

The present investigation is supported by the National Key R&D Program of China (2018YFE0116100). The authors wish to thank the CIAE team who performed the critical flow test under supercritical and subcritical pressure and provided the test data for the model validation. Special thanks to Professor Chen Yuzhou who contributed so much data for this paper.

## REFERENCES

Abdollahian, D., Healzer, J., Janssen, E., Amos, C., and Levy, S. (1982). EPRI Report No. NP-2192. Critical flow data review and analysis, final report.

Chen, Y., Yang, C., Zhang, S., Zhao, M., Du, K., and Cheng, X. (2008). "An experimental study of critical flow of water at steady-state with pressure of up to 22 MPa," in Proceedings of the 7th international symposium of heat transfer, Beijing, October 26–29, 2008.

Chen, Y., Yang, C., Zhang, S., Zhao, M., Du, K., and Cheng, X. (2009). Experimental study of critical flow of water under near-critical and supercritical pressures. *Front. Energy Power Eng.* 3, 175–180. doi:10.1007/s11708-009-0029-6

Chen, Y., Zhao, M., Yang, C., Bi, K., Du, K., and Zhang, S. (2012). Research on critical flow of water under supercritical pressures in nozzles. *J. Energy Power Eng.* 6, 201–208.

Dobran, F. (1987). Non-equilibrium modeling of two-phase critical flows in tubes. *J. Heat Transf.* 109, 731–738. doi:10.1115/1.3248151

Fauske, H. K. (1962). Contribution to the theory of two-phase, one-component critical flow. Ph.D. Thesis.

Henry, R. E., and Fauske, H. K. (1971). The two-phase critical flow of one composition mixtures in nozzle, orifices, and short tubes. *J. Heat Tran.* 93, 179–187. doi:10.1115/1.3449782

Lee, D. H., and Swinnerton, D. (1983). Report No. EPRI NP-3086. Evaluation of critical flow for supercritical steam-water.

Mignot, G., Anderson, M., and Corradini, M., (2008). Critical flow experiment and analysis for supercritical fluid. *Nucl. Eng. Technol.* 40 (2), 133–138. doi:10.5516/net.2008.40.2.133

Moody, F. J. (1965). Maximum flow rate of a single component, two-phase mixture. *Trans. ASME J. Heat Transf.* 87, 134–141. doi:10.1115/1.3689029

Richter, H. J. (1983). Separated two-phase flow model: application to critical two-phase flow. *Int. J. Multiphase Flow.* 9 (5), 511–530. doi:10.1016/0301-9322(83)90015-0

Starkman, E. S., Schrock, V. E., Neusen, K. F., and Maneely, D. J. (1964). Expansion of a very low quality two-phase fluid through a convergent-divergent nozzle. *J. Basic Eng.* 86 (2), 247–254. doi:10.1115/1.3653047

Zhao, M., Li, W., and Lv, Y. (2015). China National Nuclear Corporation Excellent Military Report. Research of steady state critical flow test.

**Conflict of Interest:** The authors declare that the research was conducted in the absence of any commercial or financial relationships that could be construed as a potential conflict of interest.

frontiers in Energy Research

ORIGINAL RESEARCH
published: 21 December 2020
doi: 10.3389/fenrg.2020.503918

# Simulation of a Station Blackout Accident for the SMART Using the CINEMA Code

*Hyoung Tae Kim*, Jin Ho Song and Rae-Joon Park*

*Korea Atomic Energy Research Institute, Daejeon, South Korea*

SMART is a small-sized integral type PWR containing major components within a single reactor pressure vessel. Advanced design features implemented into SMART have been proven or qualified through experience, testing, or analysis according to the applicable approved standards. After Fukushima accident, a rising attention is posed on the strategy to cope with a Station Blackout (SBO) accident, which is one of the representative severe accidents related to the nuclear power plants. The SBO is initiated by a loss of all offsite power with a concurrent failure of both emergency diesel generators. With no alternate current power source, most of the active safety systems that perform safety functions are not available. The purpose of SBO analysis in this paper is to show that the integrity of the containment can be maintained during a SBO accident in the SMART (System-integrated Modular Advanced ReacTor). Therefore, the accident sequence during a SBO accident was simulated using the CINEMA-SMART (Code for INtegrated severe accidEnt Management and Analysis-SMART) code to evaluate the transient scenario inside the reactor vessel after an initiating event, core heating and melting by core uncovery, relocation of debris, reactor vessel failure, discharge of molten core, and pressurization of the containment. It is shown that the integrity of the containment can be maintained during a SBO accident in the SMART reactor. It has to be mentioned that the assumptions used in this analysis are extremely conservative that the passive safety systems of PSIS and PRHRS were not credited. In addition, as ANS73 decay heat with 1.2 multiplier was used in this analysis, actual progression of the accident would be much slow and amount of hydrogen generation will be much less.

**Keywords: SBO (station black out) accident, SMART reactor, CINEMA code, reactor safety, severe accident analysis**

OPEN ACCESS

***Edited by:***
*Arun Kumar Nayak,*
*Bhabha Atomic Research Centre (BARC), India*

***Reviewed by:***
*Mingjun Wang,*
*Xi'an Jiaotong University, China*
*Ivo Kljenak,*
*Institut Jožef Stefan (IJS), Slovenia*
*Liangming Pan,*
*Chongqing University, China*

****Correspondence:***
*Hyoung Tae Kim*
*kht@kaeri.re.kr*

***Specialty section:***
*This article was submitted to Nuclear Energy, a section of the journal Frontiers in Energy Research*

***Received:*** *10 October 2019*
***Accepted:*** *24 November 2020*
***Published:*** *21 December 2020*

***Citation:***
*Kim HT, Song JH and Park R-J (2020) Simulation of a Station Blackout Accident for the SMART Using the CINEMA Code. Front. Energy Res. 8:503918. doi: 10.3389/fenrg.2020.503918*

**Abbreviations:** AC, alternate current; ACSS, ancillary containment spray system; ADS, automatic depressurization system; AFWS, Auxiliary Feed Water System; CFS, cavity flooding system; CINEMA-SMART, Code for INtegrated severe accidEnt Management and Analysis-SMART; DCH, direct containment heating; DL2, Design Level 2; ECT, emergency cool down tank; CT, compensating tank; EDGs, emergency diesel generators; ERVC, external reactor vessel cooling; FAP, fuel alignment plate; FW, feed water; KAERI, Korea atomic energy research institute; LCA, lower containment area; LWR, light water reactor; MPI, message passing interface; NSSS, nuclear steam supply system; PAR, passive auto-catalytic re-combiner; PRHRS, passive decay heat removal systems; PSIS, passive safety injection system; RCP, reactor coolant pump; RCS, reactor coolant system; RPV, reactor pressure vessel; RRT, radioactive material removal tank; SA, severe accident; SBO, station blackout; SMART, system-integrated modular advanced reactor; SRVs, safety relief valves; TLOFW, total loss of feed water; UCA, upper containment area; UGS, upper guide structure

## INTRODUCTION

The KAERI (Korea Atomic Energy Research Institute) started developing SMART (System-integrated Modular Advanced ReacTor) (IAEA, 2005; Kim et al., 2014) in 1997, aiming to export it to countries with small electric grids and water supply issues. SMART is a small-sized integral type PWR with a rated thermal power of 365 MWt, which adopts a sensible mixture of new innovative design features and proven technologies aimed at achieving highly enhanced safety and improved economics.

SMART is an integral-type reactor containing major components within a single reactor pressure vessel, as shown in **Figure 1**. Eight (8) modular-type once-through steam generators consist of helically coiled tubes producing 30°C superheated steam under normal operating conditions, and a small inventory of secondary side water sources at the steam generator prohibit a return to power following a steam line break accident. Four (4) reactor coolant pumps with a canned motor, which has no pump seals, inherently prevents a loss of coolant associated with a pump seal failure. Four (4) channel control rod position indicators contribute to the simplification of the core protection system and to an enhancement of the system reliability. The in-vessel pressurizer is designed to control the system pressure at a nearly constant level over the entire design basis events.

The SMART design has several levels of protection and multiple barriers to prevent releases of radioactive materials and to minimize the possibility of failures leading to significant radiological consequences. It is enhanced in requiring to consider the severe accident prevention and mitigation features in the design stage for a high level of safety and reliability, which is especially emphasized after Fukushima accident.

After Fukushima accident, a rising attention is posed on the strategy to cope with a Station Blackout (SBO) accident, which is one of the representative severe accidents related to the nuclear power plants. The SBO is initiated by a loss of all offsite power with a concurrent failure of both Emergency Diesel Generators (EDGs). With no Alternate Current (AC) power source, most of the active safety systems that perform safety functions are not available.

The SMART adopts passive residual heat removal system (PRHRS) to reinforce the capability of mitigating beyond design-basis accidents, such as a SBO accident. The PRHRS consists of four independent trains with 50% of the heat removal capacity for each train. Two trains are sufficient to remove the decay heat generated in the primary system after the reactor trip. Each train is composed of an emergency cool down tank (ECT), a condensation heat exchanger, a compensating tank (CT), and several valves, pipes, and instrumentations.

The purpose of SBO analysis in this paper is to show that the integrity of the containment can be maintained during a SBO accident in the SMART. Therefore, the accident sequence during a SBO accident was simulated using the CINEMA-SMART (Code for INtegrated severe accidEnt Management and Analysis-SMART) (Kim et al., 2017; KAERI, 2018) code to evaluate the transient scenario inside the reactor vessel after an initiating event, core heating and melting by core uncovery, relocation of debris, reactor vessel failure, discharge of molten core, and pressurization of the containment.

This paper describes the CINEMA-SMART calculation results of accident sequences in the reactor vessel and the containment when a SBO accident occurs in the SMART. This calculation analyses the SBO accident involving the core damage due to a failure of actuating all safety systems except for the reactor trip, and presents the result. The present calculation is based on the DL2 (Design Level 2) (Lee, 2018) of SMART and has been performed assuming a loss of the offsite power concurrent with a turbine trip and unavailability of the emergency AC power system, leading to unavailability of all safety injection systems.

The CINEMA-SMART code consists of the in-core phenomenon analysis module, CSPACE [SPACE (KHNP KEPCO E&C KAERI KEPCO NF, 2017) and COMPASS (KAERI, 2018; SMART, 2018a)], the ex-core phenomenon analysis module (SACAP) (KAERI, 2017), and the module to analyze the fission product behavior (SIRIUS) which analyzes the individual phenomenon of a severe accident (**Figure 2**). The analysis modules were developed independently, and the master program [MASTER (KAERI, 2018)] integrates the functions of each module using the MPI (Message Passing Interface) library to analyze the phenomena of severe accidents comprehensively.

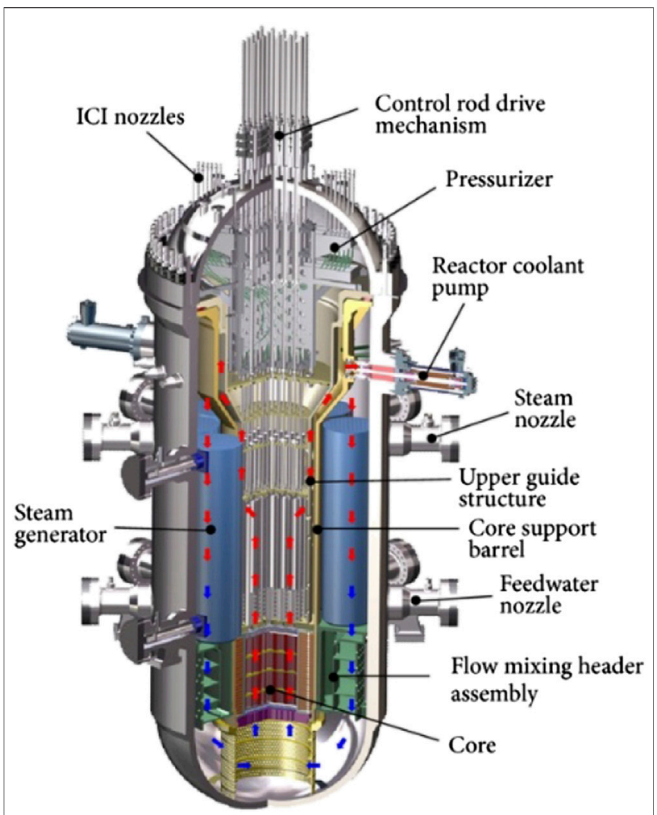


**FIGURE 1 |** SMART reactor vessel assembly.

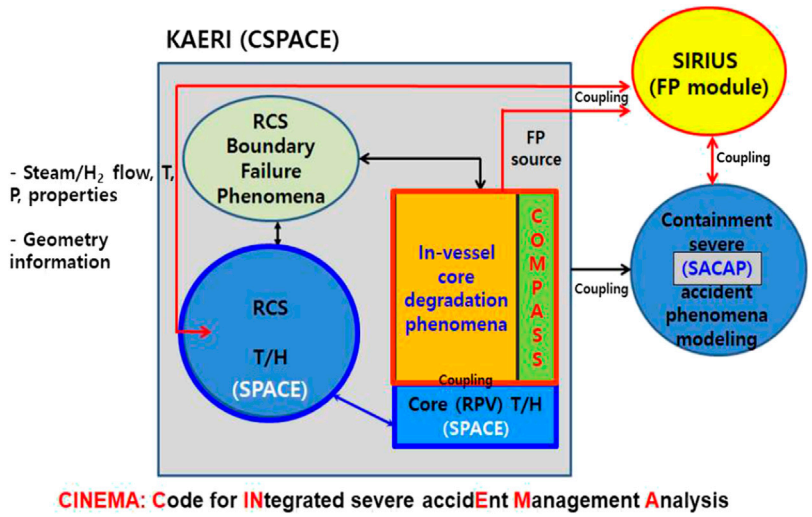


**FIGURE 2 |** Inter link of CINEMA modules.

CSPACE provides the corium and cooling release data from the primary system to SACAP, which predicts the containment behavior to determine the integrity of the containment using the data. SIRIUS simulates the release and transport of fission products from the primary system and containment during the process. The CINEMA-SMART code was verified and validated against existing experimental data on severe accident progression and used for the analysis of APR-1400. Therefore, in this analysis there is no separate verification and validation effort for the CINEMA-SMART code.

However, the version of the codes used in this analysis is different from those used in the analysis of APR-1400. Modifications and improvement are made for COMPASS (SMART, 2018b) and SACAP (SACAP, 2018), which are documented separately. The version of the code are identified with the size and date of the files. The detailed description of input models for CSPACE, COMPASS, SACAP, and MASTER of the CINEMA-SMART code is provided in the reference (SMART-PPE, 2018), where the Total Loss Of Feed Water (TLOFW) accident is simulated. The input deck for simulation of SBO is nearly the same as that in the reference (SMART-PPE, 2018). The only difference between these two input decks is the start of reactor trip. The transient is initiated by the reactor trip in the SBO scenario, while the transient is initiated by a loss of feed water flow in the TLOFW scenario.

## Input Model for CSPACE

A node-flow path network for the modeling of SMART nuclear steam supply system is provided in **Figure 3**. There are two kinds of volume. First kind of volume is used for both SPACE and COMPASS and the second kind of volume is used only for SPACE. For the first kind of volume, SPACE calculates all the thermal thermal-hydraulic conditions, while COMPASS calculates the response of heat structures that COMPASS provides heat flux to and from the SPACE. COMPASS calculates the response of heat structures such as damage and melting of the core and failure of the reactor vessel.

The first modification has to be made to the input for SPACE. We need to define the SAM-Nodes, which are shared by COMPASS and SPACE. The SAM-Nodes includes 25 core nodes of B120-B144, down-comer (FMHA) B145, lower plenum B146, Fuel Alignment Plate (FAP) B147, and Upper Guide Structure (UGS) B148. They should use the keyword SAM in the input. For these nodes CXXX-SAM-2000 card is needed for assigning the power fraction for each node. And heat structures presented in the SPACE have to be taken out because COMPASS will take care of heat structures in those nodes. Also, reference heat structure for KINE-XXX input should be assigned to the heat structures in the SPACE node such as heat structures of the pressurizer. Finally, modifications are needed to adjust minor edits incorporating the changes made above.

Use or Removal of Safety Systems: In the SMART NSSS (Nuclear Steam Supply System) design, various safety systems such as Automatic Depressurization System (ADS), Passive Safety Injection System (PSIS), and Passive Decay Heat Removal Systems (PRHRS) are employed for mitigating the design basis accident. They can also be utilized during the progression into and during the severe accidents.

For SBO accident leading to the core damage, we had to assume that PSIS and PRHRS do not work, since the possibility of failure of the passive safety systems are very low. In the actual scenario, as those safety systems are operable, SBO event would not lead to the core damage. In this analysis, the input cards for thermal-hydraulics and heat structures for describing the operation of PSIS, PRHRS were removed from the SPACE input.

However, ADS was modeled that the operator would open the ADS 30 min after reaching the sever accident management entry condition which is defined as the time when the core exit temperature of C147-01 reach the 650°C (923.15 K). SMART has two ADS lines and the exit of ADS lines are connected to the SIT room 1 and 3. The diameter of orifices of ADS line is

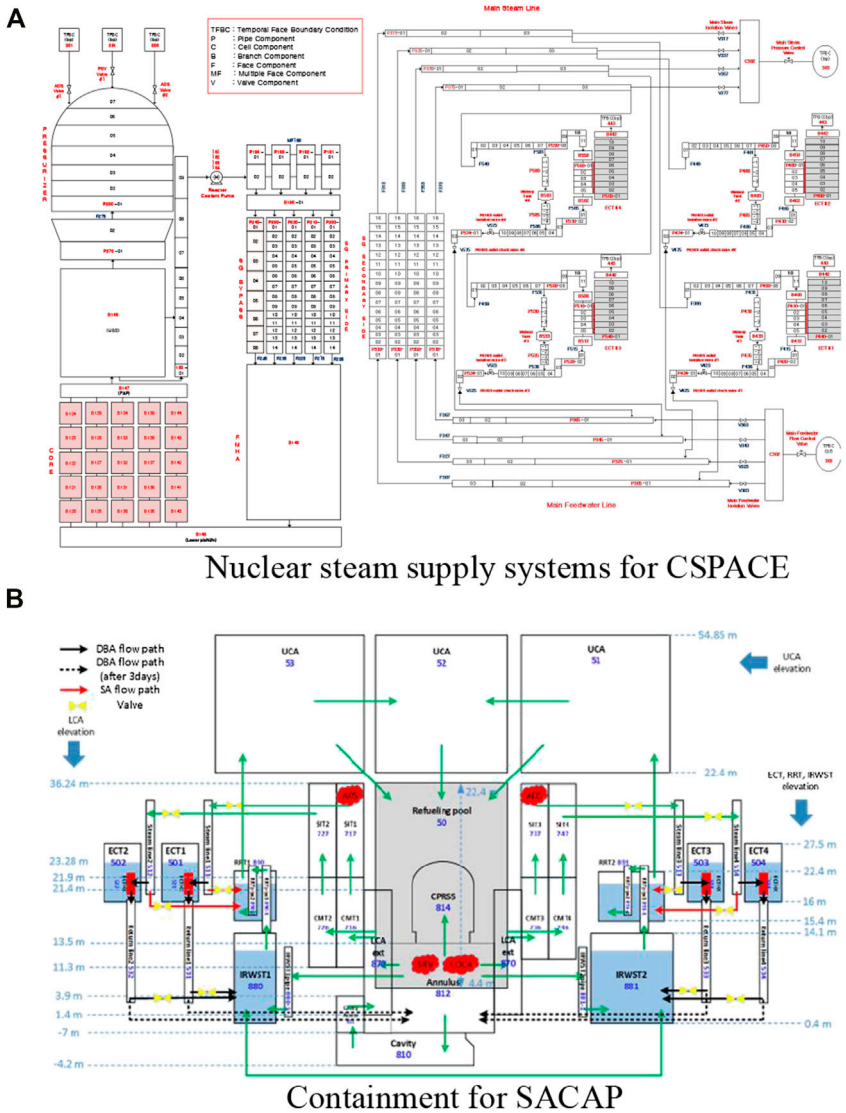


**FIGURE 3 |** Nodalization of SMART365. **(A)** Nuclear steam supply systems for CSPACE. **(B)** Containment for SACAP.

35.6 mm. Based on this are, the flow area of ADS, $9.95382 \times 10^{-4}$, is determined as an input for CSPACE for TFBCs of C281 and C283.

Ransom–Trap model is used for the break flow through the ADS and PSVs. This is because Henry–Fauske model option in the SPACE has an error when non-condensible gas such as hydrogen is included in the break flow. Also, internal choking was not allowed to minimize numerical instability.

Main Steam Relief valves are implemented as a part of PRHRS. Each steam line has one MSRVs that 4 valves are installed in total. The design data is shown in page 40 of the document that inlet line size is 0.75 inch, opening set point is 17MPa with 3% blowdown. These data are incorporated in the C319, C339, C359, and C379 and related input cards for actuation. MSRVs are especially necessary when PRHRS was not working properly that secondary heat removal capability was lost. Especially, during a severe accident with significant core damage hot steam coming from the core would flow through the steam generator that it would heat up and pressurize the confined secondary volume

**TABLE 1 |** Steady-state calculation results.

| Parameter | SMART | CINEMA | Error (%) |
|---|---|---|---|
| Core power [MW] | 365.0 | 365.0 | 0.0 |
| PZR pressure [MPa] | 15.0 | 15.1 | 0.4 |
| PZR level [%] | 70.0 | 70.6 | 0.9 |
| Core inlet/outlet temp. [°C] | 295.5/320.9 | 298.8/324.5 | 1.1/1.1 |
| Total RCS flow [kg/s] | 2,507.0 | 2,420.6 | −3.4 |
| Steam pressure [MPa] | 5.76 | 5.92 | 5.4 |
| FW pressure [MPa] | 6.71 | 6.77 | 0.9 |
| Steam temp. [°C] | 302.3 | 301.5 | −0.3 |
| FW temp. [°C] | 230 | 230.1 | 0.0 |
| Total FW flow [kg/s] | 190.61 | 190.61 | 0.0 |

**TABLE 2 |** Times of major events during a SBO accident.

| Major events | Time (sec) | Note |
|---|---|---|
| Reactor trip | 0 | |
| Main feed water isolation | 0 | |
| RCP trip | 0 | |
| Initial pressurizer SRV opening | 770 | |
| Start of core uncover | 11,450 | |
| Fuel rod dry-out | 13,690 | |
| Entry of severe accident (SA) | 35,725 | When core outlet gas temperature reaches 923.15 K |
| ADS opening | 37,525 | 1,800 s after SA |
| Start of corium relocation | 41,060 | |
| RV rupture | 58,366 | |

between the main steam isolation valve and main feed water isolation valve.

ANS 73 decay heat with 1.2 multiplier instead of ANS79 decay heat (Lee et al., 2014) is used to provide conservative core melt progression.

Addition to the reference case, we performed the sensitivity studies for a PRHRS and operator action time after reaching Severe Accident (SA) entry condition. Since a PRHRS is adopted as a heat sink by a natural circulation in the secondary side instead of Auxiliary Feed Water System (AFWS), the isolation valves connected with the main steam line is open when the primary pressure is below 11.3 MPa. For sensitivity of operator action time, two cases for 0 s and 3,600 s as well as 1,800 s of reference case are simulated.

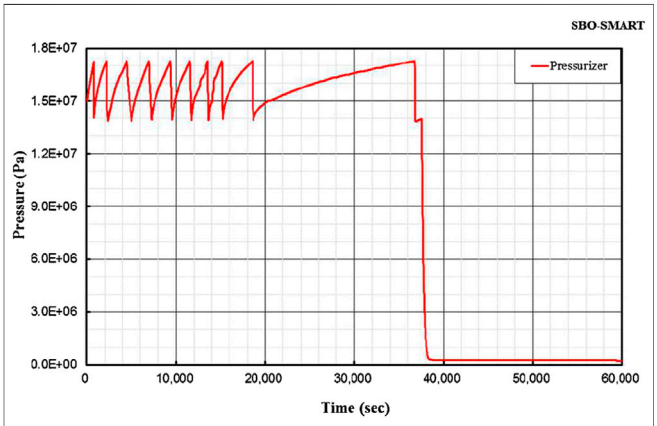


**FIGURE 4 |** Primary RCS pressure.

# CODE SIMULATIONS

## In-Vessel Accident Sequence

The results of steady state calculation are used as the initial conditions of the transient calculation. **Table 1** shows the steady state calculation results compared with the target design values of SMART.

As long as the geometrical information and initial fluid information of the SMART reactor are well implemented in the code calculation, the target steady-state results can be recalculated by the code.

The history of major accident progression for a SBO accident is given in **Table 2**. The SBO occurs at 0.0 s assuming the complete loss of on-site and off-site power. The reactor trip is automatically initiated, from this moment any active system of the plant becomes unavailable in particular the Reactor Coolant Pump (RCP) and the Feed Water (FW) pumps run down. The Automatic opening and closing are repeated when the temperature of the coolant inside the Reactor Coolant System (RCS) rises and the pressure setting of Safety Relief Valves (SRVs) on the top of pressurizer is reached. The safety injection system is not available as well as the recovery of the RCP and FW pump is not performed. From a SBO analysis of a loop type PWR (Wang et al., 2012), it was shown that the availability of passive safety system can remove the core decay heat from the primary loop effectively. However, without any safety systems during a SBO in the SMART reactor, continuous loss of inventory through the pressurizer SRVs results in dry-out of the fuel rods and subsequent heat-up of the reactor core.

The top of the core begins to be exposed at the time of 11,450 s and hydrogen is generated at 38,550 s from the cladding in the fuel rod zone.

The hot water vapor is released and the vapor temperature at the outlet of core is increased to 923.15 K at 35,725 s, which is the Severe Accident (SA) entry condition. It is assumed that the operator opens two out of four Automatic Discharge Valves (ADSs) 1,800 s after the SA entry condition because a portable power generator can provide only one of two electric trains. When ADS valves are opened the RCS is rapidly depressurized below to 1.7 MPa. The accident scenario progresses to core melting, corium relocation to the lower plenum and, eventually, Reactor Pressure Vessel (RPV) failure.

### RCS Pressure

The pressure changes inside the RCS of the primary system is shown in **Figure 4**. The RCS pressure remains high (17.3 MPa, which is the pressurizer SRV opening pressure) showing a cycling trend around the valve opening set point of SRVs. However the RCS pressure is rapidly decreased and maintained to about 0.23 MPa after ADS valve opening.

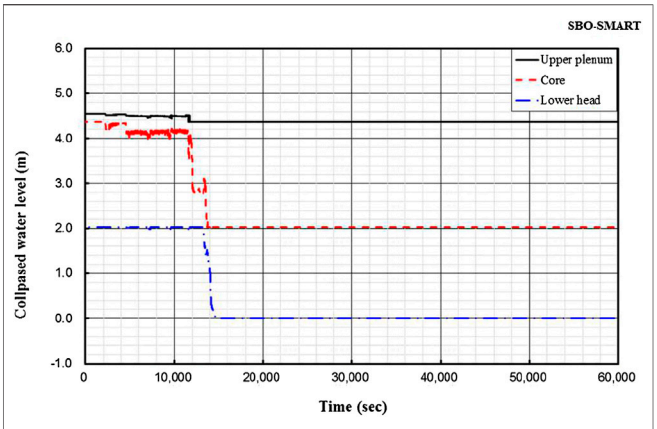


**FIGURE 5 |** Reactor core level.

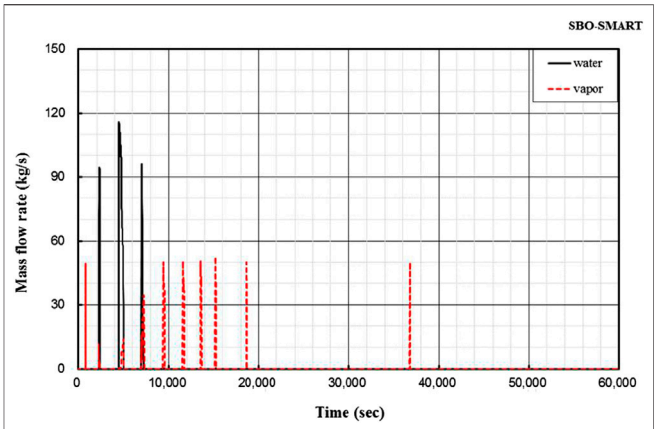


**FIGURE 7 |** Discharge flow rate through SRV.

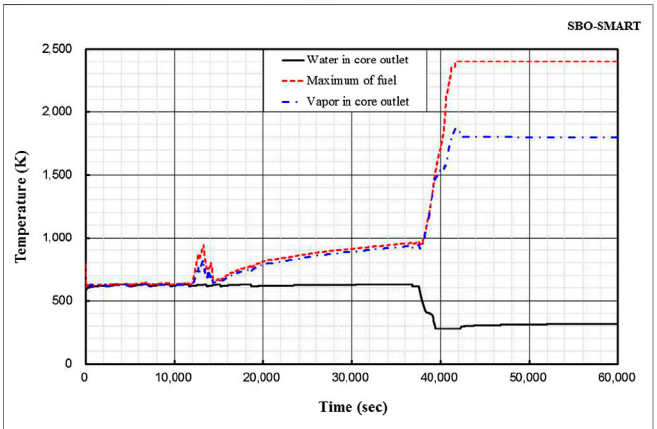


**FIGURE 6 |** Reactor temperature.

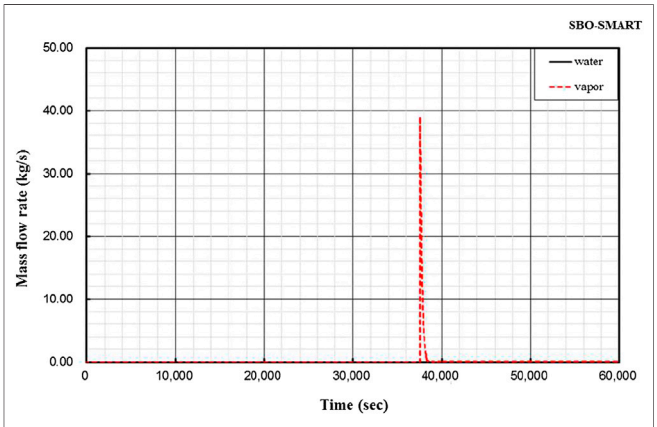


**FIGURE 8 |** Discharge flow rate through ADS valve.

High-pressure corium ejection/direct containment heating is one of the phenomena of severe accidents following the reactor vessel break. The RCS pressure is the key factor affecting this phenomenon. It is shown that the RCS pressure remains lower than 1.7 MPa since the safety depressurization by ADS valves are effective.

The critical pressure to occur Direct Containment Heating (DCH) has been known not to be lower than 2.07 MPa (300 psia) through the experimental studies on the containments of commercial LWR nuclear power plants and, in general, 1.72 MPa (250 psia) is conservatively used. It is shown that when the depressurization system is operated in a SBO sequence, RCS is depressurized up to 1.7 MPa as shown in **Figure 4**, therefore, DCH would not occur.

## Reactor Core Level

**Figure 5** shows the variation in coolant level inside the reactor pressure vessel. The reference point is the bottom of the lower head of the reactor vessel. As the loss of coolant due to automatic opening of POSRV continues, inventory of the coolant decreases smoothly. After the water level of the upper plenum is depleted the core exposure begins from the top side. The water level of the core quickly falls to the bottom of the core at 13,690 s. Note that the levels shown in **Figure 5** below are based on the liquid fraction calculated from the thermal-hydraulic element at the corresponding elevation of the core.

## RCS Temperature

**Figure 6** shows the temperature variation of the coolant in the core area and the lower head of the reactor vessel. The change of the maximum fuel temperature is also taken into account. The temperature variation of the vapor coolant follows that of the heated fuel rods and reaches the maximum, which is the fuel melting temperature (2,400 K). However the water coolant temperature maintains nearly the same but decreases after ADS opening at 37,525 s.

## Discharge Flow Through SRV and ADS Valves

**Figure 7** shows the discharge mass flow through the SRV on the top of the pressurizer. The steam of the RCS starts to release

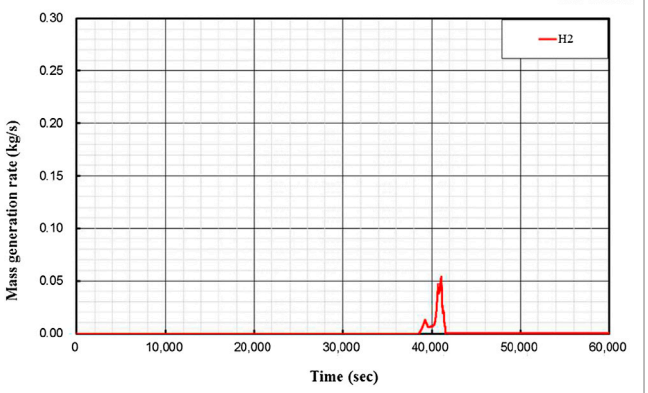


**FIGURE 9 |** Discharge flow rate of $H_2$ through ADS valve.

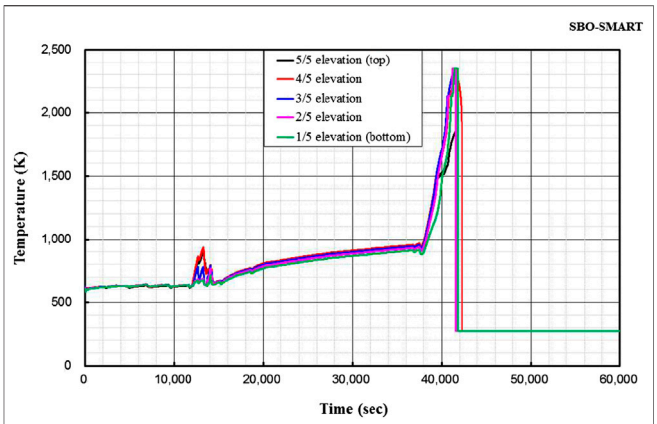


**FIGURE 12 |** Cladding temperature.

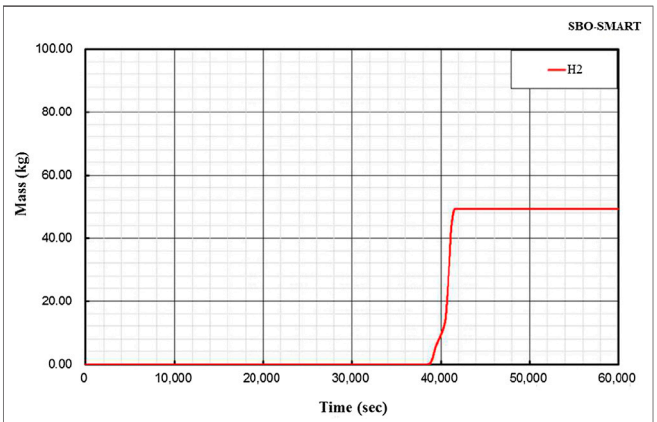


**FIGURE 10 |** Hydrogen mass.

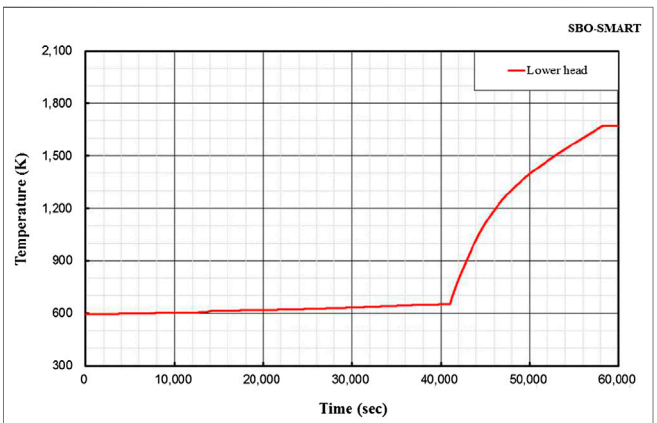


**FIGURE 11 |** Lower head temperature.

from the point of the opening of SRVs. At the beginning of the opening, only release of vapor was found to be about 50 kg/s, followed by the release of the water inventory up to about 116 kg/s. After 7,000 s only the steam is released through the SRVs.

**Figure 8** shows the discharge mass flow through the ADS valves. As the ADS valve starts to open the steam is rapidly released up to 39 kg/s. Any water inventory is not released during the ADS venting. The Ransom–Trapp model is used for the choking option of the SRVs.

## Hydrogen Generation Rate

The fuel cladding temperature rapidly increases with core uncovery when the level in the reactor vessel falls below the active core, and it leads to the oxidation reaction of the clad metal with steam to generate hydrogen.

The hydrogen generation rate inside the reactor vessel is shown in **Figure 9**. The hydrogen generation characteristics due to cladding oxidation depend heavily on the hot cladding-steam contact area characteristics and the depletion of water vapor that are determined by the degree to which the core structure is destroyed. It is also greatly affected by the physical-chemical interaction caused by the mixing of multiple metals and oxide metals at very high temperatures. This information is highly dependent on approach of the core modeling and the thermal-hydraulic modeling between severe accident analysis codes.

The predicted hydrogen production rate from core melt in this SBO accident analysis is predicted to be up to about 0.05 kg/s.

**Figure 10** shows the cumulative hydrogen mass produced in the reactor vessel, and the total mass of hydrogen generation is about 49 kg.

## Lower Head Wall Temperature

**Figure 11** shows the temperature of the inner wall of the reactor vessel lower head. In this calculation, the wall temperature shown in this figure is the average surface temperature over the lower head, since a model is considered to be a single node with uniform properties. It is judged that the average temperature of the lower head is increased smoothly until the start of relocation. After the relocation to the lower head, the wall temperature begins to rise rapidly, and about 17,500 s

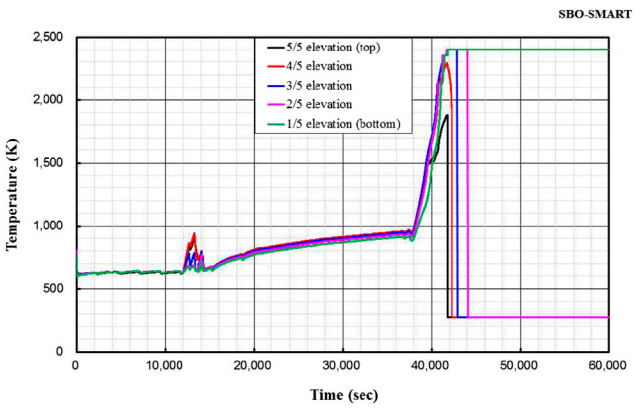


**FIGURE 13 |** Fuel temperature.

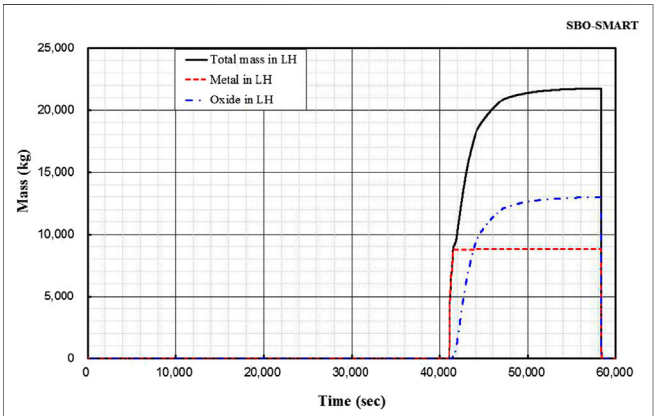


**FIGURE 14 |** Corium mass.

after the relocation, the wall temperature reached the melting temperature of the material and the reactor vessel was expected to break.

## Cladding Temperature

In this analysis, the effective core region by the COMPASS module input is modeled by dividing the effective core section into five rings and five nodes in the radial and axial direction, respectively. Of these, the cladding surface temperature according to the axial position in the central ring is shown in **Figure 12**. The first factor determining the cladding temperature is the exposure of the corresponding node at each elevation. As shown in **Figure 12** the cladding temperatures increase from the start of core uncovery and rapidly increase after opening of ADS valves, since the rapid discharge of core inventory through the ADS valves enhances the core heat up.

The cladding temperatures start to rise with a difference of time after exposure of the core nodes lower than the upper core plenum. The cladding temperatures reach the maximum value corresponding to the melting temperature and decreased to 0 K when the fuel material in the node is relocated and there is no more mass left.

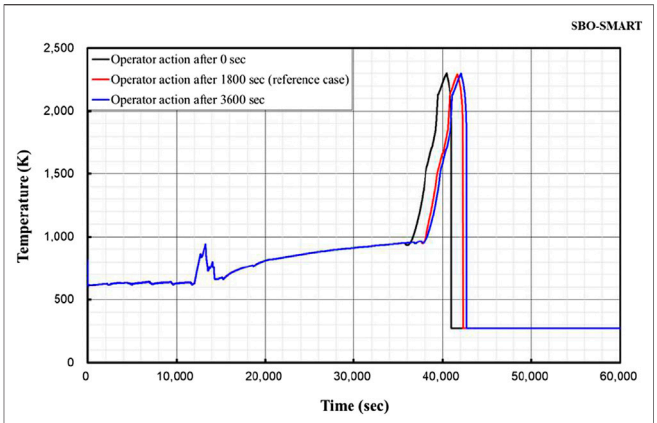


**FIGURE 15 |** Comparison of fuel temperatures for different operator action times.

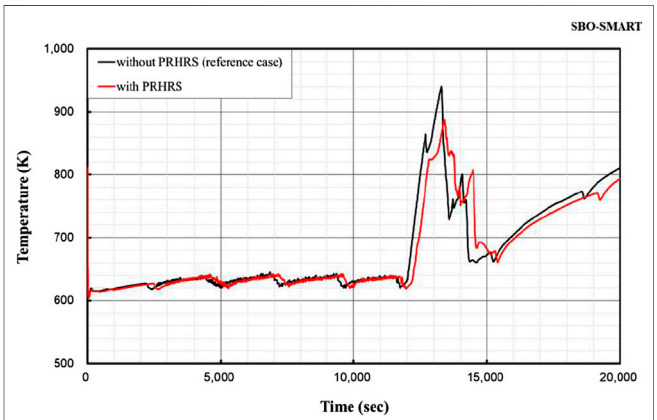


**FIGURE 16 |** Effect of PRHRS operation on the peak fuel temperature before severe accident.

## Fuel Temperature

The fuel temperatures at each axial nodes in the core of the central ring are shown in **Figure 13**. The trend of temperature variation for fuel rods is similar to that of cladding material. The temperature is expressed to be 0 K when the fuel material in the node is relocated and there is no more mass left. The maximum temperature corresponding to the fuel melting temperature is 2400 K.

## Mass of Corium in Lower Head

**Figure 14** shows the variation of corium mass in the lower head of the reactor vessel. At the time of initial relocation, only about 8,767 kg of metal corium is relocated, and after that, the oxide corium starts to be relocated. This is because the melting temperature of the metal corium is lower than that of the oxide corium.

The oxidation corium is continuously relocated following accident progress, and at the time of the reactor vessel damage, it is expected that the oxidation corium eventually increases to about 12,980 kg resulting in a total of

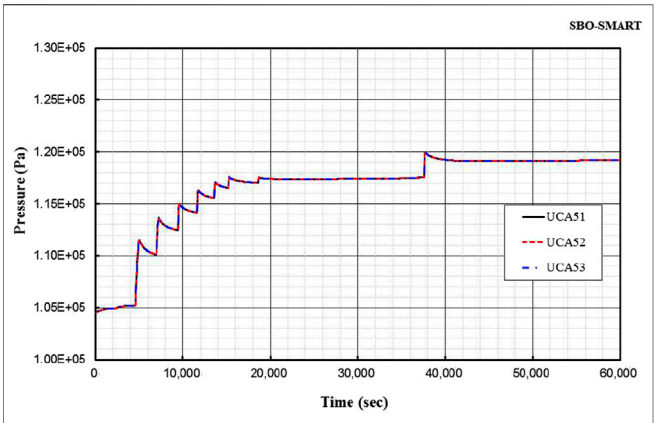


**FIGURE 17 |** Containment pressure in the UCA.

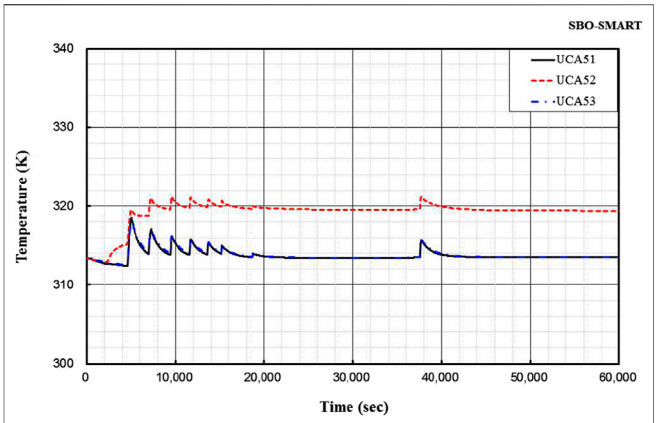


**FIGURE 18 |** Containment temperature in the UCA.

approximately 21,750 kg. Since the melting pool in the lower head is modeled to a single volume, it is possible to verify that all of the melting corium in the lower head is released immediately upon failure of the reactor vessel. At the time of initial relocation, only metallic materials such as Zr, SS and Inconel of which melting temperature is relatively low are melted and relocated to the lower head. And then, the oxide corium such as $UO_2$ is relocated to the lower head.

### Sensitivity Studies

#### *Operator Action Time After Severe Accident Conditions*

Three cases for different opening time for ADS valves after SA condition are simulated and the maximum fuel temperatures for each case are compared in **Figure 15**. As the operator action time to open ADS valves is increased, the heat up of fuel temperature showing the progress of severe accident is also delayed. However, the assumption of 30 min (1,800 s) for reference case is not much different from more delayed case of 3,600 s.

#### *PRHRS Operation*

The fuel temperature behaviors with and without PRHRS are compared in **Figure 16**. After the core exposure begins around 1,300 s (see **Figure 5**) the fuel temperature shows the peak value. When the PRHRS is actuated to remove the decay heat in the secondary side, the peak fuel temperature becomes lower than the reference case without PRHRS.

## Ex-Vessel Accident Progression

### Containment Pressure

**Figure 17** shows the pressure variation in the Upper Containment Area (UCA) of the reactor building. The containment pressure increases as the high pressure of RCS is discharged into the containment by opening and closing of the pressurizer SRV after the accident. After about 20,000 s, the pressure remains nearly constant as about 117 kPa and suddenly increased up to 120 kPa when ADS valves are open. The accident sequence shows the maximum pressure at the time of reactor vessel damage is 119 kPa.

After the RCS inventory is released through the reactor vessel break, it shows a momentary rise due to the inflow of corium discharged through the reactor vessel break.

The total number of PARs (Passive Auto-catalytic Recombiners) and those locations are determined based on the assessment on the hydrogen distributions over the compartments of Low Containment Area (LCA) and UCA during the representative severe accident progression.

The containment pressure decreases gradually since the PAR is successfully actuated. It is shown that the containment integrity is not threatened by the high containment pressure.

### Containment Temperature

**Figure 18** shows the containment temperature in the UCA of the reactor building. The containment temperature follows a similar trend to the containment pressure. However, there is no sudden temperature increase following the reactor vessel break, and the temperature remains below 400 K with a maximum temperature of 321 K throughout the analysis period.

## CONCLUSION

A SBO analysis was performed by CINEMA code that the transient scenario inside the reactor vessel after an initiating event, core heating and melting by core uncovery, relocation of debris, reactor vessel failure, discharge of molten core, and pressurization of the containment were simulated.

When the core is fully molten and most of the core materials relocate to the lower head, the integrity of the reactor vessel is maintained by the External Reactor Vessel Cooling (ERVC) via the coolant surrounding the reactor vessel which is supplied from IRWST after opening the valve of the Cavity Flooding System (CFS). Depressurization of the containment area is done by mainly venting to RRT (Radioactive material Removal Tank) during the severe accident condition. The design such as containment cooling system of the ACSS (Ancillary Containment

Spray System) is considered as a supplementary system for overpressure protection for the extended period.

SMART containment area has very large volume and has open-type internal structure so that hydrogen is mixed well and hydrogen concentration is maintained uniformly at low level. Also, the containment area is designed firmly enough to withstand hydrogen combustion. The accumulated amount of the hydrogen during the severe accident can be reliably controlled by PARs. The containment analysis results are as follows.

- Hydrogen mixing in the containment area is assured.
- It is shown that the uniform hydrogen concentration in the containment area is less than 10% in volume when the hydrogen mitigation system is operated.
- When hydrogen is generated by the reaction between 100% of fuel clad metal and water, the containment integrity is maintained if the hydrogen mitigation system is operated.

Finally, it is shown that the integrity of the containment can be maintained during a SBO accident in the SMART reactor. It has to be mentioned that the assumptions used in this analysis are extremely conservative that the passive safety systems of Passive Safety Injection System (PSIS) and Passive Residual Heat Removal System (PRHRS) were not credited. In addition, as ANS73 decay heat with 1.2 multiplier was used in this analysis, actual progression of the accident would be much slow and amount of hydrogen generation will be much less.

## DATA AVAILABILITY STATEMENT

All datasets generated for this study are included in the article/ Supplementary Material.

## AUTHOR CONTRIBUTIONS

All authors have made a substantial, direct, and intellectual contribution to the work and approved it for publication.

## FUNDING

This work was supported by the National Research Foundation of Korea (NRF) grant funded by the Korea government (Ministry of Science, ICT, and Future Planning) (No. 2012M2A8A4025889).

## REFERENCES

IAEA (2005). *Innovative small and medium sized reactors: design features, safety approaches and R&D trends*. Vienna, Austria: IAEA-TECDOC 1451IAEA.

KAERI (2017). *Development of severe accident containment analysis module, June*. S11NJ16-2-F-PR-5.10.5.

KAERI (2018). *Development document for CINEMA-SMART*. S-916-NB437-001.

KHNP, KEPCO E&C, KAERI, KEPCO NF (2017). *SPACE 3.0 manual 2 user manual*.

Kim, D. H., Song, J. H., Lee, B. C., Na, J. H., and Kim, H. T. (2017). "Development of an Integrated severe accident analysis computer program packages in Korea" in *Proceedings of the 8th European review meeting on severe accident research (ERMSAR-2017)*. Warsaw, Poland.

Kim, K. K., Lee, W., Choi, S., Kim, H. R., and Ha, J. (2014). SMART: the first licensed advanced integral reactor. *J. Energy Power Eng.* 8, 94–102.

Lee, D. H. (2018). *Development of SPACE Input for severe accident analysis of SMART 365 MWth(DL2), Rev. 00*. KAERI/CM-264/2018, Technical Report. Republic of Korea:KAERI.

Lee, S. W., Chung, B. D., Bang, Y-S., and Bae, S. W. (2014). Analysis of Uncertainty quantification method by comparing Monte–Carlo method and Wilk's formula. *Nucl. Energy Technol.* 46, 481–468. doi:10.1021/es302971d

SACAP (2018). *Description of SMART*. KAERI/CM-2677/2018. (CPRSS & Containment) SACAP input.

SMART (2018a). *COMPASS Code Input Calculation for severe accident analysis in SMART*. KAERI/TR-7495/2018.

SMART (2018b). *COMPASS Modeling for severe accident*. KAERI/TR-7496/2018. SMART.

SMART-PPE (2018). *Analysis of TLOFW in*. S-916-NB475-007. SMART-PPE.

Wang, M., Zhao, H., Zhang, Y., Su, G., Tian, W., and Qiu, S. (2012). Research on the designed emergency passive residual heat removal system during the station blackout scenario for CPR1000. *Ann. Nucl. Energy* 45, 86–93. doi:10.1016/j.net. 2019.11.003

**Conflict of Interest:** The authors declare that the research was conducted in the absence of any commercial or financial relationships that could be construed as a potential conflict of interest.

# Advantages of publishing in Frontiers

**OPEN ACCESS**
Articles are free to read for greatest visibility and readership

**FAST PUBLICATION**
Around 90 days from submission to decision

**HIGH QUALITY PEER-REVIEW**
Rigorous, collaborative, and constructive peer-review

**TRANSPARENT PEER-REVIEW**
Editors and reviewers acknowledged by name on published articles

**Frontiers**
Avenue du Tribunal-Fédéral 34
1005 Lausanne | Switzerland

**Visit us:** www.frontiersin.org
**Contact us:** frontiersin.org/about/contact

**REPRODUCIBILITY OF RESEARCH**
Support open data and methods to enhance research reproducibility

**DIGITAL PUBLISHING**
Articles designed for optimal readership across devices

**FOLLOW US**
@frontiersin

**IMPACT METRICS**
Advanced article metrics track visibility across digital media

**EXTENSIVE PROMOTION**
Marketing and promotion of impactful research

**LOOP RESEARCH NETWORK**
Our network increases your article's readership